Structural and Biophysical Studies of Hair Cell Mechanotransduction Proteins

Gilman Dionne

Submitted in partial fulfillment of the
requirements for the degree of
Doctor of Philosophy
under the Executive Committee
of the Graduate School of Arts and Sciences

COLUMBIA UNIVERSITY

2020

ABSTRACT

Structural and Biophysical Studies of Hair Cell Mechanotransduction Proteins

Gilman Dionne

Our senses of hearing, balance, and motion are the result of hair cells that act as cellular accelerometers to transmute mechanical forces into electrical signals for decoding by the central nervous system. To accomplish this task of mechanoelectrical transduction (MET), hair cells use an array of stereocilia that conduct electrical currents in response to mechanical stimuli. At the tips of these stereocilia, hair cells assemble over a dozen protein components to construct a sophisticated nanomachine that couples the movement of their stereocilia with the opening of mechanically gated ion channels. When forces impinge on stereocilia, they pivot at their base, slide past each other, and impart tension on the tip link, a protein linkage that connects the side of one stereocilium to the mechanically gated ion channel of an adjacent, shorter stereocilium.

While this conceptual framework of hair cell of mechanoelectrical transduction has been established, a precise molecular description of the proteins that comprise the machinery is still lacking. A structural understanding of the molecular components of the MET complex and how they function in mechanoelectrical transduction are limited. While previous structural studies on MET-related molecules have been performed, they have not yet produced a clear understanding of the molecular mechanisms underlying MET. The work presented in this thesis seeks to expand our structural descriptions of different components of the transduction machinery, and to validate the functional mechanisms suggested by these descriptions.

The tip link that couples adjacent stereocilia is composed of two large proteins – cadherin 23 and protocadherin 15 (PCDH15). It had previously been demonstrated that the extracellular region of the tip link protein PCDH15 was *cis*-dimeric, yet the molecular details of PCDH15

self-interaction remained elusive despite the existence of structural information for two-thirds of the molecule. Using a series of biophysical experiments and electron microscopy, we revealed that dimerization of the PCDH15 ectodomain is mediated by two distinct interfaces at opposite ends of the molecule. We determined the crystal structure of one of these interfaces, allowing us to engineer monomeric versions of PCDH15 through structure-guided mutations. By expressing these monomeric versions of PCDH15 in hair cells, we were able to demonstrate the functional importance of PCDH15 *cis*-dimerization for transduction.

Within the MET machinery is an elastic element that is in series with the mechanically gated ion channel. While some have postulated the molecular identity of this so-called gating spring to be the tip link proteins, others have cast doubts on this idea due to an apparent mismatch in their stiffness. Along with our collaborators, we performed single-molecule photonic force microscopy studies to directly measure the elasticity of monomeric PCDH15. By analyzing unfolding events observed in these single-molecule experiments, we determined the unfolding behavior of PCDH15 domains. Our results suggested that individual domains of PCDH15 unfold in the force regime of native sound response, and suggest that the domains of PCDH15 and CDH23 can be unfolded in functional hair bundles.

On the cytoplasmic side of the MET machinery, it was recently shown that the cytosolic calcium and integrin-binding proteins CIB2 and CIB3 interact with the MET associated membrane protein TMC1. This interaction has been shown to be critical for MET, but the molecular functions of these proteins remained unknown. Using a series of co-immunoprecipitation experiments and peptide binding assays, we defined the CIB2 binding region of TMC1. By determining the crystal structures of CIB3 and its complex with a TMC1-peptide, we were able to visualize the molecular determinants that allow CIB3 to interact with itself and TMC1. We demonstrate that CIB2 mutations affect the single channel conductance of the MET channel, indicating that CIB2 is a regulator of the MET complex.

Lastly, I sought to develop methods and protocols for producing samples of MET associated membrane proteins TMIE and TMC1 for structural studies, ultimately producing milligram quantities of TMIE. Using multi-angle light scattering, I found evidence that TMIE forms a hexamer. I also explored the potential of using *Caenorhabditis elegans* to generate a sample of native-like TMC protein. Both of these lines of work require continuing experimentation.

Overall, the works presented here provide molecular descriptions of various MET related proteins. Our structural and biophysical studies of PCDH15 revealed the molecular determinates of PCDH15 *cis*-dimerization and enabled us to engineer PCDH15 mutants with novel properties. The helical nature of PCDH15 suggests a mechanism for tip link extension through helical unwinding. Our single molecule investigations of PCDH15 strongly implicate it and CDH23 as the gating spring molecules. Our work with CIB2 establishes it as regulator of TMC1 function, and thus MET properties. The crystal structure of the CIB3:TMC1-peptide complex suggests potential mechanisms for this regulation that need to be investigated further.

TABLE OF CONTENTS

LIST OF FIGURES AND TABLES

ACKNOWLEDGMENTS

I owe so much to my advisor Larry Shapiro. Over the years he has provided me with endless guidance with my projects that has been clever, keen, and correct. He has also provided me with a plethora of advice for life outside the lab that is often suspect and questionable. I have learned more than I thought possible from Larry. All of our conversations are memorable, and I am sure I will have difficulty convincing people I meet in the future that you are in fact a real person who has said all these strange things.

I would like to thank Barry Honig, whose guidance and incite over the years have been invaluable to me. His approach to thinking about scientific problems is one I can only hope to emulate in my future endeavors. I am in his debt, as all of my future presentations are vastly improved by having him at lab meetings to offer poignant critiques about how to be a more effective presenter.

The vast majority of the work presented in this thesis would not have been possible without the counsel of my collaborators Ulrich Müller and Jim Hudspeth. It has been such a privilege and honor to learn and work with Jim and Uli, who are titans in the field of hair cell biology. They have provided me a greater understanding of my work, and have been an inspiration for the type of scientist I strive to be.

I must thank my Master's advisor Vikki Robinson, without whom I would not have been at Columbia. Her mentorship and tutelage helped laid the foundation for me to pursue my doctoral studies. By letting me into her lab, I was able to get the research experience that was invaluable for getting into Columbia.

My time in Larry's lab would not have been the same with out the amazing people that comprise it. Kerry Goodman was my first mentor and friend in the lab. Her instruction allowed

me to quickly acclimate to the lab and become independent. Julia Brasch and Oliver Harrison were huge sources of inspiration, carrying out some of the most beautiful experiments that assured me that joining Larry's lab was the right decision. Phini Katsamba and Göran Ahlsén have helped me achieve a number of the scientific goals I had for my projects, as well have being wonderful friends. Seetha Mannepalli and Fabiana Bahna are lifesavers, helping me many times when I could not get key molecular biology tasks done. Site-direct mutagenesis still gives me trouble, but they can do like magic. Micah Rapp is the man. I learned so much about cryo-em from him and have always enjoyed our talks about experiments to push the boundaries of what's currently possible. Filip Cosmanescu has been a great friend in the lab, even if he deserves all of the verbal torment I have given him. It has been a privilege to be mistaken for Jared Sampson so often. I can't think of a more genuine and smart person I would want to be confused for. Saurabh Patel has provided me with much needed guidance, particularly when it comes to handling Larry. Lastly, it has been an absolute joy to work with Ryan, Natalie, Jude and Seniha; while the members of lab have changed over the years, these newer members make me excited to see what great things are coming next for the Shapiro Lab.

I owe the fact that my sanity remains in tact after all these years to the wonderful friends I have made through out this process. I was honored to live and commiserate with Filip Cvetkovski. I cherish all our conversations at the kitchen table and complaining about the entire process. I owe a shout out to Ed Twomey, who is a both an amazing friend and severe threat to my liver. I also want to thank Arvin, Nathan, Tal, Ethan, and Chelsea for being great friends during my thesis work.

I also want to thank my friends from undergrad who have helped to support me from a distance: Dwyer and Connie, Pete and Laura, Matt, Will and Meg, and Sam and Krissy. I had the great blessing to still be apart of many of their major life events, which served as constant reminders of what is still in store for me.

I want to also thank my family. I can never repay my mom and dad for supporting me through this entire strange process. I owe a lot of my drive to my brothers, Mike and Brendan. By being born before me, you have provided me the need to do something to stand out. I also had the best encouragement from my Aunt Kate and Babci (grandmother), who always wanted me to go into the world to pursue my dreams, in spite of the concerns from my mother.

Even though she cannot read, I need to thank my dog Eevee. While she isn't much of a talker, she has been my companion through this entire process. For putting up with all of my odd hours and city living, she deserves her own Ph.D.

Lastly, I cannot thank enough my truly marvelous girlfriend, Allie. I struggle to find the words to express how much your love and support have helped me get to where I am. I can honestly say that without you, this thesis would have taken much longer and would not have been near as good as it is. But now that it's done, I can't wait for what's ahead of us.

– Chapter 1–

Introduction

1.1 Introduction

Our sense of hearing confers us with the ability to perceive sounds, gauge their intensities, and distinguish their frequencies. When reduced to its most fundamental elements, hearing is the conversion of mechanical energy into an electrophysiological signal, a process termed mechanoelectrical transduction or MET. This process of transduction, and the highly specialized cells that perform this task, have been the focus of extensive research over the last half-century. Over this time, our understanding of this fascinating and intricate process has grown immensely, yet there remain plenty of outstanding questions have not been answered. In particular, our molecular descriptions of the various protein components that comprise the transduction machinery are astonishingly limited. Presented in this thesis are structural and biophysical investigations of molecular components involved in mechanoelectrical transduction.

1.2 An Overview of Hair Cell Physiology and Mechanoelectrical Transduction

Various anatomical structures endow organisms with the ability to detect a diverse array of mechanical perturbations, enabling them to utilize the information contained in these stimuli to inform their behavior. In fishes and amphibians, the lateral line organ allows for these organisms to detect movement and pressure gradients in their aquatic environments. The sensory information encoded by this system allow fish to detect nearby predators as well as sources of food, and it is required for proper shoaling and schooling behavior in social fish (Faucher et al., 2010). In the inner ear of vertebrates, the vestibular system detects accelerations experienced by the head of the organism. These include linear accelerations (from translational motion), angular acceleration (from rotational motion), and acceleration due to gravity. The information relayed to an organism by the vestibular system is critical for its proper orientation, movement through space, and balance. A few organisms use their vestibular system to detection of some low-frequency vibrations. Similarly, the auditory system of vertebrates allows for the detection of vibrations from sound waves.

At the heart of all these mechanosensory systems are hair cells, a highly specialized type of epithelial cell capable of transducing these various mechanical inputs into electrochemical signals used in biological systems. On the apical surface of hair cells protrudes the hair bundle, a collection of membrane-covered projections that act as mechanical sensors. Each of the aforementioned sensory systems utilize hair cells as cellular accelerometers, coupling their hair bundles to highly specialized anatomical features that allow for the detection of specific mechanical forces.

1.3 Anatomical Descriptions of Mechanosensory Organs

The lateral line systems of fish and some life stages of amphibians consists of a set of mechnosensitive structures called neuromasts that decorate an animal's sides, as well as their heads and tailfins (Figure 1.1A). Neuromasts can either be exposed directly to the environment, or reside in fluid filled canals. Each neuromast contains a number of hair cells, whose hair bundles are connected to a structure called the cupula. Forces due to the flow of fluids around the neuromast or sheering forces from pressure waves causes movement of the cupula which is detected by the hair cells in the neuromasts, allowing for the sensation of movement or other disturbances in an aquatic environment (Bleckmann and Zelick, 2009).

The vestibular system consists of the utricle, the saccule, and the crista ampullaris in the semicircular canals (Figure 1.1B). The utricle and saccule, also referred to as the otolithic organs, are two fluid filled chambers in the inner ear that contain patches of hair cells. The hair cells in these patches are directly connected to the otoconial membrane, a sheet embedded with calcium carbonate crystals (otoconia). The otoconial membranes in the utricle and saccule

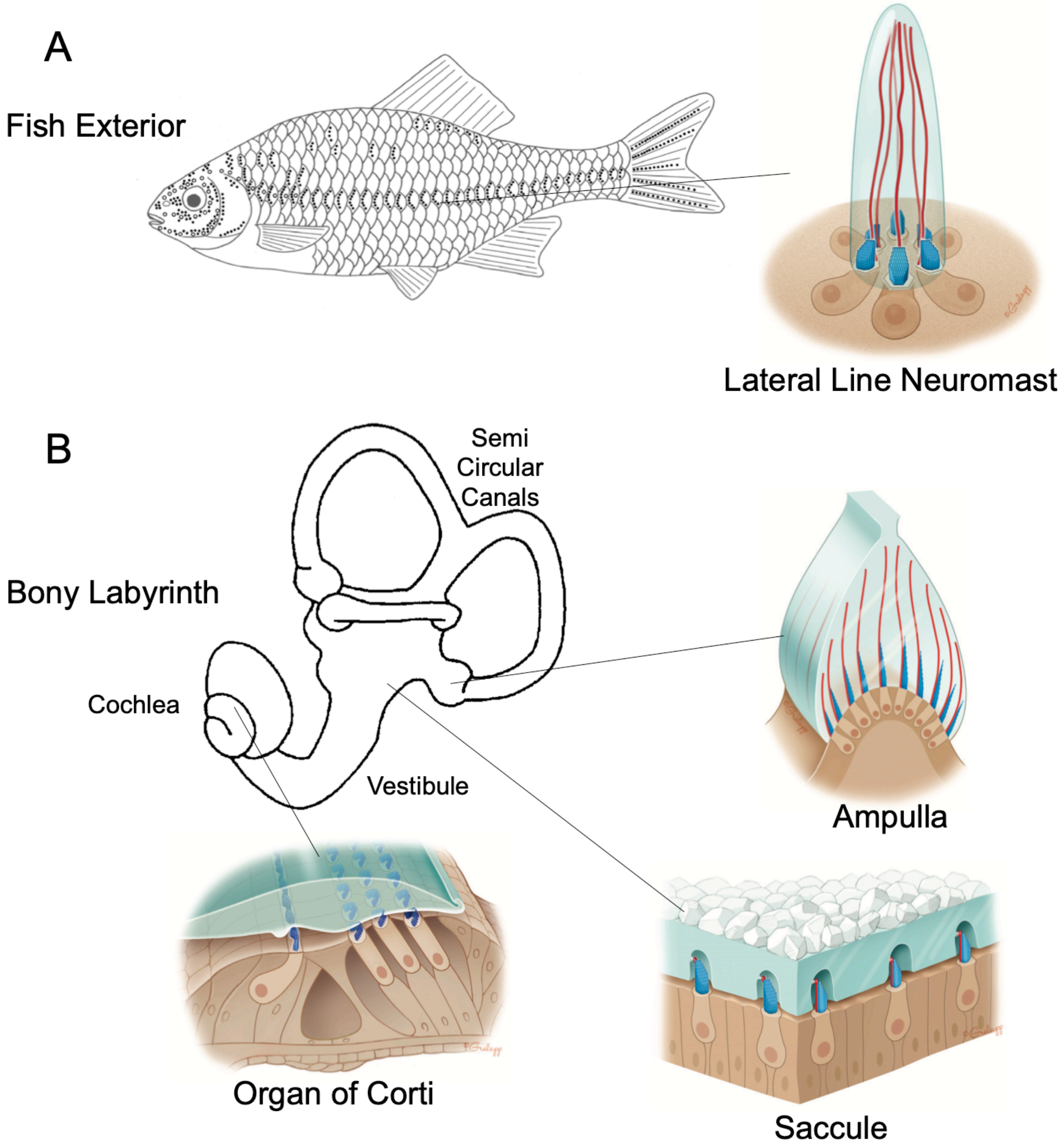

Figure 1.1: Mechanosensitive organs and their arrangement of hair cells
(Top) The lateral line system of fish consists of puncta of sensory epithilia arranged around the exterior of fish. (Bottom) The bony labyrinth consists of three semicircular canal, vestibule, and cochlea. (Images adapted from Bleckmann and Zelick, 2009; O'Maoileidigh and Ricci, 2019; Spoor and Zonneveld, 1998)

provide what would be analogous to a proof mass in a linear accelerometer. When an organism undergoes linear acceleration, the inertia of the otoconia will impart a force on the hair bundles of the attached hair cells. This force is then transduced into a useful electrical signal for the nervous system by the hair cells. Additionally, gravitational forces can also be detected in a similar manner, enabling the detection and orientation of gravitational field. The patches of sensory epithelia in the utricle and saccule are oriented along different orthogonal planes, and as such, detect motions within those planes: the utricle within the horizontal plane, and the saccule along the sagittal plane.

Adjacent to the otolithic organs are the three semicircular canals (Figure 1.1B). Each of these fluid-filled channels are oriented approximately orthogonal to each other along, with one channel aligned to each of the sagittal, coronal, and horizontal planes. At one end of each canal is an enlarged chamber called the ampulla. Inside the ampulla, hair cells are arranged on a small protrusion, the crista ampullaris, with their hair bundles projecting out from the protrusion into a gelatinous cap called the cupula, reminiscent of neuromasts found in the lateral line organ. When an organism rotates its head, the inertia of the fluid in the canals resists the motion and imparts a force on the hair bundles; similarly the fluid imparts a force again when the organisms head stops rotating and the fluids inertia keeps it in motion. An organism uses this detection of fluid motion in the semicircular canals to detect rotations of its head.

The detection of auditory stimuli involves the deconvolution of sound waves into their component frequencies and the subsequent detection of these components. In mammals, this process is carried out in the spiral-shaped cochlea (Figure 1.1B). Inside the cochlea are three parallel fluid-filled channels, the scala tympani, scala media, and scala vestibuli (Figure 1.2A). Separating the scala media and scala tympani is the basilar membrane, a sheet of epithelial tissue whose dimensions and stiffness varies along the length of the cochlea. This variation in mechanical properties allow the basilar membrane to act as a both a band-pass filter and an amplifier, separating and increasing the signal of a particular frequency, the characteristic frequency, at a given point along the length of the cochlea (Hudspeth, 1985; Sellick et al., 1982; von Bekesy, 1970). The delineation of distinct character frequencies to a particular position along the cochlear length is known as the tonotopic map or gradient (Figure 1.2B). A number of processes and anatomical features work in concert with the band-pass properties of the basilar membrane to aid in improving the resolution and amplification of characteristic frequencies along the tonotopic map.

Running along the length of cochlea is the organ of Corti, the epithelial structure responsible for mechanosensation. The organ of Corti contains two distinct types of hair cells, Inner Hair Cells (IHC) and Outer Hair Cells (OHC), as well as the tectorial membrane (Figure 1.2A). The cochlear hair cells are stimulated by differential movement between the basilar membrane, which is basal to the hair cells, and the tectorial membrane at their hair bundles, apical to the hair cells. The hair bundles of OHCs are directly attached to the tectorial membrane, while the hair bundles of IHC are simply proximal. While both IHCs and OHCs are mechanosensitive, OHC do not relay any electrical signals to the central nervous system. Instead, they act as preamplifiers, utilize somatic electromotility to contract when stimulated and increase the mechanical signal for the IHCs (Ashmore, 1987; Hudspeth, 1997; Johnson et al., 2011; Zenner, 1986). IHCs are the true sensory cells, and through afferent neurons, transmit sensory information to the central nervous system.

Birds and reptiles do not have a true spiral cochlea, but instead posses an analogous structure that is shorter and linear called a lagena. Additionally, while birds and reptiles do not

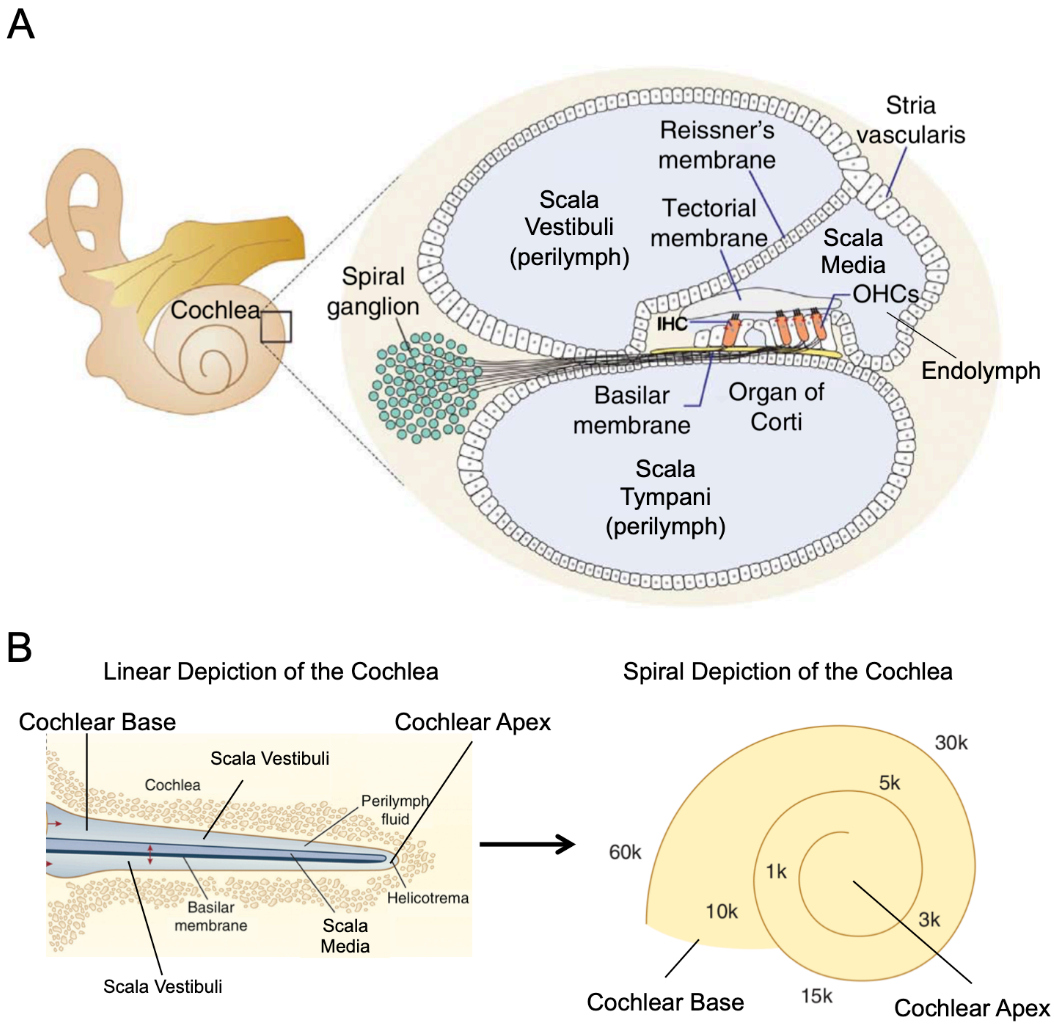

Figure 1.2: Diagram of a cochlea cross section
(A) The mammalian cochlea contains three parallel ducts – the scala vestibuli, scala media, and scala tympani – that are coiled up. The Reissner's membrane separates the scala vestibuli and scala media. The basilar membrane separates the scala media, and scala tympani. In the organ of Corti the mechosensitive hair cells are sandwich between the basilar membrane and the tectorial membrane, which drapes over the tops of the hair cells (Adapted from Xiong et al., 2014). (B) Sound waves move through cochlea as a traveling wave, whose component frequencies are separated in part by the basilar membrane. Different locations on the cochlea corresponded to different characteristic frequencies. By adopting a coiled shape, the structure can be more compact (Adapted from Fettiplace, 2017; Fettiplace and Kim, 2014).

possess a proper organ of Corti, they have a homologous structure referred to as the basilar papilla, which is similar apart from a few key differences. Reptiles have a single type of auditory hair cell, while Aves have two types, referred to as tall and short hair cells. These tall and short hair cells are either predominantly afferently enervated or efferently enervated, respectively (Tanaka and Smith, 1978).

Regardless of the organ in which a hair cell resides, the hair bundle is bathed in an atypical extracellular fluid. Hair bundles are exposed to fluid that is high in potassium, with extracellular potassium levels similar to typical intracellular concentrations. Lateral line organs maintain a high local concentration of potassium in the cupula of the neuromasts (Russell and Sellick, 1976). The hair bundles of cochlea and vestibular hair cells are bathed in endolymph, a fluid high in potassium and low in sodium. The endolymph of the cochlea is additionally noted for having a much lower concentration of calcium, approximately 20-40 µM, which is similar to the 30 µM concentration of calcium found in the cupula of lateral line systems of *Xenopus laevis*. However, despite being continuous with the cochlear endolymph, the vestibule endolymph has an elevated concentration of calcium, approximately 90-130 µM (Bosher and Warren, 1978; McGlone et al., 1979; Salt et al., 1989). Additionally, in the cochlea the endolymph in the scala media is held at large positive potential with respect to the perilymph of the scala tympani (Bosher and Warren, 1971; Koppl et al., 2018). This potential helps drives potassium into hair cells despite the minimal concentration gradient between the endolymph and inside of hair cells.

1.4 The Hair Bundle and Mechanosensation

The hair bundle is an array of modified microvilli termed stereocilia. In mice, these stereocilia are typically 200 µm in width and can range in length from 0.5 µm to 10 µm. However, stereocilial dimensions can vary dramatically between species, mechanosensitive organs, and different positions along the tonotopic gradient (Figure 1.3A) (Fettiplace and Kim, 2014). Within a particular hair bundle, stereocilia of similar height are organized into rows, which are in turn arranged by height. This organizing principle is maintained despite the fact that hair cells of different mechanosensory organs arrange their hair bundles into different shapes. Vestibular hair cells have multiple rows of stereocilia arranged in a circular shape bundle; cochlear hair cells have fewer rows of stereocilia that arranged into 'U' or 'W' shaped bundles (Figure 1.3A and B) (Engstrom and Engstrom, 1978). Hair bundles also contain a single kinocilium, a structure that is morphologically distinct from stereocilia as it is a true cilium. The kinocilium is on one side of the hair bundle, positioned toward the center of the tallest row of stereocilia. Kinocilia can also vary dramatically in length, from a few microns to tens of microns (Fontilla and Peterson, 2000). Kinocilia are extensively connected to hair bundles and couple hair bundles to other functionalizing structures such as the cupula or otolithic membranes. While most hair cells have a kinocilium, the kinocilium of mammalian cochlear hair cells degrades and is not present after the maturation of hair bundle.

When the hair bundle is pushed in the direction that runs from the shortest row of stereocilia toward the kinocilium (or tallest row), an inward electrical current can be measured in hair cell (Shotwell et al., 1981). Mechanical stimulation of hair cells displays anisotropic sensitivity, as electrical response to off-axis stimuli falls off in a angular dependent manner (Corey and Hudspeth, 1983a). This transduced current is dependent only on the stereocilia, as evident by the lack of kinocilia in adult mammalian cochlear hair cells and from experiments in which physical removal of the kinocilium did not disrupt MET (Hudspeth and Jacobs, 1979).

Being related to microvilli, stereocilia are filled with a rigid skeleton of a near-crystalline and highly cross-linked bundle of actin filaments. As a result of this actin scaffold, stereocilia do

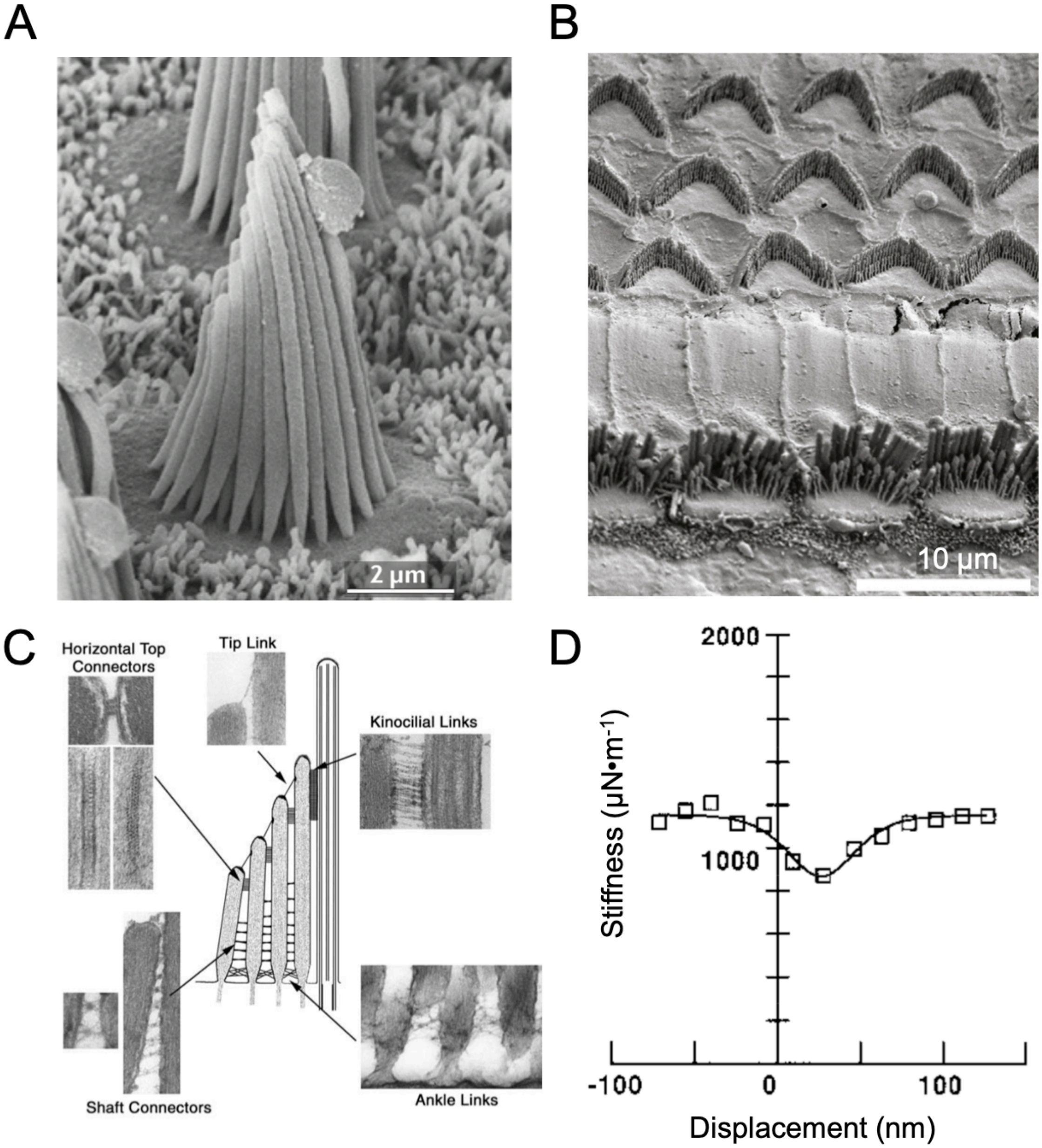

Figure 1.3: Different Hair Bundle Morphologies, hair bundle linkages, and stiffness measurements
(A) Hair bundle from a Bullfrog Saccule Hair Cell. (B) W-shaped hair bundles from Outer Hair Cells, top, and U-shaped hair bundles Inner Hair Cells, bottom, from an adult mouse organ of Corti. (C) Schematic diagram of a hair cell bundle depicting the location, arrangement, and example TEM micrographs of the various hair bundle linkages. TEM images of these linkages (D) Measurement of hair bundle stiffness with characteristic decrease in stiffness known as the gating compliance (Images adapted from Howard and Hudspeth, 1988; Hudspeth, 2014; McGrath et al., 2017; Nayak et al., 2007).

not bend or deform, but rather they pivot at their base with the hair bundle moving as a unit (Howard and Ashmore, 1986). This deflection of the hair bundle is associated with a particular mechanical stiffness, i.e. a spring-like behavior. This stiffness of hair bundles, which is on the order of a few hundred $\mu N \bullet m^{-1}$, varies markedly between species, sensory organ, and characteristic frequency (Crawford and Fettiplace, 1985; Flock and Strelioff, 1984; Howard and Hudspeth, 1988; Tobin et al., 2019). The stiffness of hair bundles varies nonmonotonically with external calcium concentrations, reaching a maximum stiffness when the hair bundle is exposed to calcium concentrations in the low tens of micromolar (Beurg et al., 2008; Marquis and Hudspeth, 1997). When the hair bundle is deflected along the mechanosensitive direction a measurable decrease in stiffness can be detected; this decrease in stiffness is not detected in off-axis deflections (Figure 1.3C) (Howard and Hudspeth, 1988). This increased compliance is associated with the onset of transduction and is interpreted to be the opening of MET channels that are in series with an elastic element, known as the gating spring. This gating compliance is not detected when hair bundles are treated with MET channel blockers, such as the aminoglycoside antibiotics gentamycin or dihydrostreptomycin (DHS), indicating that these compounds lock the channel gate in the open state (Denk et al., 1992; Howard and Hudspeth, 1988; Jaramillo and Hudspeth, 1993). The compliance can also become so great that a hair bundle can exhibit negative stiffness, a curious phenomenon in which the hair bundle will actively move in response to applied force and can even spontaneously oscillate (Kennedy et al., 2005; Markin and Hudspeth, 1995; Martin et al., 2000). This spontaneous oscillation is speculated to be part of an active process of amplification (Bozovic and Hudspeth, 2003; Hudspeth, 2014; Kennedy et al., 2003; Martin et al., 2000).

The stereocilia in an individual hair bundle are interconnected by an assortment of cross linkages that couple neighboring stereocilia and enable the hair bundle to move as a unit (Figure 1.3D) (Reviewed in Richardson and Petit, 2019). These include ankle linkages, shaft connectors, lateral links, kinociliary links, and tip links.

Near the base of stereocilia are the ankle linkages. These are associated with the 690 kDa very large G-protein coupled receptor, VLGR1 (also called GPR98 and ADGRV1), and the 576 kDa USH2A (Adato et al., 2005a; Yagi et al., 2007). However, whether ankle links are formed by an interaction between these two proteins is an outstanding question. Shaft connectors have been associated with the 257 kDa phosphatidylinositol phosphatase PTPRQ; the expression of functionally null constructs of PTPRQ is associated with the loss shaft connectors (Goodyear et al., 2012; Goodyear et al., 2003). While it is possible that PTPRQ ectodomains may constitute the shaft connectors, no biochemical or biophysical experiments have been published that indicate whether or not PTPRQ ectodomains form dimers. Horizontal top connectors, also known as lateral links, have been associated with the 193 kDa protein stereocilin in mice. In addition to forming lateral links, stereocilin connects the tips of OHC stereocilia to the tectorial membrane (Verpy et al., 2011).

The last hair bundle linkages to discuss are the kinociliary links and the tip links. Both of these linkages are *trans* interactions, i.e. coming from opposing membranes, of Protocadherin 15 and Cadherin 23. These proteins will be covered in more depth later in this introduction as well as in chapters 2 and 3. The following are brief discussions of these linkages.

The kinocilium is connected to the hair bundle by an extensive band of linkages between itself and adjacent stereocilia. Measurements from TEM micrographs put the length of these kinociliary links at approximately 150 nm (Furness and Hackney, 1985; Furness et al., 2008).

These links help mechanically couple the stereocilia of the hair bundle to the kinocilium, and are important for hair cells whose stimuli are predominantly conferred via the kinocilium (Fontilla and Peterson, 2000). However, kinociliary links are not directly involved in transduction and are therefore not technically needed.

Tip links emanate from the very tops of stereocilia, span a distance of ~150-200 nanometers, and embed into the side of a nearby taller stereocilium (Pickles et al., 1984). The asymmetric nature of tip links presented an explanation for why hair bundles responsiveness is anisotropic. Pushing on a hair bundle in the short-tall direction put tension on the tip link, which opens the transducer channels; pushing on the hair bundle in the tall-short direction slackens the tip link and promotes channel closure. It was later shown that exposure to calcium chelators such as BAPTA or EGTA disrupted MET currents (Figure 1.4A) (Assad et al., 1991). When the hair bundles of these treated cells were examined in both scanning and transmission electron micrographs, the vast majority of tip links were absent, suggesting that tip links were a necessary component of the MET machinery (Figure 1.4B). This association of tip links with MET function was strengthened by the observation that transduction currents return to BAPTA treated cells after several hours with a corresponding restoration of tip links (Zhao et al., 1996). Recent studies have shown that pulling directly on tip links, without hair bundle deflection, is sufficient to induce MET currents (Basu et al., 2016). The severing of tip links is associated with a decrease in hair bundle stiffness and the loss of the gating compliance, indicating that the tip links are in series with the gating spring and possibly the gating spring itself (Howard and Hudspeth, 1988). In addition to being sensitive to calcium depletion, calcium concentration can modulate the physical length of the tip link (Furness et al., 2008).

High-resolution freeze-etch SEM images provided some clues about the architecture of the tip link. The micrographs show an incredibly fine filament of constant width that displays double helical characteristic, as if two pieces of twine were twisted together (Kachar et al., 2000). This double helical superstructure was supported later by Fourier image analysis of high resolution TEM images of tip links from avian utricule hair cells (Tsuprun et al., 2004). The implication of his double-helical motif was that the tip link is possibly a dimer. However, this dimer interpretation was used to conjecture that the tip link could not be gating spring, as a dimeric molecule would be too stiff.

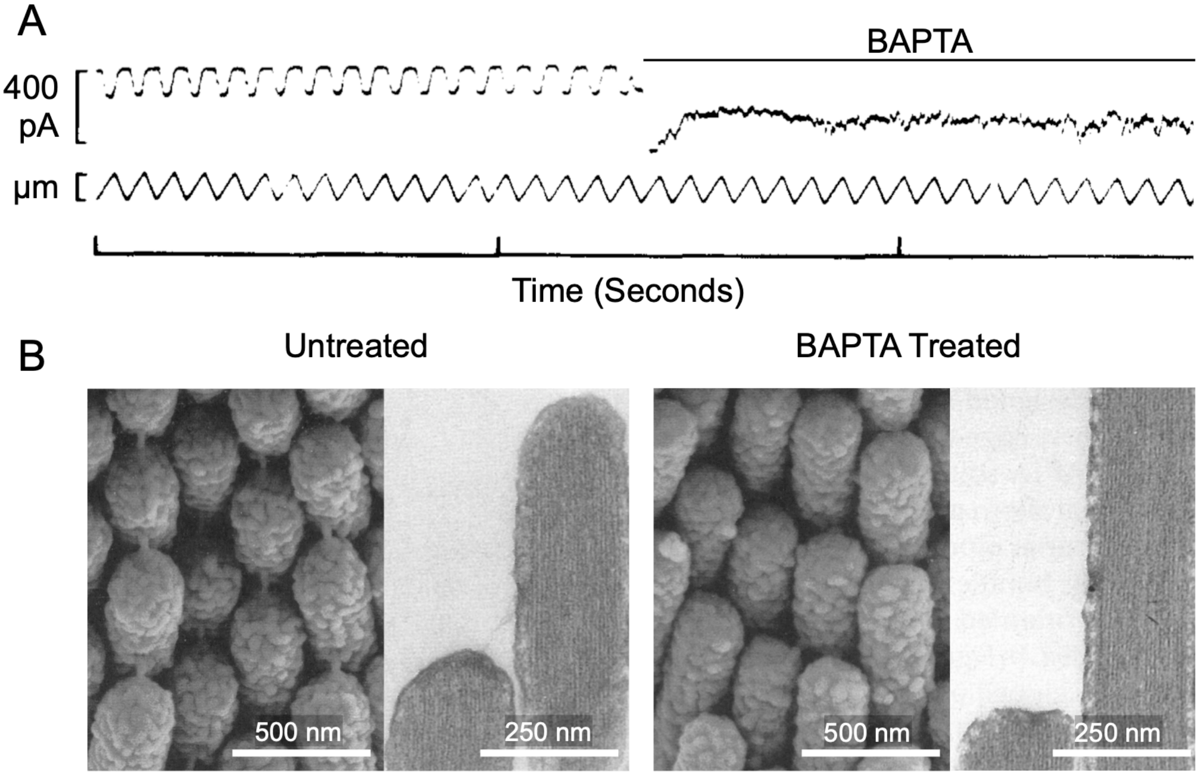

Figure 1.4: BAPTA treatment disrupts tip links and abolishes MET currents
(A) Measured MET current, top, from from bullfrog saccule hair cell in response to triangle-wave displacement. Exposure to 5 mM BAPTA abolishes transduction currents. (B) SEM and TEM images of stereocilia from bullfrog saccule hair cells that were untreated, left, or treated with BAPTA, right (Adapted from Assad et al. 1991).

1.5 Brief Overview of Assays Used to Investigate MET

Numerous investigations over the years have contributed to our understanding of hair cell mechanotransduction and careful experiments have been designed to infer some molecular properties of the MET channel. The following are brief descriptions of some of the assays used to interrogate different aspects of mechanoelectrical transduction and the MET channel.

An auditory brain stem response assay is a method that uses a surface electrode to detect activity in an organism's brain stem that is elicited by some auditory stimulus (Jewett et al., 1970). When an organism with proper auditory function is exposed to either a click or sustained tone, electrodes placed near the brain stem can detect changes of potentials; a defective auditory system results in no detectable changes. These assays are relatively quick and do not require surgery. However, these assays alone are not sufficient to diagnose defects of the MET machinery, as defects in other auditory-critical systems can result in abnormal signals.

The measuring of the microphonic potentials involves the measuring of currents generated by the sensory epithelia elicited by stimulation of large number of hair cells (Butler and Honrubia, 1963; Corey and Hudspeth, 1983a). These experiments can be done in vivo or in excised tissue. Microphonic potentials represent the average signals from multiple hair cells, each of which can have slightly different properties.

The next set of assays examines the specific uptake of a variety of cationic dyes by hair cells. These dyes include but are not limited to: Texas Red conjugated gentamycin, FM1-43, FM4-64, DASPEI, 4-Di-2-ASP, YO-PRO and Texas Red conjugated 3 kDa dextran (Ballesteros et al., 2018; Gleason et al., 2009; Nishikawa and Sasaki, 1996; Shen et al., 2008). Disruptions that affect MET currents, such as tip link severing or chemical blockade, prevent the uptake of these dyes. Additionally, their uptake has been shown to be independent of endocytosis. These properties support the use of these dyes as a tool to assay for the presence of open transduction channels. However, screening with small molecule libraries have identified compounds that prevent the uptake of some of these dyes without impacting MET currents, which may indicate that these dyes are able to enter hair cells by some other channel instead of the MET channel (Kenyon et al., 2017).

A more direct measurement of MET currents comes from the use a whole-cell patch clamping in conjunction with mechanical deflections of the hair bundle, typically by either a piezo controlled stiff probe or a fluid jet. These assays allow for the direct assay of mechanotransduction currents and have allowed for studies of various channel properties, such as the permeability of different ions, the effect of chemical blockers. However, the current recordings that one can obtain can vary greatly depending on the method of hair bundle displacement. Stiff probe manipulations can elicit different current profiles based on the size, shape, and placement of the probe tip (Indzhykulian et al., 2013; Nam et al., 2015). Fluid jets suffer from a slower rise time of bundle displacement compared to stiff probes, and jets have recently been shown to also be susceptible hair bundle “creep”, the continued displacement of the hair bundle under maintained force (Caprara et al., 2019; Vollrath and Eatock, 2003).

A recent technique to investigate MET measures calcium-dependent fluorescence from hair cells that heterologously express GCaMP3 (Xiong et al., 2014). While this technique simplifies the experimental set up, calcium imaging is slower and not useful for quantifying kinetic aspects of MET currents.

One of the more technically challenging assays for analyzing a protein’s contributions to MET are measurements of unitary currents (Crawford et al., 1991; Ohmori, 1985). Through the use of either titration of chemical blockers or careful disruption of tip links, whole cell current recordings can be reduced to discrete binary events. Given the binary nature of these unitary currents the data are thought to correspond to a single MET channel. The advantage of unitary currents is the unmasking of details that are lost due to the averaging signals from large numbers of channels found in standard whole cell recordings.

1.6 Properties of Mechanoelectrical Transduction Currents and Associated Channel

The MET channel conducts cations through the membrane in a fairly nonspecific manner. The relative permeability sequence is Li>Na>K>Rb>Cs for monovalent ions, and Ca>>Sr>Ba>Mn>Mg for divalent ions (Corey and Hudspeth, 1979; Ohmori, 1985). Given the potassium rich nature of the endolymph, the majority of current is carried by this ion. The higher permeability for calcium helps drive calcium into the stereocilium, even at the low concentration found in the cochlear endolymph where calcium is estimated to constitute about 10% of MET currents. (Lumpkin et al., 1997; Ricci and Fettiplace, 1998). Calcium that enters into the stereocilia is quickly cleared by PMCA2 (Beurg et al., 2010; Lumpkin and Hudspeth, 1998; Yamoah et al., 1998). Higher concentrations of calcium, however, decrease the magnitude of MET currents (Corey and Hudspeth, 1983b; Crawford et al., 1991).

Numerous recordings of unitary currents have measured the conductance of the MET channel to be typically in the range of 60-150 pS (Figure 1.5A), with one report as high as 300 pS (Beurg et al., 2019; Beurg et al., 2015a; Beurg et al., 2015b; Crawford et al., 1991; Effertz et al., 2017; Kim et al., 2013; Liu et al., 2019; Ohmori, 1985; Pan et al., 2018; Ricci et al., 2003). Most of the variation in these conductance values arises not from difference between studies, but the intriguing observation that MET channel conductance varies over the tonotopic map, predominantly in OHCs. High frequency hair cells at the cochlear base have channels with a higher single channel conductance; single channel conductance smoothly decreases in hair cells of the lower and lower characteristic frequency toward the cochlear apex (Ricci et al., 2003). The mechanism for this variation is an outstanding question. Some have proposed this variation arises from the expression of different channel isoforms, however none of the channel candidates has such a genetic structure. Knocking-out or mutation of various MET associated membrane proteins greatly reduces this tonotopic variation which may indicate a mechanism based on channel modulation via accessory proteins, but more experiments are needed to explore this hypothesis (Beurg et al., 2019; Beurg et al., 2015b; Kim et al., 2013; Ricci et al., 2003). Additionally, measuring conductance in the presence of high calcium can reduce or almost entirely ablate the tonotopic variation of conductance (Liu et al., 2019; Ricci et al., 2003). How calcium reduces the tonotopic variation of MET channel conductance is unclear. One idea is that calcium blocks a leak channel, yet how this leak channel modulates unitary currents is unclear but may suggest an electrostatic mechanism (Liu et al., 2019). Regardless, the model of calcium acting as a permeable channel block may need revision.

A few structural properties of the MET channel have been inferred by the structural properties of various compounds that are able to permeate it. By assaying the permeability of various *n*-alkyl amines along with correlating different channel blocker's dimensions with their efficacy, the external pore of the MET channel was estimated to be ~12 Å in diameter (Farris et al., 2004). Similar experiments using internally applied *n*-alkyl amines measured the internal pore size to be 6 Å, interpreting this result to mean that the MET pore is asymmetric with a larger extracellular pore lined with negative charges (Pan et al., 2012).

Early attempts to localize the site of transduction in the hair bundle used the careful placement of a microelectrode to systematically interrogate different positions on a bullfrog sacculus hair bundle, and limited the region of MET to the distal 20% of stereocilia (Hudspeth, 1982). Experiments that localized the MET channels to the tips of stereocilia exploited the calcium permeability of the channel in conjunction with calcium-sensing fluorescent dyes and high-speed, high-resolution confocal microscopy (Beurg et al., 2009; Denk et al., 1995; Lumpkin and Hudspeth, 1995).

MET currents undergo a process of adaptation in response to constant stimulus. Unlike a process of desensitization, in which successive stimuli of same magnitude produce smaller and smaller responses due to decreased sensitivity, the MET channel maintains the same sensitivity but shifts the current-displacement relationship to a new set point. This process may play a role in the active hair bundle motion associated with the gating compliance, as well as act as a mechanism for tuning of hair cells for particular frequencies (Ricci et al., 2000; Ricci et al., 2005). Adaptation is observed on separate time scales with a fast adaptation process that has a time-constant of a few milliseconds, typically observed as a decay of instantaneous current (Figure 1.5B), and a slow adaptation process that has a time constant of tens to hundreds of milliseconds, typically observed in as shifts in the current-displacement ($I/\Delta X$) relationship after a pre-displacement step (Figure 1.5D) (Crawford et al., 1989; Eatock et al., 1987; Wu et al., 1999). Positive pre-displacements result in rightward shifts of $I/\Delta X$, while negative pre-displacements result in leftward shifts (Eatock et al., 1987). The details of adaptation, such as the molecular mechanisms and the proteins responsible, are the basis of continuous and contentious debate in the field. Early work on adaptation established the effects of external calcium concentrations on adaptation (Assad et al., 1989; Crawford et al., 1989; Hacohen et al., 1989; Ricci and Fettiplace, 1997; Ricci et al., 1998; Wu et al., 1999). Low external calcium, approximately around the concentration found in cochlear endolymph, decreases the rate of adaptation as well as shifts the $I/\Delta X$ curve toward the left, such that at rest approximately 40% of transducer channels are open. The correlation between external calcium and adaptation has led to the hypothesis that calcium influx through MET channels modulates adaptation; sustained opening of the channel leads to calcium accumulation in stereocilia prompting a physical rearrangement of the MET machinery to establish a new set point, while sustained closure would decrease intracellular calcium levels and promote movement of the set point in the opposite direction. This hypothesis is supported by two additional observations: 1) an increase intracellular calcium buffering through the use of BAPTA or EGTA slows the rate of adaptation and shifts I/ΔX curve to the left, similarly to low extracellular calcium concentrations, and 2) holding the membrane at a positive potential (which prevents calcium entry) slows or abolishes adaptation (Assad et al., 1989; Crawford et al., 1989; Ricci and Fettiplace, 1997; Ricci et al., 1998).

The bulk of experiments establishing a link between calcium and adaptation were preformed primarily on bullfrog (*Rana catesbeiana*) saccule hair cells or turtle (*Pseudemys scripta elegans*) lagena hair cells. Work investigating the relationship between calcium and adaptation in mammalian cochlear hair cells has led to conflicting reports (Corns et al., 2014; Kennedy et al., 2003; Peng et al., 2013). Some of these discrepancies may arise from the use of different stimulus methods; one group used a stiff probe while the other used a fluid jet. Recent experiments that couple fluid jet stimulus with real time monitoring of hair bundle displacement suggest the results from the original fluid jet experiments with mammalian hair cells may have been artifactual (Caprara et al., 2019).

One of the more prominent hypotheses about how adaptation comes about is through the coupling of the MET machinery to myosin motors (Holt et al., 2002). In an elegant set of experiments, myosin-Ic was shown to be critical for adaptation in mouse (*Mus musculus)* utricle

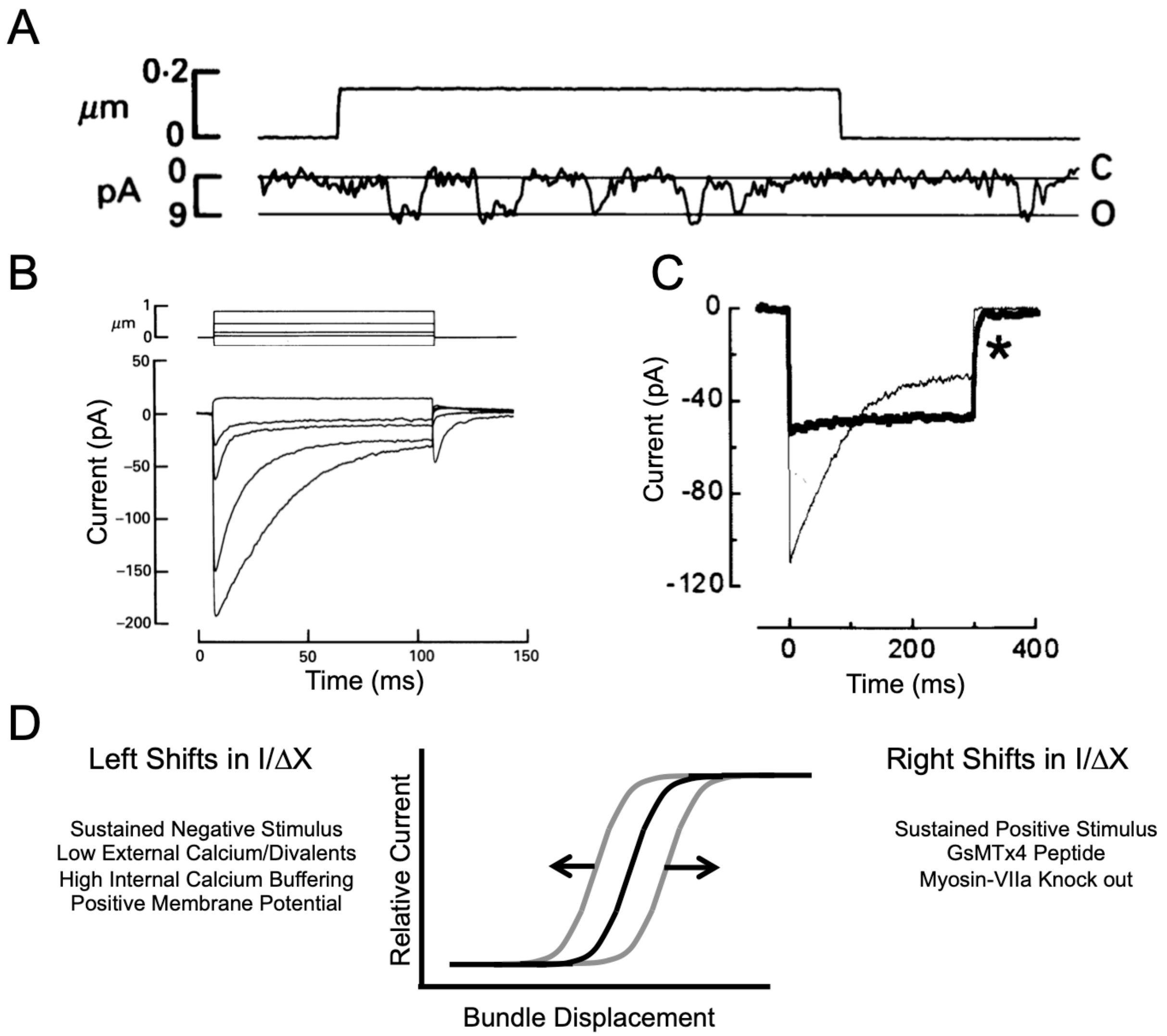

Figure 1.5: MET Channel currents exhibit changes due to adaptation and P_{open}
(A) Example of unitary channel recorded from turtle hair cells demonstrating the open and closed states of the MET channel. (B) Typical whole-cell patch clamp recordings for stepped displacements. Greater displacements of the hair bundle result in larger currents. (C) Difference in measured transduction currents from a WT hair cells and hair cell that expresses myosin-Ic Y61G treated with NMD-ADP. After a few minutes, MET currents demonstrate a lack of adaptation. (D) Summary of various treatments that affect the I/ΔX relationship (Images adapted from Crawford et al., 1989; Holt et al., 2002).

hair cells (Holt et al., 2002; Stauffer et al., 2005). Briefly, mice that encode a mutant form of myosin-Ic, myosin-Ic Y61G, displayed a dramatic loss of adaptation when exposed to the modified nucleotide NMB-ADP (Figure 1.5C); wild type myosin motors cannot accommodate this bulkier nucleotide and are thus unaffected. While these experiments demonstrated a clear link between myosin-Ic and adaptation, the exact mechanism that accomplishes this effect is still unclear. In this motor model, myosin-Ic puts tension on the MET machinery and calcium causes detachment and slipping. How this modulation by calcium of myosin-Ic is achieved still needs to be elucidated, but it is possible it can be through a mechanism involving a calcium-sensing protein such as calmodulin (Phillips et al., 2006; Walker and Hudspeth, 1996). However, if calcium only enters through the tips of stereocilia, it is unclear how calcium would reach myosin-Ic motors at the upper tip link density in the tallest row of stereocilia. Additionally, artificially raising intracellular calcium concentration does not cause a shift in the MET machinery's set point nor does it effect adaptation in response to a pre-displacement (Peng et al., 2013).

While lowering of external calcium concentration still produced a leftward shift in I/ΔX for mammalian cochlear hair cells, this was shown to be independent of the effects from intracellular calcium buffering and adaptation (Peng et al., 2013; Peng et al., 2016). Peng et al. argue that the shift in I/ΔX associated with low extracellular calcium is not a result of adaptation but rather a shift in the open state probability (P_{open}) of the MET channel. The P_{open} can be modulated by other divalent ions, particularly barium and strontium, and a particular divalent ion's ability to modulate P_{open} correlates with its ionic radius. This is argued to be the result of some global properties of the membrane, such as surface charge, as opposed to the binding of divalent ions to a specific site (Peng et al., 2016). This hypothesis that global physical properties of the membrane can affect MET behavior is supported by observations that the GsMTx4 peptide, a known inhibitor of stretch activated mechanosensitive channels, shifts the I/ΔX curve rightward by approximately 120 nm (Peng et al., 2016). Additionally, GsMTx4 prevents the modulation of P_{open} by extracellular divalents, another indication that divalents affect MET by modifying some property of the membrane.

Furthering the link between membrane properties and MET is the observation that the lipid composition of the stereocilia membrane has an impact on MET. Phosphoinositol-4,5-biphosphate (PIP_2) localizes to the apical regions of stereocilia in bullfrog saccule hair cells as well as in mouse IHCs and OHCs (Effertz et al., 2017; Hirono et al., 2004). The lack of PIP_2 in the basal regions of stereocilia is due to the presence of PTPRQ, the shaft connector associated protein, localizing to those regions. Decreasing PIP_2 levels by interfering with its synthesis leads to a decrease in MET currents by ~33%, an increase in base line current, a loss of fast adaptation, and a slowing of slow adaptation. Exactly how PIP_2 modulates MET is unknown but a few hypotheses have been proposed. These include PIP_2 mediating interactions between myosin-Ic and the membrane (Phillips et al., 2006). Myosin-Ic is not confined to either upper or lower tip link densities, and instead exhibits diffuse localization across the stereocilia in a similar pattern to PIP_2 (Gillespie et al., 1993; Hirono et al., 2004; Schneider et al., 2006). It is possible that disruption of PIP_2 interferes with myosin-Ic function, however the converse may be equally valid and it may be that myosin-Ic is necessary for PIP_2 trafficking. Disruption of MET currents in both the myosin-Ic Y61G experiments and PIP_2 take place over a period of minutes, while in vitro inhibition of myosin-Ic Y61G is much quicker (Gillespie et al., 1999). The latter hypothesis further posits that PIP_2 interacts directly with components of the MET channel, however more investigations are needed.

1.7 An Overview of Proteins involved in Mechanoelectrical Transduction

Proteins involved in MET have typically been identified by forward genetics that have implicated them as the cause of either dominant or recessive forms of hereditary nonsyndromic deafness (DFNA and DFNB, respectively), as well as the cause of Usher Syndrome, a condition typified by profound deafness at birth, vestibular defects, and early degeneration of the retina. These proteins additionally have been localized to the site of transduction at the lower tip link insertion site or to the upper tip link density. Functional assays, as described early, are used to demonstrate the loss of MET functions when these proteins are disrupted genetically. As of now, our current description of the MET machinery is that of a complex of about twelve different proteins that comprise the tip link, the MET channel or channel complex, a number of molecular motors, and adaptor proteins (Figure 1.6). The following is an overview of the current known components of the MET machinery.

1.7.1 Protocadherin 15 and Cadherin 23

Protocadherin 15 (PCDH15) and Cadherin 23 (CDH23) were first identified as hearing related genes through genetic associations that implicated them as the cause of the *Ames Waltzer* phenotype in mice as well as the cause of USH1F, DFNB23 (both PCDH15), USH1D, and DFNB12 (both CDH23) in humans (Ahmed et al., 2003b; Ahmed et al., 2001; Alagramam et al., 2001; Bolz et al., 2001; Bork et al., 2001; Di Palma et al., 2001; Schwander et al., 2009). Further studies identified PCDH15 and CDH23 as the lower and upper components of the tip link, respectively (Ahmed et al., 2006; Kazmierczak et al., 2007; Siemens et al., 2004).

PCDH15 and CDH23 are members of the cadherin superfamily of proteins. Cadherin superfamily proteins are typically are single-pass transmembrane proteins whose extracellular regions include extracellular cadherin (EC) domains. EC domains are composed of seven ß-

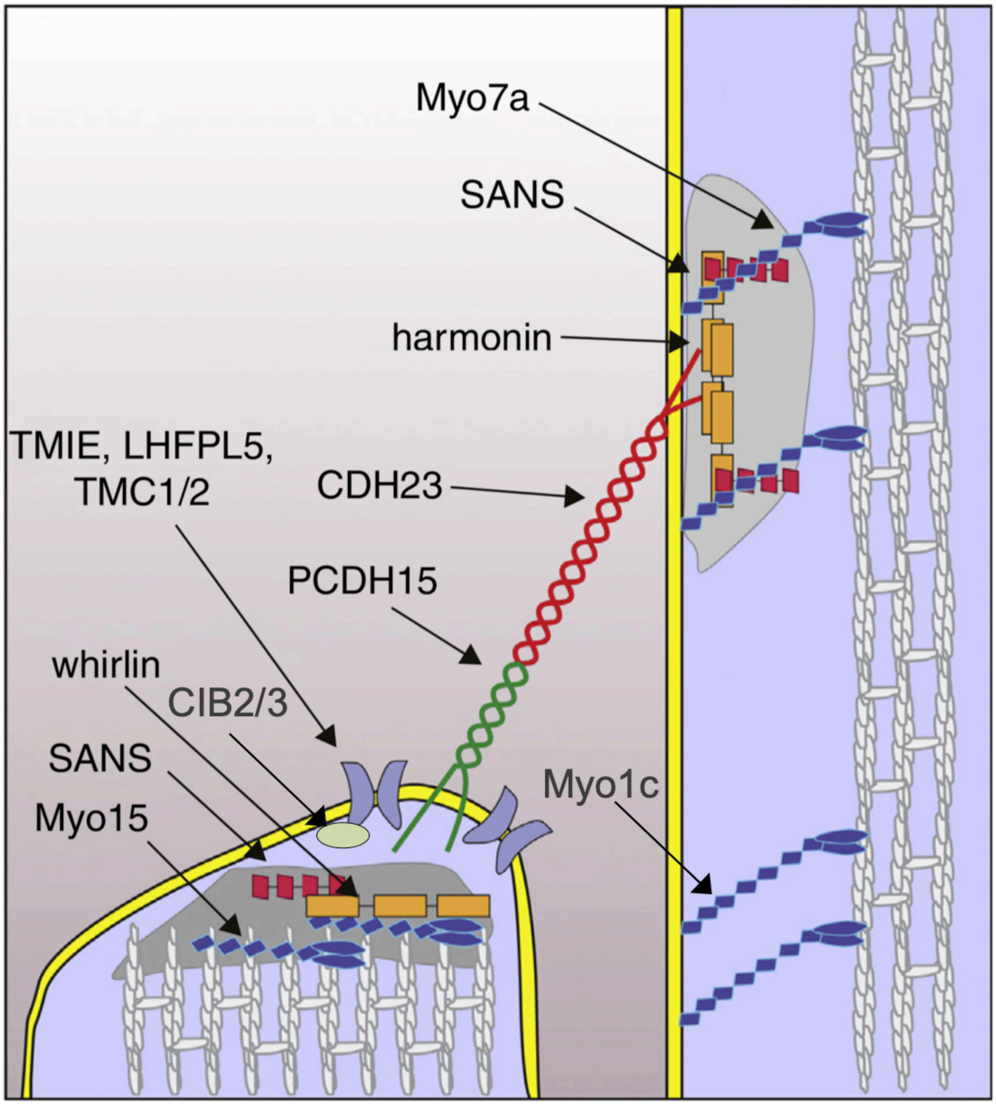

Figure 1.6: Overview of proteins associated with MET machinery
The MET machinery is associated with a number of integral membrane proteins, scaffold proteins, and myosin motors. Disruption to these components either by deletion or mutation result in effects in MET and result in deafness or Usher Syndrome (Zhao and Muller, 2015).

strands in an immunoglobulin-like fold that contain motifs that are responsible for the binding of three calcium ions at the linker regions between two sequential EC domains. Compared to other members of the cadherin superfamily, for which the majority of members contain between five and seven EC domains, PCDH15 and CDH23 are much larger with 11 and 27 EC domains, respectively. Additionally, PCDH15 and CDH23 have a number of splice isoforms. CDH23 has at least six splice isoforms, of which only four have extracellular regions (Lagziel et al., 2005). PCDH15 has twenty-four different splice isoforms, segregated into three groups based on the identity of their cytoplasmic domain – referred to as CD1, CD2, or CD3 – which are encoded by selective splicing of different exons (Pepermans and Petit, 2015). The functional implications of these splice isoforms are poorly understood. Experiments in developing animals found no impact on MET currents from the deletion of different PCDH15 splice isoforms, but demonstrated that PCDH15-CD2 is necessary for tip links of IHCs in adult mice (Pepermans et al., 2014).

Immunogold labeling experiments with antibodies specific for either CDH23 or PCDH15 localized CDH23 to the upper part of the tip link and PCDH15 to the lower portion (Kazmierczak et al., 2007). Consistent with this finding, biochemical experiments found that the ectodomains PCDH15 and CDH23 form a dimer-of-dimers, with a parallel homodimer of PCDH15 interacting through its amino termini with amino termini of a parallel homodimer of CDH23 (Kazmierczak et al., 2007). After disruption of the tip link by calcium depletion, tip link restoration is inhibited by the presence of soluble ectodomain fragments of PCDH15 and CDH23 (Lelli et al., 2010).

In 2010, two separate groups published the crystal structure of two cadherin domains from the amino terminus of CDH23 (Elledge et al., 2010; Sotomayor et al., 2010). One of the most striking features of these structures is the presence of a calcium ion at the very amino terminus of EC 1. This calcium ion is coordinated in a manner similar to the coordination of canonical site-3 calcium ion in typical EC domains. Using this structure in steered molecular dynamic simulations, *in silico* experiments were used to measure the stiffness of these two cadherin domains. Sotomayor et al. reported a stiffness inconsistent with the values calculated from measurements of whole hair bundles (Sotomayor et al., 2010). However, this *in silico* measurement is an extrapolation of the entire tip link from a fragment that is roughly ~2.5% of its total mass. Further discussions of stiffness calculations from *in silico* experiments will be discussed in chapter 3.

In 2012, Sotomayor et al. published a structure of a heterophilic complex of PCDH15 EC1-EC2 and CDH23 EC1-EC2 (Sotomayor et al., 2012). In this crystal structure, PCDH15 and CDH23 interact in an antiparallel fashion, described in the text as being akin to a handshake. At the time, it represented a new paradigm in interactions for cadherin superfamily proteins, which previously utilized a strand- swap and buried tryptophan mechanism for homodimerization.

The interaction observed in the crystal structure implies there is region of the tip link that has twice the thickness as compared to the rest of the length of the tip link, which appears to be inconsistent with both SEM and TEM images of the tip link (Figure 1.7A) (Auer et al., 2008; Kachar et al., 2000; Tsuprun et al., 2004). The interaction observed in the crystal structure may be consistent with the kinociliary links, which have an increase in electron density in the expected location (Figure 1.7B) (Goodyear et al., 2010). TEM images of kinocilairy links have a region of increased density about a third the way across the span, closer to the kinocilium (Goodyear et al., 2010). This density band is similar to the mid-line seen in desmosome junctions mediated by the desmosomal cadherins (Figure 1.7C) (Al-Amoudi et al., 2004).

Further structural characterizations of PCDH15 and CDH23 have produced structures for nine domains if the eleven PCDH15 EC domains, and eighteen of the twenty-seven CDH23 EC domains. Further discussion of these structures and their associated studies will be covered more in chapters 2 and 3.

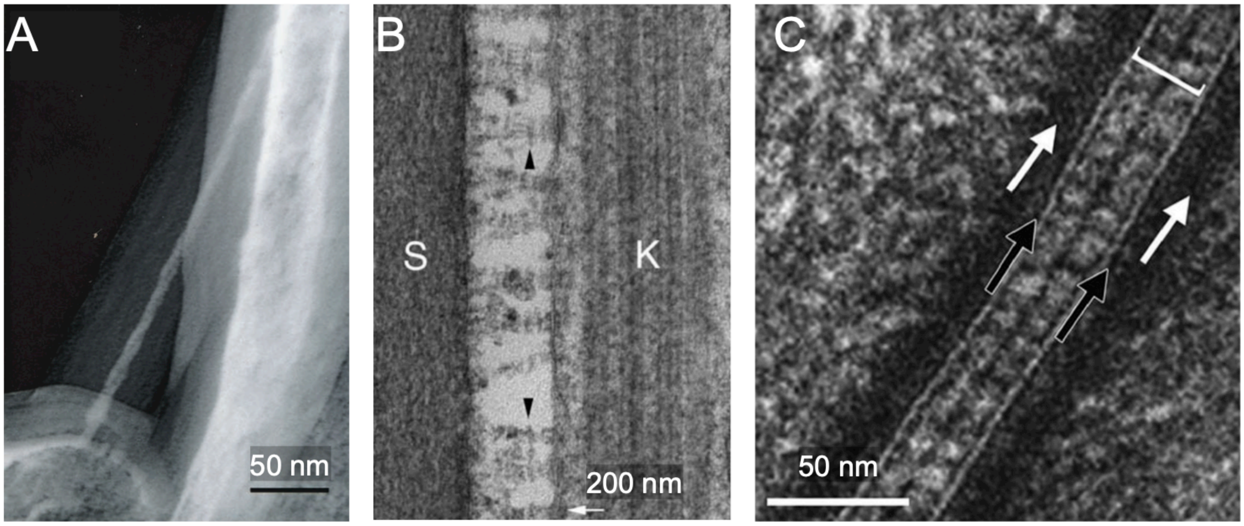

Figure 1.7:Comparison of electron micrographs of different CDH23/PCDH15 linkages to electron micrographs of desmosomes
(A) High resolution freeze-etch micrograph of tip link that shows the continuous thickness of the tip link. (B) TEM micrograph of kinociliary links. Black arrows indicate band of increased density, approximately where would be expected to interact PCDH15 and CDH23 interact. (C) TEM micrograph of a demosome from a cryo-section of human epidermis. Black arrows indicate cell membranes, white arrows indicate intracellular plaques (Images adapted from Al-Amoudi et al., 2004; Goodyear et al., 2010; Kachar et al., 2000).

1.7.2 Transmembrane Channel-like Protein 1 and 2

In 2002, Kurima et al. genetically mapped several mutations linked to both dominant (DFNA36) and recessive (DFNB7/B11) hearing loss to a novel gene, which they named Transmembrane Cochlear-Expressed Gene 1 (TMC1) (Kurima et al., 2002; Vreugde et al., 2002). In addition to this genetic mapping, they identified a highly similar protein, TMC2, and showed that both TMC1 and TMC2 mRNA is present in the inner ear. They used *in situ* hybridization to show TMC1 mRNA transcription is particularly concentrated in hair cells. TMCs were soon grouped with six additional paralogues including TMC6 and TMC8, proteins that are linked with epidermaldysplasia verrucruciformis. Due to the extra-cochlear expression of the new members, the gene family was rechristened to Transmembrane Channel-like genes (Keresztes et al., 2003; Kurima et al., 2003).

TMC1 and TMC2 are 760 and 906 residues long with corresponding sequence-calculated molecular masses of 87.7 kDa and 102.6 kDa, respectively. The exact number and location of TMCs transmembrane helices is a matter of some debate; transmembrane helix prediction algorithms differ in the number of transmembrane helices for TMC1 (Figure 1.8) (Labay et al., 2010; Pan et al., 2018). While some topological mapping of TMC1 has been done, it has not established a definitive topological map.

While these initial studies implicated TMC1 and TMC2 in proper hair cell function, their role in MET only became established after the realization that TMC1 and TMC2 have some redundancy, as TMC1/TMC2 double knockout mice are both deaf and have vestibular defects (Kawashima et al., 2011; Pan et al., 2013). A double knock out is necessary as TMC2 can compensate for TMC1, at least in the vestibular system (Asai et al., 2018). Exogenous expression of just one of the TMCs results in the restoration of MET currents. TMC-GFP or TMC-mCherry fusion proteins were localized to stereocilia tips (Kawashima et al., 2011; Kurima et al., 2015). The localization to stereocilia tips suggests to some that the TMCs may be a component of the MET channel (Kurima et al., 2015).

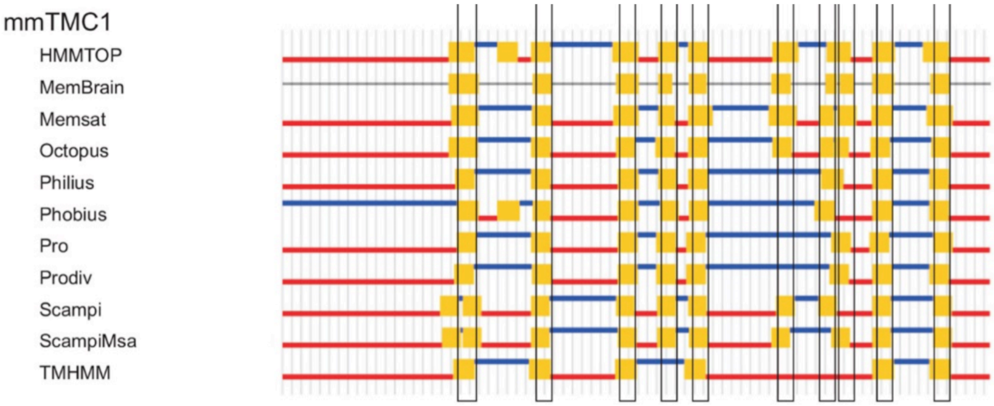

Figure 1.8: Summary of outputs from various transmembrane helix prediction algorithms for TMC1
Outputs of various TM prediction algorithms. Predicted TMs regions are in yellow, intracellular regions are in red, and extracellular regions are in blue (Adapted from Pan et al., 2018).

Evidence for TMC1 forming a pore in the membrane comes from a series of experiments utilizing a set of cysteine mutants and the thiol reactive compound 2-(trimethylammonium)-ethyl methanethiosulfonate (MTSET) (Pan et al., 2018). When exposed to MTSET, a hand full of TMC1 cysteine mutants displayed a decrease in MET currents, indicating TMC1 has connection to MET currents. Furthermore, when hair cells are exposed to the known MET channel blockers amiloride or DHS, a few of these cysteine mutants no longer demonstrate the MTSET-induced loss of current, indicating these residues are in the pore that is blocked by the channel blockers (Pan et al., 2018).

While poor expression has hindered structural studies of TMC proteins, computational methods with hidden Markov models have suggested that the TMCs are homologous to the Anoctamin or (ANO or TMEM) family of proteins (Hahn et al., 2009). This potential relation between TMCs and TMEMs, however, is limited as pair-wise sequence identity is rather low. Nonetheless, groups have used structures of TMEM16, a lipid scrambalase, to generate homology models of TMC1 (Ballesteros et al., 2018; Pan et al., 2018). While the prospect of having a structural model for TMC1 is exciting, the homology model has some key defects, mainly the lack of a clearly defined pore. Furthermore, the model proposed by these studies disagrees with a topology map determined through epitope tagging done previously, and even the interpretation of their own data (Labay et al., 2010; Pan et al., 2018).

The picture is further muddied by characterizations of TMC1 deafness mutants. The mutation responsible for the Beethoven (M412K) phenotype has limited effect, if any, on currents measured in either whole cell or unitary channel recordings (Beurg et al., 2015a; Corns et al., 2016). However, the M412K mutation reduces calcium permeability, DHS sensitivity, and reduces the modulation of channel P_{open} by calcium (Beurg et al., 2015a; Corns et al., 2016). Similarly, the DFNB36 mutation (D569N) reduces whole cell currents, but the single-channel conductance is similar to wild type (Beurg et al., 2019). As with M412K mutation, D569N mutation also decreases the permeability of calcium but interestingly, these mutations have limited effect on adaptation suggesting that calcium influx may not regulate adaptation (Goldring et al., 2019).

In addition to having a direct role in MET currents, TMC1 has been suggested as having a role in establishing the gradient observed in OHC MET currents along the tonotopic map; TMC1 knockout decreases the variation of unitary channel conductance along the tonotopic map (Beurg et al., 2018; Kim et al., 2013). It has been suggested that TMC1 is expressed in a gradient along the tonotopic map, and this leads to different numbers of TMC1 molecules at stereocilia tips (Beurg et al., 2018). If TMC1 were the MET channel, different numbers of channels at sterocilia tips would be able to account for differences in whole cell currents, but not the changes in unitary currents, which exhibit binary characteristic.

Studies of TMC protein function in *Drosophila melanogaster* and *Caenorhabditis elegans* homologues have provided little clarity into mammalian TMC function. In *Caenorhabditis elegans*, TMC-1 has been implicated in having a role in the detection of high concentrations of sodium and strong alkalinity (Chatzigeorgiou et al., 2013; Wang et al., 2016). Although the sodium chemosensation of TMC-1 was demonstrated in vivo and in CHO-K1 cells that heterologously expressed TMC-1, others have failed to replicate the *in vivo* findings. In *Drosophila* larva, *tmc* knockout leads to a defect in larval motion, attributed to defects in the proprioceptive ddaE and ddaD neurons (Guo et al., 2016; He et al., 2019). The dependence of larval locomotion on *tmc* in *Drosophila* could be the result of *tmc* being mechanosensitive, however the exact function *tmc* plays in this process has yet to be established. Independent of the exact function of *Drosophila tmc,* defective larval motion can be rescued by expression of mouse TMC1 or TMC2, indicating that *Drosophila tmc* and mammalian TMC1/TMC2 have similar functional properties (Guo et al., 2016).

The most thorough investigation of non-mammalian TMCs was done in *Caenorhabditis elegans*. In *Caenorhabditis elegans*, knock outs of TMC-1 and TMC-2 results in a defective egg laying phenotype (Yue et al., 2018). Egg laying is controlled by a simple circuit: stimulation of HSN neurons leads to the neurons in turn stimulating the vulval muscles (VM) to contract; TMC-1 is expressed in the HSN while both TMC-1 and TMC-2 are expressed in the VM. Briefly, after numerous experiments it was shown that the *C. elegans* TMC proteins function by modulating the membrane potential through a leak current (Yue et al., 2018). Interestingly, a similar leak current was observed when the worms expressed mammalian TMC1, TMC2, or TMC3; the mammalian TMCs also rescued the defective egg laying phenotype (Yue et al., 2018).

Mammalian outer hair cells were also shown to have a leak current that is associated with TMC1. A leak current can be measured in wild type hair cells, but it is not detected in hair cells that have TMC1 knocked out; knock out of TMC2 had no effect (Liu et al., 2019). Exogenous expression of TMC1 restores this leak current. While this leak current in hair cells has some properties in common with the MET channel, such as being blocked by similar compounds, the IC50s for transduction current and the leak current are substantially different (Liu et al., 2019). Additionally, the leak current seems to be conducted through a calcium impermeable channel.

Recently, a group has reported measuring currents in liposomes with purified *Chelonia mydas* TMC1 and *Melopsittacus undulatus* TMC2 that was expressed in Sf9 cells (Jia et al., 2019). The currents are mechanically sensitive and are blocked by known MET channel blockers.

While the results are promising, there are a few discrepancies between their results and previous measurements of the MET channel, which could indicate that TMCs are not the MET channel. The single channel conductance they report for both proteins are a smaller, at 40 and 35 pS, compared to the conductance measured from MET unitary currents (Jia et al., 2019). Additionally, they could not measure any current for TMC1 D569N. In hair cells that express only TMC1 D569N the MET unitary conductance is the same as wild type. However, their measurements are done in a system that may not recapitulate the native environment of the MET channel, which could explain the discrepancies. More experiments will be needed to validate these findings and explain the discrepancies.

1.7.3 Calcium and Integrin Binding Proteins 2 and 3

Compared to the other proteins discussed, CIB2 and CIB3, members of the Calcium and Integrin Binding family of proteins, were identified as deafness genes rather recently in 2012. CIB2 has been associated with DFNB48 and USH1J (Patel et al., 2015; Riazuddin et al., 2012; Seco et al., 2016). However, subsequent studies call into doubt CIB2 characterization as an Usher gene, as only a single mutation was associated with the USH1J, and mouse homozygous CIB2 knockouts lack vestibular defects as expected for type 1 Usher genes (Booth et al., 2018). This lack of vestibular defects can be explained by expression of CIB3, which is 61% identical to CIB2, in vestibular hair cells (Giese et al., 2017). CIB2 was shown to localize to the tips of stereocilia by fluorescent immunostaining with an anti-CIB2 antibody and by imaging of a CIB2-GFP fusion (Michel et al., 2017). CIB2 was implicated in having a more direct role in

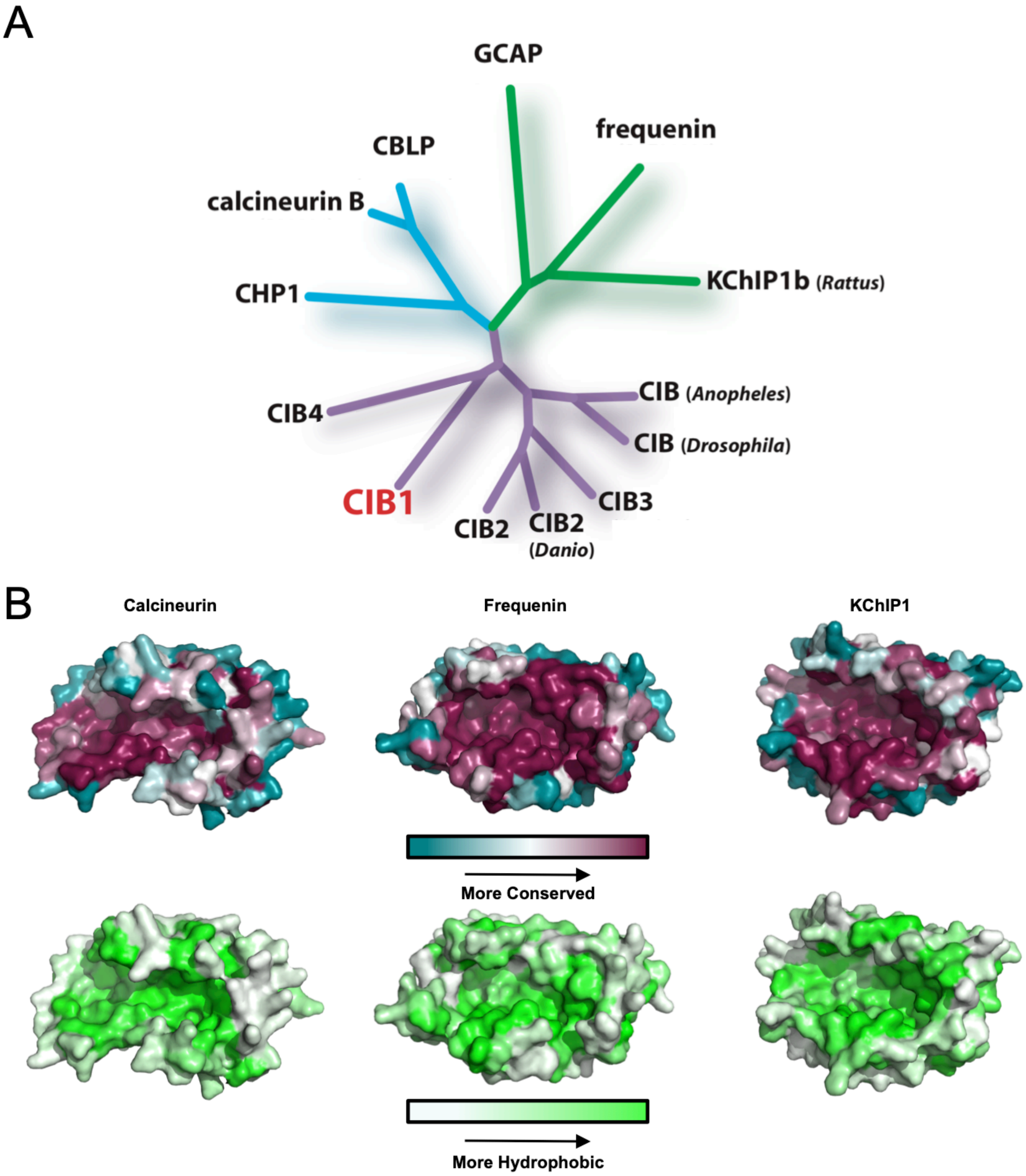

Figure 1.9: CIB proteins are related to the NCS family of proteins
(A) Dendrogram depicting the relationship between CIB proteins and NCS family of proteins (Gentry et al., 2005). (B) NCS family proteins utilize a common hydrophobic binding pocket. Top, conservation scores calculated by Consurf are mapped on the surface of various NCS proteins. Bottom, Eisenberg hydrophobicity values mapped onto the same NCS for comparison (Jin and Harrison, 2002; Landau et al., 2005; Pandalaneni et al., 2015; Wang et al., 2007).

MET through demonstrations that cochlear hair cells that have CIB2 knocked-out or express CIB2 mutants lack transduction current (Giese et al., 2017; Michel et al., 2017). A potential mechanism for CIB2 may be through an interaction with TMC1 and TMC2. GFP-tagged TMC1 and TMC2 co-localize with V5 tagged CIB2, and FRET efficiency measurements indicate that the associations are structurally close (Giese et al., 2017).

CIB2 and CIB3 are both 187 residues in length and 21.6 kDa and 21.8 kDa, respectively. CIB proteins are related to the neuronal calcium sensor family (NCS) of proteins, a family of EF hand containing proteins that modulate various components throughout the nervous system, such as potassium channels (KChIPs), guanylyl cyclase (GCAPs), rhodopsin kinase (recoverin), and neurotransmission (frequenin) (Figure 1.9A) (Gentry et al., 2005). These single-domain proteins are typified by having four EF hand motifs of which the first EF hand is defunct; in a few members the second EF hands are defunct as a well. These nonfunctioning EF hands are also present in CIB1, and sequence suggests this is true as well in CIB2 and CIB3 (Burgoyne, 2004).

While only a few members of the NCS family have structures in complex with their binding partner, the few that do suggest they use a similar mechanism involving a conserved, hydrophobic patch or grove (Figure 1.9B) (Ames and Lim, 2012). This conserved hydrophobic grove of NCS proteins sits on one face of the protein, adjacent to the C termini. This recognition scheme can be directly observed in the crystal structures of Frequenin, Calcineurin, and KChIP1in complex with their respective binding partners (Jin and Harrison, 2002; Pandalaneni et al., 2015; Wang et al., 2007).

A significant number of NCS proteins are myristoylated, and regulate the exposure of their mysristoyl modification in a calcium dependent manner, termed Ca^{2+}-myristoyl switching. Both CIB1 and CIB2, similarly, have been shown to be myristoylated, but lack the Ca^{2+}-

myristoyl switching observed in NCS proteins (Blazejczyk et al., 2009). Myristoylation of CIB proteins, therefore, serves more to constitutively localize them to the cell membrane.

Many members of the NCS family form dimers in solution. However, the dimerization mechanisms vary drastically within the NCS family. For example, GCAP1 forms a symmetric dimer through a hydrophobic interface, while GCAP5 uses cysteine residues to bind Fe^{3+} in order to dimerize (Reviewed in Ames, 2018). The dimerization of NCS proteins may help facilitate their trafficking to the membrane, as well as being necessary for binding to downstream partners. As for CIB proteins, only CIB2 has evidence for dimer formation; in contrast CIB1 behaves as a monomer in solution (Dal Cortivo et al., 2019; Gentry et al., 2005; Giese et al., 2017). The functional relevance of CIB2 dimerization is not yet understood.

1.7.4 Transmembrane Inner Ear

Transmembrane Inner Ear (TMIE) is the smallest and one of the least studied proteins related to MET. TMIE was discovered after genetic mapping identified it as the cause of DFNB6 in humans as well as the causative mutation of auditory and vestibular defects in spinner and circling mice (Mitchem et al., 2002; Naz et al., 2002). TMIE is a rather small integral membrane protein with only 153 amino acids and a total molecular mass of 17 kDa. TM prediction algorithms predict that TMIE has two transmembrane helices, but the first helix maybe superfluous.

Work in zebrafish demonstrated TMIE is necessary for the uptake of the dyes DASPEI, 4-Di-2-ASP, and FM4-64 (Gleason et al., 2009; Shen et al., 2008). Additionally, microphonic potentials measured in TMIE deficient fish were consistent with other forms of MET disruption. Taken together with the dye uptake assays, it suggests a possible role for TMIE in the transduction machinery.

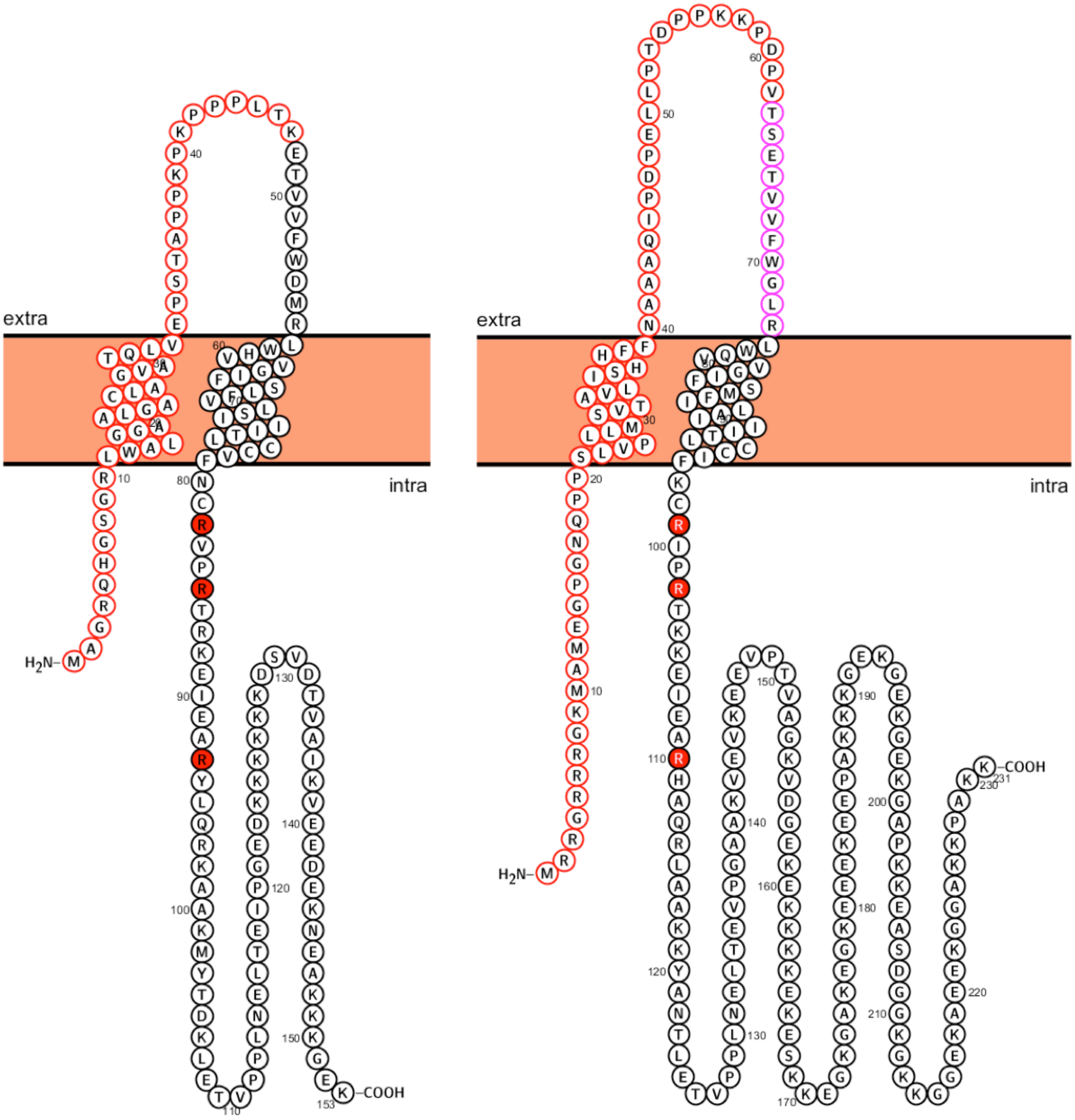

Figure 1.10: Topology of TMIE with MET critical regions highlighted
Predicted topology diagrams of mouse and zebrafish TMIE. Known deafness mutants indicated with a red background. Red outlines indicate N-terminal deletions that result in a dominant negative protein fragment used in Zhao et al. (2014) and Pacentine et al. (2019). Magenta outlines indicate deleted extracellular region that results dominant negative protein from Pacentine et al. (2019).

Fluorescent staining for TMIE or TMIE-HA localize TMIE to the tips of the shorter, transducing stereocilia in mouse IHCs and OHCs (Zhao et al., 2014). Whole cell transduction currents are affected in both TMIE deficient and TMIE mutant hair cells. Further, transduction currents can also be affected in a dominant negative fashion through the exogenous expression of a TMIE constructs in which extracellular residues have been deleted in wild-type backgrounds (Figure 1.10) (Pacentine and Nicolson, 2019; Zhao et al., 2014).

One hypothesis of TMIE's function is that it is a potential transport protein for TMC1/2 (Pacentine and Nicolson, 2019). This hypothesis was driven by observations of decrease localization of TMC1/2 in hair cells of the neuromasts in *Danio rerio* that lack TMIE. However, this hypothesis is challenged by data in the same publication showing proper TMC2 trafficking in animals expressing deletion constructs of TMIE that disrupts MET, as well as the dominant negative effects of other TMIE deletion constructs previously mentioned (Pacentine and Nicolson, 2019).

1.7.5 Tetraspan Membrane Protein of Hair Cell Stereocilia

Tetraspan Membrane Protein of Hair Cell Stereocilia (TMHS), also known as lipoma HMGIC fusion partner-like 5 (LHFPL5), was identified as the cause of hearing and vestibular defects in hurry-scurry mice, and later associated with DFNB67 (Kalay et al., 2006; Longo-Guess et al., 2005; Shabbir et al., 2006). Later studies localized TMHS to the site of MET and established an interaction between TMHS and PCDH15. Mouse OHCs with TMHS knocked-out display a decreased amplitude of whole cell MET currents (Xiong et al., 2012). Unitary currents measured from mouse OHC display a decrease in variation along the tonotopic gradient (Beurg et al., 2015b).

TMHS is a small 27.8 kDa protein with four transmembrane helices. TMHS is homologous to TARPS, another family of tetraspan proteins that modulate behaviors of ion channels. Structures of TMHS in complex with fragments of PCDH15 have been published, however, they provide limited insight into the potential mechanisms for TMHS's function (Ge et al., 2018). The positions of known deafness mutations, as well as regions corresponding to functional motifs in other TARPS, are either unresolved or not in contact with PCDH15 in these structures (Twomey et al., 2016).

1.7.6 Myosin Isozymes

As mentioned in previous sections, a number of different myosin motors are associated with proper MET function. Myosin-Ic and its implicated role in adaptation have been discussed previously. The following are brief descriptions of a few other myosin isozymes that have been associated with deafness or Usher syndrome and have potential roles in MET.

Myosin-IIIa is responsible for causing DFNB30 (Walsh et al., 2002). Little work has been done to expound the exact role of myosin-IIIa, GFP-tagged myosin-IIIa localizes to the apical tips of stereocilia and is thought to play a role in regulating stereocilia height (Schneider et al., 2006; Walsh et al., 2002).

Myosin-VI is unique among myosin motors as it is the only myosin that moves in retrograde. Mutations in myosin-VI can cause either DFNA22 or DFNB37 (Ahmed et al., 2003a; Melchionda et al., 2001). Myosin-VI has been implicated as having a role for adaptation, however it is unclear whether the defect is due to a failure to develop adaptation or it has a direct functional role (Marcotti et al., 2016).

Myosin-VIIa is associated with DFNA11, DFNB2, and USH1B, making it the only myosin to be associated with Usher Syndrome (Liu et al., 1997a; Liu et al., 1997b; Weil et al., 1995; Weil et al., 1997). Myosin-VIIa localizes to the upper tip link density and has been shown to interact with PCDH15 in co-immunoprecipitation experiments (Grati and Kachar, 2011; Senften et al., 2006). Disruption of myosin-VIIa shifts the I/ΔX relationship far to the right, suggesting that myosin-VIIa may be responsible for putting tension on the tip link and other MET components (Kros et al., 2002).

Myosin-XVa has been linked to DFNB3 (Wang et al., 1998). Myosin-XVa localizes to the lower tip link at the tips of stereocilia and is necessary for the persistence of mechanotransducing stereocilia (Belyantseva et al., 2003; Belyantseva et al., 2005; Fang et al., 2015; Stepanyan and Frolenkov, 2009).

1.7.7 SANS, Harmonin, Whirlin

A number of adaptor proteins have been associated with the MET machinery and play a role in organizing these structures. The following are brief descriptions of these proteins and a few of their known interactions.

Scaffold protein containing ankyrin repeats and SAM domain (SANS) has been found to cause USH1G (Weil et al., 2003). SANS is 461 residue long protein that contains, as the name implies, three ankyrin domains and a amino terminal SAM domain. SANS localizes to both ends of the tip link and is known to interact with CDH23, Harmonin, Whirlin, and Myosin-VII (Adato et al., 2005b; Caberlotto et al., 2011; Grati and Kachar, 2011; Maerker et al., 2008).

Harmonin and Whirlin are 910 and 918 residues long and each contains three PDZ domains. Harmonin is linked to DFNB18 and USH1C (Ahmed et al., 2002; Verpy et al., 2000). Harmonin localizes to the upper tip link density and associates with CDH23, Myosin-VIIa and SANS. Whirlin is the cause of DFNB31 and usher syndrome type 2D (Adato et al., 2005b).

Whirlin localizes to the lower tip link site and associates with CIB2, myosin-XVa and SANS (Ebermann et al., 2007; Mburu et al., 2003).

1.8 Scope of This Work

The works presented in this thesis aim to forward our understanding of the MET machinery by providing structural details of the molecules involved. In the following chapters, you will find structural and biophysical investigations of PCDH15, CIB2, TMC1, and TMIE. The specific topics covered in these chapters are as follows:

a) *Biophysical and structural studies of PCDH15.* We used analytical ultracentrifugation to examine a series of PCDH15 fragments to localize the dimeric interfaces of PCDH15. We solved the crystal structure of one of these interfaces to elucidate the molecular mechanisms that drive PCDH15 self-interaction. Using this structure, we designed mutants that abolished homodimerization, which were then used in MET assays that demonstrate the functional importance of PCDH15 dimerization in MET.

b) *Single-molecule studies of PCDH15.* We used photonic force microscopy to measure the mechanical properties of PCDH15. The stiffness of PCDH15 determined from these experiments was consistent with the elasticity of the gating spring. Analysis of unfolding rates suggest that some tip link cadherin domains may be unfolded *in situ*.

c) *Biochemical and structural studies of the CIB2:TMC1 interaction.* We used biochemical assays to redefine the region of TMC1 that interacts with CIB2. Using x-ray crystallography, we determined the molecular mechanism that CIB3 uses to dimerize. Additionally, we solved the crystal structure of CIB3 in complex with a fragment of TMC1. Using unitary current recordings, we show that CIB2 mutations affect the single channel conductance of the MET channel.

d) *Preliminary ventures into expressing TMIE and TMC1*. We used a bacterial expression system approach to heterologously produce TMIE. We performed preliminary experiments to establish protocols for generating a sample of TMIE. Additionally, we carried out a proof-of-concept experiment in using a CRISPR/CAS9 edited *Caenorhabditis elegans* to generate a sample of TMC1.

– Chapter 2–

Mechanotransduction by PCDH15 Relies on a Novel *cis*-Dimeric Architecture

2.1 Introduction

Presented in this chapter is a paper, of which I was the first author, published in *Neuron*. The work described in this paper reveals the molecular architecture of PCDH15. Through a biophysical dissection of PCDH15, we showed that the extracellular region of PCDH15 dimerizes through two distinct interfaces: one at the membrane distal end of the molecule, and one in the membrane proximal region. By solving the crystal structure of the membrane-distal interface, we were able to understand the structural principles that contribute to dimerization and utilize this information to interrogate the interface through mutations. Using these structure-guided mutants, we were able to demonstrate the importance of PCDH15 dimerization for MET in ex vivo functional assays.

2.2 An Overview of previously published PCDH15 Structures

The first crystal structure of PCDH15 came from the structure of a complex between CDH23 EC1-EC2 and PCDH15 EC1-EC2 (Sotomayor et al., 2012). The structure of PCDH15 EC1-EC2 is similar to other cadherins overall, albeit with a few cadherin-noncanonical features. There is a short acidic helix at the amino terminus of PCDH15 whose function is unknown. Mutation of the acidic helix has been shown to have little effect on PCDH15/CDH23 interaction in co-immunoprecipitation experiments, however it remains possible that this helix has some functional role *in situ* (Elledge et al., 2010). In addition to the acidic helix, PCDH15 has an internal disulfide bond between Cys10 and Cys98. While the location of this disulfide suggests it could mechanically stabilize the EC1 domain of PCDH15, particularly from pulling forces on the acidic helix, it is not clear how this disulfide would contribute to stabilization of the tip link in the context of the complex structure between CDH23 EC1-EC2 and PCDH15 EC1-EC2. The interface between CDH23 EC1-EC2 and PCDH15 EC1-EC2 involves only a limited number of side chain interactions. Tyr8 of PCDH15 engages in a hydrogen bond with Ser159 and packs against Leu145 of CDH23. Hydrophobic residues Ile22 and Val116 from PCDH15 interact with the hydrophobic regions of Tyr16, Leu18, and Gln98 on CDH23. The primary reason for the limited number of contacts in this interface is due to the presence of 121 water molecules in the interface between PCDH15 and CDH23. It is interesting to note that according to isothermal titration calorimetry data the interaction between PCDH15 EC1-EC2 and CDH23 EC1-EC2 is endothermic, and its formation is thermodynamically favorable due to an increase in entropy. It remains to be understood how this entropically driven interaction involves such a substantial amount of water.

In 2016, the crystal structure of PCDH15 EC8-EC10 was published (Araya-Secchi et al., 2016). PCDH15 EC8-EC10 crystalized with a rather dramatic ~90° angle between EC9 and EC10. The linker region between EC9 and EC10 lacks all three of the cadherin-canonical bound Ca^{2+} ions. This is consistent with the protein sequence, which shows deviations from the cadherin calcium binding motifs. The kink between EC9 and EC10 is mediated by a number of hydrophobic residues, with EC9 using Met913, Thr978, Ile980, and Leu1004 and EC10 contributing Leu1006, Ile1011, Val1093, Leu1098, and Val1100. This inter-domain angle of the PCDH15 EC8-EC10 fragment appeared to be stable in solution, as indicated by data from SAXS experiments (Araya-Secchi et al., 2016).

In contrast to the plainly evident bend in the EC9-EC10 junction, the EC8-EC9 fragment deviates from the typical cadherin junction in a more subtle way. The distance between the site 2 and site 3 Ca^{2+} is longer than the average, 8.48 Å compared to 6.84 Å. The DxD motif between the B and C β-strands of EC9, residues 931-933, is further away from the interdomain junction in comparison to DxD motifs in typical cadherin domains. As a result Asp933, which would typically to coordinates both site 2 and site 3 Ca^{2+} in other cadherins fails to do so. The functional effect of this modified cadherin calcium junction is yet to be determined.

The crystal structure of PCDH15 EC3-EC5, published in 2017, has mostly canonical cadherin domains but contains a few intriguing features (Powers et al., 2017). First, the EC3-EC4 junction lacks the site-1 Ca^{2+}. This is due to deviations from the DxE motif between the E and F β-strands, which is NxD in PCDH15 EC3, and the DxND motif in the inter-domain linker being DxNN in the linker between PCDH15 EC3 and EC4. In addition to this non-canonical cadherin junction, both EC3 and EC4 have small insertions that embellish the domains with additional loops. The A β-strand of EC3 has cysteine stabilized loop, while EC4 has a loop inserted in the B strand. Apart from these features, the PCDH15 EC3-EC5 structure resembles other cadherin structures.

In the crystal structure of PCDH15 EC3-EC5, EC3 forms an interface, using the cysteine-stabilized loop, between the two molecules of the asymmetric unit. This interface was not discussed in the publication, as it was most likely interpreted as a crystal contact. However, as discussed in the paper presented in this chapter, this interface mediates dimerization at the membrane distal ends of PCDH15 and is functionally important to MET.

While these structures cover 8 of the 12 domains in the PCDH15 extracellular region, they provided little insight into some of the functionally relevant questions. All of these fragments of PCDH15 were monomers, or interpreted as if they were monomers. Thus, prior structural analyses of PCDH15 left unanswered the most pertinent questions relevant to its function.

2.3 Mechanotransduction by PCDH15 Relies on a Novel cis-Dimeric Architecture

Presented here in its entirety is our paper as published in *Neuron*.

Neuron

Article

Mechanotransduction by PCDH15 Relies on a Novel *cis*-Dimeric Architecture

Highlights

- Biophysical studies of PCDH15 fragments reveal two *cis*-dimerization regions
- Membrane-distal *cis* interface revealed by crystal structure of PCDH15 EC1-EC3
- Negative-stain EM depicts the overall architecture of the PCDH15 *cis*-dimer
- Assays in hair cells show the *cis* dimer to be necessary for mechanotransduction

Authors

Gilman Dionne, Xufeng Qiu,
Micah Rapp, ..., Barry Honig,
Ulrich Müller, Lawrence Shapiro

Correspondence

bh6@cumc.columbia.edu (B.H.),
umuelle3@jhmi.edu (U.M.),
lss8@columbia.edu (L.S.)

In Brief

The tip link, a filament linking stereocilia, is critical for auditory mechanotransduction. Dionne et al. describe structural studies of protocadherin-15 that reveal its *cis*-dimeric architecture. Assays in hair cells using structure-guided mutations show the *cis* interface is critical for mechanotransduction.

Dionne et al., 2018, Neuron *99*, 480–492
August 8, 2018 Published by Elsevier Inc.
https://doi.org/10.1016/j.neuron.2018.07.006

CellPress

Neuron
Article

Mechanotransduction by PCDH15 Relies on a Novel *cis*-Dimeric Architecture

Gilman Dionne,[1,2] Xufeng Qiu,[3] Micah Rapp,[1,2,4] Xiaoping Liang,[3] Bo Zhao,[3] Guihong Peng,[3] Phinikoula S. Katsamba,[1,2,5]
Goran Ahlsen,[1,2,5] Rotem Rubinstein,[1,5,6] Clinton S. Potter,[1,4] Bridget Carragher,[1,4] Barry Honig,[1,2,5,6,7,*] Ulrich Müller,[3,*]
and Lawrence Shapiro[1,2,6,8,*]
[1]Department of Biochemistry and Molecular Biophysics, Columbia University, New York, NY 10032, USA
[2]Zuckerman Mind Brain Behavior Institute, Columbia University, New York, NY 10027, USA
[3]The Solomon H. Snyder Department of Neuroscience, Johns Hopkins University School of Medicine, Baltimore, MD 21205, USA
[4]National Resource for Automated Molecular Microscopy, Simons Electron Microscopy Center, New York Structural Biology Center, New York, NY 10027, USA
[5]Howard Hughes Medical Institute, Columbia University, New York, NY 10032, USA
[6]Department of Systems Biology, Columbia University, New York, NY 10032, USA
[7]Department of Medicine, Columbia University, New York, NY 10032, USA
[8]Lead Contact
*Correspondence: bh6@cumc.columbia.edu (B.H.), umuelle3@jhmi.edu (U.M.), lss8@columbia.edu (L.S.)
https://doi.org/10.1016/j.neuron.2018.07.006

SUMMARY

The tip link, a filament formed by protocadherin 15 (PCDH15) and cadherin 23, conveys mechanical force from sound waves and head movement to open hair-cell mechanotransduction channels. Tip-link cadherins are thought to have acquired structural features critical for their role in mechanotransduction. Here, we biophysically and structurally characterize the unusual *cis*-homodimeric architecture of PCDH15. We show that PCDH15 molecules form double-helical assemblies through *cis*-dimerization interfaces in the extracellular cadherin EC2-EC3 domain region and in a unique membrane-proximal domain. Electron microscopy studies visualize the *cis*-dimeric PCDH15 assembly and reveal the PCDH15 extracellular domain as a parallel double helix with *cis* cross-bridges at the two locations we defined. The helical configuration suggests the potential for elasticity through helix winding and unwinding. Functional studies in hair cells show that mutations that perturb PCDH15 dimerization contacts affect mechanotransduction. Together, these data reveal the *cis*-dimeric architecture of PCDH15 and show that dimerization is critical for sensing mechanical stimuli.

INTRODUCTION

Mechanosensitive hair cells use a bundle of stereocilia at their apical surface to detect mechanical stimuli evoked by sound (acoustic) or motion (vestibular) and transduce them into electrical signals, a process termed mechanoelectrical transduction (MET) (Hudspeth, 2014; Pan and Holt, 2015; Pepermans and Petit, 2015; Ricci et al., 2006; Zhao and Muller, 2015) (Figure 1A). Rows of stereocilia in hair bundles are arranged by height; deflections from the shortest toward the tallest stereocilia lead to the opening of mechanically gated ion channels near the tips of stereocilia (Assad et al., 1991; Hudspeth, 2014; Hudspeth and Jacobs, 1979). These ion channels are located near a ~200-nm-long protein tether—the tip link—which couples the tip of one stereocilium to a more apical location on the side of a taller stereocilium (Figure 1B) (Pickles et al., 1984; Assad et al., 1991; Kachar et al., 2000; Kazmierczak et al., 2007; Beurg et al., 2009). Freeze-etched electron microscopy (EM) images obtained *in vivo* and low-resolution negative-stain EM images obtained *in vitro* suggest that the tip link is a tightly wound helix consisting of two associated strands (Kachar et al., 2000; Kazmierczak et al., 2007). Forces from sound or motion induce deflection of hair bundles, imparting increased tension on the tip link, leading to an increase in the open probability of the mechanically gated ion channels (Hudspeth, 2014). There remains a debate as to whether the tip link functions as the putative gating spring for the opening of the associated mechanotransduction channel (Ricci et al., 2006; Zhao and Muller, 2015).

The tip link is composed of PCDH15 and cadherin 23 (CDH23), both members of the cadherin superfamily. Tip-link cadherins show unusual features, which clearly distinguish them from classical cadherins. First, tip-link cadherins are unusually large. While the extracellular regions of classical cadherins consist of 5 extracellular cadherin (EC) domains, the extracellular regions of PCDH15 and CDH23 contain 11 and 27 EC domains, respectively (Ahmed et al., 2001, 2006; Bolz et al., 2001; Kazmierczak et al., 2007; Siemens et al., 2004). Additionally, PCDH15 has a conserved region of approximately 130 amino acids between EC11 and the transmembrane domain. This region has no homology to any protein of known structure, yet secondary structure prediction algorithms suggest it to be a folded domain. Since this region is localized at the expected site of ion-channel interaction, we refer to this domain as the protocadherin 15 interacting-channel associated—or PICA—domain. Second, unlike classical cadherins, the extracellular domains of PCDH15 and CDH23 are thought to form helical parallel *cis*-homodimers,

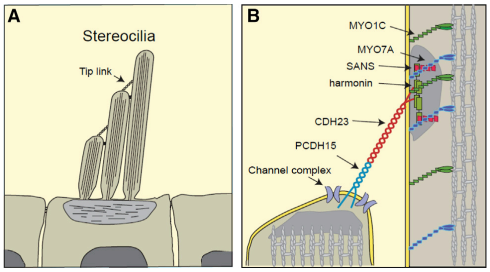

Figure 1. Diagram of a Hair Bundle of a Mechanosensory Hair Cell
(A) Overview of the hair bundle indicating the tip link.
(B) The double-helical tip link is a homodimer of PCDH15 interacting in *trans* with a homodimer of CDH23. The mechanically gated ion channel (channel complex) is located at the lower end of tip links. Several proteins such as harmonin, SANS, MYO7A, and MYO1C are located at the upper end of the tip link.

suggesting multiple tight contact points between parallel strands (Kazmierczak et al., 2007). The parallel *cis*-homodimer is thought to be the principle functional unit of PCDH15 and CDH23 (Ahmed et al., 2006; Kazmierczak et al., 2007; Siemens et al., 2004; Sotomayor et al., 2012). Classical cadherins instead form large lateral clusters consisting of many cadherin monomers (Harrison et al., 2011; Indra et al., 2018; Vester-Christensen et al., 2013). Finally, the *trans*-dimer interface between PCDH15 and CDH23 differs from the interface between classical cadherins. *Trans*-interactions in classical cadherins are mediated by EC1 and critically depend on a conserved tryptophan (Boggon et al., 2002; Shan et al., 1999; Shapiro et al., 1995). In contrast, the EC1 domains of PCDH15 and CDH23 lack this conserved tryptophan, and the two cadherins instead appear to interact through a "handshake"-like mode via distinct interfaces in their EC1 and EC2 domains (Elledge et al., 2010; Sotomayor et al., 2010, 2012). Thus, lateral homodimerization, helix formation, and a novel *trans*-adhesive dimer interface are specializations of PCDH15 and CDH23 that likely evolved for their critical function in mechanotransduction. Crystallographic studies have provided first insights into the structure of monomeric fragments of PCDH15 (Araya-Secchi et al., 2016; Powers et al., 2017; Sotomayor et al., 2010, 2012), but we know little about the mechanisms that drive dimerization and helix formation, or that constitute the adhesive interface in the *trans* tetramer.

Here, we have used crystallography, EM, and solution biophysics to show that *cis*-homodimerization of PCDH15 is mediated by a novel interaction mode not observed previously for other members of the cadherin superfamily. While previous structural studies of PCDH15 utilized fragments expressed in bacteria, most of which appeared monomeric (Araya-Secchi et al., 2016; Powers et al., 2017; Sotomayor et al., 2012), we focused on proteins expressed in eukaryotic cells thus containing modifications such as glycosylations that might affect protein function. We identified two distinct interfaces that mediate homodimerization in PCDH15: one near the *trans*-adhesive interface that is contained within domains EC2 and EC3, and the other adjacent to the membrane mediated by the non-cadherin PICA domain. The crystal structure of the *cis*-dimeric EC1-EC3 region of PCDH15 reported here reveals the structural elements that drive homodimerization in the membrane-distal *cis*-dimer interface. Negative-stain single-particle EM and 3D reconstruction reveal the overall *cis*-dimeric architecture of the PCDH15 ectodomain. Functional assays provide strong evidence that the molecular interactions that drive *cis*-dimerization of PCDH15 are critical for sensing mechanical stimuli by hair cells.

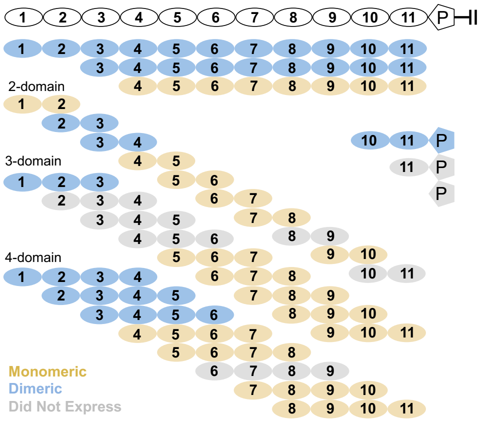

Figure 2. Schematic of Protein Fragments Used to Interrogate PCDH15 for *cis*-Dimeric Interactions
Two-, three-, and four-domain constructs were cloned, expressed, and analyzed via AUC experiments to check for homodimerization; see also Figure S1 and Table S2. A PCDH15 fragment containing the PICA domain was analyzed by MALS; see also Figures S2 and S3. Proteins that formed dimers are colored light blue, while monomers are colored tan. Constructs that did not express are colored in gray.

RESULTS

Identifying the Minimal *cis*-Dimeric Region of PCDH15

To investigate the structural basis for PCDH15 *cis*-homodimerization, we first endeavored to identify fragments from within the PCDH15 cadherin repeat region that form dimers. Using a mammalian HEK293 cell expression system, we produced a series of constructs that "walk" the length of the 11 cadherin domains of the mouse PCDH15 ectodomain in two-domain fragments and interrogated their dimeric properties via sedimentation equilibrium analytical ultracentrifugation (AUC) (Figures 2 and S1; Table S2). Only the EC2-EC3 and EC3-EC4 constructs—constructs that both contained EC3—were dimers in solution. While the EC7-EC8 construct appeared weakly dimeric (K_D = 208 μM), the value of the isodesmic constant (K_I = 343 μM) indicates that this interaction is nonspecific.

While most two-domain constructs of PCDH15 could be produced, two constructs, EC8-EC9 and EC10-EC11, failed to express. To ensure full coverage of the PCDH15 ectodomain, and to potentially enhance weak binding affinities of the

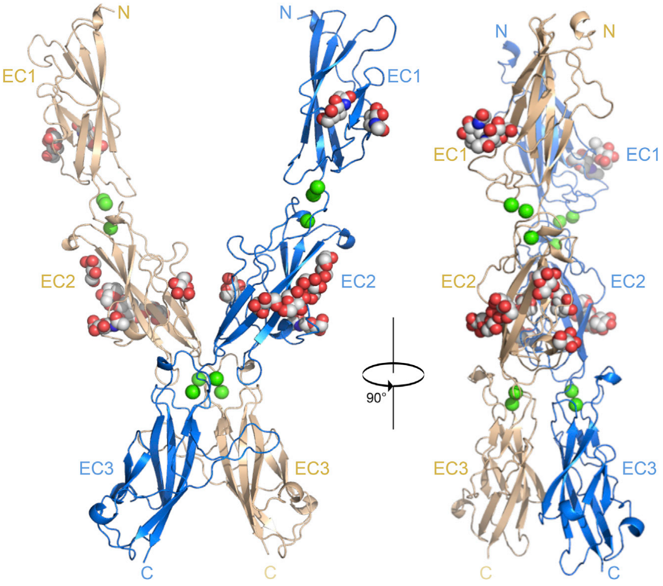

Figure 3. Structure of the PCDH15 EC1-EC3 *cis*-Dimer

PCDH15 EC1-EC3 *cis*-dimer forms through a surface that spans the EC2-EC3 linker region, the "top" of EC3, and the disulfide-stabilized loop formed by an inserted segment between the A and A′ strands of EC3. This interface is also present, yet not described, in a previously published structure of PCDH15 EC3-EC5 (PDB: 5T4M; see also Figure S5). Calcium ions are represented as green spheres (see also Figure S4) and glycans as red, white, and blue spheres (see also Figure S6).

two-domain fragments, we carried out similar "domain walking" experiments with both three- and four-domain constructs (Figure 2; Table S2). Although three of these additional thirteen fragments did not express, the combination of two-, three-, and four-domain fragments achieved full coverage of the cadherin repeat region of the PCDH15 ectodomain. The only four-domain construct that was dimeric was EC3-EC6, which showed dimerization behavior similar to the other constructs containing EC3. Overall, these data show that PCDH15 forms a relatively strong *cis*-dimeric interaction that involves the EC3 domain.

Analysis of PCDH15 sequences from numerous species revealed that the PICA domain succeeding the 11 EC domains and preceding the membrane insertion point was highly conserved (Figure S2). We produced constructs that contained the PICA domain to characterize their *cis*-association state. Although the PICA domain region failed to express in isolation or when preceded by the final EC domain, a construct encoding EC10-EC11-PICA was well behaved. Multi-angle light scattering (MALS) analysis showed that this EC10-EC11-PICA domain construct was also dimeric (Figure S3). The dimeric nature of the EC10-EC11-PICA domain protein, combined with the monomeric nature of fragments lacking the PICA domain but containing EC10-EC11, suggests that the PICA domain mediates *cis*-dimerization of PCDH15 near the membrane insertion point.

Crystal Structure of an EC1-EC3 PCDH15 *cis*-Homodimer

Since we detected *cis*-dimerization in the EC3 region, we produced an EC1-EC3 construct for structure determination. This construct contained both the *cis*-interacting region and the Cadherin-23-*trans*-interacting region located in EC1-EC2. Consistent with the AUC results (Figure 2), the PCDH15 EC1-EC3 protein acted as a dimer in MALS (Figure S3), with a measured molecular mass of 88 kDa that is about twice the mass of the predicted mass of a monomer (41.7 kDa). PCDH15 EC1-EC3 also acted as a dimer in sedimentation equilibrium AUC with a binding affinity of 1.2 μM (Figure S1). We determined the crystal structure of this molecule to 1.7 Å resolution (Figure 3) by molecular replacement using a two-domain structure of PCDH15 (PDB: 4APX) as a search model (Sotomayor et al., 2012). Data and refinement statistics are shown in Table S1.

The PCDH15 EC1-EC3 protomers are arranged in a parallel homodimer in which the overall architecture resembles an open pair of scissors with the homodimer interface, centered around the EC2-EC3 junction, forming the "hinge" of the scissors (Figure 3). The protomer structure of the EC1-EC2 region is highly similar to the previously reported structure of a two-domain PCDH15 fragment, with a root-mean-square deviation (RMSD) of 1.07 Å (Sotomayor et al., 2012). The only notable difference is a slight change in the position of the N-terminal helix, which appears to be displaced due to binding of CDH23 in the earlier structure.

The structure of the PCDH15 *cis*-homodimer reveals a number of features that are atypical with respect to other published structures of cadherin superfamily proteins. The EC3 domain of PCDH15 contains an embellishment to the typical cadherin fold where the A/A* strand connection is interrupted by an inserted disulfide-stabilized A/A* loop (Figure 4). The A/A* loop from one protomer wraps around its partner, as if the two protomers are embracing each other.

Importantly, while the EC1-EC2 linker region contains the canonical arrangement with three bound calcium ions, the EC2-EC3 junction did not contain electron density for Ca1. To confirm the absence of Ca1, we collected a low-energy X-ray anomalous scattering dataset to visualize Ca^{2+} in Bijvoet difference maps. Inspection of the Bijvoet difference maps revealed the three expected peaks in the PCDH15 EC1-EC2 junction region, corresponding to the canonical binding of three Ca^{2+} ions (Figure S4A). However, the Bijvoet difference maps showed only two peaks in

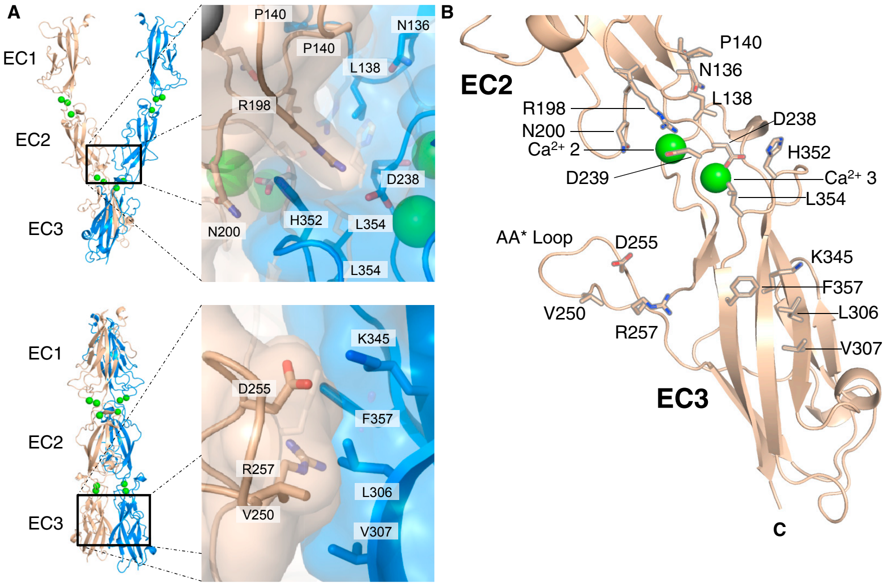

Figure 4. Structural Details of the *cis*-Dimer Interface

(A) Expanded views of the cis-dimer interface, with details of the EC2-EC3 junction interface (upper panel) and the EC3-EC3 interface (lower panel).

(B) Interfacial residues shown on a single PCDH15 protomer.

the PCDH15 EC2-EC3 junction, corresponding to only two calcium ions bound at this non-canonical site (Figure S4B).

The PCDH15 homodimer interface buries 740 $Å^2$ of interfacial surface area per protomer. While burying a relatively small surface area, the interface has high calculated shape complementarity (S_c) of 0.702. For comparison, the *trans*-interface between PCDH15 EC1-EC2 and CDH23 EC1-EC2 buries 907 $Å^2$ and has an S_c of 0.511. The interface can be divided into two functional regions, one that is dominated by interactions between partner EC2-EC3 linker regions and the other that is located between the extended disulfide-stabilized A/A* loop of one protomer and the surface formed by the C, F, and G β strands of EC3 in the partner molecule (Figure 4). The EC2-EC3 junction sub-region contains hydrophobic interactions in which residues Leu138, Pro140, and Leu354 interact with copies of themselves across the 2-fold symmetry axis. Additionally, His352 from one protomer associates with Arg198 in the other through a cation-π interaction. Val250 in the A/A* loop of one protomer forms interactions with a hydrophobic patch on the partner protomer lined by Leu306, Val307, and Val343. Additional interactions include a salt bridge formed between Asp255 and Lys345, and a cation-π interaction formed between Arg257 and Phe357 (Figure 4B). Interestingly, though not identified by the authors, this interface exists in an already published crystal structure of PCDH15 EC3-EC5 (PDB: 5T4M), with an RMSD of 1.73 Å, providing additional support for its biological relevance (Figure S5) (Powers et al., 2017).

We also observe a number of sugar decorations, particularly on the adhesive domains. PCDH15 EC1 contains two N-linked glycans, one on Asn31 and the other on Asn76; EC2 has a single N-glycan at Asn180. Cadherins and protocadherins are among a small number of protein families known to be modified by the addition of single-O-mannose moieties to threonine residues (Vester-Christensen et al., 2013). Five threonine residues in PCDH15 EC2 were modified by single-O-mannose moieties: Thr144, Thr225, Thr227, Thr229, and Thr231 (Figure S6). The last four of these O-mannosylated residues are all on the G-strand of EC2 and are arranged in a single row of mannose moieties on the molecular surface. It is interesting that numerous cadherins and protocadherins have O-man sites clustered in EC2 (Larsen et al., 2017). Nevertheless, the functional role of O-mannosylation is not yet well understood. While the structure shows that O-man is likely to play no role in either *cis* or *trans* recognition, our data do not shed further light on other possible functions.

Point Mutations that Interfere with *cis* Dimerization

To biophysically validate the homodimer interface observed in the PCDH15 EC1-EC3 structure, we produced several point mutations designed to disrupt the interface, and subjected these mutant proteins to analysis by both AUC and surface plasmon resonance (SPR) to assess their dimer-formation properties.

We designed targeted mutations in both parts of the PCDH15 EC1-EC3 *cis* interface: in the interface between EC2-EC3-linker

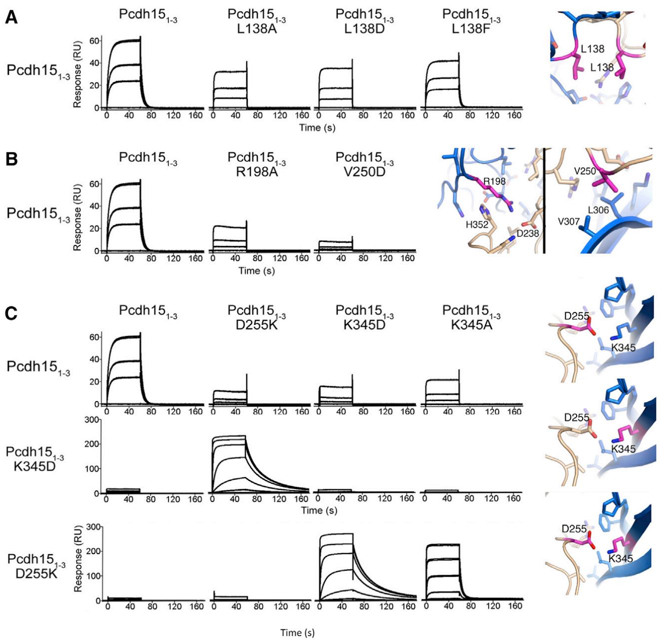

Figure 5. Surface Plasmon Resonance Binding Curves for Point Mutants in the PCDH15 *cis*-Interface

(A) SPR response curves for mutations targeting the EC2-EC3 interface through residue Leu138.

(B) SPR response curves for mutations targeting Arg198 in the EC2-EC3 interface and Val250 in the EC3-EC3 interface.

(C) SPR response curves for mutations targeting the Asp255/Lys345 salt bridge in the EC3-EC3 interface, showing disruption of binding (upper panel) and rescue through complementation (lower two panels). See also Figure S7.

regions and the EC3-EC3 interface between the extended A/A* loop and the body of the EC3 protomer (Figure 4). To target the EC2-EC3-linker interface, we mutated Leu138 and Arg198 to various amino acids. Leu138, near the *cis*-dimer 2-fold axis, interacts with a copy of itself across the 2-fold symmetry axis through hydrophobic interactions. Leu138Ala, Leu138Asp, and Leu138Phe mutations were designed to remove hydrophobic surface area, to introduce like-charge repulsion, or to cause steric clashing, respectively. Arg198Ala was designed to destabilize the interaction observed between Arg198 and His352.

To disrupt the EC3-EC3 protomer interface, Val250, Asp255, and Lys345 were mutated to disrupt interactions between the A/A* loop and the body of the EC3 domain. Val250Asp on the A/A* loop was chosen to disrupt the interface by burying a charged residue in a natively hydrophobic region. Asp255Lys, Lys345Ala, and Lys345Asp were designed to disrupt the salt bridge observed between Lys 345 and Asp 255.

AUC analysis revealed each of these *cis*-interface-targeted point mutants to show a significant decrease in dimerization affinity, with most showing no detectable homodimerization. Leu138Ala, Leu138Asp, Arg198Ala, Val250Asp, Asp255Lys, Lys345Ala, and Lys345Asp were all monomeric in solution. Leu138Phe failed to fully disrupt dimerization but showed attenuated binding, with a K_D of 15.3 μM, as compared to 1.2 μM for wild-type (Table S2).

We also performed SPR experiments in which wild-type PCDH15 EC1-EC3 was immobilized on the chip surface, and interactions between wild-type and mutant protein analytes were assessed (Figure 5). As expected, the greatest binding response was elicited when wild-type PCDH15 EC1-EC3 was flowed over the chip surface; no binding was detected when PCDH15 EC1-EC2, lacking EC3, was used as the analyte, and all point mutants showed attenuated binding responses, compared to wild-type (Figure 5). Of the mutant proteins, Leu138Phe generated SPR binding curves with a maximum response closest to the wild-type curves, which is consistent with its inability to disrupt dimerization in AUC. Val250Asp showed the strongest inhibition of *cis*-dimerization in the SPR experiments (Figure 5B).

We next attempted to determine the effects of these mutations on dimerization in the context of the larger PCDH15 ectodomain. Since the PICA domain mediates *cis*-dimerization, all PICA domain-containing constructs were dimeric. We therefore introduced the EC2-EC3 *cis*-interface region mutations in the context of an eleven-domain construct, which includes all EC domains of PCDH15 but lacks the PICA domain. Wild-type PCDH15 EC1-EC11 formed dimers with 1.8 μM affinity in solution as assessed by AUC. PCDH15 EC1-EC11 Arg198Ala appeared dimeric in AUC experiments, but partial precipitation during the experiment prevented us from calculating a K_D with confidence; PCDH15 EC1-EC11 Val250Asp, however, was monomeric, both in AUC and negative-stain transmission electron microscopy (TEM) (Figure S8). Taken together, these results indicate that while a majority of the binding energy derives from the EC2-EC3 interface observed in the crystal structure, the rest of the ectodomain does contribute to dimerization, but with binding energy too low to be detected by AUC.

Validation of EC3 *cis*-Dimerization Interface by Charge-Reversal Experiments

We sought to demonstrate definitively that the effects observed from targeted mutation of Asp255 and Lys345 resulted from disruption of a salt bridge between them; to accomplish this, we employed a strategy using charge-reversal experiments. Asp255Lys and Lys345Asp mutations were designed to introduce like-charge repulsion in homogeneous populations of either mutant, yet, as they should compensate for one another,

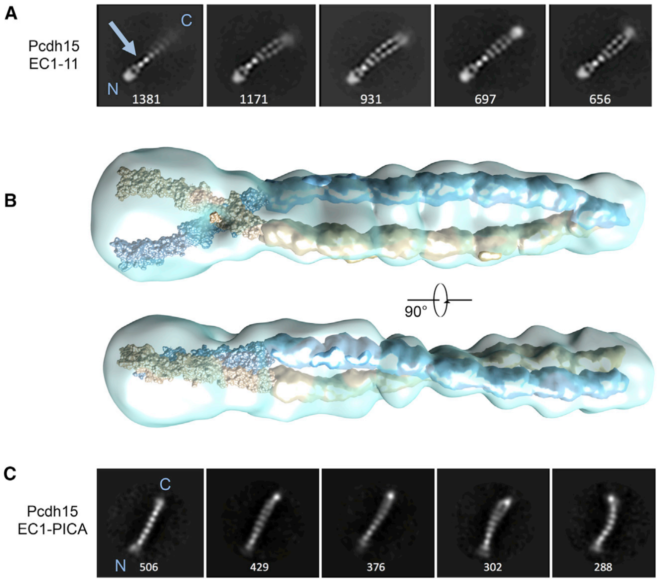

Figure 6. 2D Class Averages and a 3D Reconstruction of Negative-Stain Electron Micrographs

(A) 2D class averages of WT PCDH15 EC1-EC11 from negative-stain electron micrographs. The number of individual images used is presented at the base of the image. See also Figure S8.

(B) 3D class average generated from negative stain. Manually placed into the density for reference is the crystal structure of PCDH15 EC1-EC3, as well as simulated 11 Å electron density for an additional 14 cadherin domains.

(C) 2D class averages of WT PCDH15 EC1-PICA from negative-stain electron micrographs

cis-heterodimers are expected to form when the two mutant proteins are mixed together. Each of these mutant proteins is monomeric in solution. To determine whether these two mutations compensate for each other as predicted, we performed SPR experiments in which each mutant protein was immobilized on the chip surface. These surfaces showed no measurable binding for wild-type PCDH15 EC1-EC3 or for other non-compensatory mutations (Figure 5C). The Lys345Asp surface, however, showed robust binding to Asp255Lys; similarly, the Asp255Lys surface showed robust binding to Lys345Asp, as well as some moderate binding to Lys345Ala, possibly as a result of the mutation permitting a new salt bridge to form with Glu347 (Figure 5C). These charge-reversal experiments show that the *cis*-dimerization mode we observe crystallographically indeed represents the biophysically observed dimer.

We also generated a select few PCDH15 EC1-EC3 double mutants and one triple mutant and analyzed their oligomeric state using size exclusion chromatography (Figure S7). Leu138Ala/Asp255Lys eluted predominately as a monomer, as expected. Leu138Ala/Lys345Asp eluted as a mixed population with a slightly higher monomer peak. Asp255Lys/Lys345Asp eluted predominately as a dimer, which is in agreement with the SPR data for the two complementary salt bridge mutations. Last, the Leu138Ala/Asp255Lys/Lys345Asp eluted primarily as a monomer, with a small shoulder corresponding to the dimer.

Single-Particle Reconstruction from Negative-Stain EM

We next used single-particle negative-stain EM and 3D reconstruction to visualize the ectodomain of PCDH15. We separately imaged both the full-length ectodomain, which as described below was complicated by aggregation mediated by the PICA domain, as well as a PCDH15 EC1-EC11 protein lacking the PICA domain. Particles were picked via template picking with FindEM (Roseman, 2004) and 2D class averages were generated using RELION (Kimanius et al., 2016). The 2D class averages were of sufficient resolution so that most individual EC domains are resolved; overall, the class averages clearly show a PCDH15 dimer arranged as a parallel double helix (Figure 6A). Toward one end of the dimer is a region of increased electron density for two successive domains (blue arrow), which corresponds to the EC3 *cis*-dimer interface observed in the crystal structure. Two lobes, corresponding to the EC1-EC2 CDH23-interacting regions, can be seen adjacent to these EC2-EC3 dimerization regions in many of the 2D classes. Notably, for the PCDH15 EC1-EC11 protein, slight feathering is observed at the opposite EC11-proximal end, indicating flexibility or conformational heterogeneity, which is not surprising in the absence of *cis*-dimeric PICA domain.

We used the program cryoSPARC (Punjani et al., 2017) to reconstruct a 3D map to 20 Å nominal resolution. The positions of individual EC domains are clear in this map, enabling us to position the structure of PCDH15 EC1-EC3 dimer, and also to place 7 additional EC domains for each monomer using a model of the EC3 domain from N-cadherin, such that the positions of 10 EC domains in total were modeled for each PCDH15 monomer (Figure 6B). The final EC domain could not be modeled, likely due to the apparent disorder at the C-terminal end evident as feathering in the 2D class averages. The model generated is that of a right-handed, parallel double helix. The overall dimensions of the *cis*-dimeric structure of the PCDH15 ectodomain, with 10 visualized EC domains per protomer, is ~485 Å in total length, with a helix diameter of ~85 Å. The 10-domain structure completes ~0.5 helical turns; thus, the helical rise per turn is ~690 Å. This is in agreement with the helical rise measured in Kachar et al. (2000). Importantly, this structure is for PCDH15 under zero tension; thus the helix winding is expected to be near its maximum. At 20 Å nominal resolution, only the overall domain positions are defined. We therefore view this model as defining the overall architecture of PCDH15; however, given the low resolution, we hesitate to extract details from the model beyond its overall dimensions.

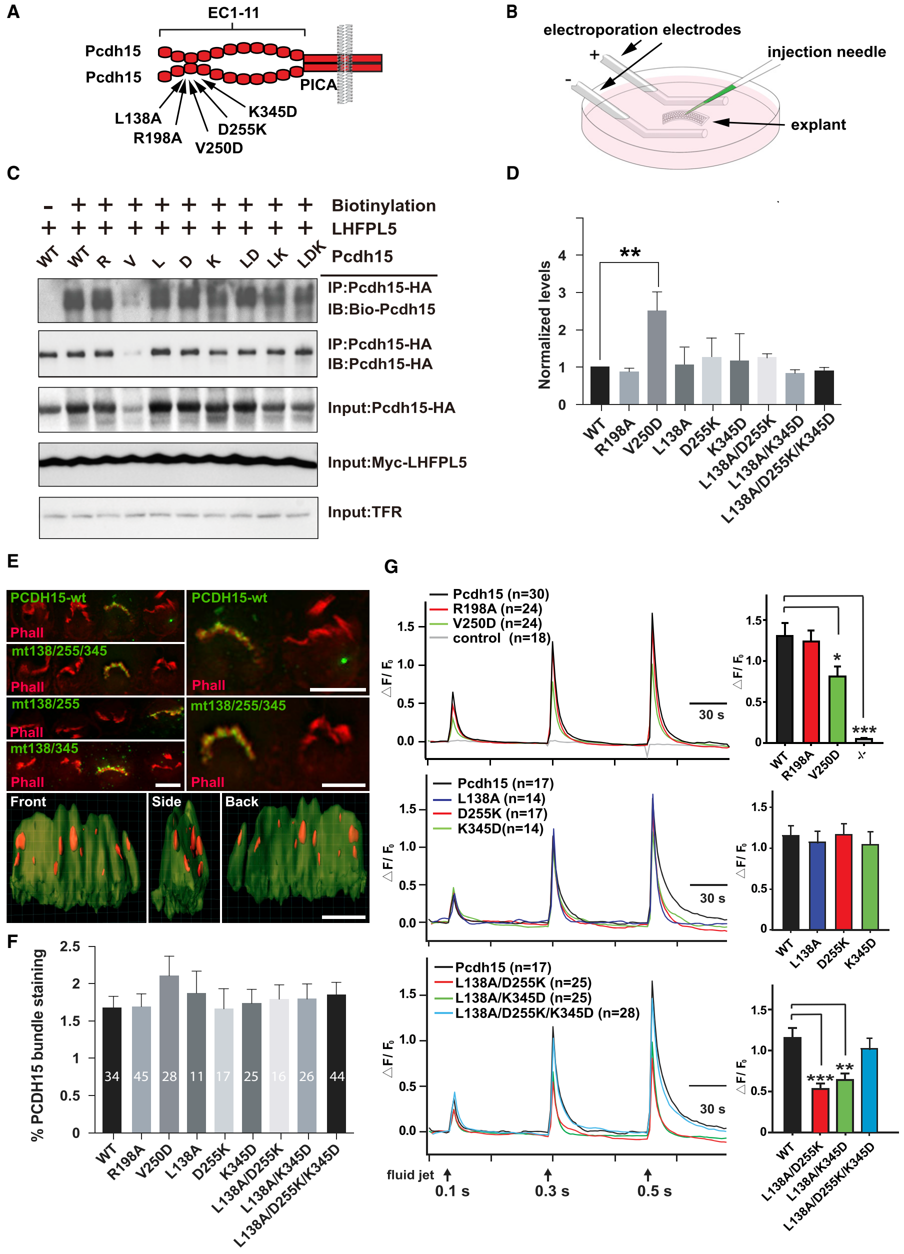

(legend on next page)

We also produced a construct of the full ectodomain (EC1-PICA) for imaging by single-particle negative-stain EM. As before, 2D class averages were generated using RELION. However, far fewer isolated particles could be obtained due to the formation of higher-order oligomers. These oligomers, which were directly visualized in EM images, show associations between PCDH15 dimers forming through the PICA domain region. Nonetheless, we were able to generate 2D class averages of PCDH15 EC1-PICA (Figure 6C). Similar to the PCDH15 EC1-EC11 protein, the overall orientation of the PCDH15 ectodomain was clear in the class averages due to the distinctive structures at either end of the molecule. The CDH23-interacting N-terminal end appears as a forked bi-lobed structure. Unlike the EC1-EC11 structure, where the C-terminal end becomes increasingly disordered, in the PICA domain containing structure, the C-terminal end instead culminates in a bright region corresponding to the dimeric PICA domain. Indeed, the most notable difference between the two sets of class averages is the dramatically reduced amount of feathering in the PICA domain-containing full-length ectodomain. This is consistent with our biophysical results showing that the PICA domain provides an additional mediator of membrane-proximal *cis* dimerization.

Mutations that Affect PCDH15 Homodimerization Perturb Its Function in Hair Cells

We have previously shown that injectoporation is a useful method to express the genetically encoded Ca^{2+} sensor G-CaMP3 in hair cells and to then analyze mechanotransduction by changes in the fluorescence intensity of G-CaMP3 following stimulation of hair bundles with a fluid jet (Figure 7B) (Xiong et al., 2012, 2014; Zhao et al., 2014). To determine the extent to which PCDH15 homodimerization is critical for its function in hair cells, we used injectoporation to express recombinant PCDH15 molecules carrying point mutations together with G-CaMP3 in hair cells from PCDH15-deficient homozygous *Ames-waltzer*^{av3J} mice (Alagramam et al., 2001) and measure effects of the mutations on transduction. We engineered mutations that alter one, two, or three amino acids in the EC2-EC3 dimerization domain (Arg198Ala, Val250Asp, Leu138Ala, Asp255Lys, Lys345Asp; Leu138Ala/Asp255Lys, Leu138Ala/Lys345Asp; Leu138Ala/Asp255Lys/Lys345Asp) in full-length PCDH15 (Figure 7A). To test that the mutations did not interfere with cell-surface expression, we next transfected the constructs containing a hemagglutinin (HA) tag at the C terminus into HEK293 cells together with LHFPL5, which is necessary for efficient expression of wild-type PCDH15 at the cell surface (Xiong et al., 2012). We then biotinylated proteins at the cell surface, prepared extracts, and immunoprecipitated PCDH15 with HA antibodies. Western blotting with antibodies to HA demonstrated that all constructs were efficiently expressed in HEK293 cells with the exception of Val250Asp, which was consistently expressed at lower levels (Figure 7C). Analysis of the cell-surface-expressed protein with streptavidin-coupled detection reagents revealed that all proteins were expressed at the cell surface with similar efficiency, with the exception of Val250Asp, which was present at lower levels (Figure 7D). However, relative to total levels of PCDH15-Val250Asp, the mutant construct was expressed more efficiently at the cell surface compared to wild-type PCDH15 (Figure 7D).

Next, we expressed by injectoporation PCDH15 constructs in hair cells. For this experiment, we used PCDH15 constructs lacking the epitope tag. Efficient expression of mutant constructs was observed in hair bundles using immunolocalization experiments (Figures 7E and 7F). For a quantitative assessment of expression levels, we used Imaris 9.1 software to generate 3D reconstructions of hair bundles that were stained with phalloidin to reveal their F-actin cytoskeleton. PCDH15 expression was detected with PCDH15 antibodies (Figure 7E, bottom three panels). We determined the volume ratio of PCDH15 staining and phalloidin staining (Figure 7F). There was no significant difference in

Figure 7. Functional Characterization of PCDH15 Mutants in Hair Cells

(A) Diagram of the PCDH15 homodimer. Mutations used in functional studies are indicated.

(B) Diagram of the injectoporation procedure. Cochlear explants are injected with plasmid solution, and the plasmid is transferred into hair cells by electroporation.

(C) HEK293 cells were transfected to express wild-type and mutant PCDH15 constructs that contained a C-terminal HA tag (PCDH15-HA). Myc-LHFPL5 was co-expressed to achieve efficient PCDH15 cell-surface expression (Xiong et al., 2012). Where indicated, proteins at the cell surface were biotinylated. Protein extracts were prepared and immunoprecipitated (IP) with antibodies to HA. PCDH15-HA was detected by western blotting (IB) using streptavidin-conjugated detection reagent (biotinylated [Bio]-PCDH15) or antibodies to HA (PCDH15-HA). The lower lanes show input protein prior to immunoprecipitation detected with antibodies to HA or Myc or Transferrin Receptor (TFR) (loading control).

(D) Levels of PCDH15-HA at the cell surface were determined by densitometric scanning of gels from three independent experiments. Values are expressed as a ratio between levels at the cell surfaceversus total levels, where levels for wild-type PCDH15-HA are set at 1. All data are mean ± SEM. Student's two-tailed unpaired t test was used to determine statistical significance (*$p < 0.05$, **$p < 0.01$, ***$p < 0.001$).

(E) Hair cells at P3 were injectoporated to express the indicated PCDH15 constructs without and HA tag. Hair cells were stained 2 days later with phalloidin (red) and with antibodies to PCDH15 (green). Both wild-type and mutant PCDH15 were targeted to stereocilia. The lowest three panels show 3D rendering (Imaris 9.1) of a hair bundle expressing wild-type PCDH15 (red) where the hair bundle was visualized with phalloidin (green). A front side and back view of a hair bundle is shown.

(F) Quantification of expression levels of PCDH15 constructs in hair bundles by determining the volume ratio of PCDH15 staining and phalloidin staining. The number of quantified hair bundles is indicated. All values are mean ± SEM. Student's two-tailed unpaired t test was used to determine statistical significance (*$p < 0.05$, **$p < 0.01$, ***$p < 0.001$).

(G) Hair cells from homozygous *Ames-waltzer*^{av3J} mice were injectoporated at P3 to express GCaMP3 and the indicated PCDH15 constructs. After 2 days in culture, mechanotransduction was evaluated by deflecting hair bundles for increasing amounts of time while simultaneously measuring increases in GCaMP3 fluorescence. On the right, representative traces are shown for individual constructs. The number of analyzed cells is indicated. On the right, the amplitude of the 2nd Ca^{2+} response peak was quantified. All data are mean ± SEM. Student's two-tailed unpaired t test was used to determine statistical significance (*$p < 0.05$, **$p < 0.01$, ***$p < 0.001$).

expression levels for the different PCDH15 mutants, even for Val250Asp, which was less efficiently expressed in heterologous cells compared to other PCDH15 constructs (Figure 7F). Notably, the stereocilia that form the hair bundle of a hair cell are devoid of vesicles and transmembrane proteins in stereocilia are inserted into the plasma membrane near the base of stereocilia from where they are transported into stereocilia. Thus, the protein levels that we observed in the hair bundle likely reflect PCDH15 levels at the cell surface, and the data suggest that all constructs are expressed efficiently and at comparable levels in hair bundles of hair cells.

For functional studies, Ca^{2+} imaging was applied while hair bundles were mechanically stimulated with a fluid jet by applying three consecutive pulses of increasing duration (0.1, 0.3, and 0.5 s). Hair cells from *Ames-waltzer*^{av3J} mice did not show any significant increase in fluorescence intensity following mechanical stimulation of their hair bundles (Figure 7G). In contrast, reexpression of wild-type PCDH15 lead to a robust increase in fluorescence in response to mechanical stimulation of the bundle (Figure 7G). Next, we analyzed PCDH15 molecules carrying different mutations in the EC2-EC3 *cis*-homodimerization interface. Although our biophysical experiments demonstrated that *cis*-dimerization is dependent not only on the EC2-EC3 interface, but also on the PICA domain, we reasoned that weakening this structurally defined membrane-distal interface, which significantly contributes to *cis*-dimerization, would lead to detectable functional impairment in the biologically relevant environment of hair cells. For functional studies, we engineered both the Arg198Ala and Val250Asp mutations into full-length PCDH15. Significantly, PCDH15-Arg198Ala rescued mechanotransduction defects in hair cells from *Ames-waltzer*^{av3J} mice similar to wild-type PCDH15, while PCDH15-Val250Asp only restored transduction partially (Figure 7G) even though it was targeted to stereocilia (Figure 7F). Biophysical experiments show that, in an EC1-EC11 construct lacking the PICA domain, Val250Asp but not Arg198Ala perturbed *cis*-dimerization between the 11 EC repeat fragment. These results are consistent with the requirement of *cis*-dimerization for functional transduction.

For further verification of the dimerization interface, we also tested single mutations Leu138Ala, Asp255Lys, and Lys345Asp; double mutations Leu138Ala/Asp255Lys and Leu138Ala/Lys345Asp; and the triple mutation Leu138Ala/Asp255Lys/Lys345Asp. Single-mutant constructs restored mechanical sensitivity to hair bundles from PCDH15-deficient *Ames-waltzer*^{av3J} mice to a similar degree as wild-type PCDH15 (Figure 7G), suggesting that single mutants were not sufficiently strong to disrupt dimerization in the presence of the remainder of the extracellular PCDH15 domain including the PICA domain. However, double mutants were efficiently targeted to stereocilia (Figures 7C and 7D) but had significantly impaired PCDH15 function (Figure 7G). Strikingly, triple-mutation constructs containing the charge reversal mutations Asp255Lys and Lys345Asp that should enable a salt bridge to form in the reverse orientation restored PCDH15 function (Figure 7G). Taken together, these data suggest that mutations in the EC2-EC3 dimerization surface that weaken *cis*-homodimerization of PCDH15 affect its function in hair cells. Unfortunately, as we have so far not succeeded in obtaining crystals of the *cis*-homodimer interface within the PICA domain, structure-guided mutational analysis to test the function of amino acids critical for homophilic *cis*-interactions mediated by PICA domains remains out of reach.

DISCUSSION

The adhesion complex formed by PCDH15 and CDH23 in tip links of hair cells shows features different from other cadherin adhesion complexes, reflecting likely functional adaptations of tip-link cadherins for their role in mechanotransduction. *Cis* dimerization is predicted to affect the mechanical properties of tip links, providing stability through lateral *cis*-interactions and by increasing the effective adhesive strength through formation of a dimeric *trans* interface. These features are expected to be critical for mechanotransduction by affecting the transfer of mechanical force to transduction channels, and by opposing rupture of the PCDH15/CDH23 *trans* bond during mechanical stimulation. Here, we have used single-particle EM and solution biophysical measurements to gain insights into the overall architecture of the *cis*-dimeric PCDH15 ectodomain, and X-ray crystallography to define at atomic resolution structural features of PCDH15 that are critical for *cis*-homodimerization. Our functional studies in hair cells provide evidence that disruption of the *cis*-homodimeric architecture of PCDH15 affects its function in hair cells.

Our findings reveal a lateral interaction mode that drives *cis* dimerization, which has not been previously recognized for a member of the cadherin superfamily. This lateral interaction leads to the formation of a *cis* dimeric double helical filament. The PCDH15 EC domain region (EC1-EC11) forms a parallel double-helical dimer ∼485 Å in length from the first cadherin domain EC1 to EC10, the final well-ordered domain in the reconstruction, making ∼0.5 helical turns in total. The membrane-proximal PICA domain and the preceding EC11 domain will add to this length in the complete ectodomain. Two *cis*-dimeric interfaces are present in the PCDH15 ectodomain: one that forms through the membrane-proximal PICA domain, and the other encompassing regions of domains EC2 and EC3. Thus, the overall architecture of the PCDH15 ectodomain is a parallel double-helical dimer bridged in *cis* by two distinct interfaces distal from one another. The *cis*-dimeric architecture of PCDH15 defined here, combined with a prior structure of the *trans*-interaction of PCDH15 with CDH23, allows us to model the interaction region of the native 2:2 complex (Figure 8) and shows that the PCDH15 *cis* dimer can accommodate the known *trans* binding mode with CDH23 positioned internally (toward the *cis*-dimer 2-fold axis) relative to PCDH15.

Tip links have been proposed to function both in the conveyance of force and as a gating spring for the transduction channel (Corey and Hudspeth, 1983; Howard and Hudspeth, 1987; Pickles et al., 1984). It is still unclear whether the tip link contributes to the gating spring, or whether the gating spring is provided by one or more molecules connected in series to the tip link. Earlier structural studies of CDH23 and PCDH15 have focused on the question of tertiary structural elasticity—whether force applied to PCDH15 will result in protein extension without unfolding (Araya-Secchi et al., 2016; Powers et al., 2017;

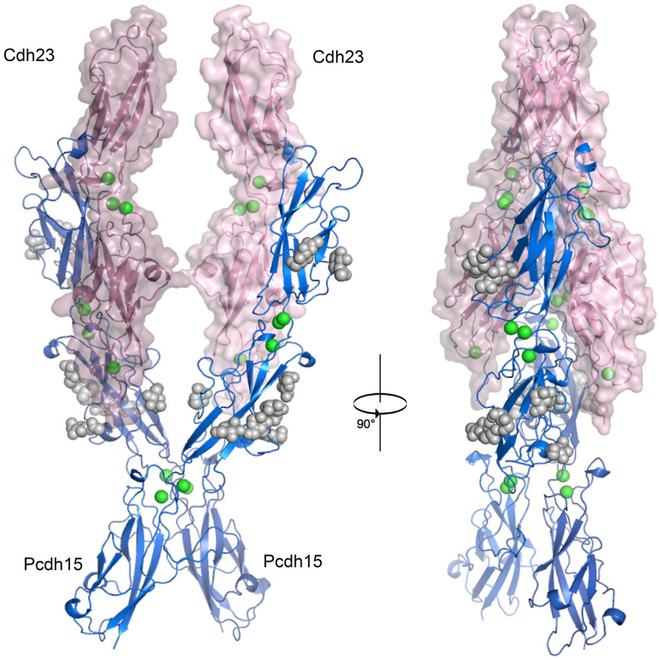

Figure 8. Model of PCDH15 EC1-EC3 in Complex with CDH23 EC1-EC2

A model of CDH23 EC1-EC2, in lilac, in complex with the PCDH15 EC1-EC3 *cis*-dimer, in blue. Ca^{2+} is presented in green; glycans are presented in gray. Model was generated by aligning PCDH15 EC1-EC2 from the PCDH15 EC1-EC2:CDH23 EC1-EC2 complex structure (PDB: 4APX) to the PCDH15 EC1-EC3 *cis*-dimer.

Sotomayor et al., 2010, 2012). In these studies, Sotomayor and coworkers have reported crystal structures for monomeric EC domain pairs or triples and computationally assessed the spring properties of these *cis*-monomeric ectodomain fragments using steered molecular dynamics. *In silico* simulation of monomeric protein fragments encompassing the EC1 and EC2 domains of CDH23 was reported to suggest that tip links might be too stiff to function as the gating spring, a hypothesis that was initially based on the observed double-stranded nature of the tip link (Kachar et al., 2000; Sotomayor et al., 2010). However, subsequent studies suggested that only some regions of the tip link might be too stiff to act as the gating spring, whereas other regions could potentially elongate significantly in response to force (Araya-Secchi et al., 2016; Powers et al., 2017; Sotomayor et al., 2012). These conclusions were based on crystal structures of PCDH15 ectodomain fragments EC1-EC2, EC3-EC5, EC8-EC10, and EC9-EC10 (Araya-Secchi et al., 2016; Powers et al., 2017; Sotomayor et al., 2010, 2012). Steered molecular dynamics simulations were used to generate force extension curves, which suggested that each of these fragments were too stiff to extend significantly under forces of the magnitude experienced by the tip link. One structural element, however, a bent connection between the successive domains EC9 and EC10, could be extended by straightening the bend at physiological levels of force (Araya-Secchi et al., 2016). Straightening this EC9-EC10 bend was postulated to mediate lengthening of PCDH15 by up to 4 nm.

Our structural studies now provide insight into structural features of the entire PCDH15 ectodomain, which indicate additional potential for structural flexibility. While some modes of PCDH15 elasticity might depend on effects that can be understood by investigating sub-regions in isolation, others may depend on its overall quaternary structure. One potential mode of structural elasticity that becomes apparent in light of the overall structure of PCDH15 we describe here is elongation in response to force through helix unwinding. Since the two molecules of the *cis* dimer are bridged by two interfaces distal from one another and that comprise only a fraction of the available molecular surface area, molecular elasticity is perhaps provided by unwinding and rewinding of the PCDH15 double helix. We estimated the maximum elongation possible through helix unwinding, both by measuring the distance traversed through the helical electron density of one molecule, and with the equation for helix path length, $L = (\text{HelixRise}^2 + \text{circumference}^2)^{1/2}$, and obtained similar values. In a completely unwound state, this helical path could in principle be straightened to elongate the molecule from ~485 Å—the length we measure from the zero-tension single-particle reconstructions—to ~520 Å in length, yielding an extension of ~35 Å. PCDH15 accounts for about one-third the length of the tip link (11 EC domains plus the PICA domain), with about two-thirds in cadherin 23 (27 EC domains)—also a giant cadherin that appears in freeze-etched EM images and in low-resolution negative-staining EM images to form a tightly wound helix (Kachar et al., 2000; Kazmierczak et al., 2007). Thus, a helical tip link consisting of 38 EC domains and a PICA domain might have significant structural flexibility through helix unwinding and rewinding that goes well beyond the 6-nm upper limit defined so far by structural studies of PCDH15. Notably, tip links in hair cells at rest already experience substantial force. Measurements in bullfrogs suggest a resting force of approximately 8 pN (Jaramillo and Hudspeth, 1993). With a gating spring stiffness of 500 μN/m, the spring would already be extended at rest by ~16 nm (Jaramillo and Hudspeth, 1993), and helix unwinding might substantially contribute to this extension.

In experimental settings, gating springs can extend under extreme conditions by as much as ~150 nm (Shepherd and

Corey, 1994), a range that far exceeds the dimensions possible with flexibility in the EC9-EC10 region and helix unwinding. However, hair bundles *in vivo* are extraordinarily sensitive to deflection, responding maximally to ~1° angular deflection (Corey and Hudspeth, 1983). At the threshold of hearing, bundles are deflected by less than 1 nm (Rhode and Geisler, 1967). Thus, the gating spring likely extends far less than 150 nm under physiologically relevant conditions. To accomplish extensions in the order of 150 nm by elongation of PCDH15 and CDH23 alone would likely require protein unfolding. One mode of extension that has been proposed involves β strands "popping out" of individual EC domains to add length to the tip link (Powers et al., 2017; Sotomayor et al., 2010). However, due to auditory response times, this would require refolding to be faster than 50 μs. To accommodate extension on the order of 150 nm therefore likely involves other elements, potentially including the cell membrane. Notably, the persistence of the tip link under extreme mechanical deflection suggests that the specific *trans*-adhesive interface formed between the *cis*-homodimer of PCDH15 and the *cis*-homodimer of CDH23 is exceptionally strong.

In summary, our findings provide first insights into the *cis*-homodimeric structure of the PCDH15 ectodomain and reveal unique mechanisms of lateral dimerization not observed for any other cadherin. It will be interesting to determine whether other members of the cadherin superfamily can adopt a helix conformation similar to PCDH15. For example, PCDH24 has been shown to be a component of intermicrovillar adhesions in intestinal brush border cells (Crawley et al., 2014). Intriguingly, the ectodomain of PCDH24 shares features with tip-link cadherins (Elledge et al., 2010; Sotomayor et al., 2010). Like in PCDH15 and CDH23, the PCDH24 ectodomain is substantially larger than in classical cadherins. It also lacks N-terminal tryptophan residues in EC1, which are critical for *trans*-interactions between classical cadherins (Boggon et al., 2002; Shan et al., 1999; Shapiro et al., 1995), suggesting possible similarities in structural organization and *trans* binding. It will thus be important to determine ectodomain structures for other atypical members of the cadherin superfamily. We anticipate that the structural organization that we describe here will apply to other cadherins thus defining a subfamily within the larger superfamily with potentially shared functions.

STAR★METHODS

Detailed methods are provided in the online version of this paper and include the following:

- KEY RESOURCES TABLE
- CONTACT FOR REAGENT AND RESOURCE SHARING
- EXPERIMENTAL MODEL AND SUBJECT DETAILS
  - ○ Cell lines
- METHOD DETAILS
  - ○ Plasmids, protein expression and purification
  - ○ Crystallization and structure determination of the PCDH15 EC1-3
  - ○ Surface plasmon resonance (SPR)
  - ○ Sedimentation Equilibrium Analytical Ultracentrifugation
  - ○ Negative Stain Electron Microscopy
  - ○ Cell surface biotinylation and immunoprecipitation experiments
  - ○ Injectoporation and Ca^{2+} imaging
  - ○ Whole mount Immunostaining
- QUANTIFICATION AND STATISTICAL ANALYSIS
- DATA AND SOFTWARE AVAILABILITY

SUPPLEMENTAL INFORMATION

Supplemental Information includes eight figures and two tables and can be found with this article online at https://doi.org/10.1016/j.neuron.2018.07.006.

ACKNOWLEDGMENTS

We thank Surajit Banerjee and Igor Kourinov for help with synchrotron data collection conducted at the APS NE-CAT 24-ID-C beamline, which is supported by NIH P41 GM103403. We acknowledge the support of National Science Foundation grants to B.H. (MCB-1412472), M.R. (GRFP DGE-1644869), and a joint NIH grant (R01DC016960) to U.M. and L.S. G.D. was supported by NIH T32GM008281. The computing in this project was supported by two NIH instrumentation grants (S10OD012351 and S10OD021764) received by the Department of Systems Biology at Columbia University. Electron microscopy was performed at the Simons Electron Microscopy Center and National Resource for Automated Molecular Microscopy located at the New York Structural Biology Center, supported by grants from the Simons Foundation (349247), NYSTAR, and the NIH National Institute of General Medical Sciences (GM103310) with additional support from Agouron Institute (grant number: F00316) and NIH S10 OD019994-01.

AUTHOR CONTRIBUTIONS

G.D., X.Q., C.S.P., B.C., B.H., U.M., and L.S. designed experiments and analyzed data; M.R. performed electron microscopy experiments; X.Q. carried out functional studies in hair cells; X.L. analyzed PCDH15 expression in heterologous cells; B.Z. and G.P. cloned PCDH15 expression constructs. P.S.K. performed SPR experiments; G.A. performed analytical ultracentrifugation experiments; R.R. performed sequence alignments; and G.D. produced proteins and performed crystallography experiments. G.D., U.M., and L.S. wrote the paper.

DECLARATION OF INTERESTS

The authors declare no competing interests.

Received: January 19, 2018
Revised: June 6, 2018
Accepted: June 29, 2018
Published: July 26, 2018

REFERENCES

Adams, P.D., Gopal, K., Grosse-Kunstleve, R.W., Hung, L.W., Ioerger, T.R., McCoy, A.J., Moriarty, N.W., Pai, R.K., Read, R.J., Romo, T.D., et al. (2004). Recent developments in the PHENIX software for automated crystallographic structure determination. J. Synchrotron Radiat. *11*, 53–55.

Ahmed, Z.M., Riazuddin, S., Bernstein, S.L., Ahmed, Z., Khan, S., Griffith, A.J., Morell, R.J., Friedman, T.B., Riazuddin, S., and Wilcox, E.R. (2001). Mutations of the protocadherin gene PCDH15 cause Usher syndrome type 1F. Am. J. Hum. Genet. *69*, 25–34.

Ahmed, Z.M., Goodyear, R., Riazuddin, S., Lagziel, A., Legan, P.K., Behra, M., Burgess, S.M., Lilley, K.S., Wilcox, E.R., Riazuddin, S., et al. (2006). The tip-link antigen, a protein associated with the transduction complex of sensory hair cells, is protocadherin-15. J. Neurosci. *26*, 7022–7034.

Alagramam, K.N., Yuan, H., Kuehn, M.H., Murcia, C.L., Wayne, S., Srisailpathy, C.R., Lowry, R.B., Knaus, R., Van Laer, L., Bernier, F.P., et al. (2001). Mutations in the novel protocadherin PCDH15 cause Usher syndrome type 1F. Hum. Mol. Genet. *10*, 1709–1718.

Araya-Secchi, R., Neel, B.L., and Sotomayor, M. (2016). An elastic element in the protocadherin-15 tip link of the inner ear. Nat. Commun. *7*, 13458.

Assad, J.A., Shepherd, G.M., and Corey, D.P. (1991). Tip-link integrity and mechanical transduction in vertebrate hair cells. Neuron *7*, 985–994.

Beurg, M., Fettiplace, R., Nam, J.H., and Ricci, A.J. (2009). Localization of inner hair cell mechanotransducer channels using high-speed calcium imaging. Nat. Neurosci. *12*, 553–558.

Boggon, T.J., Murray, J., Chappuis-Flament, S., Wong, E., Gumbiner, B.M., and Shapiro, L. (2002). C-cadherin ectodomain structure and implications for cell adhesion mechanisms. Science *296*, 1308–1313.

Bolz, H., von Brederlow, B., Ramírez, A., Bryda, E.C., Kutsche, K., Nothwang, H.G., Seeliger, M., del C-Salcedó Cabrera, M., Vila, M.C., Molina, O.P., et al. (2001). Mutation of CDH23, encoding a new member of the cadherin gene family, causes Usher syndrome type 1D. Nat. Genet. *27*, 108–112.

Cole, J.L., Lary, J.W., Moody, P., and Laue, T.M. (2008). Analytical ultracentrifugation: sedimentation velocity and sedimentation equilibrium. Methods Cell Biol. *84*, 143–179.

Corey, D.P., and Hudspeth, A.J. (1983). Kinetics of the receptor current in bullfrog saccular hair cells. J. Neurosci. *3*, 962–976.

Crawley, S.W., Shifrin, D.A., Jr., Grega-Larson, N.E., McConnell, R.E., Benesh, A.E., Mao, S., Zheng, Y., Zheng, Q.Y., Nam, K.T., Millis, B.A., et al. (2014). Intestinal brush border assembly driven by protocadherin-based intermicrovillar adhesion. Cell *157*, 433–446.

Edelstein, A., Amodaj, N., Hoover, K., Vale, R., and Stuurman, N. (2010). Computer control of microscopes using microManager. Curr. Protoc. Mol. Biol. *92*, 14.20.1–14.20.17.

Elledge, H.M., Kazmierczak, P., Clark, P., Joseph, J.S., Kolatkar, A., Kuhn, P., and Müller, U. (2010). Structure of the N terminus of cadherin 23 reveals a new adhesion mechanism for a subset of cadherin superfamily members. Proc. Natl. Acad. Sci. USA *107*, 10708–10712.

Emsley, P., and Cowtan, K. (2004). Coot: model-building tools for molecular graphics. Acta Crystallogr. D Biol. Crystallogr. *60*, 2126–2132.

Evans, P.R., and Murshudov, G.N. (2013). How good are my data and what is the resolution? Acta Crystallogr. D Biol. Crystallogr. *69*, 1204–1214.

Harrison, O.J., Jin, X., Hong, S., Bahna, F., Ahlsen, G., Brasch, J., Wu, Y., Vendome, J., Felsovalyi, K., Hampton, C.M., et al. (2011). The extracellular architecture of adherens junctions revealed by crystal structures of type I cadherins. Structure *19*, 244–256.

Howard, J., and Hudspeth, A.J. (1987). Mechanical relaxation of the hair bundle mediates adaptation in mechanoelectrical transduction by the bullfrog's saccular hair cell. Proc. Natl. Acad. Sci. USA *84*, 3064–3068.

Hudspeth, A.J. (2014). Integrating the active process of hair cells with cochlear function. Nat. Rev. Neurosci. *15*, 600–614.

Hudspeth, A.J., and Jacobs, R. (1979). Stereocilia mediate transduction in vertebrate hair cells (auditory system/cilium/vestibular system). Proc. Natl. Acad. Sci. USA *76*, 1506–1509.

Indra, I., Choi, J., Chen, C.S., Troyanovsky, R.B., Shapiro, L., Honig, B., and Troyanovsky, S.M. (2018). Spatial and temporal organization of cadherin in punctate adherens junctions. Proc. Natl. Acad. Sci. USA *115*, E4406–E4415.

Jaramillo, F., and Hudspeth, A.J. (1993). Displacement-clamp measurement of the forces exerted by gating springs in the hair bundle. Proc. Natl. Acad. Sci. USA *90*, 1330–1334.

Kabsch, W. (2010). Xds. Acta Crystallogr. D Biol. Crystallogr. *66*, 125–132.

Kachar, B., Parakkal, M., Kurc, M., Zhao, Y., and Gillespie, P.G. (2000). High-resolution structure of hair-cell tip links. Proc. Natl. Acad. Sci. USA *97*, 13336–13341.

Kazmierczak, P., Sakaguchi, H., Tokita, J., Wilson-Kubalek, E.M., Milligan, R.A., Müller, U., and Kachar, B. (2007). Cadherin 23 and protocadherin 15 interact to form tip-link filaments in sensory hair cells. Nature *449*, 87–91.

Kimanius, D., Forsberg, B.O., Scheres, S.H., and Lindahl, E. (2016). Accelerated cryo-EM structure determination with parallelisation using GPUs in RELION-2. eLife *5*. Published online November 15, 2016. https://doi.org/10.7554/eLife.18722.

Krissinel, E., and Henrick, K. (2007). Inference of macromolecular assemblies from crystalline state. J. Mol. Bio. *372*, 774–797.

Lander, G.C., Stagg, S.M., Voss, N.R., Cheng, A., Fellmann, D., Pulokas, J., Yoshioka, C., Irving, C., Mulder, A., Lau, P.W., et al. (2009). Appion: an integrated, database-driven pipeline to facilitate EM image processing. J. Struct. Biol. *166*, 95–102.

Larsen, I.S.B., Narimatsu, Y., Joshi, H.J., Siukstaite, L., Harrison, O.J., Brasch, J., Goodman, K.M., Hansen, L., Shapiro, L., Honig, B., et al. (2017). Discovery of an O-mannosylation pathway selectively serving cadherins and protocadherins. Proc. Natl. Acad. Sci. USA *114*, 11163–11168.

Pan, B., and Holt, J.R. (2015). The molecules that mediate sensory transduction in the mammalian inner ear. Curr. Opin. Neurobiol. *34*, 165–171.

Pepermans, E., and Petit, C. (2015). The tip-link molecular complex of the auditory mechano-electrical transduction machinery. Hear. Res. *330* (Pt A), 10–17.

Pickles, J.O., Comis, S.D., and Osborne, M.P. (1984). Cross-links between stereocilia in the guinea pig organ of Corti, and their possible relation to sensory transduction. Hear. Res. *15*, 103–112.

Powers, R.E., Gaudet, R., and Sotomayor, M. (2017). A partial calcium-free linker confers flexibility to inner-ear Protocadherin-15. Structure *25*, 482–495.

Punjani, A., Rubinstein, J.L., Fleet, D.J., and Brubaker, M.A. (2017). cryoSPARC: algorithms for rapid unsupervised cryo-EM structure determination. Nat. Methods *14*, 290–296.

Rhode, W.S., and Geisler, C.D. (1967). Model of the displacement between opposing points on the tectorial membrane and reticular lamina. J. Acoust. Soc. Am. *42*, 185–190.

Ricci, A.J., Kachar, B., Gale, J., and Van Netten, S.M. (2006). Mechano-electrical transduction: new insights into old ideas. J. Membr. Biol. *209*, 71–88.

Roseman, A.M. (2004). FindEM–a fast, efficient program for automatic selection of particles from electron micrographs. J. Struct. Biol. *145*, 91–99.

Shan, W.S., Koch, A., Murray, J., Colman, D.R., and Shapiro, L. (1999). The adhesive binding site of cadherins revisited. Biophys. Chem. *82*, 157–163.

Shapiro, L., Fannon, A.M., Kwong, P.D., Thompson, A., Lehmann, M.S., Grübel, G., Legrand, J.F., Als-Nielsen, J., Colman, D.R., and Hendrickson, W.A. (1995). Structural basis of cell-cell adhesion by cadherins. Nature *374*, 327–337.

Shepherd, G.M., and Corey, D.P. (1994). The extent of adaptation in bullfrog saccular hair cells. J. Neurosci. *14*, 6217–6229.

Siemens, J., Lillo, C., Dumont, R.A., Reynolds, A., Williams, D.S., Gillespie, P.G., and Müller, U. (2004). Cadherin 23 is a component of the tip link in hair-cell stereocilia. Nature *428*, 950–955.

Sotomayor, M., Weihofen, W.A., Gaudet, R., and Corey, D.P. (2010). Structural determinants of cadherin-23 function in hearing and deafness. Neuron *66*, 85–100.

Sotomayor, M., Weihofen, W.A., Gaudet, R., and Corey, D.P. (2012). Structure of a force-conveying cadherin bond essential for inner-ear mechanotransduction. Nature *492*, 128–132.

Suloway, C., Pulokas, J., Fellmann, D., Cheng, A., Guerra, F., Quispe, J., Stagg, S., Potter, C.S., and Carragher, B. (2005). Automated molecular microscopy: the new Leginon system. J. Struct. Biol. *151*, 41–60.

Vester-Christensen, M.B., Halim, A., Joshi, H.J., Steentoft, C., Bennett, E.P., Levery, S.B., Vakhrushev, S.Y., and Clausen, H. (2013). Mining the O-mannose glycoproteome reveals cadherins as major O-mannosylated glycoproteins. Proc. Natl. Acad. Sci. USA *110*, 21018–21023.

Webb, S.W., Grillet, N., Andrade, L.R., Xiong, W., Swarthout, L., Della Santina, C.C., Kachar, B., and Müller, U. (2011). Regulation of PCDH15 function in mechanosensory hair cells by alternative splicing of the cytoplasmic domain. Development *138*, 1607–1617.

Xiong, W., Grillet, N., Elledge, H.M., Wagner, T.F., Zhao, B., Johnson, K.R., Kazmierczak, P., and Müller, U. (2012). TMHS is an integral component of the mechanotransduction machinery of cochlear hair cells. Cell *151*, 1283–1295.

Xiong, W., Wagner, T., Yan, L., Grillet, N., and Müller, U. (2014). Using injectoporation to deliver genes to mechanosensory hair cells. Nat. Protoc. *9*, 2438–2449.

Zhao, B., and Muller, U. (2015). The elusive mechanotransduction machinery of hair cells. Curr. Opin. Neurobiol. *34*, 172–179.

Zhao, B., Wu, Z., Grillet, N., Yan, L., Xiong, W., Harkins-Perry, S., and Müller, U. (2014). TMIE is an essential component of the mechanotransduction machinery of cochlear hair cells. Neuron *84*, 954–967.

STAR★METHODS

KEY RESOURCES TABLE

REAGENT or RESOURCE	SOURCE	IDENTIFIER
Antibodies		
anti-HA antibody	Cell Signaling Technology	Cat# 2367S; RRID: AB_10691311
anti-Myc antibody	Cell Signaling Technology	Cat# 2276S; RRID: AB_331783
Transferrin Receptor Antibody	Invitrogen	Cat# 13-6800; RRID: AB_86623
Rabbit anti-PCDH15-CD2 antibody	Webb et al., 2011	N/A
Alexa Fluor 488- goat anti-rabbit	Invitrogen	Cat# A11070; RRID: AB_142134
Alexa Fluor 555 Phalloidin	Invitrogen	Cat# A34055
Chemicals, Peptides, and Recombinant Proteins		
PCDH15 fragments and point mutants	This paper	N/A
PCDH15-CD2	Webb et al., 2011, This paper	N/A
G-CaMP3	Addgene	Cat#22692
Myc-LHFPL5	This paper	N/A
Triton X-100	Sigma	Cat# T8532
DMEM/F12	GIBCO	Cat# 11330-057
DMEM/F12, no phenol red	GIBCO	Cat# 21041-025
HBSS	GIBCO	Cat# 14175095
FBS	Gemini	Cat# 100–106
Tris Base	Fisher Scientific	Cat# BP152-5
Sodium Chloride	Fisher Scientific	Cat# S271-10
Calcium Chloride Dihydrate	JT Baker	Cat# 1336-01
Imidazole	ACROS	Cat# 301870025
Endoglycosidase HF	New England Biolabs	Cat# P0703S
Ethylene Glycol	Fluka	Cat# 03760
HEPES	Sigma	Cat# H3375
Polyethylenimine	Polysciences	Cat# 24765-2
N-Hydroxysuccinimide	Thermo Fisher Scientific	Cat# 24500
1-Ethyl-3-(3-dimethylaminopropyl) carbodiimide	Thermo Fisher Scientific	Cat# 22980
Sodium Acetate	Sigma	Cat# S7545
Ethanolamine	Sigma	Cat# 398136
Tween-20	Sigma	Cat# P7949
BSA	Sigma	Cat# A7906
Uranyl Formate	Electron Microscopy Sciences	Cat# 22451
Freestyle 293 Expression Media	Thermo Fisher Scientific	Cat# 12338-018
Opti-MEM Reduced Serum Media	Thermo Fisher Scientific	Cat# 31985-070
CM4 chip	GE Healthcare	Cat# BR100534
Poly-L-lysine	Sigma	Cat# P2636
Lipofectamine 3000	Thermo Fisher Scientific	Cat# L3000015
EZ-LinkSulfo-NHS-SS-Biotin	Thermo Fisher Scientific	Cat# 21217
EZview-Red Anti-HA Affinity beads	Sigma	Cat# E6779
Glycine	Sigma	Cat# G7126-5KG
Critical Commercial Assays		
Spin Miniprep Kit	QIAGEN	Cat# 27106
Hispeed Plasmid Maxi Kit	QIAGEN	Cat# 12663
QuikChange II XL site-directed mutagenesis Kit	Agilent	Cat # 200521

(*Continued on next page*)

Continued

REAGENT or RESOURCE	SOURCE	IDENTIFIER
Deposited Data		
Crystal structure of mouse PCDH15 EC1-3	This paper	PDB: 6CV7
Experimental Models: Cell Lines		
Human: FreeStyle 293-F cells	Thermo Fisher Scientific	Cat# R79007
Human: HEK293S GnTI- Cells	ATCC	Cat# CRL-3022
HEK293 cells	ATCC	Cat# CRL-1573
Experimental Models: Organisms/Strains.		
Ames-waltzer^{av3J} mice	The Jackson Laboratory	Cat# 002072
Recombinant DNA		
pα-H vector	Laboratory of Daniel Leahy	N/A
PCDH15 vector	Webb et al., 2011	N/A
Software and Algorithms		
XDS	Kabsch, 2010	http://xds.mpimf-heidelberg.mpg.de
AIMLESS	Evans and Murshudov, 2013	http://www.ccp4.ac.uk
Phenix	Adams et al., 2004	http://www.hkl-xray.com/
Coot	Emsley and Cowtan, 2004	https://www2.mrc-lmb.cam.ac.uk/personal/pemsley/coot/
Pymol	Schrödinger	https://pymol.org/2/
PDBePISA	Krissinel and Henrick, 2007	http://www.ebi.ac.uk/pdbe/pisa/
Scrubber 2.0	BioLogic Software	http://www.biologic.com.au
SednTerp	Dr. Thomas Laue	http://bitcwiki.sr.unh.edu/index.php/Main_Page
HeteroAnalysis	Cole et al., 2008	https://core.uconn.edu/auf
FindEm	Roseman, 2004	http://emg.nysbc.org/redmine/projects/appion/wiki/Appion_Home
Appion	Lander et al., 2009	http://emg.nysbc.org/redmine/projects/appion/wiki/Appion_Home
RELION	Kimanius et al., 2016	https://www2.mrc-lmb.cam.ac.uk/relion/index.php?title=Main_Page
cryoSPARC	Punjani et al., 2017	https://cryosparc.com
Patchmaster 2.35	HEKA	http://www.heka.com/downloads/downloads_main.html
Micro-Manager 1.4 software.	Edelstein et al., 2010	https://micro-manager.org/wiki/
Igor pro 6	WaveMetrics	https://www.wavemetrics.com/
Imaris 9.1	Oxford Instruments	http://www.bitplane.com/imaris
ImageJ	NIH	https://imagej.nih.gov/ij/

CONTACT FOR REAGENT AND RESOURCE SHARING

Further information and requests for resources and reagents should be directed to and will be fulfilled by the Lead Contact, Lawrence Shapiro (lss8@columbia.edu).

EXPERIMENTAL MODEL AND SUBJECT DETAILS

Cell lines

The FreeStyle 293F cell line was obtained from Thermo Fisher. The HEK293S GnTI- cells were obtained from ATCC. Human Embryonic Kidney (HEK) 293 cell line, of which the sex is female, is the parental cell for Freestyle 293F and HEK293S GnTI- cell lines. HEK293S GnTI- cells are transformed with adenovirus 5 DNA and lack N-acetyl-glucosaminyltransferase I (GnTI) activity, thus rendering them unable to produce complex-type N-glycans. HEK293S GnTI- cells were adapted to suspension culture in Freestyle 293 Expression Medium with 2% FBS at 37°C. Freestyle 293F was obtained from Thermo Fisher and adapted to suspension culture in Freestyle 293 Expression Medium at 37°C.

METHOD DETAILS

Plasmids, protein expression and purification

Our expression vector, pα-H, was a gift from the Laboratory of Daniel Leahy, The University of Texas at Austin. All PCDH15 fragments were cloned into the pα-H vector. All fragments that started with EC1 use the native signal sequence, while all other fragments use the signal sequence from human BiP. All PCDH15 fragments and point mutants were expressed by transient transfection of FreeStyle 293F cells or GnTI- and initially purified using nickel-affinity with IMAC Sepharose 6 FF Resin (GE Healthcare). All Freestyle 293F cell produced fragements were then purified by size exclusion chromatography (Superdex S200 Increase 10/300 GL; GE Healthcare) with buffer containing 150 mM NaCl, 10 mM Tris (pH 8.0), and 3 mM $CaCl_2$. GnTI- produced PCDH15 EC1-EC3 was digested with Endogylcosidase H for 24 hours and then purified by size exclusion chromatography (Superdex S200 Increase 10/300 GL; GE Healthcare).

Crystallization and structure determination of the PCDH15 EC1-3

The PCDH15 EC1-EC3 fragment was prepared as described above. Fractions of GNTI- produced, Endoglycosidase H treated PCDH15 EC1-EC3 were concentrated to ~10 mg/ml and used for crystallization experiments. Initial crystallization screening was performed with 96 conditions using a Mosquito Crystallization Robot by the vapor diffusion method in sitting drops containing 0.1μl of protein and 0.1μl of reservoir solution at 20°C. Screens were imaged in Formualtrix R1-1000 Imaging Robots. Crystals were picked from a sitting drop from the 96-well plate screen in a condition of 35% ethylene glycol. Crystals were flash frozen in liquid nitrogen with no additional cryoprotectant.

Diffraction data for were collected with 0.979 Å X-ray at NE-CAT beamline 24-ID-C (Advanced Photon Source, Argonne National Laboratory) and processed with the XDS and AIMLESS (Evans and Murshudov, 2013; Kabsch, 2010). A dataset collected at 1.907 Å was used to calculate a Bijvoet difference Fourier maps to visualize calcium ions. Structures were solved by molecular replacement using PHASER, and iterative model building and refinement were carried out in COOT and PHENIX, respectively (Adams et al., 2004; Emsley and Cowtan, 2004). A cross validation (Rfree) test set consisting of 5% of the data was used throughout the refinement processes.

Surface plasmon resonance (SPR)

SPR binding assays were performed using a Biacore T100 biosensor equipped with a Series S CM4 sensor chip. PCDH15 EC1-EC3, PCDH15 EC1-EC3 D255K, and PCDH15 EC1-EC3 K345D were immobilized over independent flow cells using amine-coupling chemistry in HBS pH 7.4 (10 mM HEPES, 150 mM NaCl,) buffer supplemented with 3mM $CaCl_2$, at 25°C using a flow rate of 20 μL/min. Prior to immobilization the three PCDH15 EC1-EC3 variants, which were originally stored in a TRIS buffer, were desalted into HBS pH 7.4/3mM $CaCl_2$ using Zeba spin desalting columns (Thermo Scientific). Dextran surfaces were activated for 7 minutes using equal volumes of 0.1 M NHS (N-Hydroxysuccinimide) and 0.4 M EDC (1-Ethyl-3-(3-dimethylaminopropyl) carbodiimide). Each PCDH15 EC1-EC3 protein was immobilized at 37.5 μg/mL in 10 mM sodium acetate, pH 4.0, until the desired immobilization level was achieved. The immobilized surface was blocked using a 4-minute injection of 1.0 M ethanolamine, pH 8.5. Typical immobilization levels ranged between 600-900 RU. An unmodified flow cell served as a reference surface to subtract bulk refractive index changes from the binding signal.

Binding analysis was performed at 25°C in a running buffer of 10 mM Tris-HCl, pH 8.0, 150 mM NaCl, 3mM $CaCl_2$, 0.5 mg/mL BSA and 0.005% (v/v) Tween-20. PCDH15 EC1-EC3 analytes were prepared in running buffer using a three-fold serial dilution ranging between 27 and 3 μM, with the exception of D255K, K345D and K345A mutants which were tested at 27- 0.0005 μM using a nine-fold serial dilution. All analyte concentrations were tested in duplicate. During a binding cycle, the association phase between each analyte and the immobilized Pcdh molecule was monitored for 1 minute followed by a two-minute dissociation phase, each at 50 μL/min. At the end of the dissociation phase the signal returned back to baseline thus eliminating the need for a regeneration step. The last step was a buffer wash injection at 100 μL/min for 60 s. Every 3 analyte binding cycles, a buffer cycle was introduced to double-reference the binding signals by removing systematic noise and instrument drift. The data was processed using Scrubber 2.0 (BioLogic Software).

Sedimentation Equilibrium Analytical Ultracentrifugation

All AUC experiments were performed using a Beckman XL-A/I analytical ultracentrifuge (Beckman-Coulter, Palo Alto CA, USA), utilizing six-cell centerpieces with straight walls, 12 mm path length, and sapphire windows. All proteins were dialyzed over-night and then diluted in 10 mM Tris, 150 mM NaCl, 3 mM $CaCl_2$, pH 8.0. The samples were diluted to an absorbance at 10 mm and 280 nm of 0.65, 0.43 and 0.23 in channels A, B and C, respectively. Dilution buffer was used as blank. The samples were run at four speeds, the lowest speed held for 20 h then four scans with 1 h interval, the second lowest held for 10 h then four scans with 1h interval, the third lowest and the highest speed were recorded similar the second lowest. Various speeds were used, as detailed in the accompanying Table S2. Measurements were performed at 25°C, and detection was by UV absorbance at 280 nm. Solvent density and protein v-bar were determined using the program SednTerp (Alliance Protein Laboratories, Corte Cancion, Thousand Oaks, CA, USA). For calculation of dimeric K_D and apparent molecular weight, all useful data were used in a global fit, using the program HeteroAnalysis, obtained from University of Connecticut. (http://biotech.uconn.edu/auf).

Negative Stain Electron Microscopy

PCDH15 EC1-EC11 (10 μg/mL) and PCDH15 EC1-PICA (20 μg/ml) were applied to 400-mesh carbon-coated copper grids that had been plasma cleaned at 20 mA for 30 s using a Gatan Solarus Model 950. The sample was incubated on the grid for 30 s and stained with 2% uranyl formate for 30 s. Electron micrographs were collected on an FEI Tecnai T20 operating at 120 keV with a magnification of 49,000x, resulting in a pixel size of 3.44 A. The electron dose was 30 e-/A2 with an exposure time of 1000 ms. Images were acquired with a Tietz 4k x 4k TemCam-F416 CMOS detector and a defocus of −2.00 μm, using the Leginon software package (Suloway et al., 2005).

Approximately 2,000 particles were manually picked and used to generate 2D templates for use in the FindEM Template Picker, implemented in the Appion package (Lander et al., 2009; Roseman, 2004). The resulting 267,706 particles were subjected to 2D classification using RELION (Kimanius et al., 2016). After 2D classification, 37,133 particles were used for the *ab initio* reconstruction of eight classes using cryoSPARC (Punjani et al., 2017). One of these classes showed clearly defined EC domains and significant density for most of the protein's expected length, and was subjected to homologous refinement, where C2 symmetry was applied. Resolutions were determined using gold-standard FSC.

Cell surface biotinylation and immunoprecipitation experiments

PCDH15-CD2 cDNA (Webb et al., 2011; Xiong et al., 2012) was cloned into the pcDNA3.1 vector with a C-terminal HA tag to increase immunoprecipitation efficiency. LHFPL5 cDNA was cloned to pcDNA3.1 with an N-terminal Myc tag (Xiong et al., 2012). HEK293 cells on 10 cm culture plates coated with Poly-L-lysine were transfected with 8 μg PCDH15 plasmid and 2 μg LHFPL5 plasmid using Lipofectamine 3000. 16 hours later, culture plates were transferred onto ice, cells were washed twice with ice cold PBS, and incubated for 30 min on ice with 4 mL PBS containing EZ-LinkSulfo-NHS-SS-Biotin (1mg/ml). Cells were subsequently washed twice for 5 min with 0.1M Glycine in PBS and twice with PBS. Cells were harvested and lysed in RIPA buffer. Immunoprecipitations were carried out with EZview-Red Anti-HA Affinity beads. Following western blots were carried out with anti-HA antibody, anti-Myc antibody and Transferrin Receptor Antibody.

Injectoporation and Ca^{2+} imaging

Injectoporation experiments were carried out essentially as described (Xiong et al., 2012, 2014; Zhao et al., 2014). In brief, the organ of Corti was isolated from *PCDH15*-deficient *Ames-waltzer*^{av3J} mice (Alagramam et al., 2001) and cultured in DMEM/F12 with 1.5 μg/ml ampicillin. For electroporation, glass electrodes (2 μm diameter) were used to deliver plasmid (500 ng/μl in 1x HBSS) to the sensory epithelium. A series of 3 pulses was applied at 1 s intervals with a magnitude of 60V and duration of 15 msec (ECM 830 square wave electroporator; BTX). We used G-CaMP3 for Ca^{2+} imaging. Imaging was carried out on an upright Olympus BX51WI microscope mounted with a 60x water-immersion objective and Qimaging ROLERA-QX camera, controlled by Micro-Manager 1.3 software (Edelstein et al., 2010). Hair bundles were stimulated with a fluid jet that was applied through a glass electrode (2 μm tip-diameter), which was filled with bath solution. Stimuli were applied using Patchmaster 2.35 software (HEKA) and 20 psi air pressure (Picospritzer III microinjector). Images were collected with a 2 s sampling rate. A series of fluid-jet stimulations (0.1, 0.3, 0.5 s) was applied (60 s intervals).

Plasmids used for injectoporation were as follows: (i) CMV-GCaMP3 has been described previously (Xiong et al., 2012, 2014); (ii) CMV-PCDH15-CD2 (Webb et al., 2011; Xiong et al., 2012) was used to express wild-type PCDH15 in hair cells. All PCDH15 point mutations were generated using the QuikChange II XL site-directed mutagenesis Kit from Agilent.

Whole mount Immunostaining

Whole mount staining was carried out as described (Zhao et al., 2014). Stereocilia were visualized by phalloidin staining, and PCDH15 was evaluated with antibodies to PCDH15-CD2 (Webb et al., 2011). Additional reagents were Alexa Fluor 488- goat anti-rabbit, Alexa Fluor 555 phalloidin (Invitrogen, Carlsbad, CA). Immunostaining imaging were obtained with Deltavision Imaging System (GE Healthcare Life Sciences).

QUANTIFICATION AND STATISTICAL ANALYSIS

To quantify PCDH15 expression levels in the heterogenous cell membrane, western blots from three independent experiments ($n = 3$) were scanned with a densitometer using a G-box from Syngene, and analyzed with ImageJ. All values are mean ± SEM. One-way ANOVA was used to determine statistical significance ($^*p < 0.05$, $^{**}p < 0.01$, $^{***}p < 0.001$).

For quantitative assessment of PCDH15 expression levels in hair bundles, we used Imaris 9.1 (Oxford Instruments) to generate 3D reconstructions of hair bundles. We calculated the fluorescence volume of PCDH15 and phalloidin, and used the volume ratio to determine relative PCDH15 expression level between wild-type and mutant constructs in hair cells ($n = 11$-45). All data are mean ± SEM. Student's two-tailed unpaired t test was used to determine statistical significance ($^*p < 0.05$, $^{**}p < 0.01$, $^{***}p < 0.001$).

Ca^{2+} imaging was analyzed with Excel (Microsoft) and Igor Pro 6 (WaveMetrics, Lake Oswego, OR). Calcium signal ($\Delta F/F$) was calculated with the equation: $(F\text{-}F_0)/F_0$, where F_0 is the averaged fluorescence baseline at the beginning. Calcium signals induced by 0.3 s fluid-jet stimulation were used for quantitative comparison. All data are mean ± SEM. Student's two-tailed unpaired t test was used to determine statistical significance (*p < 0.05, **p < 0.01, ***p < 0.001). The number of cells analyzed is shown in each panel of Figure 7G (n ranges from 14 to 30).

DATA AND SOFTWARE AVAILABILITY

The accession number for the coordinates and structural factors for PCDH15 EC1-EC3 Dimer reported in this paper is PDB: 6CV7.

Neuron, Volume *99*

Supplemental Information

Mechanotransduction by PCDH15 Relies on a Novel *cis*-Dimeric Architecture

Gilman Dionne, Xufeng Qiu, Micah Rapp, Xiaoping Liang, Bo Zhao, Guihong Peng, Phinikoula S. Katsamba, Goran Ahlsen, Rotem Rubinstein, Clinton S. Potter, Bridget Carragher, Barry Honig, Ulrich Müller, and Lawrence Shapiro

Table S1

Pcdh15 EC1-3	
Wavelength (Å)	0.979 Å
Resolution range (Å)	99.11 - 1.692 (1.753 - 1.692)
Space group	P 65 2 2
Unit cell	114.444 114.444 172.011 90 90 120
Total reflections	1345148 (45588)
Unique reflections	73884 (6959)
Multiplicity	18.2 (6.6)
Completeness (%)	99.26 (92.50)
Mean I/sigma(I)	20.19 (0.69)
Wilson B-factor	29.23
R-merge	0.1154 (1.97)
R-meas	0.1186
CC1/2	0.992 (0.362)
CC*	0.998 (0.729)
Reflections used for R-free	
R-work	0.1630 (0.3748)
R-free	0.1946 (0.729)
Number of non-hydrogen atoms	3620
macromolecules	2988
ligands	126
water	506
Protein residues	366
RMS(bonds)	0.017
RMS(angles)	1.65
Ramachandran favored (%)	1.00E+02
Ramachandran allowed (%)	0
Ramachandran outliers (%)	0
Clashscore	4.82
Average B-factor	35.7
macromolecules	33.9
ligands	40.8
solvent	44.9

Table S1. Crystallography Statistics for Pcdh15 EC1-3, Related to Figure 3

Table S2

Speeds, rpm	Construct	K_D (µM)
15000, 19000, 23000, 27000	EC 1-2 WT	Monomer
	EC 2-3 WT	18.1 ± 0.4
	EC 3-4 WT	120.0 ± 7.2
	EC 4-5 WT	Monomer
	EC 5-6 WT	Monomer
	EC 6-7 WT	Monomer
	EC 7-8 WT	208 ± 10.7
	EC 9-10 WT	Monomer
	EC 5-7 WT	Monomer
	EC 6-8 WT	Monomer
	EC 7-9 WT	Monomer
	EC 8-10 WT	Monomer
	EC 9-11 WT	Monomer
	EC 1-3 K345A	Monomer
	EC 1-3 K345D	Monomer
	EC 1-3 D255K	Monomer
	EC 1-3 L138D	Monomer
	EC 1-3 L138A	Monomer
	EC 1-3 L138F	15.3 ± 3.1
11000, 14000, 17000, 20000	EC 1-4 WT	Dimer (MALS)
	EC 2-5 WT	Dimer (MALS)
	EC 3-6 WT	Dimer (MALS)
	EC 4-7 WT	Monomer
	EC 5-8 WT	Monomer
	EC 7-10 WT	Monomer
	EC 8-11 WT	Monomer
9000, 11000, 13000, 15000	EC 1-3 WT	1.2 ± 0.5
	EC 1-3 R198A	Monomer
	EC 1-3 V250D	Monomer
	EC 3-11 WT	220.0 ± 78
	EC 4-11 WT	Monomer
	EC 5-11 WT	Monomer
7000, 9000, 11000, 13000	EC 1-11 WT	0.2 ± 0.1
	EC 1-11 R198A	21.0 ± 3.4
	EC 1-11 V250D	Monomer
	EC 3-11 WT	220.0 ± 78

Table S2. Rotor Speeds and K_Ds for various Pcdh15 protein fragments in AUC experiments, Related to Figure 2

Figure S1

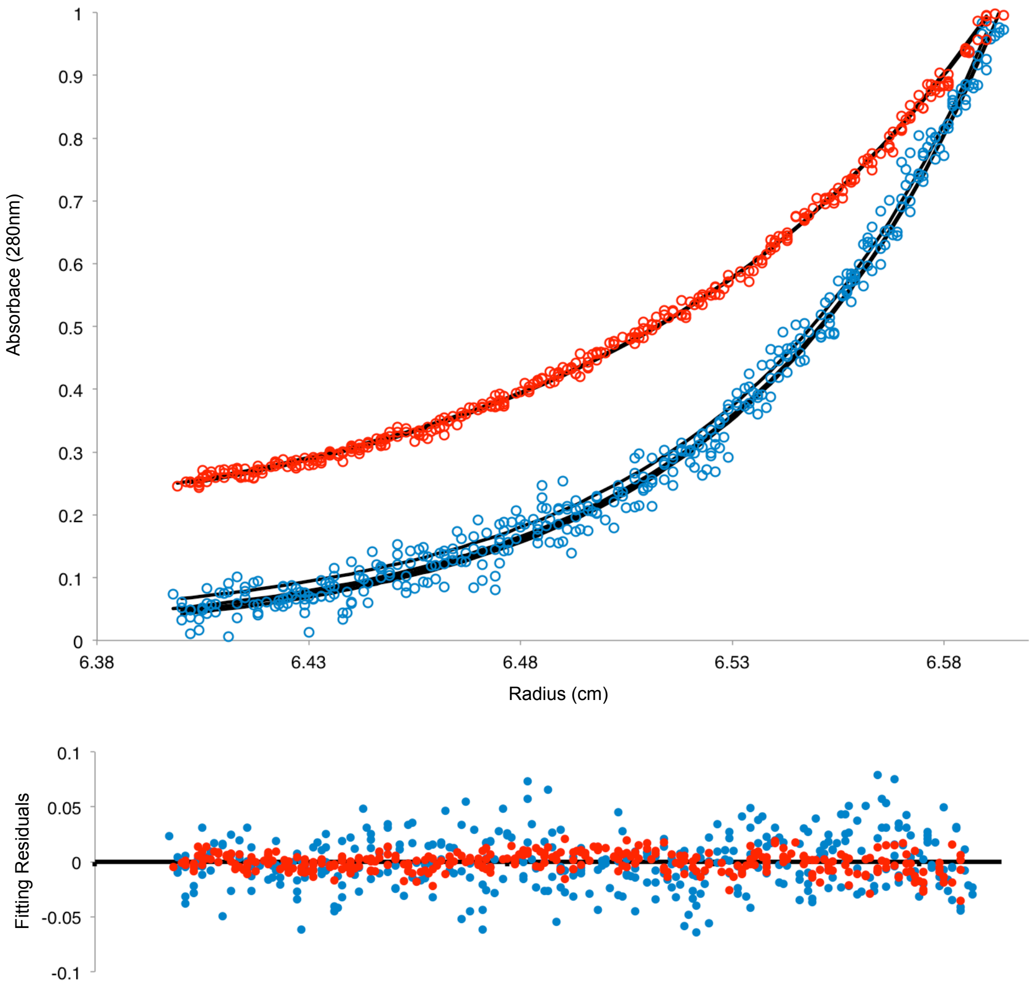

Figure S1. Sample Sedimentation Equilibrium traces for Wild-type and Mutant Pcdh15 EC1-3, Related to Figure 2
Purified wild-type Pcdh15 EC1-3, raw data plotted in blue, and Pcdh15 EC1-3 V250D, raw data plotted in red, were loaded at concentrations of 0.58 mg/ml and analyzed by sedimentation equilibrium analytical ultracentrifucation, with a rotor speed of 15000 rpm. Non-linear fits for a monomer-to-dimer model are plotted as black lines. Residuals to the non-linear fitting are plotted below the raw data.

Figure S2

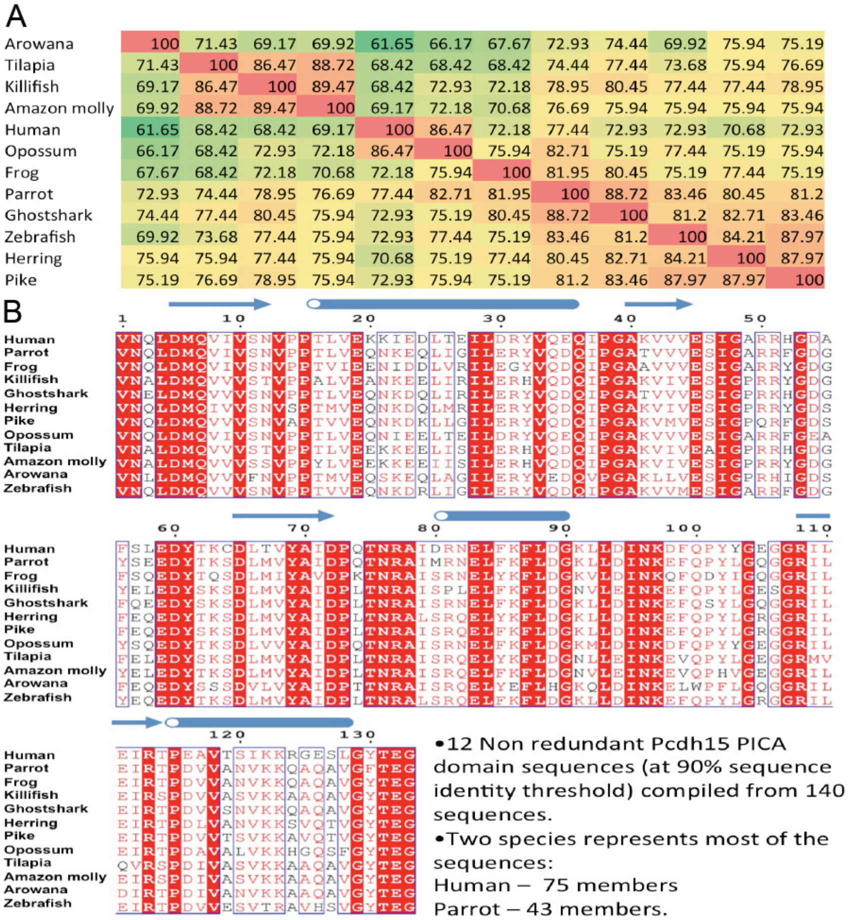

Arowana	100	71.43	69.17	69.92	61.65	66.17	67.67	72.93	74.44	69.92	75.94	75.19
Tilapia	71.43	100	86.47	88.72	68.42	68.42	68.42	74.44	77.44	73.68	75.94	76.69
Killifish	69.17	86.47	100	89.47	68.42	72.93	72.18	78.95	80.45	77.44	77.44	78.95
Amazon molly	69.92	88.72	89.47	100	69.17	72.18	70.68	76.69	75.94	75.94	75.94	75.94
Human	61.65	68.42	68.42	69.17	100	86.47	72.18	77.44	72.93	72.93	70.68	72.93
Opossum	66.17	68.42	72.93	72.18	86.47	100	75.94	82.71	75.19	77.44	75.19	75.94
Frog	67.67	68.42	72.18	70.68	72.18	75.94	100	81.95	80.45	75.19	77.44	75.19
Parrot	72.93	74.44	78.95	76.69	77.44	82.71	81.95	100	88.72	83.46	80.45	81.2
Ghostshark	74.44	77.44	80.45	75.94	72.93	75.19	80.45	88.72	100	81.2	82.71	83.46
Zebrafish	69.92	73.68	77.44	75.94	72.93	77.44	75.19	83.46	81.2	100	84.21	87.97
Herring	75.94	75.94	77.44	75.94	70.68	75.19	77.44	80.45	82.71	84.21	100	87.97
Pike	75.19	76.69	78.95	75.94	72.93	75.94	75.19	81.2	83.46	87.97	87.97	100

```
Human         VNQLDMQVIVSNVPPTLVEKKIEDLTEILDRYVQEQIPGAKVVVESIGARRHGDA
Parrot        VNQLDMQVIVSNVPPTLVEQNKEQLIGILERYVQDQIPGATVVVESIGARRFGDG
Frog          VNQLDMQVIVSNVPPTVIEENIDDLVRILEGYVQDQIPGAAVVVESIGARRYGDG
Killifish     VNALDMQVVVSTVPPALVEANKEELIRILERHVQDQIPGAKVIVESIGPRRYGDG
Ghostshark    VNELDMQVVVSNVPPTLVEQNKDQLIRILERYVQDQIPGATVVVESIGPRKHGDG
Herring       VNQLDMQIVVSNVSPTMVEQNKDQLMRILERYVQDQIPGAKVIVESIGPRRYGDS
Pike          VNQLDMQVVVSNVAPTVVEQNKDKLLGILERYVQDQIPGAKVMVESIGPQRFGDS
Opossum       VNQLDMQVIVSNVPPTLVEQNIEELTEILDRYVQEQIPGAKVVVESIGARRFGEA
Tilapia       VNALDMQVVVSTVPPTLVEEKKEELISILERHVQDQIPGAKVIVEAIGPRRHGDG
Amazon molly  VNALDMQVVVSSVPPYLVEEKKEEIISILERHVQDQIPGAKVIVESIGPRRYGDG
Arowana       VNLLDMQVVVFNVPPTMVEQSKEQLAGILERYVEDQVPGAKLLVESIGPRHIGDS
Zebrafish     VNQLDMQVVVSNVPPTVVEQNKDRLIGILERYVQDQIPGAKVVMESIGARRFGDG

Human         FSLEDYTKCDLTVYAIDPQTNRAIDRNELFKFLDGKLLDINKDFQPYYGEGGRIL
Parrot        YSEEDYTKSDLMVYAIDPQTNRAIMRNELFKFLDGKLLDINKEFQPYLGQGGRIL
Frog          FSQEDYTQSDLMIYAVDPKTNRAISRNELYKFLDGKVLDINKQFQDYIGQGGRIL
Killifish     YELEDYSKSDLMVYAIDPLTNRAISPLELFKFLDGNVLEINKEFQPYLGESGRIL
Ghostshark    FQEEDYSKSDLMVYAIDPLTNRAISRNELFKFLDGKLLDINKEFQSYLGQGGRIL
Herring       FEQEDYTKSDLMVYAIDPLTNRALSRQELYKFLDGKLLDINKEFQPYLGRGGRIL
Pike          FEQEDYSKSDLMVYAIDPLTNRAISRQELFKFLDGKLLDINKEFQPYLGRGGRIL
Opossum       YSQEDYTKSDLVVYAIDPQTNRAISRNELFKFLDGKMLDINKDFQPYYGEGGRIL
Tilapia       FELEDYSKSDLMVYAIDPLTNRAISRQELYKFLDGNLLEINKEVQPYLGEGGRMV
Amazon molly  YELEDYTKSDLMVYAIDPLTNRAISRQELFKFLDGNVLEINKEVQPHVGEGGRIL
Arowana       FEQEDYSSSDVLVYAIDPTTNRAISRQELYEFLHGKQLDINKELWPFLGQGGRIL
Zebrafish     YEQEDYTKSDLMVYAIDPLTNRALSRQELFKFLDGKLLDINKEFQPYLGRGGRIL

Human         EIRTPEAVTSIKKRGESLGYTEG
Parrot        EIRTPDVVANVKKQAQAVGFTEG
Frog          EIRTPDVVANVKKQAQAVGYTEG
Killifish     EIRSPDVVASVKKAAQAVGYTEG
Ghostshark    EIRTPDVVSNVKKQAQAVGYTEG
Herring       EIRTPDLVANVKKSVQTVGYTEG
Pike          EIRTPDVVTSVKKAVQTVGYTEG
Opossum       EIRTPDAVALVKKHGQSFGYTEG
Tilapia       QVRSPDIVASVKKAAQAVGYTEG
Amazon molly  EIRSPDIVASVKKAAQAVGYTEG
Arowana       DIRTPDIVANVKKAAQAVGYTEG
Zebrafish     EIRTPDVVESVTRAVHSVGYTEG
```

- 12 Non redundant Pcdh15 PICA domain sequences (at 90% sequence identity threshold) compiled from 140 sequences.
- Two species represents most of the sequences:

Human – 75 members
Parrot – 43 members.

Figure S2. Conservation of the Pcdh15 PICA domain, Related to Figure 2

(A) Interspecies conservation of the PICA domain among 12 group-representative species.

(B) Sequence alignment of the PICA domains from PCDH15 from the same species. About 40% of residues are completely conserved, with almost all others conserved by chemical type. Secondary structure elements, shown in blue above the sequence alignment, are conserved across species.

Figure S3

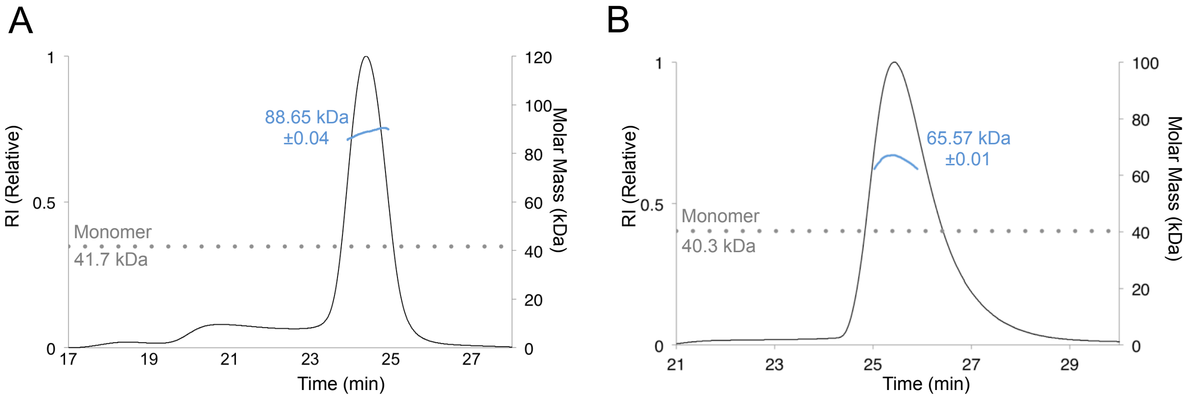

Figure S3. Evidence of Pcdh15 EC1-3 and Pcdh15 EC10-PICA Dimerization by SEC-MALS, Related to Figure 2

(A) Purified wild-type Pcdh15 EC1-3 was analyzed by size exclusion chromatography with in-line multi-angle light scattering (SEC-MALS). Refractive index changes (RI, relative) from the protein of interest is plotted in black. Molecular mass, calculated from light scattering analysis, is plotted in blue and labeled with the fitted value. The theoretical molecular mass (by sequence) is plotted as a horizontal dotted-line in grey and accompanied by a label.

(B) Purified wild-type Pcdh15 EC10-PICA analyzed by SEC-MALS.

Figure S4

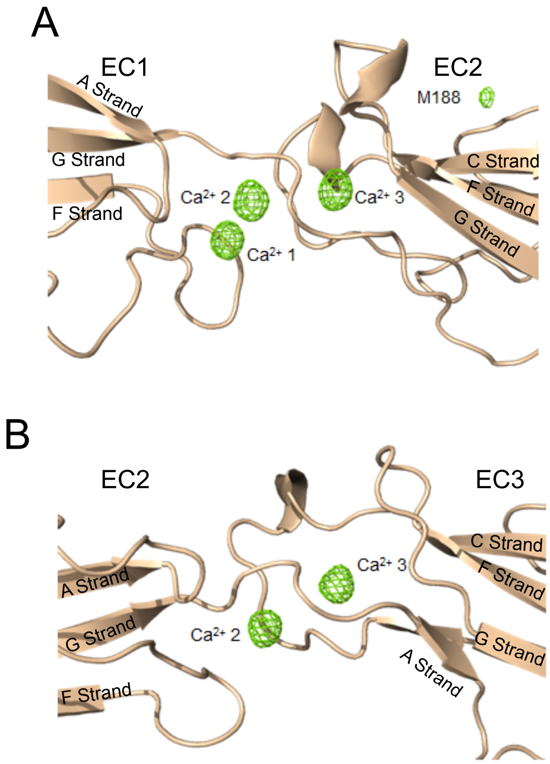

Figure S4. Non-canonical Ca^{2+} Interactions Observed Through Ca2+ Bijvoet Difference Analysis, Related to Figure 3

(A and B) Ca^{2+} anomalous difference electron density for the EC1-EC2 linker (A) and the EC2-EC3 linker (B). The EC2-EC3 linker region, which helps mediate the cis dimer, binds only two Ca^{2+} ions, rather than the canonical three.

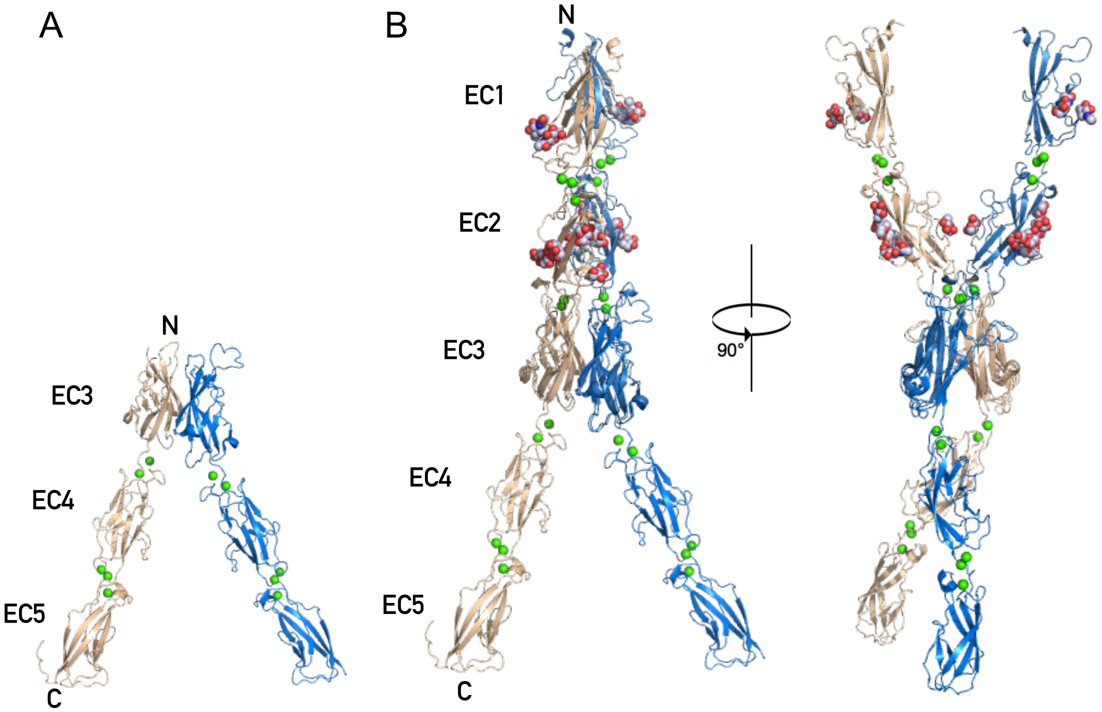

Figure S5. ***Cis*** **Assemblies of Pcdh15 in Pcdh15 Crystal Structures, Related to Figure 3**

(A) *Cis* dimer of Pcdh15 observed in Pcdh15 EC3-5, generated by application of crystallographic symmetry. (PDB ID: 5T4M)

(B) *Cis* dimer of Pcdh15 from Pcdh15 EC1-3 aligned to Pcdh15 EC3-5, RMSD= 1.73 Å.

Figure S6

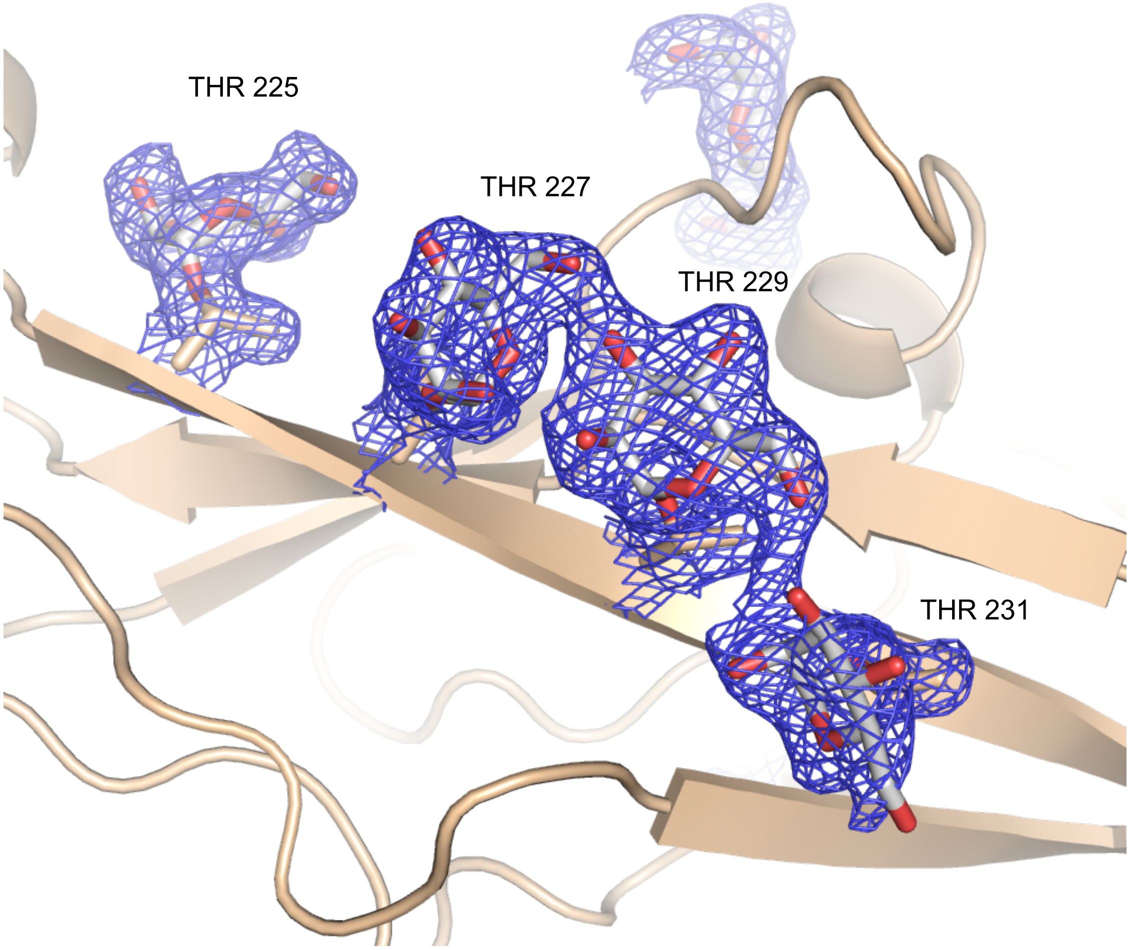

Figure S6. Electron Density for o-Mannose Moieties of Pcdh15 EC1-3, Related to Figure 3
Electron density from an F(o)-F(c) density map contoured at a σ level of 1 shown in blue mesh

Figure S7

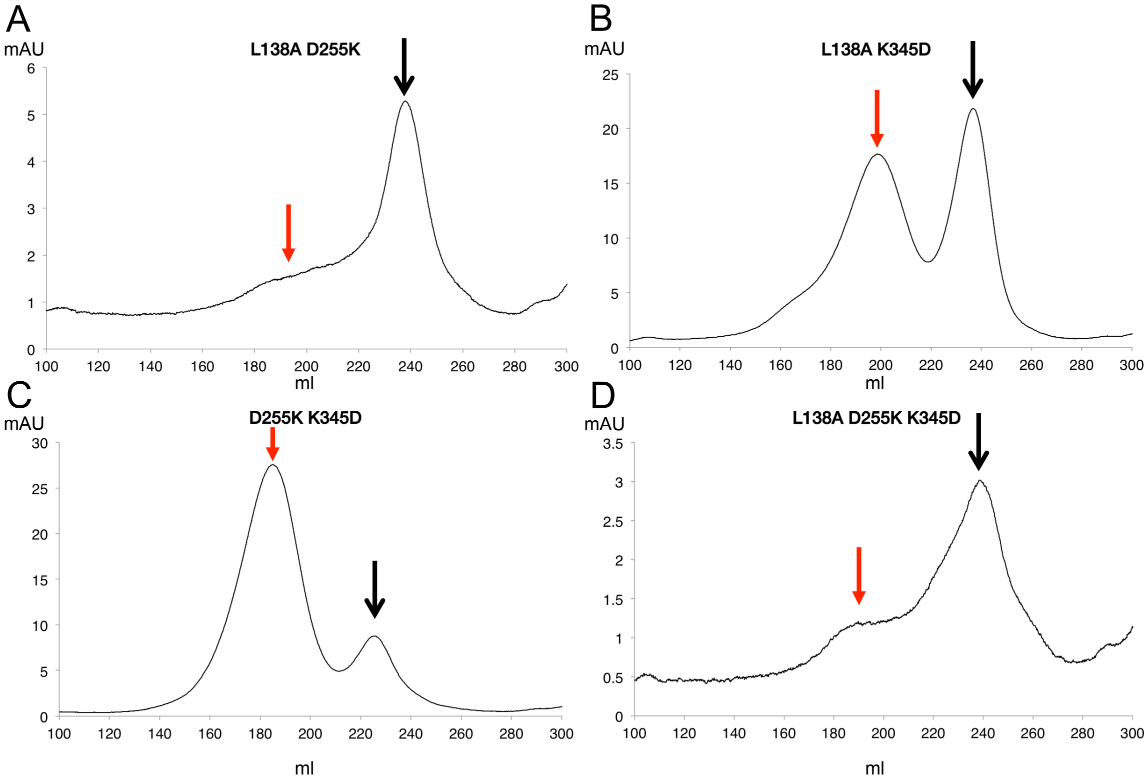

Figure S7. Size Exclusion Chromatography Traces of Pcdh15 EC1-3 Double and Triple Mutants, Related to Figure 5 (A-D) Chromatograms of Pcdh15 EC1-3 (A) L138A D255K, (B) L138A K345D, (C) D255K K345D, and (D) L138A D255K K345D . Red arrows demark dimer peaks or shoulders. Black arrows demark monomer peaks.

Figure S8

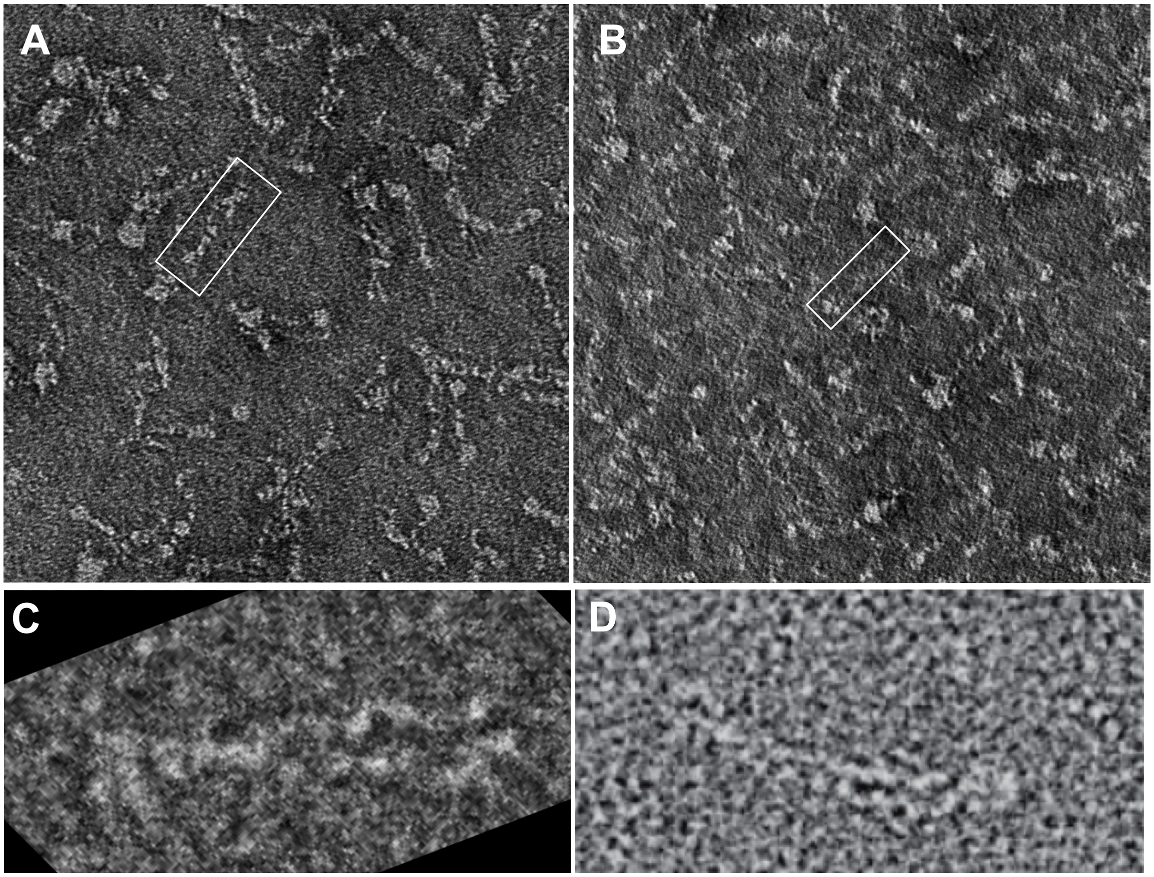

Figure S8. Negative Stain Transmission Electron Micrographs of Pcdh15 EC1-11, Related to Figure 6

(A) Electron Micrograph of Pcdh15 EC1-11 WT with a dimer singled out in the white box.
(B) Electron Micrograph Pcdh15 EC1-11 V250D with a monomer singled out in the white box.
(C and D) A comparison of negative stain transmission electron micrographs from (C) our sample and (D) the micrographs reported in Kazmeirczak et al. 2007. Image in (C) has been rotated and cropped to match the orientation in (D).

2.4 Conclusions

In this paper, we mapped the PCDH15 dimer interfaces to two separate locations at alternate ends of the extracellular region. The crystal structure of the membrane distal PCDH15 interface enabled for design mutants that allowed us confirm the molecular logic of dimerization as suggested by the placement of side chains. A noncanonical disulfide-stabilized loop in EC3 provides a hydrophobic surface on one protomer that interacts with a cognate hydrophobic patch on EC3 of its binding partner. This interaction between hydrophobic surfaces is mediated in part by electrostatics, as we were able to modify a salt bridge to prevent binding. We used this principle to further engineer PCDH15 mutants that were no longer homophilic, but could engage heterophilically with mutants of complementary salt bridge mutations.

The *cis* dimerization of PCDH15 – which utilizes a disulfide-stabilized loop that interacts with the β-sheet formed by F-, G-, and C-β-strands – represents a novel dimerization mechanism among the cadherin superfamily. Thus far, the molecular determinants for more than a half-dozen dimerization mechanisms have been described for the cadherin superfamily, with additional biochemical and biophysical evidence suggesting there are other mechanisms that still have yet to be elucidated (Brasch et al., 2012). The earliest structural mechanism for cadherin dimerization was unraveled by the determination of the crystal structure of the first EC domain of N-cadherin, a type-I classical cadherin (Shapiro et al., 1995). In the crystal structure, N-cadherin dimerizes through a 3D-domain swap mechanism, in which the five amino terminal residues in the first β-strand from one protomer swap places with the same residues from another. This interaction is mediated by the exchanging of conserved tryptophan residues at position two of the mature processed protein – classical cadherins are expressed with a pro-domain that is enzymatically cleaved in order for the protein to become functional. In the monomeric state, this tryptophan is docked into a hydrophobic pocket; in the dimeric state, two protomers will swap their A-β-strands and the tryptophan of one protomer will bury into the unoccupied hydrophobic pocket of its partner protomer.

This strand-swap mechanism is utilized in Type-II cadherins as well, albeit with a few key differences (Patel et al., 2006). Type-II cadherins exchange two conserved tryptophan residues, that are at amino acid positions two and four. Additionally, while type-I cadherins utilize only the exchanged tryptophans, type-II cadherins extend the dimer interface to include additional hydrophobic residues. These residues include Phe8, Ile10, and Tyr13 (Patel et al., 2006). Interestingly, VE-cadherin is distinct among classical cadherins and utilizes a mechanism that has aspects of both type-I and type-II cadherins (Brasch et al., 2011). It utilizes two tryptophan residues, similar to type-II cadherins, but does not have an additional hydrophobic interface, similar to type-I cadherins.

The desmosomal cadherins, desmocollins and desmogleins, utilize a dimerization mechanism that is highly similar to type-I cadherins; utilizing a conserved tryptophan residue at position two in a strand-swap mechanism (Harrison et al., 2016). In addition to utilizing a strand-swap mechanism, the desmosomal cadherins utilize electrostatics to drive heterophilic interactions between the two groups while minimizing homophilic interactions. Desmocollins have acidic residues present at position 99, which interacts favorably with basic residues at position 17 and 18 in desmogleins (Harrison et al., 2016).

In addition to the strand-swap mechanism, classical cadherins have been shown to form a kinetic intermediate known as the X-dimer (Harrison et al., 2010; Kudo et al., 2016). After the publication of the original strand-swap structure, a few structures of E-cadherin were published that adopted a significantly different dimeric arrangement that notably did not exhibit any strand swapping (Nagar et al., 1996; Pertz et al., 1999; Tamura et al., 1998). Originally, these structures obfuscated the true nature of type-I cadherin interactions, causing some authors to conclude the strand-swap mechanism was an artifact while others postulated it was involved in the lateral assembly of cadherins (Pertz et al., 1999; Tamura et al., 1998). Eventually, these non-strand swapped structures became to be regarded as artifacts as the result of amino termini sequences (as a result of their recombinant production) after the structures of the full-length extracellular fragment of C-cadherin and EC1 domains of the type-II cadherins cadherin-8, cadherin-11, and MN-cadherin all had the strand-swapped dimer mechanism (Boggon et al., 2002; Patel et al., 2006). However, when the crystal structure of the divergent T cadherin was published, which lacks the conserved tryptophan residues of either type-I or type-II cadherins, it was found that it uses a dimerization mechanism nearly identical to the non-strand-swapped dimers of E-cadherin, suggesting that these non-strand-swapped may have some physiological relevance. (Ciatto et al., 2010). Further structural studies of strand swap-incompetent mutants of both type-I and type-II cadherins demonstrated that when the strand-swap mechanism is hindered these molecules still adopted this X-dimer structure. Surface plasmon resonance experiments, which showed robust real-time binding responses with wild type E-cadherin and Cadherin-6, lost all binding response when examining mutants that were designed to disrupt x-dimer formation; these same X-dimer mutants still showed the ability to form dimers wild type in analytical ultracentrifugation sedimentation equilibrium experiments with comparable dissociation constants (Harrison et al., 2010). When these mutants were examined again with analytical ultracentrifugation sedimentation velocity experiments, it was shown that the X-dimer mutations were in a slower kinetic exchange between monomeric and dimeric forms, leading to the conclusion that the x-dimer is a kinetic intermediate that facilitates the formation of the strand-swap dimer (Harrison et al., 2010; Kudo et al., 2016).

While the X-dimer and strand swapped dimer represent *trans* interactions between two opposing membrane surfaces, type-I cadherins have an additional interface that forms between molecules in *cis, i.e.* on the same membrane surface. This interfaces was first observed in the structure of C-cadherin (Boggon et al., 2002). This interface forms between EC1 of one cadherin protomer, using opposite face of the domain with regard to the strand-swap pocket which engages primarily with EC2 of another protomer as well as some small contribution from three residues of EC3. This interaction is incredibly weak and not detectable in solution (Harrison et al., 2011). Mutagenesis experiments, however, have successfully demonstrated this *cis*-interface is critical for the proper formation of ordered adherens junctions (Harrison et al., 2011).

The members of the clustered protocadherin subfamily of cadherins have recently been shown to dimerize in *trans* through a large interface that spans multiple domains (Goodman et al., 2016a; Goodman et al., 2016b). Clustered protocadherins, whose ectodomains are comprised of six EC domains, use the four amino terminal EC domains to form a symmetric, antiparallel interface (Goodman et al., 2016a; Goodman et al., 2016b). In this antiparallel configuration, EC1 and EC2 of one protomer interact with EC4 and EC3 of its partner protomer, respectively, and vice versa. In contrast to the strand-swap dimers of classical cadherins, which has an interfacial surface area of about ~700 $Å^2$ in size and utilizes a little over a dozen residues, the *trans* interfaces of the clustered protocadherins are much larger with interfaces that have surface areas between ~3,900-5,200 $Å^2$ and utilize over 65 residues (Goodman et al., 2016a; Goodman et al., 2016b). The large sizes of their interfaces have allowed clustered protocadherins to achieve their remarkable homophilic specificity despite having high sequence similarity. This antiparallel interface formed between the first four EC domains is also shared with the related δ1- and δ2-families of non-clustered protocadherins (Cooper et al., 2016; Harrison et al., 2020; Modak and Sotomayor, 2019).

While the four amino terminal EC domains of cluster protocadherins mediate *trans* interaction, the two membrane proximal EC domains mediate a *cis* interaction that is promiscuous (Goodman et al., 2017). This interaction is described as promiscuous in the sense that the EC5-EC6 fragment of one particular clustered protocadherin isoform can potentially interact with the EC5-EC6 of any other clustered protocadherin isoform, although this is not strictly true for all isoforms. Surprisingly, the interface that mediates the *cis* interaction is asymmetric (Goodman et al., 2017). The two protomers in a clustered protocadherin *cis* dimer are related by an Euler rotation axis of 159.5° and a translation down the Euler axis of 13.96 Å. This results in protocadherin protomers adopting one of two possible interfaces; one protomer uses both EC5 and EC6 to contribute to *cis* binding, and one protomer utilizes EC6 exclusively (Goodman et al., 2017). This asymmetry in the *cis* interface explains the observation that certain clustered protocadherin subfamilies are unable to traffic to the cell surface, which seems dependent on their ability to *cis*-dimerize; sequence variation in the α- subfamily compared to the β- and the γ- subfamilies results in the α- subfamily being able to participate in forming the EC5-EC6 side of the asymmetric interface only (Goodman et al., 2017). As with E-, N-, and C-cadherin, the clustered protocadherin utilize their ability to form both *cis* and *trans* interfaces to facilitate the formation of larger zipper-like clusters; when two cell surfaces come into contact that have a mismatch set of cluster protocadherin isoforms, the inability to form trans interaction due to mismatching stunts the growth of this zipper cluster – which presumably prevents the identification of this contact as a self-interaction (Brasch et al., 2019; Rubinstein et al., 2017).

All of these aforementioned dimerization mechanisms represent our current knowledge of molecular interfaces in the cadherin superfamily of proteins that have corroborating structures. However, we have biophysical evidence that other interfaces exist that have yet to have corresponding structure determined. Drosophila N-cadherin and E-cadherin – DN- and DE-cadherin – do not utilize any of the interfacing mechanisms previously detailed (Jin et al., 2012). They lack the amino terminal tryptophan(s) found in vertebrate classical cadherins, and do not dimerize using the four amino terminal EC domains. Instead, AUC data of various size fragments of DN-cadherin suggest that in uses a mechanism involving EC9, as fragments lacking EC9 are monomeric; sequence analysis suggests that EC4 of DE-cadherin would play an analogous adhesive role (Jin et al., 2012). Thus, while there is yet to be determined a structure of the dimerization mechanism of DN- or DE-cadherin, the biophysical data necessitates a structural mechanism that is novel among the cadherin superfamily.

The tip link cadherins PCDH15 and CDH23 themselves have a number of interaction mechanisms that are unique among the cadherin superfamily. As discussed in the introduction of this chapter, first of these interactions to be resolved structurally was the ‘hand-shake’ mechanism of the *trans* heteromeric dimer between CDH23 EC1-EC2 and PCDH15 EC1-EC2. The paper presented in this chapter resolved the *cis* homodimeric interface observed in PCDH15 EC3. Additionally discussed in the paper presented in this chapter was the distinct *cis* homodimeric interface mediated by the membrane-proximal PICA domain of PCDH15, as evidenced by biophysical experiments. Since the publication of our paper, this finding has been corroborated in subsequent publications from other groups with crystal and cryo-EM structures of the dimer interface between EC11 and the PICA domain (De-la-Torre et al., 2018; Ge et al., 2018). The PICA domain adopts a ferrodoxin-like fold and interfaces with EC11 domains from both the same polypeptide chain as well as from the *cis*-dimer partner protomer. The interaction between EC11 and the PICA domain on the same chain is mediated by hydrophobic interactions between Ile1155, Leu1244, and Val1248 in EC11 and Lys1288, Try1316, and Ile1318 on the PICA domain which dock into an indentation on EC11 from sequential glycine residues at positions 1156 and 1157. Dimerization between PICA domains is mediated by a salt bridge between Lys1210 on EC11 and Glu1266 in the PICA domain as well the interaction of hydrophobic residues Met1164 and Phe1165 from EC11 with a hydrophobic patch formed by residues Pro1262, Thr1263, Glu1266, Ile1294, Gly1295, Ala1296, and Tyr1308 on the PICA domain. As with other cadherins that use *cis* interactions to form clusters, it may be possible that the PICA domain interfaces helps facilitate the dense packing of PCDH15 observed in kinociliary links.

In addition to these PCDH15 structures, ten structures of either two or three EC domain fragments of CDH23 were published. These structures together provide structural information that cover 18 of the 27 EC domains (Jaiganesh et al., 2018). Despite this extensive coverage of the CDH23 extracellular region, none of the ten structures were dimeric or had potential dimer interfaces masquerading as crystal contacts. These structures do provide context for 76 of the 116 CDH23 point-mutants that are associated with deafness. Most of these mutations map to either calcium binding residues or to the hydrophobic core of an EC domain. Other mutations that map to the protein surface have no immediate mechanism but may have a potential role in mediating CDH23 dimerization. While structural analysis of CDH23 fragments of two to three contiguous EC domains have failed to provide much insight into the mechanism of CDH23 ectodomain dimerization, I have generated biophysical data that suggest CDH23 *cis*-homodimerization require larger sized fragments. I produced CDH23 amino-terminal fragments that contained between three and ten EC domains. By analyzing these fragments with size-exclusion chromatography with in-line multi-angle light scattering measurements, I have determined that the amino terminus of CDH23 requires a minimum eight EC domains in order to dimerize. All fragments smaller than eight domains were monomeric in solution, while all those with more than eight domains were dimeric. These data suggest that CDH23 *cis* dimerization may utilize a novel structural mechanism among cadherin superfamily molecules.

While it's difficult in infer a mechanism for the decrease in GCaMP3 signals in our hair cell assays of mutant PCDH15, it is likely originate from a decrease in avidity of the PCDH15:CDH23 interaction. PCDH15 dimerization is not a requisite for CDH23 interaction, as evident by the crystal structure of monomeric versions of PCDH15:CDH23 (Sotomayor et al., 2012). However, by disrupting PCDH15 dimerization at EC3, it cannot be assumed that two PCDH15 *trans*-interfaces are in close proximity for the two CDH23 *trans*-interfaces to interact with.

Our negative-stain EM 3D reconstruction of the PCDH15 ectodomain was helical in nature, with each protomer completing half of a helical turn in a span of ~485 Å. We calculated that unwinding of this helix could contribute ~35 Å of length. Assuming CDH23 has a similar helicity, we can extrapolate the extensibility of the entire tip link to be ~120 Å. As discussed in the paper, experimental deflections may extend the tip link by ~150 nm but extensions *in vivo* are likely to be smaller in magnitude. Thus, while the tip link may undergo extensions via helix unwinding *in vivo* for mild stimuli, extreme extensions may involve other mechanisms, such as the unfolding of cadherin domains.

The cryo-EM structure of a complex between PCDH15 EC11-TM and the associated integral membrane protein TMHS was published in late 2018 (Ge et al., 2018). However, due to the limited resolution of this structure, the authors did not discuss any side-chain mediated interactions. Inspection of their structure indicates that the PCDH15:TMHS interaction is mediated almost entirely through the transmembrane helix of PCDH15 and the first and last transmembrane helices of TMHS. While the extracellular β-sheet of TMHS is positioned within a few angstroms of PCDH15, only one hydrogen bond and one potential salt bridge appear to form. The deafness-causing hurry-scurry mutation, Cys161Phe, which weakens the interaction between TMHS and PCDH15 in co-immunoprecipitation experiments, does not make contact with PCDH15 in this structure (Xiong et al., 2012). While the structure of the TMHS:PCDH15 complex presents the first picture of interactions between MET associated membrane proteins, our understanding of mechanisms related to MET were not significantly advanced.

The unusual inter-domain angle observed in the PCDH15 EC8-EC10 was not observed in our 2D class averages or the 3D reconstruction derived from the negative stain electron micrographs of PCDH15 EC1-EC11 or EC1-PICA. Interestingly, the cryo-EM structure of dimeric PCDH15 EC8-PICA in complex with TMHS adopts both the bent conformation seen in the PCDH15 EC8-EC10 and the more linear conformation observed in our negative stain 2D class averages (Ge et al., 2018). However, in the cryo-EM 2D class averages reported in Ge et al. (2018) that do adopt the bent EC9-EC10 conformation, the amino termini of both protomers point in different directions. It seems unlikely the EC9-EC10 linker can adopt this dramatically kinked conformation in the context of the full length, dimeric PCDH15.

2.5 Future Directions

While the work presented in this chapter delineated the dimerization mechanisms of PCDH15, PCDH15 only constitutes about a third of the length of the tip link. Questions about how CDH23 dimerizes currently remains unanswered. Additionally, it remains to be seen what the repercussions of disrupting CDH23 dimerization are. The structural data published by Jaiganesh et al. (2018) and our biophysical data suggest that CDH23 dimerizes through a different mechanism than PCDH15, as evidenced by the lack of any interfaces let alone ones with relatively high affinity. It seems likely that CDH23 may spread its dimer interface over a large portion of its 27 EC domains, with multiple low affinity interfaces. Indeed, a dimeric structure of CDH23 may require the crystallization of large fragments with eight or more EC domains. In addition to structural and biochemical characterization of the extracellular regions of the tip link cadherins, structural information about their various cytoplasmic domains could provide further insight into their function.

– Chapter 3–

Elasticity of individual protocadherin 15 molecules implicates tip links as the gating springs for hearing

3.1 Introduction

In this chapter of my thesis I present a paper published in *PNAS*, of which I was a contributing author. In this publication, we report the results from single molecule photonic force microscopy experiments of the extracellular region of PCDH15 that were performed by members of the Hudspeth group at The Rockefeller University using tagged recombinant constructs which I designed and produced. Prior to this publication, there was ongoing debate about the molecular identity of the gating spring. Some have regarded the tip link proteins as the primary candidates for the gating spring. Others have expressed doubts about this hypothesis, primarily arguing that the tip link cadherins were too stiff to play this role. To address this outstanding issue, the Hudspeth group utilized a custom built photonic force microscope to measure the elastic properties of a monomeric version of the PCDH15 extracellular region. In addition to measuring the elastic properties of this PCDH15 protein fragment, the paper characterizes the unfolding rates of cadherin domains under various tensions, potentially providing a mechanism to explain the variability observed in the lengths of the tip link (Furness et al., 2008).

3.2 An Overview of Previous Stiffness Measurements of Tip Link Proteins

The first estimations for the stiffness of the gating spring emerged from measurements of whole hair bundle stiffness. The total stiffness of a hair bundle is the combination of the stiffness associated with stereocilia pivoting and the stiffness associated with the gating springs (Howard and Hudspeth, 1988). The stereocilia pivoting stiffness is a function of the number of stereocilia, their heights, and the rotational stiffness around the pivot (Howard and Ashmore, 1986). The stiffness component associated with the gating springs is a function of the number of intact tip links, which are thought to be in series with the gating springs, a geometrical gain factor denoted as γ, and the stiffness of individual gating springs (Howard and Hudspeth, 1988). Measurements of hair bundle stiffness in bullfrog saccular hair cells estimated the stiffness of individual gating springs to be on the order of 0.5 mN/m (Howard and Hudspeth, 1988). Recently, studies in rat cochlear hair cells indicate that the stiffness of individual gating springs vary over the tonotopic gradient, with individual gating springs having a stiffness in OHCs that range from 1.3-3.7 mN/m, corresponding to cells with characteristic frequencies of 1-4 kHz; individual gating springs had a stiffness in IHCs that range from 0.5-1.7 mN/m, corresponding to cells with characteristic frequencies from 1 to 15 kHz (Tobin et al., 2019).

While the tip links are associated with the gating springs, it is debated whether they are the molecules that give rise to the gating spring phenomenon or whether they are simply elements that are in series with them. Some of the earliest doubts about the tip links being the gating spring arises from interpretation of freeze etch electron micrographs of the tip link. It was argued that the double helical nature observed in the EM images implied the molecular components of the tip link to be rigid and thus too stiff to be the gating spring (Kachar et al., 2000). However, a 1314 nm strand of B-form DNA, a famously double helical molecule, exhibits a Hookean spring constant of 0.9 mN/m when under tension (Wang et al., 1997).

The first attempts to quantify the stiffness of the tip link proteins PCDH15 and CDH23 were performed *in silico* by the application of steered molecular dynamics (SMD) simulations using the crystal structure of CDH23 EC1-EC2 (Sotomayor et al., 2010). By ‘pulling’ on atoms at the amino and carboxyl termini of the atomic model of CDH23 EC1-EC2 with virtual springs moving apart at a constant velocity *in silico*, force-extension measurements can be computed, from which the spring constants for the simulated molecule can be extracted. For a simulation of a single cadherin domain, CDH23 EC1, being pulled apart at 0.1 m/s, the reported stiffness was 710 mN/m while for two EC domains, CDH23 EC1-EC2, the stiffness was 570 mN/m, or 1,140 mN/m for each EC domain (Sotomayor et al., 2010). Sotomayor extrapolated these *in silico* stiffness measurements to the whole tip link by using a very simple model in which the tip link is comprised of two parallel springs that are themselves made of 38 identical springs that are in series and have the stiffness of an individual cadherin domain. Using this model, they estimated the total spring constant for the tip link to be between 37-60 mN/m, a value that is an order of magnitude too stiff to be consistent with the gating spring. Similar *in silico* measurements have been made for the crystal structure of PCDH15 EC3-EC5 and PCDH15 EC8-EC10. PCDH15 EC3-EC5, despite having a linker region lacking a site 1 Ca^{2+} ion, had a stiffness estimate of 659 mN/m, or 1977 mN/m for individual domains (Powers et al., 2017). This value was also used in the aforementioned model to extrapolate a stiffness measurement for the entire tip link that was even stiffer with a value of 104 mN/m.

As mentioned previously, the crystal structure of PCDH15 EC8-EC10 contains an ~90° bend between domains EC9 and EC10 (Araya-Secchi et al., 2016). In the SMD simulations, the unbending of this region was associated with a stiffness of 8 mN/m. Two of these hinge-like regions in parallel would have a stiffness of ~16 mN/m, a value that is closer to the predicted stiffness of the gating spring. However, as discussed at the end of chapter 2 this bend may not be physiological in the context of the assembled tip link. As such, this pliability of the EC9-EC10 junction measured *in silico* may not be relevant. Once the kink between EC9 and EC10 has been straightened, the *in silico* stiffness of PCDH15 EC8-EC10 increases to between 320-445 mN/m, which extrapolates to a value of 50-70 mN/m for the entire tip link, again using the simple model (Araya-Secchi et al., 2016). These *in silico* values suggest that PCDH15 and CDH23 are an order of magnitude too stiff. However, SMD may be prone to overestimating forces, as they have for titin (Lu et al., 1998; Oberhauser et al., 2001). While SMD might provide insight into the molecular mechanisms of unfolding, it may not be able to reproduce the results from physical measurements of single molecules *in vitro*.

To interrogate the stiffness of molecules, two primary methodologies exist: atomic force microscopy (AFM) and optical traps. In AFM, a microfabricated cantilever made from silicon is calibrated and attached to one end of a single molecule of interest; the other end of the molecule is affixed to a peizoelectric mobile stage. Manipulations of the stage position allow one to pull on the molecule, which in turn pulls on the cantilever. The tension experienced by the molecule is determined by measuring the deflection of the cantilever, while the extension of the molecule is determined by calculating the distance between the stage and the flexed cantilever. AFM has previously been successful in studying the unfolding of immunoglobulin domains of titin (Oberhauser et al., 2001). However, one of the most significant limitations of AFM stems from the intrinsic stiffness of the cantilevers, that are on the order of 10-10,000 mN/m, limiting the ability of this method to interrogate molecules that are less stiff (Neuman and Nagy, 2008). For titin, which is involved in the high forces experienced in muscle tissue, this isn't an issue. In the context of hearing and the gating spring, whose stiffness is expected to be on the order of ~1 mN/m, AFM would have a difficult time accurately exploring the relevant stiffness and force regimes.

As opposed to the mechanical nature of AFM, optical traps use highly focused laser light to trap a dielectric particle in a harmonic trap with a stiffness and force range that are relevant to hair bundle mechanics. The stiffness of an optical trap is in the range of 0.001-1 mN/m, and can be adjusted by modulating the laser power (Neuman and Nagy, 2008). By incorporating sensors that measure the three-dimensional positions of the trapped particle, one can construct a photonic force microscope (PFM) capable of measuring the forces that act on the trapped particle. A more thorough description of the custom built photonic force microscope used in these studies will be given in the next section.

My role in the study reprinted below was primarily in the design and production of the protein reagents. Our early work with full-length wild type PCDH15 ectodomains revealed a problem with aggregation. Negative stain electron micrographs showed that one of the termini served as a point of interaction for multiple copies of PCDH15, leading to the formation of molecular ‘starfish’. Such aggregation would make interpretation of data from single-molecules difficult, as analysis is highly dependent on only one molecular tether being present between the stage and the probe bead. Additionally, if the dimerization constant of either interface of PCDH15 is low enough, there exists the potential for dimeric PCDH15 extracellular regions to attach to either the pedestal or probe bead with a slight splay. A fully dimeric tether would be difficult to tease apart from one with a slight splay. It would then be hard to interpret whether we were looking at single conformation of PCDH15 molecules or a spectrum of PCDH15 molecules attached with different amounts of splaying. To overcome these obstacles, I engineered monomeric fragments of the PCDH15 ectodomain, using information from the structural and biophysical characterization of PCDH15 I carried out previously. The potent V250D mutation was used to disrupt the dimer interface at EC3, and the PICA domain was deleted. We added to this monomeric PCDH15 fragment an amino terminal Avitag and a carboxyl terminal SpyTag. The resulting construct was monomeric in solution and allowed for confident single molecule analysis by Dr. Tobias Bartsch at Rockefeller University.

3.3 Technical Interlude: The Photonic Force Microscope Constructed by Dr. Tobias Bartsch

Dr. Tobias Bartsch designed and assembled a custom built PFM that is capable of tracking the three dimensional position of a probe bead, manipulating the position of the probe bead, and maintaining the nano-scale experimental configuration for long timescale experiments. These combinations of technical features allowed for this custom PFM to reliably perform thousands of extension-relaxation cycles with multiple samples.

Using a quadrant photodiode (QPD) placed in the back focal plane, the lateral and axial positions of the trapped bead can be deduced. In brief, the trapped bead acts as a Rayleigh scatterer. The light scattered by the bead interferes with the unscattered laser light and the resulting interference pattern that hits the QPD in the back focal plane is dependent on the three dimensional position of the bead within the beam. Lateral positions are calculated from the differences in the signal between two halves of the QPD, e.g. top vs bottom halves. The information for axial position is related to the total intensity measured by the QPD (Pralle et al., 1999; Rohrbach and Stelzer, 2002).

The particular PFM used in these studies employed two optical traps that separately measure and manipulate the position of a 1-µm diameter polystyrene bead. The wavelengths of the lasers used in these optical traps were chosen to reduce potential photodamage of the biological reagents (Neuman et al., 1999). A 1,064 nm wavelength laser beam was used to establish a primary weak trap and to measure the 3D position of the bead. This primary trap was kept fairly weak to minimize its contribution to the net force on the trapped bead. This amounted to a maximal restoring force on the bead on the order of a single piconewton. A second 852 nm beam was added in order to apply an external pulling force for extension experiments. The manipulator beam was positioned a few hundred nanometers away from the bead and allowed for the application of ~60 pN of force on the bead, thus enabling the generation of the force-extension data necessary to measure the stiffness of PCDH15.

Multiple cycles of extensions and relaxations were carried out on each individual molecule in order to generate large data sets for statistical analysis. With each extension–relaxation cycle being on the order of a second in time, entire data sets needed to be collected over the timescales of several minutes. However, over these long timescales an appreciable mechanical drift between the sample chamber and optical trap occurred, on the order of 250 $\mathrm{pm \cdot s^{-1}}$, and therefore needed correction. Using a high-resolution camera, a separate pedestal bead located tens of microns away had its three-dimensional position tracked. The location data was fed into a proportional-integral-derivative (PID) controller that was connected to the nano-positioning stage to establish a feedback control system. This compensation mechanism eliminated any net drift and the root-mean-square variation of the stage movement was small, approximately 2 nm over a 5 minute time widow.

3.4 Elasticity of individual protocadherin 15 molecules implicates tip links as the gating springs for hearing

Presented here in its entirety is our paper as published in *PNAS*.

Elasticity of individual protocadherin 15 molecules implicates tip links as the gating springs for hearing

Tobias F. Bartsch[a,b,1], Felicitas E. Hengel[a,b,2], Aaron Oswald[a,b,2], Gilman Dionne[c], Iris V. Chipendo[a,b], Simranjit S. Mangat[a,b], Muhammad El Shatanofy[a,b], Lawrence Shapiro[c], Ulrich Müller[d], and A. J. Hudspeth[a,b,1]

[a]Howard Hughes Medical Institute, The Rockefeller University, New York, NY 10065; [b]Laboratory of Sensory Neuroscience, The Rockefeller University, New York, NY 10065; [c]Department of Biochemistry and Molecular Biophysics, Zuckerman Mind Brain Behavior Institute, Columbia University, New York, NY 10032; and [d]The Solomon Snyder Department of Neuroscience, Johns Hopkins University, Baltimore, MD 21205

Contributed by A. J. Hudspeth, March 29, 2019 (sent for review February 6, 2019; reviewed by Carlos Bustamante and Pascal Martin)

Hair cells, the sensory receptors of the inner ear, respond to mechanical forces originating from sounds and accelerations. An essential feature of each hair cell is an array of filamentous tip links, consisting of the proteins protocadherin 15 (PCDH15) and cadherin 23 (CDH23), whose tension is thought to directly gate the cell's transduction channels. These links are considered far too stiff to represent the gating springs that convert hair bundle displacement into forces capable of opening the channels, and no mechanism has been suggested through which tip-link stiffness could be varied to accommodate hair cells of distinct frequency sensitivity in different receptor organs and animals. Consequently, the gating spring's identity and mechanism of operation remain central questions in sensory neuroscience. Using a high-precision optical trap, we show that an individual monomer of PCDH15 acts as an entropic spring that is much softer than its enthalpic stiffness alone would suggest. This low stiffness implies that the protein is a significant part of the gating spring that controls a hair cell's transduction channels. The tip link's entropic nature then allows for stiffness control through modulation of its tension. We find that a PCDH15 molecule is unstable under tension and exhibits a rich variety of reversible unfolding events that are augmented when the Ca^{2+} concentration is reduced to physiological levels. Therefore, tip link tension and Ca^{2+} concentration are likely parameters through which nature tunes a gating spring's mechanical properties.

auditory system | entropic stiffness | hair cell | optical trap | vestibular system

Mechanically gated ion channels are ubiquitous. In addition to underlying our senses of hearing, balance, and touch, they are involved in the regulation of such processes as muscle extension, blood pressure, pulmonary inflation, and visceral distension. These channels are opened and closed through the action of gating springs, elastic elements that are tensioned by mechanical stimulation and in turn communicate stress to the molecular gates of the respective channels. Gating springs accordingly store mechanical energy and use it to regulate channels' open probabilities. For bacterial mechanoreceptors, which respond to osmotic stress, the cellular membrane itself serves as a gating spring (1). The ubiquitous Piezo channels of vertebrates extend three membrane-embedded arms that likely act as gating springs by flexing in response to membrane stretching (2, 3). Other mechanosensitive channels, such as NOMPC (TRPN1) in *Drosophila*, appear to be gated by the tension in elastic ankyrin domains (4).

Gating springs were first posited for hair cells of the vertebrate inner ear, the sensors of the auditory and vestibular systems (5–7). Each hair cell is surmounted by a hair bundle—a cluster of erect, actin-filled processes termed stereocilia—that is deflected by mechanical stimulation. However, the identity of the gating springs in these cells has remained controversial. A plausible candidate discovered soon after the gating-spring hypothesis was advanced is the tip link. Extending approximately 150 nm between the tip of each stereocilium and the side of its longest neighbor, the tip link is positioned to sense the shear between stereocilia when a hair bundle is deflected (Fig. 1 *A* and *B*) (8–10). The tip link is a dimer of parallel dimers, comprising two PCDH15 molecules joined at their amino termini to a pair of CDH23 molecules through a "handshake," whose stability depends on the presence of bound Ca^{2+} ions (Fig. 1*C*) (11).

The mechanical properties of hair bundles imply a gating-spring stiffness (12, 13) on the order of 1 mN·m^{-1} (1 pN/nm). However, electron microscopy images suggest that the tip link is relatively rigid (14), and crystallographic studies and molecular dynamics simulations of the relevant cadherins support a stiffness 50-fold greater than that measured (15). Therefore, it has been posited that most of a gating spring's elasticity resides at a tip link's two attachments, rather than within the link itself. However, it is possible that the tip link elongates in response to force by the straightening of its lateral thermal undulations, the working principle of an entropic spring (16). To clarify the identity of the hair cell's gating spring, we examined the elastic properties of a tip link protein.

Results

Mechanical Characteristics of PCDH15. The mechanical properties of a protein can be tested by tethering it between two surfaces, applying a force that pulls the surfaces apart, and measuring the protein tether's elongation (17). To directly explore the stiffness of a tip link, we used a high-precision optical trap to determine

Significance

Our hearing depends on mechanosensitive channels in hair cells of the inner ear. Experiments suggest that each channel is opened by a "gating spring," an elastic element that conveys displacement of a hair bundle to the channel. Appropriate stiffness of the gating spring permits the discrimination of different sound amplitudes; if the spring is too stiff, then a faint sound will elicit the same response as a loud sound, opening all of a cell's channels. Although the tip link—a fine molecular filament—might be the gating spring, its properties have remained controversial. Using high-precision optical tweezers, we demonstrate that the mechanical properties of a tip link protein correlate with those of a gating spring in vivo.

Author contributions: T.F.B. and A.J.H. designed research; T.F.B., F.E.H., A.O., I.V.C., S.S.M., M.E.S., and A.J.H. performed research; G.D., L.S., and U.M. contributed new reagents/analytic tools; T.F.B., F.E.H., and A.O. analyzed data; and T.F.B., F.E.H., A.O., and A.J.H. wrote the paper.

Reviewers: C.B., University of California, Berkeley; and P.M., Institut Curie.

[1]To whom correspondence may be addressed. Email: tbartsch@rockefeller.edu or hudspaj@rockefeller.edu.

[2]F.E.H. and A.O. contributed equally to this work.

This article contains supporting information online at www.pnas.org/lookup/suppl/doi:10.1073/pnas.1902163116/-/DCSupplemental.

the mechanical properties of individual molecules of PCDH15. The extracellular portion of PCDH15 consists of 11 extracellular cadherin domains (EC1–EC11), followed by the membrane-proximal PICA domain. PCDH15 forms a homodimer through interfaces in EC3 and in PICA (Fig. 1*C*) (18, 19), hindering study of the monomeric protein. Therefore, we introduced a dimerization-disrupting mutation, V250D (18), into EC3 and truncated the protein just before the PICA domain (Fig. 1*D*).

Using a short site-specific anchor at each of the protein's ends, we placed PCDH15 between an immobile 2-μm-diameter glass pedestal bead and a mobile 1-μm-diameter probe bead. Short, stiff anchors were necessary to avoid masking the elastic properties of PCDH15 by those of the anchors (Fig. 1*E*). The probe bead was confined in a weak optical trap whose forward-scattered light we collected to determine the 3D position of the bead with subnanometer spatial resolution and 1-μs temporal resolution (20, 21). A second optical trap, displaced by a few hundred nanometers from the first, served to deliver a force stimulus (Fig. 1*E*). By increasing the trap's stiffness, we could apply forces up to at least 60 pN to the tethered protein.

Cadherin domains manifest a stereotyped, Ig-like Greek key folding motif and are separated from one another by conserved linkers that each bind up to three Ca^{2+} ions in a canonical arrangement (Fig. 1*F*) (22). Ca^{2+} binding is thought to rigidify the linker regions and to stabilize the cadherin domains against force-induced unfolding (23). The Ca^{2+} concentration of the endolymph, the fluid surrounding tip links, varies between different organs and species from tens to hundreds of micromolar (24, 25). Such concentrations are close to the Ca^{2+} dissociation constants for the various binding sites (15, 26), raising the intriguing possibility that nature adjusts the Ca^{2+} concentration to tune the mechanics of tip link cadherins. Therefore, we explored the behavior of tensioned PCDH15 at three Ca^{2+} concentrations: 3 mM, to saturate all binding sites; 20 μM, a concentration that mimics the concentration of Ca^{2+} in the endolymph of the mammalian cochlea (24); and 0 M.

Because structural changes in proteins are stochastic events driven by thermal forces, the rate at which external force is applied can dramatically change the mechanical response. If a protein is pulled too fast, thermal forces do not have sufficient time to cause barrier crossing in the protein's energy landscape before very high external forces are reached. Consequently, the forces at which structural changes occur are artificially elevated

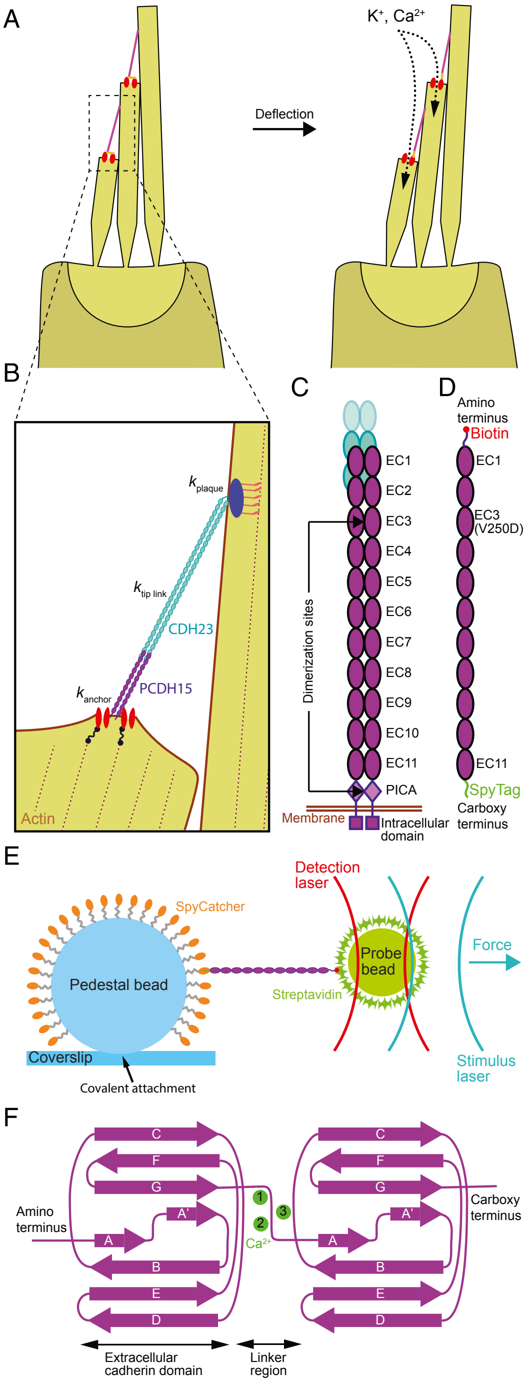

Fig. 1. The role of tip link proteins in transduction by hair cells. (*A*) The hair bundle is a cluster of stiff, actin-filled protrusions called stereocilia that stands atop each hair cell in the inner ear. Each stereocilium is connected to its tallest adjacent neighbor through a proteinaceous filament called a tip link (pink), which is coupled at its base to mechanically gated ion channels (red). Deflection of a hair bundle increases the tension in the tip links, biasing the channels toward an open state that allows the influx of positively charged ions. (*B*) The mechanical element that converts hair bundle displacement into a force capable of opening the channels is called the gating spring. Its stiffness comprises the stiffnesses of the channel and its lower anchor (k_{anchor}), the tip link proteins PCDH15 and CDH23 ($k_{tip\ link}$), and the insertional plaque that anchors the link's top end into the taller stereocilium (k_{plaque}). (*C*) The mechanical properties of the tip link emerge from its quaternary structure and from the characteristics of its constituent proteins. The lower third of the link consists of a dimer of PCDH15 molecules, each of which includes 11 extracellular cadherin (EC) domains. (*D*) To measure the mechanical behavior of monomeric PCDH15, we tagged each end with a distinct molecular handle. We eliminated dimerization by a point mutation (V250D) in domain EC3 and by truncation of the PICA domain. (*E*) We probed the mechanics of a PCDH15 monomer by confining it through molecular handles between an immobile 2-μm glass pedestal bead and a diffusive 1-μm plastic probe bead. To acquire each force-extension relationship, we measured the position of the probe bead with a detection laser while applying a force with a stimulus laser. (*F*) The folding motifs of individual EC domains influence the mechanical properties of the full-length protein. Up to three calcium ions (green) can bind between successive domains.

at high loading rates (27). Even in the absence of an acoustic stimulus, tip links experience a constant resting tension (28) that varies with the frequency sensitivity of a hair cell, from 5 pN at 1 kHz to 34 pN at 4 kHz, with possibly even greater tensions at higher frequencies (13). In each tip link, two copies of PCDH15 act in parallel, and each copy assumes one-half of the tension of the entire link, approximately 3 pN up to at least 17 pN. During stimulation from a moderately loud sound, with a 60-dB sound pressure level, a hair bundle is displaced (29) by <10 nm. Such a stimulus stretches the gating springs (12) by up to 1.4 nm, superimposing an oscillation of only a few piconewtons onto the resting tension. Therefore, in our experiments we had to apply slowly changing forces to explore the influence of resting tension on the mechanical properties of PCDH15.

Unless noted otherwise, we applied force ramps to the single molecule tethers at a loading rate of 130 $pN{\cdot}s^{-1}$ by linearly increasing the spring constant of the stimulus trap (*SI Appendix*, Fig. S1). The dynamic forces during normal hearing at a frequency of 1 kHz vary much faster, at roughly 5,000 $pN{\cdot}s^{-1}$. Our loading rate represented a compromise between slow force application and our desire to collect a statistically relevant number of extension-relaxation cycles for each molecule in a reasonable amount of time. For each cycle, we ramped the force up to 60 pN to cover the entire range of physiologically relevant tensions, then returned it at the same rate to a holding level of 2–4 pN. Depending on the Ca^{2+} concentration, we adjusted the holding level and duration to allow the protein to refold domains after many, but not all, cycles. The chosen loading rate likewise led to unfolding events in only a subset of cycles. With these parameter choices, we were able to trap the protein in a given conformational state for several extension-relaxation cycles, allowing us to precisely characterize the mechanics of each state.

Representative examples of individual force-extension relationships for Ca^{2+} concentrations of 3 mM, 20 μM, and 0 M feature hockey stick-like shapes, as expected for the extension of a biopolymer in a heat bath (Fig. 2 *A*–*C*) (30). As we quantify below, this functional shape indicates that entropic effects dominate PCDH15's elastic response. Abrupt, stepwise extensions, or "rips," in the force-extension relationship correspond to structural changes of the protein under force. In contrast to typical single-molecule experiments, under our loading conditions, PCDH15 never fully unfolded during the extension phase of the stimulus; therefore, we frequently observed extensional structural changes even during the relaxation phase of the stimulus (B_U; Fig. 2*B*). For each Ca^{2+} concentration, a set of conformational changes led to a modulated occupation of the force-extension state space, which we visualize by overlapping hundreds of extension-relaxation cycles for one representative molecule apiece (Fig. 2 *D*–*F*).

Conformational Changes. Rips in the force-extension relations at physiological forces suggest that PCDH15 exists in different structural states during hearing. At a saturating Ca^{2+} concentration, the conformational states accessible to the protein are limited; the state-space heatmap reveals only two major configurations (Fig. 2 *A* and *D*). The second of these configurations is further divided into two substates separated by a difference of only a few nanometers in contour length. State 1 reflects the extensibility of fully folded PCDH15 (*SI Appendix*, Note S1). By fitting a polymer model to the force-extension relations for five molecules, we find that state 2 arises from a combination of two classes of conformational changes, leading to mean ± SEM elongations of 4.0 ± 0.2 nm and 15.8 ± 0.7 nm (respectively, distributions of A_U and B_U in Fig. 2*G* and Table 1). The structural origin of these conformational changes is unknown and difficult to determine owing to the large size of the protein; however, was can rule out the unfolding of entire cadherin domains as the origin of the unfolding events. The length of the folded peptide in each of the 11 cadherin domains ranges from 94 to 123 aa, with a mean of 104 residues. At a contour length of 0.39 nm per residue (31), the unfolding of each cadherin domain is expected to augment the contour length by approximately 36 nm, an elongation of 40.6 nm minus 4.5 nm to account for loss of the folded cadherin domain. The observed contour length changes of the elongations A_U and B_U therefore represent protein rearrangements less extreme than the complete unfolding of a cadherin domain. At a saturating Ca^{2+} concentration and physiological forces, we never observed length changes in the wild-type protein compatible with full unfolding.

We next asked whether there are unique structural features in PCDH15 that give rise to the elongations A_U and B_U, or whether several different conformational changes, each with a similar contour length change, underlay the observed distributions. In most of the extension-relaxation cycles, we did not observe more than one of either class of events (*SI Appendix*, Fig. S2). The rare occasions in which several events A_U or B_U were detected in a single trace were not reproducible across trials or protein molecules and thus could be explained as the rupture of nonspecific interactions between the protein and either of the confining surfaces. We conclude that a single, unique structural alteration of PCDH15 is responsible for event A_U, whereas a distinct structural change results in event B_U, precluding the occurrence of several events of either type within the same cycle. Interestingly, the force sensitivity of events A_U is much narrower than that of events B_U (Fig. 2*J*). From these distributions, we determined the statistical dependence of both classes. An event A_U generally follows an event B_U ($P < 0.05$ and $P < 0.1$ for three and two of the five tested molecules, respectively). It is plausible that both structural changes resulted from the same cadherin domain, with elongation B_U leading to a destabilization that facilitated elongation A_U.

We found the protein in state 1 at the beginning of many extension-relaxation cycles and concluded that there is a high probability of refolding of both event A_U and event B_U between cycles. Indeed, we routinely detected refolding events A_F during the relaxation phase of our protocol (Fig. 2 *A* and *G*), but rarely observed refolding events B_F (*SI Appendix*, Fig. S3). The latter events likely occurred only at very low forces, for which the slight shortening was lost in Brownian noise (*SI Appendix*, Fig. S4).

We next reduced the Ca^{2+} concentration to the physiological value of 20 μM and exposed a tethered PCDH15 protein to the same force protocol. The extension-relaxation cycles showed mean conformational changes identical to those of the previously observed classes (A_U: 3.9 ± 0.4 nm; B_U: 15.0 ± 0.6 nm; $n = 8$) (Fig. 2*H*). At this Ca^{2+} concentration, however, an additional class of unfolding events emerged with a mean contour length change of 35 ± 1 nm (C_U in Fig. 2 *B* and *H*), in excellent agreement with the elongation expected for unfolding of an entire cadherin domain (32). At holding forces of 2–4 pN, the refolding of cadherin domains was a slow process and occurred on a time scale of seconds, in line with other proteins that feature Ig-like motifs (33). In some extension-relaxation cycles, we observed the successive unfolding of several cadherin domains (*SI Appendix*, Fig. S5). Because unfolding of any of the 11 extracellular cadherin domains should increase the contour length by a similar amount, we could neither assign unfolding events to particular domains nor elucidate the sequence in which the domains unraveled.

The heatmap of all force-extension relationships originated from a mixture of the unfolding events A_U, B_U, and C_U and their respective refolding events. The contour lengths that gave rise to the annotated states 1–8 (Fig. 2*E*) were a consequence of the unfolding of up to three cadherin domains in series with up to one unfolding event of type B_U. Structural changes of types A_U and A_F, which are clearly visible in the heatmap for a Ca^{2+} concentration of 3 mM as a subdivision of state 2 (Fig. 2*D*), are

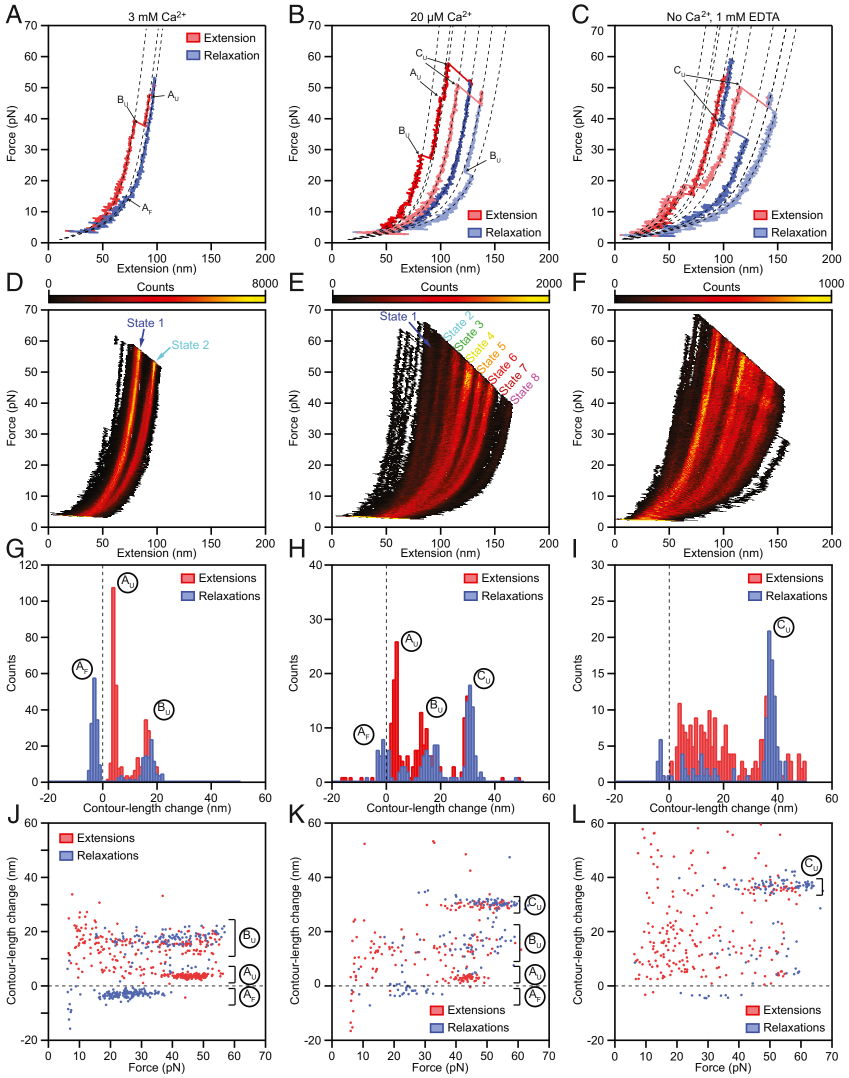

Fig. 2. Force-extension measurements of PCDH15 monomers. (*A*) At a Ca^{2+} concentration of 3 mM, individual force-extension cycles show two distinct classes of abrupt elongations, the unfolding events A_U and B_U, as well as refolding events of class A_F. The dashed lines represent fits to the trajectories by a protein model. (*B*) Reducing the Ca^{2+} concentration to 20 µM elicits an additional class of unfolding events, C_U, corresponding to the unfolding of entire cadherin domains. (*C*) In the absence of Ca^{2+}, unclassifiable structural changes occur in conjunction with the well-defined events C_U. (*D*–*F*) Heatmaps displaying all the force-extension cycles for a single representative molecule at each Ca^{2+} concentration. The data were binned into pixels of 1 nm × 0.1 pN. A much smaller portion of the state space is accessible at a Ca^{2+} concentration of 3 mM than at a Ca^{2+} concentration of 20 µM or in the absence of Ca^{2+}. The heatmaps illustrate which contour lengths of the tethered molecules occurred with increased likelihood during our force-loading protocol as an average over both extensions and relaxations. Prominent regions of elevated occupancy are labeled states 1–8, in which state 1 corresponds to the fully folded protein and state 8 results from the unfolding of three cadherin domains in series with one event of type B_u. (*G*–*I*) Histograms of the contour length changes of all abrupt elongations verify that these rips can be grouped into classes A_F, A_U, B_U, and C_U at Ca^{2+} concentrations of 3 mM and 20 µM. In the absence of Ca^{2+}, most of the contour length changes are more broadly distributed. (*J*–*L*) Plots of the contour length change of every rip against the force at which that event occurred revealing the force distributions of each class of structural change. Note that the extensions never completely unfolded a PCDH15 molecule, so elongations could occur even during the relaxation phases. Because the contour lengths observed for the folded protein correspond to the length of monomeric PCDH15 in series with its molecular anchors, the measured extensions exceed those expected for the protein alone. Our analysis corrects for this influence, resulting in values in excellent agreement with the known structure of the protein (Table 1). All force-extension cycles were sampled at intervals of 10 µs and smoothed to a temporal resolution of 1 ms. The waiting times between cycles were 0.2 s for a Ca^{2+} concentration of 3 mM, 2 s for a Ca^{2+} concentration of 20 µM, and 4 s in the absence of Ca^{2+}. The number of cycles recorded was 500 for a Ca^{2+} concentration of 3 mM and 200 for a Ca^{2+} concentration of 20 µM and in the absence of Ca^{2+}.

Table 1. Material property values of PCDH15

$[\mathrm{Ca}^{2+}]$	b, nm	lc_{linker}, nm	k_{folded}, mN/m	Δlc_{A}, nm	Δlc_{B}, nm	Δlc_{C}, nm
3 mM	2.9 ± 0.5	1.4 ± 0.5	9 ± 4	4.0 ± 0.2	15.8 ± 0.7	—
20 μM	3.1 ± 0.4	1.3 ± 0.5	11 ± 5	3.9 ± 0.4	15.0 ± 0.6	35 ± 1

The parameters of a polymer model (*SI Appendix*) were as follows: b, length of each stiff segment of the folded protein; lc_{linker}, contour length of each flexible linker between the stiff segments; k_{folded}, enthalpic stiffness of the folded protein; Δlc_{A}, contour length increase, type A; Δlc_{B}, contour length increase, type B; Δlc_{C}, contour length increase, type C. The parameter values were determined from fits of the model to the force-extension curves in Fig. 2. The values for the folded protein are largely independent of the Ca^{2+} concentration. Δlc_{C} is in good agreement with the expected contour-length change per unfolded cadherin domain. Fitted parameter values are given as mean ± SEM for five experiments at a Ca^{2+} concentration of 3 mM and for eight experiments at a Ca^{2+} concentration of 20 μM.

not apparent in the state space for a Ca^{2+} concentration of 20 μM. It is possible that there were Ca^{2+}-dependent subnanometer changes in the contour length that averaged out small effects of events $\mathrm{A_U}$ and $\mathrm{A_F}$ in the heatmap. We again investigated a potential sequential dependence of unfolding classes by their force distributions (Fig. 2*K*). Even though events of type $\mathrm{A_U}$ followed events of type $\mathrm{B_U}$ at a Ca^{2+} concentration of 3 mM, at a physiological Ca^{2+} concentration these structural changes in eight molecules were independent of one another ($P > 0.1$ for each molecule). Moreover, events of types $\mathrm{A_U}$ and $\mathrm{B_U}$ were independent of events of type $\mathrm{C_U}$, the unfolding of entire cadherin domains.

We next investigated the mechanics of PCDH15 in the absence of Ca^{2+}. Representative force-extension relationships featured a plethora of conformational changes (Fig. 2 *C* and *I*), many of which could no longer be clearly grouped into any of the classes $\mathrm{A_{U,F}}$ and $\mathrm{B_U}$. Events with a mean of 37 ± 2 nm (for five molecules) continued to characterize a well-defined class $\mathrm{C_U}$. The heatmap of all extension-relaxation cycles had a structure reminiscent of that at a Ca^{2+} concentration of 20 μM (Fig. 2*F*). The structure in the absence of Ca^{2+} arose from the unfolding of a discrete number of cadherin domains in series with the unclassifiable shorter structural changes that likely represented the partial unfolding of one or more domains. This lack of well-defined short structural changes was also evident from the force distribution of the observed rips (Fig. 2*L*).

Stiffness of PCDH15. It is unknown whether tip link cadherins are completely or only partially folded during normal hearing. Therefore, we investigated the stiffness not only of folded PCDH15, but also that of conformational states with a progressively greater number of unfolded domains. The total stiffness of PCDH15 comprises both enthalpic and entropic components, whose contributions we quantified by fitting the force-extension relationships with a model of the protein. A freely jointed chain (34) formed by the 11 folded cadherin domains, in series with a worm-like chain (35) representing the 10 unstructured linker regions, captured the protein's disorder under tension and reflected its entropic extensibility. The protein's enthalpic extensibility, which likely originates from deformations of its secondary and tertiary structures rather than from unfolding, was modeled through a Hookean spring constant. We included an additional worm-like chain to model any unfolded portions of the protein (*SI Appendix*, Fig. S6).

Because the unfolded polypeptide chains and the linker regions are structurally similar, we modeled both with the same persistence length. Fits to the data for 13 molecules yielded a mean lp_{peptide} value of 0.49 ± 0.04 nm. For folded PCDH15 at a Ca^{2+} concentration of 3 mM, we found a mean length of 2.9 ± 0.5 nm for each of the 11 solid segments of the chain, a mean length of 1.4 ± 0.5 nm for each of the 10 flexible linkers between the solid segments, and a mean enthalpic spring constant of 9 ± 4 $\mathrm{mN \cdot m^{-1}}$ for the Hookean stiffness of the protein ($n = 5$ molecules) (Table 1). The full length of a solid segment combined with its associated linker region was 4.3 ± 0.7 nm, in excellent agreement with the value of 4.5 nm per cadherin repeat from crystal structures of cadherin domains (22). Much to our surprise, these values did not change when the Ca^{2+} concentration was decreased to 20 μM, the physiological level in the cochlea. An elevated Ca^{2+} concentration stabilizes cadherin domains against unfolding but does not augment the stiffness of the folded protein. The stiffness predicted by our model is in good agreement with the slopes of the different states in the state-space heatmap (Fig. 3).

Across all states and Ca^{2+} concentrations, the measured and predicted stiffness of the protein is much smaller than its enthalpic stiffness of ~10 $\mathrm{mN \cdot m^{-1}}$. The additional compliance is entropic, arising from the thermal motion of the individual cadherin domains and from thermal undulations in the interdomain linker regions and unfolded polypeptide chains. When PCDH15 is tensed, this thermal kinking is smoothed out, and the protein elongates. The progressive unfolding of domains further softens the protein by introducing additional disordered polypeptide chains (Fig. 3*B*). At high forces, most thermal bends have been straightened, and the enthalpic elasticity begins to dominate the protein's response. Importantly, we find that for physiological tensions, the protein's response to force is determined by entropic elasticity. The protein's stiffness approaches its enthalpic value only for unphysiologically high tensions (Fig. 3 and *SI Appendix*, Fig. S7).

Unfolding of Cadherin Domains Under Forces Relevant for Hearing. Elevated tension not only increases the stiffness of PCDH15, but also increases the likelihood that entire cadherin domains unfold. Do cadherin domains unfold during normal hearing? If so, do they refold under physiological conditions, or could tip links with persistently unstructured regions exist in vivo?

To determine the unfolding rate of cadherin domains under physiological tensions, we transformed the force distributions of type $\mathrm{C_U}$ unfolding events into unfolding rates as a function of constant force (Fig. 4) (27). For a given unfolding event, we could not determine which of the 11 cadherin domains had unfolded, so our result is an average over several or all of the domains. The transformation also assumed no cooperativity between the unfolding of individual domains. If the unfolding of one domain were to increase the probability that an adjacent domain would unravel, for example, then our approach would have systematically overestimated the rate at which fully folded tip links unfold.

We computed unfolding rates for Ca^{2+} concentrations of both 20 μM and 0 M (Fig. 4). As expected, the presence of Ca^{2+} stabilized cadherin against force-induced unfolding; the domains unfolded many times faster in the ion's absence than in its presence. With a physiological Ca^{2+} concentration and at 20 pN of tension, the upper range of physiological resting values, a single cadherin domain unfolded at a rate of approximately once every 100 s. A fully folded PCDH15 molecule—consisting of 11 domains—then unfolded a domain every 10 s. At even higher tensions, this rate rapidly increased to roughly 0.4 $\mathrm{s^{-1}}$ for the unfolding of a single cadherin domain at a tension of 60 pN. Because unfolding events at forces of 10–20 pN were extremely rare and might have corresponded to transitions from molten-globule states (*SI Appendix*, Note S2), we were unable to reliably calculate force-dependent unfolding rates for this force range. Nevertheless, extrapolation of the available data suggests a rate of ~0.003 $\mathrm{s^{-1}}$ at 10 pN of tension.

These results indicate that unfolding of cadherin domains would not occur within individual cycles of an auditory stimulus. For physiological forces, the unfolding rate is much too low to

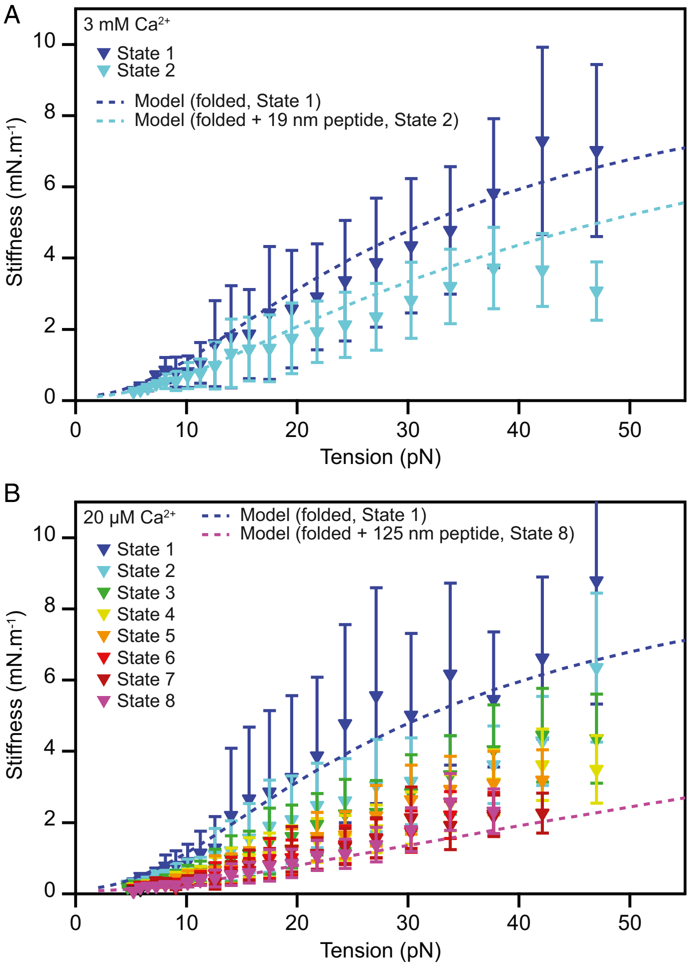

Fig. 3. Stiffness of monomeric PCDH15. (*A*) The stiffnesses of the different conformational states of PCDH15 at a Ca^{2+} concentration of 3 mM correspond to the slopes of the highly occupied regions of the state space in Fig. 2 *D* and *E* and are corrected for the stiffness of the molecular tags and anchors. The dark-blue dashed line represents the stiffness of our model of state 1, the fully folded protein, with the parameter values of Table 1 (b = 3.0 nm; lc_{linker} = 1.35 nm; k_{folded} = 10 mN·m^{-1}). Parameter values were averaged over both Ca^{2+} concentrations. The light-blue dashed line represents the model for state 2, with an additional 19-nm segment of unfolded protein with a persistence length of 0.49 nm representing the combined effect of the events A_U and B_U. (*B*) The corresponding data for a Ca^{2+} concentration of 20 μM capture a variety of unfolding events leading to states 2–8. The dark-blue dashed line represents a model of the fully folded protein (state 1); the pink dashed line depicts the modeled stiffness of the protein in state 8, with an unstructured 125-nm-long peptide to represent the unfolding of three cadherin domains in series with contour length changes of 15 nm and 4 nm. The experimental data are mean ± SEM for five molecules at a Ca^{2+} concentration of 3 mM and for six molecules at a Ca^{2+} concentration of 20 μM.

follow stimuli with frequencies ranging from hundreds to thousands of hertz. However, provided that at the link's resting tension, a domain's unfolding rate exceeds its refolding rate, cadherin domains in a tensed tip link could exist in a permanently unfolded state. We never observed refolding of cadherin domains during any of the recorded extension-relaxation cycles, even though such events should be readily detectable at tensions exceeding 4 pN (*SI Appendix*, Fig. S4). Instead, refolding occurred only during the holding phase between successive cycles, provided that the holding force was <4 pN and the waiting time was on the order of several seconds.

We conclude that for tensions >20 pN per molecule, the unfolding rate—although very small—exceeds the refolding rate. Our data indicate that this is also the case for the force range of 4–20 pN, but owing to the possible influence of molten-globule states, we could not determine this with certainty. Future experiments with force jumps and constant forces might shed light on the existence and behavior of molten-globule states in this force regime. Our result suggests that some cadherin domains of tip links in vivo exist in a perpetually unfolded state. Such unfolded states would decrease the protein's stiffness (Fig. 3*B*) and could be a mechanism by which a tip link softens even under high tension.

The critical force at which the unfolding and refolding rates of a cadherin domain are equal remains to be determined. However, the giant muscle protein titin, which has immunoglobin folds similar to those of cadherin, exhibits a critical force of 5.4 pN (33). If cadherin domains feature a similar value, the resting tensions in low-frequency hair cells might be less than the critical force and bias the tip link's domains toward a fully folded state, whereas the tip link might remain in a partially unfolded state in hair cells sensitive to high frequencies.

Effect of a Mutation Associated with Hearing Loss. More than 100 mutations of the tip link cadherins cause hearing loss in humans (36). The deletion of residue V767 in EC7 (Fig. 5*A*) is of particular interest, for it leads to deafness—stemming from a deficit in the cochlea, with its low Ca^{2+} concentration—but not loss of function in the vestibular labyrinth, which has a higher Ca^{2+} concentration (37). This mutation evidently does not hinder

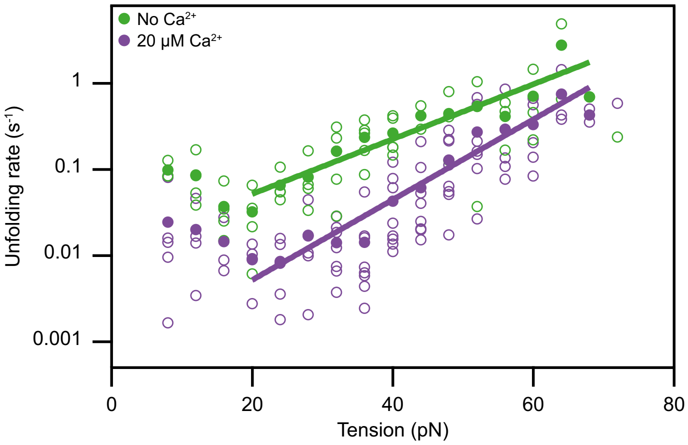

Fig. 4. Tension-dependent unfolding rates of a single cadherin domain. Assuming that all domains of PCDH15 are similar and unfold independently, we estimate the rate at which individual EC domains unfold as a function of tension. Domains unfold much more readily in the absence of Ca^{2+} (green) than at a physiological Ca^{2+} concentration of 20 μM (purple). The filled circles represent the means for eight molecules at a Ca^{2+} concentration of 20 μM and for five molecules in the absence of Ca^{2+}. The outlined circles, which represent the data for individual molecules, provide an estimate of the data's spread. The solid lines are fits of Bells' model (48) to the data. For 20 μM Ca^{2+}, the unfolding rate with no force is $k_0 = 0.0006 \pm 0.0002\ s^{-1}$, and the transition-state distance is $x^{\ddagger} = 0.44 \pm 0.04$ nm; in the absence of Ca^{2+}, these values are $k_0 = 0.012 \pm 0.006\ s^{-1}$ and $x^{\ddagger} = 0.30 \pm 0.04$ nm.

tip link formation, but it might change the elastic properties of the link.

We investigated how this deletion affects the mechanical properties of monomeric PCDH15 (V250D, ΔV767) and found a small but detectable probability that force unfolded a complete cadherin domain even when PCDH15 was saturated with Ca^{2+} (Fig. 5*B*). During identical treatment of Ca^{2+}-saturated proteins without pathological mutations, we never observed the unfolding of complete domains (Fig. 2*G*). By shortening one strand of EC7, the mutation likely caused a slight misalignment of amino acid residues and thus destabilized the domain. When we performed experiments at the physiological Ca^{2+} concentration of 20 μM, we could not detect a difference in domain unfolding between the mutant and wild-type proteins.

Discussion

The behavior of a gated ion channel is usually binary: the channel is open or closed. Nevertheless, a mechanically activated channel can signal fine nuances of a stimulus by rapidly fluttering between the two states, such that the average open probability provides a smoothly graded representation of the stimulus. A gating spring makes this possible. Tensed by a stimulus and battered by thermal noise, the spring continuously adjusts the open probability of the associated channel over a significant range of inputs. This range is determined by the gating spring's stiffness, and thus by such molecular details as the entropic elasticity and folding transitions demonstrated here.

The stiffness of gating springs in outer hair cells increases with increased resting tension along the tonotopic axis (13), from 1.3 mN·m^{-1} at 5 pN of tension to 3.7 mN·m^{-1} at 34 pN. Simulations of short segments of tip link proteins found that they are orders of magnitudes too stiff to account for these values (15, 38). However, our single-molecule experiments on the extracellular domain of PCDH15 show that the protein has a stiffness comparable to that of gating springs in vivo and displays similar strain-hardening. Across the physiological force range, most of PCDH15's compliance is of entropic origin; the protein's enthalpic stiffness of 10 mN·m^{-1} emerges only at very high tension. Our stiffness values (Fig. 3) are systematically lower than those found for gating springs in vivo, which is not surprising because our measurements tested only a monomer of one constituent protein. The dimeric arrangement of PCDH15 roughly doubles the enthalpic stiffness of the monomer. Moreover, a tip link adopts a helical structure (14, 18) that likely reduces the magnitude of its thermal undulations, decreasing the entropic contribution to the tip link's mechanics and further

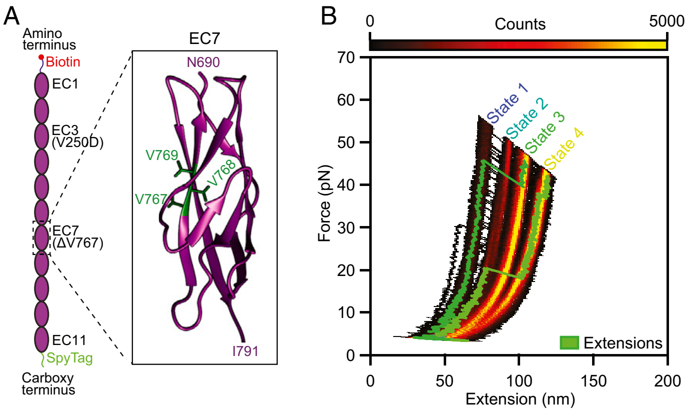

Fig. 5. Effect of a hearing loss-associated mutation on PCDH15 mechanics. (*A*) We deleted V767 in the seventh EC domain of PCDH15. As indicated in the crystal structure (Protein Data Bank ID code 5W1D; image generated with UCSF Chimera), V767 is located in the F strand of the cadherin fold. (*B*) A state-space heatmap for 500 extension-relaxation cycles reveals that at a Ca^{2+} concentration of 3 mM the mutant protein can assume four distinct conformational states. The two additional states not observed in the wild-type protein result from unfolding of the pathological cadherin domain in series with the usual states 1 and 2. Unfolding of the pathological domain is rare and occurs in only a few cycles, two of which are superimposed on the heat map (green traces). The waiting time between cycles was 0.2 s.

increasing its stiffness. Finally, the arrangement of a dimer of CDH23 in series with the PCDH15 dimer is expected to reduce the stiffness by approximately 70%. At very high tensions, when entropic effects are largely suppressed and enthalpy dominates, we estimate the stiffness of the full-length, dimeric tip link as 6 mN·m^{-1} (*SI Appendix*, Note S3), a value in good agreement with the stiffness of strongly tensioned gating springs in vivo (13). Provided that entropy further softens the tip link at lower tensions, our results suggest that the tip link cadherins are a major component of the gating spring for mechanotransduction in hair cells. The entropic contributions to the mechanics of dimeric PCDH15 and of the entire tip link remain to be determined.

The stiffness of hair bundles has a complicated, nonmonotonic dependence on Ca^{2+} concentration (39, 40), an observation that may be interpreted as the interplay between strain-hardening of the tip links and the unfolding of cadherin domains. Low Ca^{2+} levels cause molecular motors to up-regulate tip link tension (41), which suppresses each link's thermal motion and increases its stiffness. Ca^{2+} also directly affects the rate at which cadherin domains unfold under force, however, resulting in states of PCDH15 with reduced stiffness (Fig. 3). At a tension of 20 pN and a Ca^{2+} concentration of 20 μM, individual cadherin domains unfold an order of magnitude more slowly than in the absence of Ca^{2+}. We never observed the unfolding of entire cadherin domains at a Ca^{2+} concentration of 3 mM. Thus, the Ca^{2+} concentration regulates both the tension on and the structure of PCDH15, the combined effect of which on the molecule's mechanics is hard to predict. Nevertheless, the sensitivity of PCDH15 to Ca^{2+} suggests that the variable concentrations of the ion in different receptor organs tunes the mechanical properties of tip links, and thus of hair bundles, to the organs' specific requirements. Even within a single organ, the guinea pig cochlea, the Ca^{2+} concentration increases fourfold along the tonotopic axis from base to apex (25). This gradient might adjust tip link stiffness to accord with the frequency response of the individual hair cells. Finally, hair cells can enhance the local Ca^{2+} concentration around their hair bundles through the activity of membrane Ca^{2+} pumps (42). This phenomenon raises the interesting possibility that the stiffness of tip links is modulated by the locally varying Ca^{2+} concentration in response to hair cell activity.

We found that the elastic properties of folded PCDH15 are surprisingly independent of the Ca^{2+} concentration. This result seems to contradict the impression conveyed by electron micrographs (43), in which cadherins transition from a disordered globular conformation to a rod-like chain of domains in the presence of progressively larger amounts of Ca^{2+}. Disordered states should make greater entropic contributions to PCDH15's elasticity than ordered states, a difference not apparent in our data. Note, however, that the divergence between electron-microscopic images and single-molecule data has also been observed for other proteins, such as titin (44). A possible explanation is that the configurations of proteins adsorbed to substrates are far from their equilibrium conformations, so that the variations in shape do not accurately capture the thermal motion in solution (45).

The displacement-transduction current relationships of hair bundles reveal that for unphysiologically large displacements in excess of 1 μm, gating springs can stretch (46) by at least 120 nm, a value thought to be incompatible with the extensibility of tip link cadherins. Consequently, it has been suggested that the gating spring's stiffness stems from the elasticity of the plasma membrane or cytoskeleton into which the tip links insert (47). We have shown that invoking such sources of elasticity is unnecessary; cadherin domains in the tip link proteins can unfold under physiological stimuli, albeit at a low rate, and such unfolding events become very likely at high forces. Recall that physiological hair bundle displacements are on the order of 10 nm and augment the resting tension of each tip link by a few piconewtons. The stimulus in extreme deflections, which is 100-fold greater, is capable of causing the almost instantaneous unfolding of individual cadherin domains. Several unfolded cadherin domains could then account for the extreme tip link elongation of 120 nm.

In further support of domain unfolding, the length distribution of tip links in the bullfrog's hair bundles, as determined by electron-microscopic tomography, features two distinct classes (10) with means close to 110 nm and 170 nm. The unfolding of two cadherin domains per tip link monomer could account for this length difference. Such unfolding events could soften the gating spring at high resting tensions and protect both the tip link and the associated mechanotransduction machinery from damage during loud sounds.

In addition to the unfolding of entire cadherin domains, we also observed partial domain unfolding with contour length increases of 4 nm and 15 nm. Future single-molecule work is needed to elucidate the structural correlates of these conformational changes and to determine their role in hearing. Additional experiments are also needed to test the stiffness of PCDH15 dimers and of the full tip link and to confirm that domain unfolding occurs for those constructs and for tip links in vivo.

Methods

More detailed information is provided in *SI Appendix, Materials and Methods*.

Preparation of PCDH15 Monomers. Plasmids encoding murine PCDH15 were expressed in suspension-adapted HEK293 cells. To confine monomers in an optical trap, the amino terminus of the protein was labeled with an AviTag that permitted the enzymatic conjugation of biotin. The carboxyl terminus included a SpyTag that could form a covalent linkage with an immobilized SpyCatcher protein. The construct also encoded a signal peptide to promote secretion, short flexible linkers flanking the PCDH15 sequence, and a His tag for purification.

Optical Trapping and Measurements. SpyCatcher molecules were conjugated to 2-μm silicon dioxide pedestal beads that were covalently attached to a glass coverslip. PCDH15 monomers were washed into the sample chamber and allowed to attach covalently to the pedestal beads. To initiate an experiment, we optically trapped a streptavidin-coated 1-μm polystyrene bead and positioned it near a pedestal bead. Using a highly focused 852-nm laser beam, we applied stimulus forces to probe the molecule's mechanical properties. With a second, high-stability 1,064-nm laser, we monitored the position of the probe bead with a precision of ≤1 nm in each of three dimensions.

ACKNOWLEDGMENTS. We thank Julio Fernandez and Jaime Andrés Rivas-Pardo for guidance concerning the chemical functionalization of glass substrates, Brian Fabella and Vadim Sherman for high-precision fabrication, Brandon Razooky and Maria Vologodskaia for assistance with cloning, and Anna Kaczynska for help with protein expression. The crystal structure in Fig. 5 was deposited by Carissa Klanseck, Brandon Neel, and Marcos Sotomayor. F.E.H. acknowledges financial support by the Studienstiftung des Deutschen Volkes. A.O. was supported by the Medical Research Fellows Program of Howard Hughes Medical Institute. T.F.B. was partially supported by a Junior Fellow award from the Simons Foundation and a Pilot Grant from the Kavli Foundation. A.J.H. is an Investigator of Howard Hughes Medical Institute.

1. Wiggins P, Phillips R (2004) Analytic models for mechanotransduction: Gating a mechanosensitive channel. *Proc Natl Acad Sci USA* 101:4071–4076.
2. Saotome K, et al. (2018) Structure of the mechanically activated ion channel Piezo1. *Nature* 554:481–486.
3. Zhao Q, et al. (2018) Structure and mechanogating mechanism of the Piezo1 channel. *Nature* 554:487–492.
4. Jin P, et al. (2017) Electron cryo-microscopy structure of the mechanotransduction channel NOMPC. *Nature* 547:118–122.
5. Corey DP, Hudspeth AJ (1983) Kinetics of the receptor current in bullfrog saccular hair cells. *J Neurosci* 3:962–976.
6. Hudspeth AJ (2014) Integrating the active process of hair cells with cochlear function. *Nat Rev Neurosci* 15:600–614.

7. Reichenbach T, Hudspeth AJ (2014) The physics of hearing: Fluid mechanics and the active process of the inner ear. *Rep Prog Phys* 77:076601.
8. Pickles JO, Comis SD, Osborne MP (1984) Cross-links between stereocilia in the guinea pig organ of Corti, and their possible relation to sensory transduction. *Hear Res* 15: 103–112.
9. Assad JA, Shepherd GM, Corey DP (1991) Tip-link integrity and mechanical transduction in vertebrate hair cells. *Neuron* 7:985–994.
10. Auer M, et al. (2008) Three-dimensional architecture of hair-bundle linkages revealed by electron-microscopic tomography. *J Assoc Res Otolaryngol* 9:215–224.
11. Sotomayor M, Weihofen WA, Gaudet R, Corey DP (2012) Structure of a force-conveying cadherin bond essential for inner-ear mechanotransduction. *Nature* 492: 128–132.
12. Howard J, Hudspeth AJ (1988) Compliance of the hair bundle associated with gating of mechanoelectrical transduction channels in the bullfrog's saccular hair cell. *Neuron* 1:189–199.
13. Tobin M, Chaiyasitdhi A, Michel V, Michalski N, Martin P (2019) Stiffness and tension gradients of the hair cell's tip-link complex in the mammalian cochlea. *eLife* 8:e43473.
14. Kachar B, Parakkal M, Kurc M, Zhao Y, Gillespie PG (2000) High-resolution structure of hair-cell tip links. *Proc Natl Acad Sci USA* 97:13336–13341.
15. Sotomayor M, Weihofen WA, Gaudet R, Corey DP (2010) Structural determinants of cadherin-23 function in hearing and deafness. *Neuron* 66:85–100.
16. Albert JT, Kozlov AS (2016) Comparative aspects of hearing in vertebrates and insects with antennal ears. *Curr Biol* 26:R1050–R1061.
17. Smith SB, Finzi L, Bustamante C (1992) Direct mechanical measurements of the elasticity of single DNA molecules by using magnetic beads. *Science* 258:1122–1126.
18. Dionne G, et al. (2018) Mechanotransduction by PCDH15 relies on a novel cis-dimeric architecture. *Neuron* 99:480–492.e5.
19. Ge J, et al. (2018) Structure of mouse protocadherin 15 of the stereocilia tip link in complex with LHFPL5. *eLife* 7: e38770.
20. Pralle A, Prummer M, Florin E-L, Stelzer EHK, Hörber JK (1999) Three-dimensional high-resolution particle tracking for optical tweezers by forward scattered light. *Microsc Res Tech* 44:378–386.
21. Bartsch TF, Kochanczyk MD, Lissek EN, Lange JR, Florin E-L (2016) Nanoscopic imaging of thick heterogeneous soft-matter structures in aqueous solution. *Nat Commun* 7: 12729.
22. Shapiro L, et al. (1995) Structural basis of cell-cell adhesion by cadherins. *Nature* 374: 327–337.
23. Nagar B, Overduin M, Ikura M, Rini JM (1996) Structural basis of calcium-induced E-cadherin rigidification and dimerization. *Nature* 380:360–364.
24. Bosher SK, Warren RL (1978) Very low calcium content of cochlear endolymph, an extracellular fluid. *Nature* 273:377–378.
25. Salt AN, Inamura N, Thalmann R, Vora A (1989) Calcium gradients in inner ear endolymph. *Am J Otolaryngol* 10:371–375.
26. Powers RE, Gaudet R, Sotomayor M (2017) A partial calcium-free linker confers flexibility to inner-ear protocadherin-15. *Structure* 25:482–495.
27. Zhang Y, Dudko OK (2013) A transformation for the mechanical fingerprints of complex biomolecular interactions. *Proc Natl Acad Sci USA* 110:16432–16437.
28. Jaramillo F, Hudspeth AJ (1993) Displacement-clamp measurement of the forces exerted by gating springs in the hair bundle. *Proc Natl Acad Sci USA* 90:1330–1334.
29. Chen F, et al. (2011) A differentially amplified motion in the ear for near-threshold sound detection. *Nat Neurosci* 14:770–774.
30. Marko JF, Siggia ED (1994) Fluctuations and supercoiling of DNA. *Science* 265:506–508.
31. Ainavarapu SRK, et al. (2007) Contour length and refolding rate of a small protein controlled by engineered disulfide bonds. *Biophys J* 92:225–233.
32. Oroz J, et al. (2011) Nanomechanics of the cadherin ectodomain: "canalization" by Ca^{2+} binding results in a new mechanical element. *J Biol Chem* 286:9405–9418.
33. Chen H, et al. (2015) Dynamics of equilibrium folding and unfolding transitions of titin immunoglobulin domain under constant forces. *J Am Chem Soc* 137:3540–3546.
34. Rubinstein M, Colby RH (2003) *Polymer Physics* (Oxford Univ Press, Oxford).
35. Marko JF, Siggia ED (1995) Stretching DNA. *Macromolecules* 28:8759–8770.
36. Jaiganesh A, et al. (2018) Zooming in on cadherin-23: Structural diversity and potential mechanisms of inherited deafness. *Structure* 26:1210–1225.e4.
37. Zhan Y, Liu M, Chen D, Chen K, Jiang H (2015) Novel mutation located in EC7 domain of protocadherin-15 uncovered by targeted massively parallel sequencing in a family segregating non-syndromic deafness DFNB23. *Int J Pediatr Otorhinolaryngol* 79:983–986.
38. Sotomayor M, Corey DP, Schulten K (2005) In search of the hair-cell gating spring elastic properties of ankyrin and cadherin repeats. *Structure* 13:669–682.
39. Marquis RE, Hudspeth AJ (1997) Effects of extracellular Ca2^{+} concentration on hair-bundle stiffness and gating-spring integrity in hair cells. *Proc Natl Acad Sci USA* 94: 11923–11928.
40. Tinevez J-Y, Jülicher F, Martin P (2007) Unifying the various incarnations of active hair-bundle motility by the vertebrate hair cell. *Biophys J* 93:4053–4067.
41. Bechstedt S, Howard J (2007) Models of hair cell mechanotransduction. *Mechanosensitive Ion Channels, Part B*. Current Topics in Membranes, eds Simon S, Bemos D (Academic, New York), Vol 59, pp 399–424.
42. Yamoah EN, et al. (1998) Plasma membrane Ca2^{+}-ATPase extrudes Ca2^{+} from hair cell stereocilia. *J Neurosci* 18:610–624.
43. Kazmierczak P, et al. (2007) Cadherin 23 and protocadherin 15 interact to form tip-link filaments in sensory hair cells. *Nature* 449:87–91.
44. Leake MC, Wilson D, Gautel M, Simmons RM (2004) The elasticity of single titin molecules using a two-bead optical tweezers assay. *Biophys J* 87:1112–1135.
45. Broedersz CP, MacKintosh FC (2014) Modeling semiflexible polymer networks. *Rev Mod Phys* 86:995–1036.
46. Shepherd GM, Corey DP (1994) The extent of adaptation in bullfrog saccular hair cells. *J Neurosci* 14:6217–6229.
47. Powers RJ, et al. (2012) Stereocilia membrane deformation: Implications for the gating spring and mechanotransduction channel. *Biophys J* 102:201–210.
48. Bell GI (1978) Models for the specific adhesion of cells to cells. *Science* 200:618–627.

Supporting Information for

The elasticity of individual protocadherin 15 molecules implicates cadherins as the gating springs for hearing

Tobias F. Bartsch[a,1], Felicitas E. Hengel[a,2], Aaron Oswald[a,2], Gilman Dionne[b], Iris V. Chipendo[a], Simranjit S. Mangat[a], Muhammad El Shatanofy[a], Lawrence Shapiro[b], Ulrich Müller[c], and A. J. Hudspeth[a,1]

[a]Howard Hughes Medical Institute and Laboratory of Sensory Neuroscience, The Rockefeller University, New York, NY 10065;. [b]Department of Biochemistry and Molecular Biophysics, Zuckerman Mind Brain Behavior Institute, Columbia University, New York, NY 10032; [c]The Solomon Snyder Department of Neuroscience, Johns Hopkins University, Baltimore, MD 21205

[1] Corresponding authors: tbartsch@rockefeller.edu and hudspaj@rockefeller.edu

[2] These authors contributed equally.

This file contains:

- Materials and Methods
- Figs. S1 to S13
- Tables S1 to S3
- Notes S1 to S3
- References

www.pnas.org/cgi/doi/10.1073/pnas.1902163116

SI Materials and Methods

Molecular cloning

Plasmids were assembled by Gibson assembly in a one-step isothermal reaction using home-made master mixes[1]. We assembled in a pLEXm backbone[2] a construct encoding the protein **signal peptide-QYDDDWQYED-AviTag-GSGSGS-PCDH15(EC1-11, V250D)-GSGSGS-SpyTag-6×His**. The deletion mutant (V250D, ΔV767) was assembled in a similar reaction. The PCDH15 sequence was isoform 1 from *Mus musculus* (UniProtKB entry Q99PJ1). The signal peptide comprises the native sequence that leads to secretion of PCDH15. Two tags for the site-specific confinement of PCDH15 were fused to the termini of the protein. The AviTag, with the sequence **GLNDIFEAQKIEWHE**, is recognized by a biotin ligase (BirA-500, Avidity, Aurora, CO, USA), which covalently biotinylates the lysine side chain. The SpyTag had the sequence **AHIVMVDAYKPTK**. The tags were attached to PCDH15 through flexible **GSGSGS** linkers.

Expression of recombinant PCDH15

All constructs were transfected with 40 kDa polyethyleneimine (Polysciences, Inc., Warrington, PA, USA) into suspension-adapted HEK293 cells (Freestyle, R79007, Thermo Fisher Scientific, Waltham, MA, USA). Seven to nine days post transfection, the medium was collected and secreted proteins were purified by Ni^{2+}-affinity chromatography. Proteins were further purified by size-exclusion chromatography (Superose 6 10/300 GL,17517201, GE Healthcare Bio-Sciences, Pittsburgh, PA, USA) in 10 mM Tris, 150 mM NaCl, and 3 mM $CaCl_2$. The purified proteins were concentrated to 1.5 mg/ml and biotinylated for 1 hr at 30 °C with biotin ligase (BirA 500, Avidity, Aurora, CO, USA). The samples were then used immediately or mixed with equal volumes of glycerol and stored at -20 °C for up to four months.

Design of the control linker peptide

In order to test the mechanical properties of the linkers and anchors of the assay in the absence of PCDH15, we fused the SpyTag and AviTag by a flexible **GGGSGGGS** linker to produce a control linker peptide with the sequence **AHIVMVDAYKPTKGGGSGGGSGLNDIFEAQKIEWHE** (Genscript, Piscataway, NJ, USA). After biotinylation, this peptide is capable of tethering streptavidin-coated probe beads to SpyCatcher molecules on pedestal beads, representing a control single-molecule assay that contains all components except for the PCDH15 protein.

Site-specific attachment of PCDH15 through short molecular anchors

The carboxy terminus of PCDH15 was modified with a SpyTag capable of forming a covalent bond with a small, globular protein called SpyCatcher, which was linked to the surface of the pedestal bead. The protein's amino terminus was biotinylated to allow its strong, site-specific attachment to streptavidin molecules on the probe bead (Figure 1d,f). The SpyCatcher-SpyTag complex is mechanically stable up to nanonewtowns of force, well beyond the range relevant for hearing[3]. The streptavidin-biotin interaction has a lifetime of about 30 s for the highest forces applied in this work[4,5]. These properties made this set of tags and binding partners ideal for the site-specific confinement of proteins under force.

Conjugation of pedestal beads with SpyCatcher molecules

Cys-SpyCatcher molecules (EOX004, Kerafast, Boston, MA, USA) were conjugated to aminated silicon dioxide microspheres (140414-10, Corpuscular, Cold Spring, New York, USA) through short, bifunctional polyethylene glycol spacers. To deprotonate the surface amine groups, 200 µl of the beads was washed once and resuspended for 1 hr at room temperature in 100 µl of 50 mM sodium tetraborate buffer (11625, Sigma Aldrich, St Louis, MO, USA) at pH 8.5. Deprotonation is necessary for efficient covalent coupling of the *N*-hydroxysuccinimide-PEG$_{12}$-maleimide spacer (22112, ThermoFisher, Waltham, Ma, USA), which we added to the beads to a final concentration of 50 mM of the linker and a final volume of 160 µl. The resulting mixture was incubated for 30 min at room temperature, washed three times with 1 ml of Hepes-buffered saline solution (HeBS; 20 mM Hepes and 100 mM NaCl), and after the final wash resuspended into 250 µl of HeBS.

Meanwhile, 0.5 mg of Cys-SpyCatcher protein was dissolved in 50 µl of HeBS and reduced for 1 hr with tris(2-carboxyethyl)phosphine (Immobilized TCEP Disulfide Reducing Gel, 77712, ThermoFisher Scientific, Waltham, MA, USA) according to the manufacturer's instructions. The reduced SpyCatcher protein was then mixed with 55 µl of 100 mg/ml sulfhydryl-blocked bovine serum albumin (BSA; 100-10SB, Lee Biosolutions, Inc., Maryland Heights, MO, USA) in HeBS. The bead solution was injected into the protein mixture and incubated at 4 °C overnight to allow the covalent attachment of the SpyCatchers' unique cysteines to the maleimide residues on the pedestal bead. The beads were then washed three times with 1 ml of HeBS and resuspended to a volume of 100 µl in HeBS. Any unreacted maleimide was quenched by addition of 100 µl of 1 M L-cysteine (11033-016, Gibco BRL, Gaithersburg, MD, USA) in HeBS and incubation for 1 hr. Finally, the beads were washed three times and stored at 4° C in HeBS with 0.02 % sodium azide (71289, Sigma-Aldrich, St. Louis, MO, USA).

Covalent attachment of pedestal beads

We covalently attached pedestal beads through the surface amine groups of their SpyCatcher molecules to COOH-modified glass coverslips through carbodiimide crosslinking. Glass coverslips (12-545-81, Thermo Fisher Scientific, Waltham, MA, USA) were cleaned by sonication in ethanol for 15 min. After drying under a stream of oxygen, the coverslips were transferred to a solution of 1.5 g Nochromix (Godax Laboratories, Cabin John, MD, USA) in 60 ml sulfuric acid (A300S-500, Thermo Fisher Scientific, Waltham, MA, USA) and incubated for 3 hr. We then washed the coverslips three times with deionized water followed by three washes with ethanol. During each wash the coverslips were sonicated for five minutes in a bath sonicator. The slides were dried under a stream of oxygen gas and oxidized for 30 min in an ultraviolet ozone cleaner (PC440, Bioforce Nanosciences, Salt Lake City, UT, USA). In this step oxidation occurred on only one side of the coverslips, the "functional" side, which was used in all the subsequent steps.

We vapor-deposited an aminosilane layer onto the oxidized glass surfaces by placing the coverslips into a gas-tight glass container together with—but not submerged in—100 µl of

(3-aminopropyl)trimethoxysilane (281778, Sigma Aldrich, Inc, St Louis, MO, USA) dissolved in 10 ml of toluene (T324-1, Thermo Fisher Scientific, Waltham, MA, USA)[6]. The container was incubated overnight at 80 °C. Following the vapor deposition, the coverslips were washed three times in ethanol, dried, and placed into a solution of 50 mg succinic anhydride (S7626, Sigma Aldrich, St Louis, MO, USA) dissolved in 1 ml dimethyl sulfoxide (D4540, Sigma Aldrich, St Louis, MO, USA) and left to incubate at room temperature for at least 3 hr. This step converted the vapor-deposited amine groups into carboxyl groups and rendered the surface suitable for coupling. The carboxylated slides were then rinsed three times with ethanol and either used immediately or stored in ethanol for up to 72 hr.

Assembly of samples

To assemble a sample, a carboxylated coverslip was dried and secured with vacuum grease onto a metal washer, so that its functional side contacted the washer (*SI Appendix,* Fig. S8). (1-ethyl-3-(3-dimethylaminopropyl)carbodiimide and *N*-hydroxysulfosuccinimide (respectively 77149 and 24510, Thermo Fisher Scientific, Waltham, MA, USA) were equilibrated to room temperature before 10 mg of each reagent was dissolved in 1 ml of activation-buffer solution containing 10 mM NaCl and 1 mM 2-(*N*-morpholino)ethanesulfonic acid (M3671, Sigma Aldrich, St Louis, MO, USA) at pH 6. Of the resulting solution, 50 µl was pipetted onto the functional surface of the mounted slide and left to incubate at room temperature for exactly 30 min to activate the slides with amine-reactive hydroxysulfosuccinimide esters. To remove any excess reagents, we carefully washed the activated slide by pipetting 2 ml of Hepes-buffered saline solution with Ca^{2+} (HeBS-Ca, 20 mM Hepes, 100 mM NaCl, 1 mM $CaCl_2$) onto the mounted coverslip. Immediately after removing the solution except for a thin film to keep the active surface from drying, we pipetted pedestal beads in HeBS-Ca onto the activated surface and allowed to react for 2 hr. Mounting a second coverslip on the top of the washer closed the sample chamber. Access ports in the washer allowed the exchange of solutions within the chamber. To reduce non-specific interactions of PCDH15 with the beads, we exchanged the fluid to blocking-buffer solution containing 10 mg/ml sulfhydryl-blocked bovine serum albumin (100-10SB, Lee Biosolutions, Inc., Maryland Heights, MO, USA), 150 mM NaCl, 20 mM Tris-HCl, and 3 mM $CaCl_2$ at pH 8. The sample was stored overnight at 4 ˚C before addition of the PCDH15 molecules.

Sample preparation

PCDH15 monomers were diluted into blocking-buffer solution and flushed into a sample chamber. The molecules were sufficiently dilute to ensure that any tether was likely with an average probability exceeding 90 % to represent a single molecule of PCDH15, rather than two or more at once *(SI Appendix,* Table S1). We incubated the sample for 1 hr at room temperature to allow the carboxy termini of the PCDH15 molecules, each fused to a SpyTag, to covalently bind to the SpyCatcher proteins on the surface of the pedestal beads. The biotinylated amino termini were then directed radially outward from the pedestal beads and thus available for coupling to streptavidin-coated probe beads. The sample was subsequently washed with copious amounts of blocking-buffer solution to remove any unbound PCDH15 monomers.

The blocking buffer was replaced with sample-buffer solution consisting of 20 mM Tris-HCl pH 7.5, 150 mM NaCl, and 10 mg/ml sulfhydryl-blocked bovine serum albumin (100-10SB, Lee Biosolutions, Inc., Maryland Heights, MO, USA). The solution contained probe beads (CP01004, Bangs Laboratories, Fishers, IN, USA); depending on the experiment, it included 3 mM $CaCl_2$, 20 µM $CaCl_2$, or 1 mM EDTA. To protect PCDH15 from photodamage, we employed an oxygen-scavenging system consisting of 18 mM D-glucose (G-5400, Sigma-Aldrich, St. Louis, MO, USA), 13 U/ml pyranose oxidase (P4234, Sigma Aldrich, St Louis, MO, USA), and 8500 U/ml catalase (219261, Millipore Sigma, Burlington, MA, USA)[7,8].

Calibration of Ca^{2+} concentration

We used a fluorescence assay to confirm that the binding of Ca^{2+} to BSA does not significantly alter the concentration of free Ca^{2+} in sample-buffer solution (*SI Appendix,* Fig. S9A). Using 3 µM of the fluorescent calcium indicator Fluo-5N (F14203, ThermoFisher Scientific, Waltham, MA, USA), we tested the fluorescence of the solution with and without 10 mg/ml BSA at various total

Ca^{2+} concentrations. Our data show that BSA at this concentration does not noticeably change the concentration of free Ca^{2+}, whereas a very high BSA concentration, 100 mg/ml, sequesters a significant amount of Ca^{2+} (*SI Appendix,* Fig. S9B).

High-bandwidth and high-precision optical trapping and tracking

All data were acquired using a custom-built photonic-force microscope[9], which in this instance was upright rather than inverted. The microscope could track the three-dimensional position of a weakly optically trapped, 1 µm-diameter probe bead with an integration time of 1 µs, sampled at a frequency of 100 kHz, with sub-nanometer precision. In brief, the position-sensing 1064 nm laser beam (Mephisto 500 mW, Coherent, CA, USA) was expanded and focused into the sample chamber through a high-numerical aperture water-immersion objective lens (UPlanSApo 60xW, Olympus, Tokyo, Japan). This beam formed a weak optical trap that confined the probe bead. We collected light forward-scattered by the probe bead together with the unscattered portion of the beam on a quadrant photodiode, where the two waves interfered. The signals of the four quadrants were related to the three-dimensional position of the bead in the optical trap[10]. The microscope's position error over one extension-relaxation cycle with a duration of 1 s was given by integrating the power-spectral density of position noise from 1 Hz to 1 MHz, corresponding to root-mean-squared values of 0.6 nm, 0.3 nm, and 0.4 nm along the x-, y-, and z-axes respectively[11,12]. Experiments were performed with the protein tether oriented along the y-axis, that with highest precision. Typical spring constants of the weak position-sensing trap were 6 $\mu N \cdot m^{-1}$, 7.5 $\mu N \cdot m^{-1}$, and 2 $\mu N \cdot m^{-1}$ along the x-, y-, and z-axes respectively. At very high stimulus forces of tens of piconewtons the probe bead was at its maximum extension of about 150 nm along the y-axis from the center of the position-sensing optical trap, corresponding to a maximum force generated by this trap of 1.1 pN. For lower stimulus forces and smaller extensions, the force was considerably less than 1 pN. Because the force generated by the position-sensing optical trap was very small compared to the stimulus force, we disregarded it in our analysis.

To record hundreds of cycles, we required observation times greater than a few seconds and therefore had to compensate the microscope's slight mechanical drift. The position of the sample relative to the optical traps was controlled by a nano-positioning stage (Nano-View/M375HS, Mad City Labs, WI, USA), whose position we adjusted to compensate for the drift (see below). With drift compensation in effect, the root-mean-square deviation measured along the y-axis between DC and 1 MHz during 5 min of observation was 2 nm.

In addition to the previously described position-sensing weak optical trap, we added a second optical trap to the system to apply force stimuli to the tethered proteins. We chose a wavelength of 852 nm (DL852-500, Crystalaser, Reno, NV, USA), which is near a local minimum of the action spectrum of photodamage to biological material[13]. Using a beam-steering lens mounted on a three-dimensional piezoelectric-block translator (P.282.30, Physik Instrumente, Auburn, MA, USA), we could shift the position of the stimulus trap with respect to the position-sensing trap with nanometer precision. Over 18 min of observation time, the average drift of the two optical traps relative to each other was 3 $\mathrm{pm \cdot s^{-1}}$. The 852 nm laser beam traversed an electro-optical modulator (LM13, Excelitas Technologies, Fremont, CA, USA) placed between crossed polarizing beam-splitting cubes, which allowed us to modulate the intensity and thus the stiffness of the stimulus trap.

Drift compensation

Although we designed the microscope's frame to minimize thermal drifts of the sample chamber with respect to the optical traps, a small drift of about 250 $\mathrm{pm \cdot s^{-1}}$ remained[9]. To eliminate this drift, we implemented an active-feedback mechanism by using as a fiducial marker a second pedestal bead situated tens of micrometers from the pedestal to which a single molecule was tethered. The motion of the pedestal bead reflects the drift of the sample chamber with respect to the microscope frame. A camera (pco.edge 5.5, PCO, Kelheim, Germany) tracked the three-dimensional position of this pedestal bead at a frequency of 5 Hz. The pedestal's position signal was then used as the input of a proportional-integral-differential feedback loop that adjusted the position of the nano-positioning stage to compensate for the sample's drift. To test the fidelity of this method, we immobilized a probe bead on a sample chamber's coverslip, positioned it at the focus of the position-sensing optical trap, and used the microscope to determine its position while drift compensation was active. We found that linear drifts were eliminated and that the root-mean-square variation of the position signal along the y-axis of 2 nm over 5 min remained.

Calibration, linearization, and correction of the probe-position signal

The three-dimensional detector's non-linear response was linearized and calibrated *in situ* for each individual probe bead[14]. The calibration depended upon the viscosity of the buffer solution, which we corrected for the presence of 10 mg/ml bovine serum albumin as described[15].

The probe bead forward-scattered a portion of the position-sensing laser beam, and we detected the bead's three-dimensional position by monitoring the interference pattern of the beam's scattered and unscattered light wave on a quadrant photodiode[10]. Scattering of a small amount of the beam by the pedestal bead produced an artifact in the signal[9] that was eliminated by the subtraction of a reference signal.

Calibration and correction of the stimulus trap

Before each single-molecule experiment and for each individual probe bead, we measured the relation between the intensity of the stimulus laser and the stiffness of the stimulus trap. While monitoring the Brownian motion of the trapped probe bead with the position-sensing optical trap, we increased the power of the stimulus beam in 10 % increments. Fitting of the position signal's power spectral density for each intensity with a hydrodynamically correct theory[16] yielded the stiffness as a linear function of intensity. During our experiments, we sampled the intensity of the stimulus laser—and hence the trap's stiffness—with the same sampling rate as the position signal of the probe bead.

We adjusted the intensity of the stimulus laser using an electro-optical modulator. At high attenuation, close to extinction, the beam profile at the exit of the modulator deviated from a Gaussian function, which laterally shifted the position of the stimulus trap within the sample chamber by a few nanometers. We recorded this shift during the calibration procedure for each probe bead and accounted for it when calculating the laser intensity-dependent force on the probe bead.

Initiation of single-molecule experiments

To initiate a single-molecule experiment, we optically trapped a probe bead deep in solution and calibrated the position sensor and the stiffnesses of both optical traps. We next positioned the bead's center at a height of 1 µm from the functionalized coverslip, with its mean axial position at the equator of the attached pedestal beads. This height was determined by slowly moving the coverslip towards the optical trap until the probe bead's axial thermal motion began to be confined by the coverslip, then retracting the coverslip by an appropriate distance[11].

The sample was moved laterally so that the probe bead was aligned along the y-axis with a pedestal bead. After recording a reference signal to account for light scattered by the pedestal we gently maneuvered the pedestal bead towards the optical trap until the probe's Brownian motion along the y-axis began to be restricted by the pedestal. When a PCDH15 molecule was present on the surface of the pedestal bead and within reach of the Brownian motion of the probe bead, a single molecule tether formed between the amino terminal biotin on the protein and a streptavidin molecule on the probe bead. The concentration of PCDH15 was adjusted so that an average of only 17 % of such approaches resulted in tether formation, on average giving rise to a 90 % confidence of single-molecule conditions[17] (*SI Appendix,* Table S1). The position of the stimulus trap was then displaced by 200 nm along the y-axis. Before the force was lowered to the holding level, a brief increase in the intensity of the stimulus beam provided a force pulse of several tens of piconewtons to the tethered protein. This operation ensured that no portion of the protein was nonspecifically attached to either of the confining surfaces and that the full contour of the protein linked the two beads at the beginning of the extension-relaxation cycles. Force ramps were then applied to the tethered protein by repeatedly increasing and decreasing the intensity of the stimulus trap (*SI Appendix,* Fig. S1).

Control of non-specific attachments

For a successful single-molecule experiment it is imperative that the overwhelming majority of tethers between pedestal and probe beads constitutes PCDH15 molecules anchored at their amino and carboxy termini by respectively biotin and SpyTag: only a very small number of non-specific tethers should occur.

We tested whether streptavidin-coated probe beads would tether to SpyCatcher molecules on pedestal beads in the absence of PCDH15. Out of 65 attempts of initiating such non-specific tethering with two samples and four probe beads, only one bond formed, which ripped off immediately upon application of a stimulus force. We concluded that all stable tethers that we observed in our single-molecule experiments resulted from PCDH15 molecules or, in the case of control experiments to test the assay's mechanics, from linker-peptide constructs.

To exclude any non-specific interactions between PCDH15 and either of the beads, we next confirmed that these PCDH15 tethers formed only if both the SpyTag-SpyCatcher and biotin-streptavidin interactions were present. Pedestal beads were coupled to a coverslip and incubated with 0.15 mg/ml PCDH15 in blocking-buffer solution for 1 hr at room temperature to allow the proteins to react with the pedestals. The coverslip was then washed with copious amounts of blocking-buffer solution to remove any free PCDH15 molecules before the addition of a high concentration of probe beads in blocking-buffer solution. The probe beads were allowed to bind to the PCDH15 molecules on the pedestal beads for 1 hr before the coverslip was washed once more and then imaged.

As a positive control, with both sets of anchors intact, we found an average of 3.25 probe beads bound to each pedestal bead for the given reaction conditions (*SI Appendix,* Table S2). To test whether the carboxy-terminal SpyCatcher-SpyTag anchor participated in the tether, we generated pedestal beads without SpyCatcher and attempted to attach probe beads to them through PCDH15 molecules using the procedure described above. We found that tethering of probe beads was completely abolished in the absence of SpyCatcher, confirming that the

SpyCatcher-SpyTag interaction was an essential part of the formed tethers (*SI Appendix,* Table S2).

To determine whether the amino termini of our tethers were anchored to the probe beads through the biotin-streptavidin interaction, we attempted to tether probe beads to SpyCatcher-positive pedestals through PCDH15 molecules that had not been biotinylated. We again found that tether formation was completely abolished, confirming that the amino-terminal confinement in our single-molecule experiments occurred through the biotin-streptavidin interaction (*SI Appendix,* Table S2).

We concluded that our single-molecule assay was highly specific: molecular tethers formed in the presence of an appropriately tagged construct. If either of the pairs of anchors was disrupted, tether formation was completely abolished.

Determination of the molecule’s anchor position

The anchor position of the protein tether along the axis of extension was an important parameter that had to be determined before our protein model could be fit to the data. We determined this anchor position by analyzing the three-dimensional probability distribution of the motion of the tethered probe bead in the absence of externally applied tension. The pedestal bead appeared as a forbidden volume in the spatial probability distribution of the tethered probe bead, a so-called three-dimensional thermal-noise image[9]. The intersection of the surface of the pedestal bead with the axis of extension was defined as the anchor position of the tether.

Sources of uncertainty

Our data are subject to several different sources of measurement uncertainty. In the following we refer to the variability within one single-molecule experiments as “precision," whereas we use “accuracy” to refer to the uncertainty between experiments.

The extension of a molecular tether could be measured with the same precision with which the photonic-force microscope could measure the position of the probe bead. To determine this value, we attached a probe bead to a glass coverslip, positioned it in the center of the position-sensing optical trap, and activated the microscope's drift compensation. Between 1 Hz and 1 MHz, the interferometric position signal of the immobilized probe had a band-limited standard deviation of 0.3 nm along the y-axis, the axis along which we extended single-molecule tethers (*SI Appendix,* Table S3). Over 5 min of observation, the standard deviation for the full bandwidth of DC to 1 MHz was 2 nm.

The accuracy of the position sensor depends on the fidelity of its calibration, which can be tested by its comparison to a calibrated standard. We confined a probe bead in the weak position-sensing optical trap, calibrated the position sensor, and then switched on the high-intensity stimulus trap. This trap was then displaced laterally with respect to the position-sensing trap so that the position sensor reported a displacement of 250 nm. We then compared this nominal displacement to that detected by a camera that acquired brightfield images of the focal plane. The camera had previously been calibrated to accord with well-defined displacements of the nano-positioning stage. Across twelve probe beads, the camera read out an average displacement of 250 ± 13 nm (mean ± SD), values that were in excellent agreement with the microscope's position sensor. We concluded that the bead-to-bead variability of the calibration was 5 % (*SI Appendix,* Table S3). Because the radius of the probe bead was the parameter with the greatest uncertainty during the calibration procedure, this value also set an upper bound of 5 % on the coefficient of variation of the diameter of our probe beads.

The pedestal bead scattered a small portion of the position sensing beam, which led to an offset of the position signal that was dependent on the pedestal's position. Although we corrected for this effect through a reference signal, there remained a position offset of ± 4 nm peak-to-peak or 3 nm root-mean-square. This problem contributed uncertainty to the measured displacement between the position-sensing trap and the stimulus trap and thus resulted in reduced accuracy (*SI Appendix,* Table S3). The total accuracy of a nominal distance of 200 nm between the position-sensing trap and stimulus trap was then 10 nm root-mean-square (*SI Appendix,* Table S3). During a single-molecule experiment, the precision of this distance was impacted by the slow relative drift between the two optical traps, which we measured as 3 pm·s^{-1} (*SI Appendix,* Table S3).

Because the spring constant of the stimulus trap depended linearly on the intensity of the stimulus beam, any variation in the beam's intensity decreased the precision of the spring constant. The spring constant's root-mean-square noise was 0.27 µN·m^{-1} over 20 s with a vanishingly small drift (*SI Appendix,* Table S3). We computed the spring constant from the power-spectral density of the motion of a probe bead as[16] $k = 2\pi\gamma f_c$. The error of the drag γ was determined by the uncertainty of the probe bead's radius (5 %) and exceeded the error of the corner frequency f_c. Depending on the radius of the probe bead, the spring constant of the stimulus trap was therefore accurate to within 5 % of the calibrated value (*SI Appendix,* Table S3).

We determined the force on the trapped probe bead as the product of its extension from the stimulus trap and the trap's stiffness. Consequently, the precision of the force could be determined from the probe's position noise, the drift of the stimulus trap, and the noise of the trap's spring constant. With the probe bead displaced by 200 nm from the stimulus trap and for maximal power of the stimulus laser, we determined a precision of 0.7 pN over 5 min of data acquisition (*SI Appendix,* Table S3). During an experiment the displacement of the probe and the power of the laser were usually smaller than those values, resulting in a smaller uncertainty. The accuracy of the force was determined by the total accuracy of the position of the stimulus trap and that of the spring constant. At maximal power of the stimulus laser and for a displacement of the probe bead from the stimulus trap of 200 nm, we found an experiment-to-experiment uncertainty of the force of 3.8 pN (*SI Appendix,* Table S3). For smaller displacements and lower laser powers this uncertainty was lower.

Polymer model

We modeled PCDH15 as a freely-jointed chain with $N = 11$ segments, each of length b, representing the eleven stiff cadherin domains[18]. The model included in series a worm-like chain[19,20] characterized by a persistence length lp_{peptide} and a contour length $lc_{\text{linkers,total}} = 10\, lc_{\text{linker}}$, which accounted for the ten flexible disordered linker regions between the stiff domains. Any enthalpic extensibility of the protein was described by a Hookean spring with stiffness k_{folded} (*SI Appendix,* Fig. S6). Elongation of the protein through the unfolding of each domain was described by the addition of another worm-like chain. Because unfolded polypeptide chains are structurally similar to the inter-domain linker regions, the unfolded portions of the protein were described with an identical persistence length and a contour length of lc_{unfolded}.

The extension-force relation of the protein was described by the sum of the extension-force relations of the freely-jointed chain and of the worm-like chains,

$$x_{\text{protein}}(F) = x_{\text{FJC}}(F, N, b, k_{\text{folded}}) + x_{\text{WLC}}\left(F, lp_{\text{peptide}}, lc_{\text{linkers,total}}, k = \infty\right) + x_{\text{WLC}}\left(F, lp_{\text{peptide}}, lc_{\text{unfolded}}\ , k = \infty\right) \tag{1}$$

in which the elastic properties of the two worm-like chains were purely entropic ($k = \infty$). The extension-force relation of an extensible freely-jointed chain is given by[18]

$$x_{\text{FJC}}(F, N, b, k\ ) = N\ b\ \left(\coth\left(\frac{F\ b}{k_B\ T}\right) - \frac{k_B\ T}{F\ b}\right) + \frac{F}{k}\ , \tag{2}$$

whereas the elongation of an extensible worm-like chain under force is well approximated by[20]

$$x_{\text{WLC}}(F, lp, lc, k) = lc\left(\frac{4}{3} - \frac{4}{3\sqrt{\frac{F\ lp}{k_B\ T}+1}} - \frac{10\exp\left(\left(\frac{900\ k_B\ T}{F\ lp}\right)^{\frac{1}{4}}\right)}{\sqrt{\frac{F\ lp}{k_B\ T}}\left(\exp\left(\left(\frac{900\ k_B\ T}{F\ lp}\right)^{\frac{1}{4}}\right)-1\right)^2} + \frac{\left(\frac{F\ lp}{k_B\ T}\right)^{1.62}}{3.55+3.8\left(\frac{F\ lp}{k_B\ T}\right)^{2.2}}\right) + \frac{F}{k}. \tag{3}$$

When a force was applied to a single-molecule tether, not only did the tether stretch, but so did the system's remaining elastic elements, the anchors and linkers in series with the tether (*SI Appendix,* Fig. S10). We demonstrated experimentally that the combined mechanics of the assay without PCDH15 could be described by an additional extensible worm-like chain (*SI Appendix,* Fig. S11), for which we found across nine experiments an average persistence length $lp_{\text{anchors}} = 0.5 \pm 0.1$ nm, contour length $lc_{\text{anchors}} = 37 \pm 4$ nm, and Hookean spring constant $k_{\text{anchors}} = 7.2 \pm 1.3$ mNm^{-1} (means ± SEMs).

The total polymer model that we fitted to our data was therefore given by

$$x_{\text{polymer}}\left(F, N, b, k_{\text{folded}}, lp_{\text{peptide}}, lc_{\text{linkers,total}}, lc_{\text{unfolded}}, lp_{\text{anchors}}, lc_{\text{anchors}}, k_{\text{anchors}}\right)$$
$$= x_{\text{protein}}\left(F, N, b, k_{\text{folded}}, lp_{\text{peptide}}, lc_{\text{linkers,total}}, lc_{\text{unfolded}}\right) +$$
$$x_{\text{WLC}}(F, lp_{\text{anchors}}, lc_{\text{anchors}}, k_{\text{anchors}}) \quad (4)$$

Determination of the stiffness of PCDH15 and influence of molecular anchors and beads on the measured stiffness

Our force-extension relations capture the mechanics of PCDH15 in series with its molecular anchors and with any compliance of the probe and pedestal beads (*SI Appendix,* Fig. S10). To determine the contribution of these elements to our measurements, we conducted experiments without PCDH15 by fusing the amino- and carboxy-terminal anchors and testing their elastic properties in series with the pedestal and probe beads (*SI Appendix,* Fig. S11). PCDH15's stiffness could then be determined by treating the whole system as a series of nonlinear springs,

$$k_{PCDH15}(F) = \frac{k_{total}(F) \cdot k_{anchors}(F)}{k_{anchors}(F) - k_{total}(F)} \quad (5)$$

For Ca^{2+} concentrations of 3 mM and 20 µM, we computed the stiffness of the full-length construct—the protein in series with its anchors and the beads—as the spatial derivative of the mean of the force-extension relations associated with its different conformational states (*SI Appendix,* Fig. S12). Computed in an analogous way (*SI Appendix,* Fig. S11D), the stiffness of the construct without PCDH15 was much larger (*SI Appendix,* Fig. S12C,D). From the values of State 1 we computed the stiffness of folded PCDH15 and found that it is surprisingly soft under physiological tensions, offering a stiffness between 0.5 $mN \cdot m^{-1}$ at a tension of 5 pN and 6 $mN \cdot m^{-1}$ at 50 pN (Figure 3a,b).

Detection of structural changes and fitting of data

The position and force signals (Fig S1b,c), sampled at 100 kHz, were split into individual extension-relaxation cycles and smoothed with a second order Savitzky-Golay filter over a window of 101 points, which reduced the temporal resolution to 1 ms. Conformational changes of the protein were automatically detected as sudden increases or decreases in the filtered probe-position signal. To determine whether a structural change occurred at point *i* of the time trace, we computed the averages and standard deviations of 1000 points preceding and succeeding *i*, $\langle x\rangle_{\text{left}}$, $\langle x\rangle_{\text{right}}$, σ_{left}, and σ_{right}. A structural change was detected at point *i* if

$$\left|\langle x\rangle_{\text{left}} - \langle x\rangle_{\text{right}}\right| > 4\ \frac{\sigma_{\text{left}}+\sigma_{\text{right}}}{2}. \tag{6}$$

Structural changes that did not fulfill this criterion were missed by our algorithm. If two or more structural changes occurred within 10 ms of one another, our algorithm detected only one larger event.

We then segmented each extension-relaxation cycle into its individual states, demarcated by the structural changes, and fit our polymer model to each of the segments. To facilitate meaningful fits, we sought to constrain the number of free parameters in our polymer model (Equation 4) as much as possible. We first independently measured the parameter values of the worm-like chain describing the compliance of the anchors and of the rest of the assay without PCDH15 (Figs. S10 and S11), for which we found an average persistence length $lp_{\text{anchors}} = 0.5 \pm 0.1$ nm, contour length $lc_{\text{anchors}} = 37 \pm 4$ nm, and Hookean spring constant $k_{\text{anchors}} = 7.2 \pm 1.3\ \text{mNm}^{-1}$ (means ± SEMs of nine experiments). We held these values constant at their means for all subsequent fits of extension-relaxation cycles of PCDH15.

In a next step it was important to determine lp_{peptide}, the persistence length of PCDH15's unfolded polypeptide chains, for this value entangles the mechanics of State 1 (through the linker regions of the folded protein) with the mechanics of partially unfolded PCDH15. To facilitate this determination, we temporarily approximated State 1 of the protein as a worm-like chain; we then held the parameter values of State 1's worm-like chain model constant while fitting all extension-relaxation cycles with only lp_{peptide} and lc_{unfolded} as free parameters, determining $lp_{\text{peptide}} = 0.49 \pm 0.04$ (mean ± SEM, $N = 13$). Because there was no apparent difference in peptide persistence length between the results for Ca^{2+} concentrations of 3 mM and 20 µM, data were averaged across 13 experiments at both concentrations. This value of lp_{peptide} was held constant at its mean for all subsequent fits.

We then fitted State 1 with our protein model to determine the remaining free parameters of the folded protein, lc_{linker}, b, and k_{folded} (Table 1). Finally, we fitted all segments of all extension-relaxation cycles with the polymer model, with lc_{linker}, b, and k_{folded} held constant at the values determined for the individual proteins, with lc_{unfolded} as the only free parameter. The changes of lc_{unfolded} between adjacent segments then described the end-to-end elongation of the tether due to unfolding events (Fig. 2).

Statistical dependence of events A_U and B_U

In order to test whether the order of occurrence of events A_U and B_U is statistically significant, we simulated extension trials with independent probability densities for the two events such that the resulting force distributions for each of the classes of rips was identical to our experiments. We then showed that the sequence of events in these simulations did not match our experimental observations, proving that the probability densities underlying our experiments are statistically dependent.

For every simulated trial, we first drew two random numbers to determine whether both rips would occur during the extension. The probabilities p_A and p_B for respective events A_U and B_U were determined separately from the experimental data for each PCDH15 molecule. For traces that contained both rips, a parameter representing the pulling force was then linearly increased from 0 pN to 80 pN in steps dF = 0.1 pN. After each force increment we allowed rips A_U and B_U to occur with independent probabilities $\rho_A(F)\,dF$ and $\rho_B(F)dF$, in which $\rho_{A,B}$ represent probability densities. Because each class of rips represents a unique structural change, once a rip of either type had occurred no further event of that class could follow. The simulated record was discarded if neither or only one of the rips occurred over the simulated force range. The probability densities $\rho_{A,B}(F)$ were independently determined for each protein and could be calculated from the experimentally observed force histograms of rips $N_{A,B}(F)$:

$$N_{A,B}(F) = \rho_{A,B}(F)\,dF \cdot \left(1 - \int_0^F \rho_{A,B}(F')\,dF'\right) \cdot N \cdot p_{A,B} \qquad (7)$$

in which $\rho_{A,B}(F)\,dF$ is the probability of finding rip A_U (or B_U) at force F and $N \cdot p_{A,B}$ is the number of extension trials that contain rip A_U (or B_U). The factor in parentheses is the probability that at force F during an extension a rip has not yet occurred at forces lower than F. This factor accounts for the fact that we draw from $\rho_{A,B}(F)$ for linearly increasing *F*, and stop drawing from the distribution when a rip occurs. We accordingly can draw from $\rho_{A,B}(F)$ only if no other rip occurred at a lower force. It follows that

$$\rho_{A,B}(F) = \rho_{0\ A,B}(F) + \ \rho_{A,B}(F) \int_0^F \rho_{A,B}(F')\, dF' \qquad (8)$$

in which $\rho_{0\ A,B}(F) = \frac{N_{A,B}(F)}{N \cdot p_{A,B} \cdot dF}$ are the normalized force histograms of the experimentally observed rips. We numerically solved this relation to determine $\rho_{A,B}(F)$ (*SI Appendix,* Fig. S13A,C).

Our simulations successfully reproduced the experimentally observed force histograms of the rips A_U and B_U (*SI Appendix,* Fig. S13B,D). We then enumerated the trials in which rip A_U occurred before rip B_U. For the molecule shown in the left column of Figure 2, our simulations—based on the independent probability distributions $\rho_A(F)$ and $\rho_B(F)$—predicted that we should have observed 20.4 extensions in which A_U preceded B_U, a contradiction to the observed value of 8 ($p < 0.05$). Because the counts were assumed to be Poisson distributed, we made statistical comparisons by computing the Wald test statistic $Z = \frac{N_o - N_p}{\sqrt{N_o + N_p}}$, in which N_o are the observed counts and N_p are the predicted counts, followed by a two-tailed comparison of *Z* to a normal distribution to compute the *p*-value. We therefore reject the assumption that A_U and B_U are independent. An identical conclusion was reached for all five proteins tested at a Ca^{2+} concentration of 3 mM, although two were significant only at $p < 0.1$. When we tested proteins at 20 µM [Ca^{2+}] in the same manner, we again routinely observed fewer trials in which rip A_U occurred before rip B_U than predicted by our simulations. At this physiological Ca^{2+} concentration, however, the difference between the observed and expected number of sequences AB was no longer statistically significant at $p < 0.1$.

Transformation of force histograms into force-dependent rate constants

We transformed the measured distribution of rip forces of type C_U into force-dependent unfolding rate constants[21]. PCDH15 consists of 11 domains that we approximated as equivalent for this analysis. In this approximation, they are each assumed to be equally likely to unfold under force. Hence, a fully folded PCDH15 molecule is eleven times more likely to unfold a domain than a PCDH15 molecule with only one folded domain. To arrive at correct values for the unfolding rates of individual cadherin domains, we therefore computed individual force histograms of C_U events originating from each of the states of the protein. We then weighted the measured force histograms with the number of folded cadherin domains in each state: for example, the force histogram for domain unfolding from States 1 and 2, which both correspond to PCDH15 with eleven (at least partially) folded cadherin domains, was divided by $n = 11$ domains. The weighted force histograms were then combined and the remaining analysis performed[21]. Our weighting of the force histograms is similar to the weighting that has been employed in pseudo dwell time analysis for the determination of un- and refolding rates in chains of identical titin domains[22]**.**

SI Figures and Legends

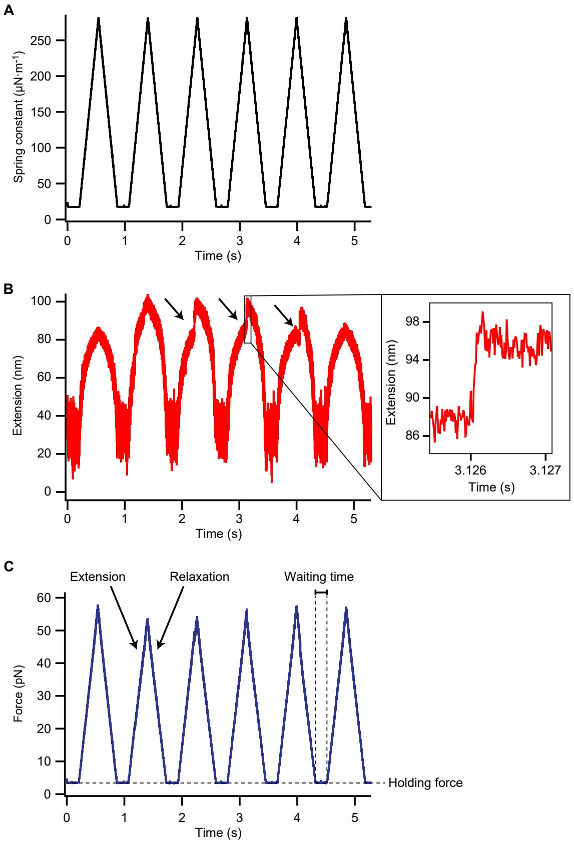

Figure S1. Time traces of extension-relaxation cycles. (*A*) The force on a PCDH15 tether was varied by adjustment of the spring constant of the stimulus trap, which was centered about two hundred nanometers from the equilibrium position of the probe bead. (*B*) The tether's extension included occasional abrupt events (arrows). Note the extensive noise owing to thermal excitation of the molecule. (*C*) The force acting on the tethered protein was computed from the probe bead's position and the spring constant of the stimulus trap. Each protein underwent hundreds of extension-relaxation cycles, between which the force was held constant for a particular waiting time so that any unfolded domains could refold. The Ca^{2+} concentration was 3 mM.

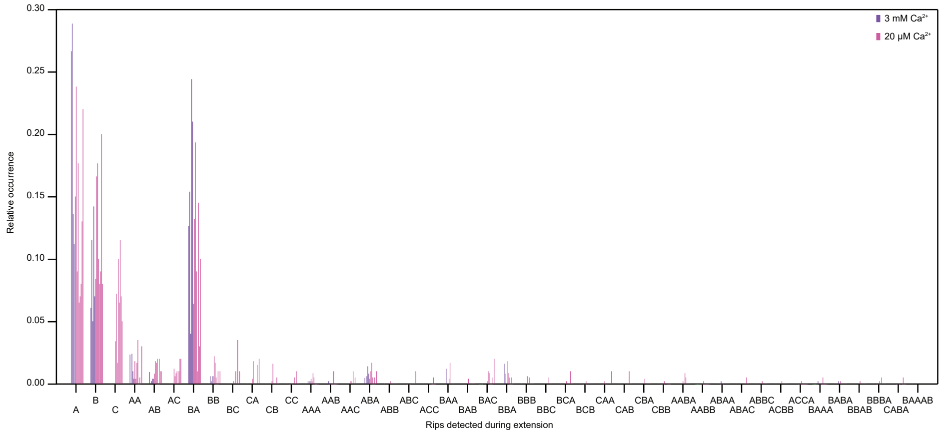

Figure S2. Sequences of structural changes during extension trials. The histogram indicates the fraction of extension traces that contained a specific sequence of unfolding events. For each possible sequence of events, each bar in a cluster represents a single molecule. Each molecule was extended at a loading rate of 130 pN·s^{-1}. Depending on the protein, the holding force between cycles was 2-4 pN and the waiting time was 0.2-2 s. This inconsistency altered the extent to which a particular molecule refolded between cycles and added variability to the results.

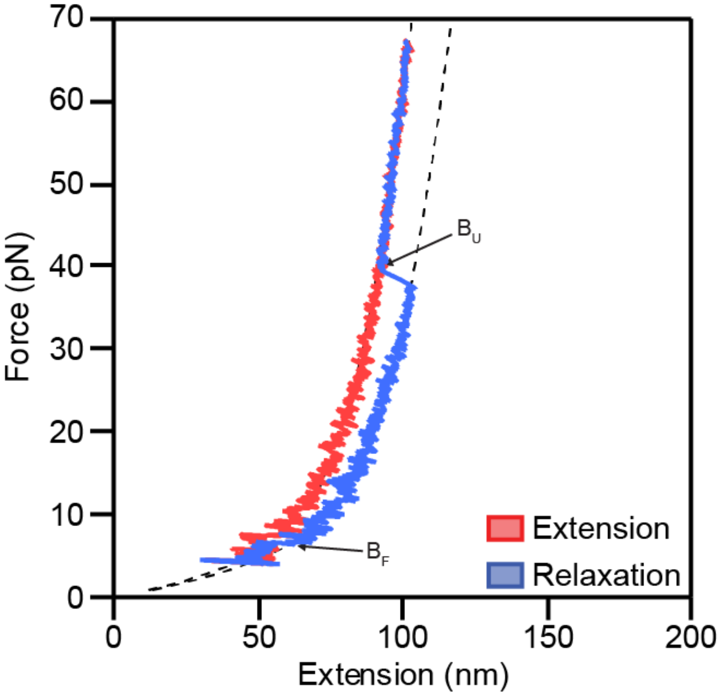

Figure S3. Refolding events of type B_F at very low forces. During most extension-relaxation cycles refolding events of type B_F occurred at forces so low that the corresponding shortening in end-to-end distance was lost in Brownian noise. Our algorithm could directly detect these events only in some rare cases (blue trace, arrow B_F). The Ca^{2+} concentration was 20 µM.

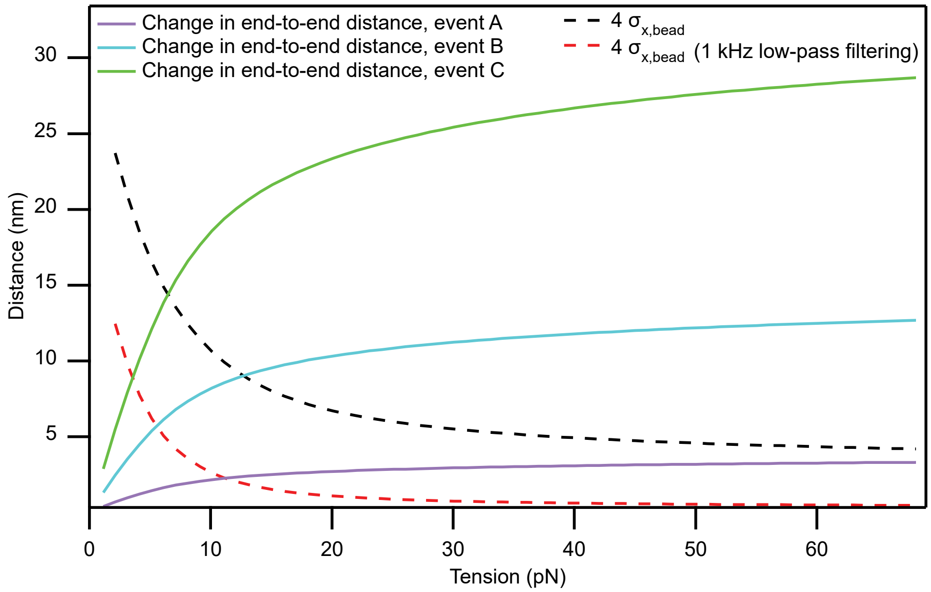

Figure S4. Effect of thermal noise on detectability of conformational changes. When a molecular tether is subjected to a low tension, unfolding or refolding of a domain results in a change in the end-to-end distance much smaller than the actual change in contour length. The expected changes (solid lines) are shown for events of types A, B, and C. If these changes are comparable to the thermal motion of the bead, they cannot be reliably detected by our method. We can confidently identify a folding event if the change in end-to-end distance is larger than four times the standard deviation of the thermal motion (black dashed line, 1 MHz bandwidth; dashed red line, signal low-pass filtered to 1 kHz). The intersection of the dashed and solid lines therefore defines the force below which a given structural change can no longer be reliably resolved for a particular temporal resolution. The band-limited thermal noise in the probe bead's position was computed as the integral of the power-spectral density of the bead's motion[16,12].

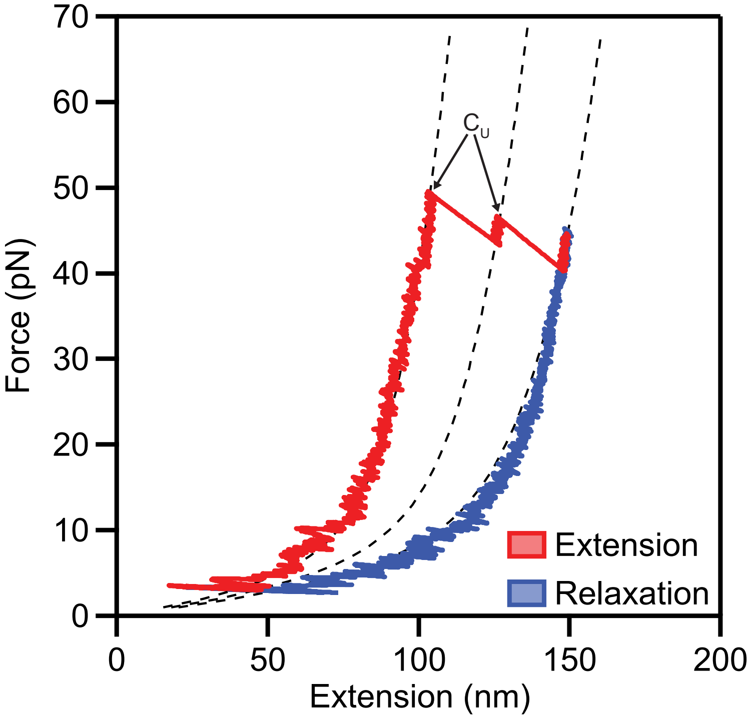

Figure S5. Unfolding of several cadherin domains during one extension-relaxation cycle. In some extension-relaxation cycles of the protein from Fig. 2B, two cadherin domains unfolded during the extension (arrows). The Ca^{2+} concentration was 20 μM.

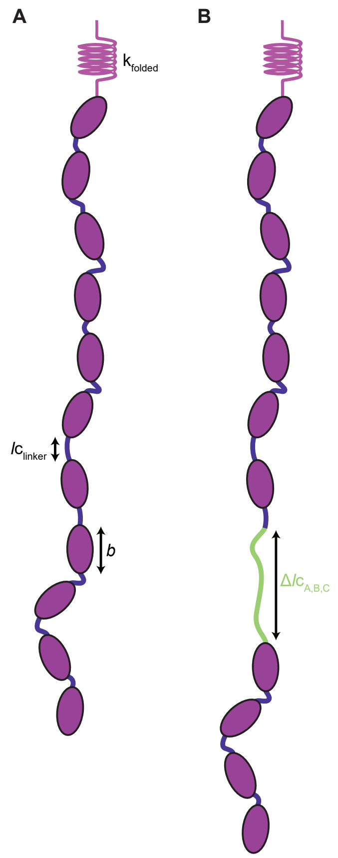

Figure S6. Protein model for PCDH15 under tension. (*A*) We modeled a folded monomer as a freely jointed chain of eleven stiff segments, each with length *b*. The linker regions between stiff segments consist of unstructured peptides of length lc_{linker}, whose combined effect was modeled as a worm-like chain with a contour length of $10 \cdot lc_{\text{linker}}$ and persistence length $lp = 0.49$ nm in series with the freely-jointed chain. A Hookean spring with stiffness k_{folded} represents the enthalpic extensibility of the protein. (*B*) Each unfolding event was represented as an additional worm-like chain (green), of the appropriate contour length and of persistence length 0.49 nm, in series with the folded protein.

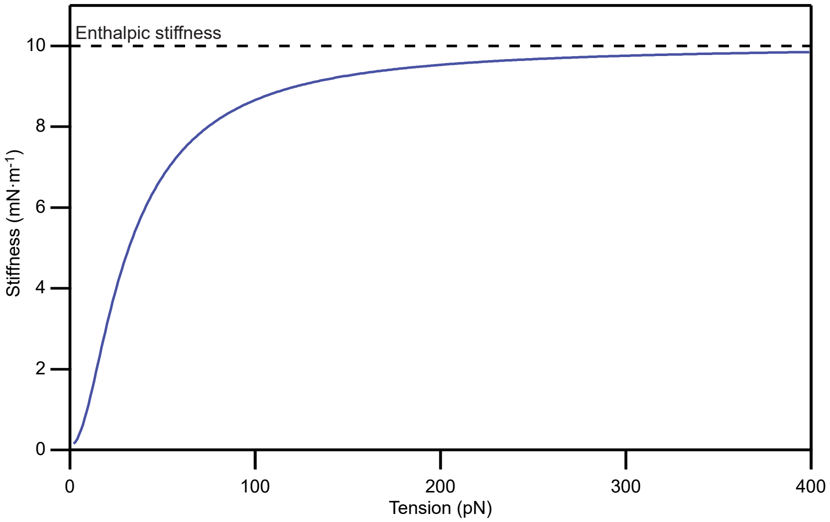

Figure S7. Predicted stiffness of PCDH15 at unphysiologically high forces. Our model predicts that monomeric PCDH15 reaches its enthalpic stiffness only for tensions exceeding hundreds of piconewtons. The physiological range of tensions, 4 pN to 25 pN per molecule, is dominated by the protein’s entropic elasticity.

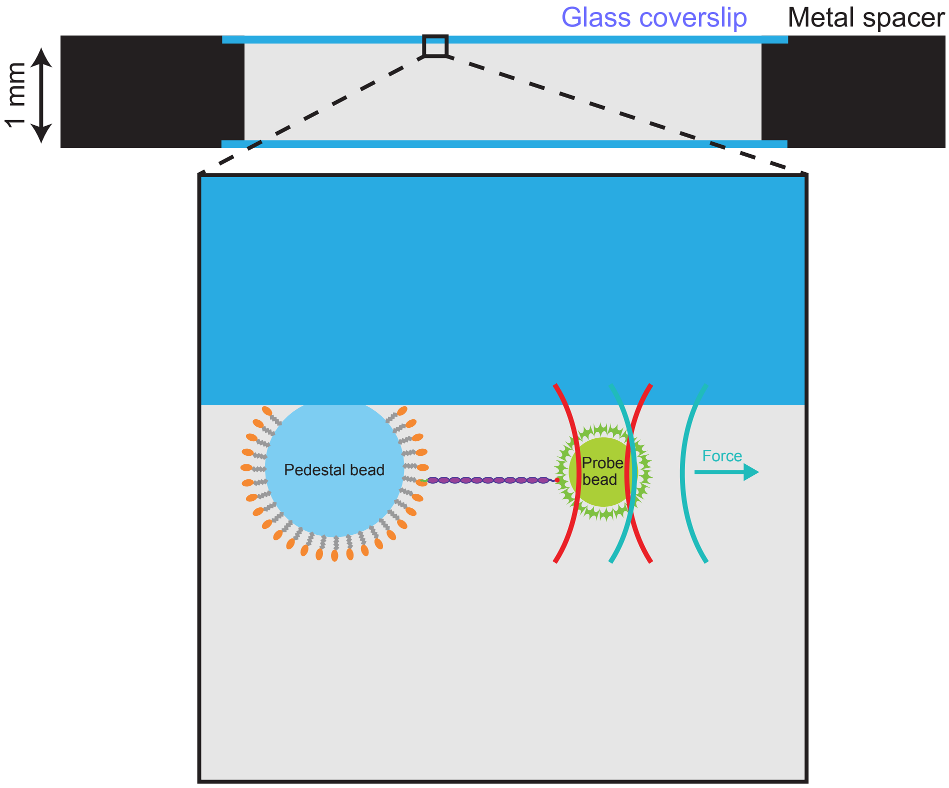

Figure S8. Design of the sample chamber. The sample chamber consisted of two glass coverslips attached by vacuum grease to a metal spacer. The sparsely distributed pedestal beads were covalently attached to the functional surface of the upper coverslip, and the chamber was filled with buffer solution containing freely diffusing probe beads. Note that the photonic-force microscope was of upright design, with the objective lens positioned above the sample chamber.

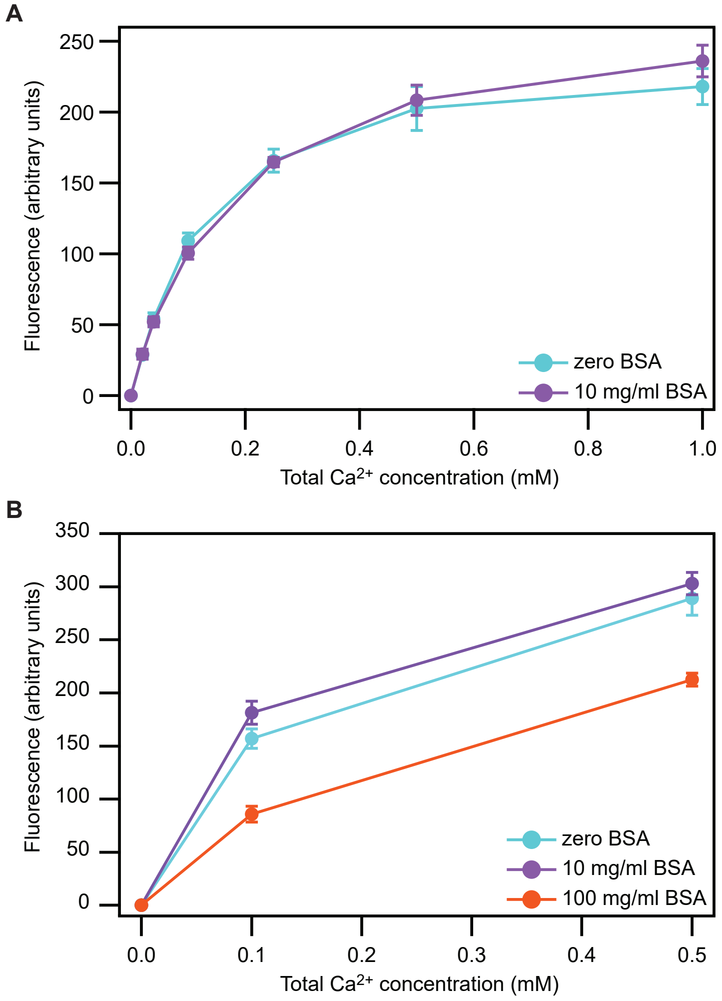

Figure S9. Lack of effect of bovine serum albumin (BSA) on the concentration of free Ca^{2+} ions. (*A*) The fluorescence of the Ca^{2+} indicator Fluo-5N (F14203, ThermoFisher Scientific, Waltham, MA, USA) is unchanged in the presence of 10 mg/ml BSA. (*B*) The concentration of free Ca^{2+} is diminished only by the presence of a BSA concentration as great as 100 mg/ml. Data are plotted as means ± SDs for three experiments.

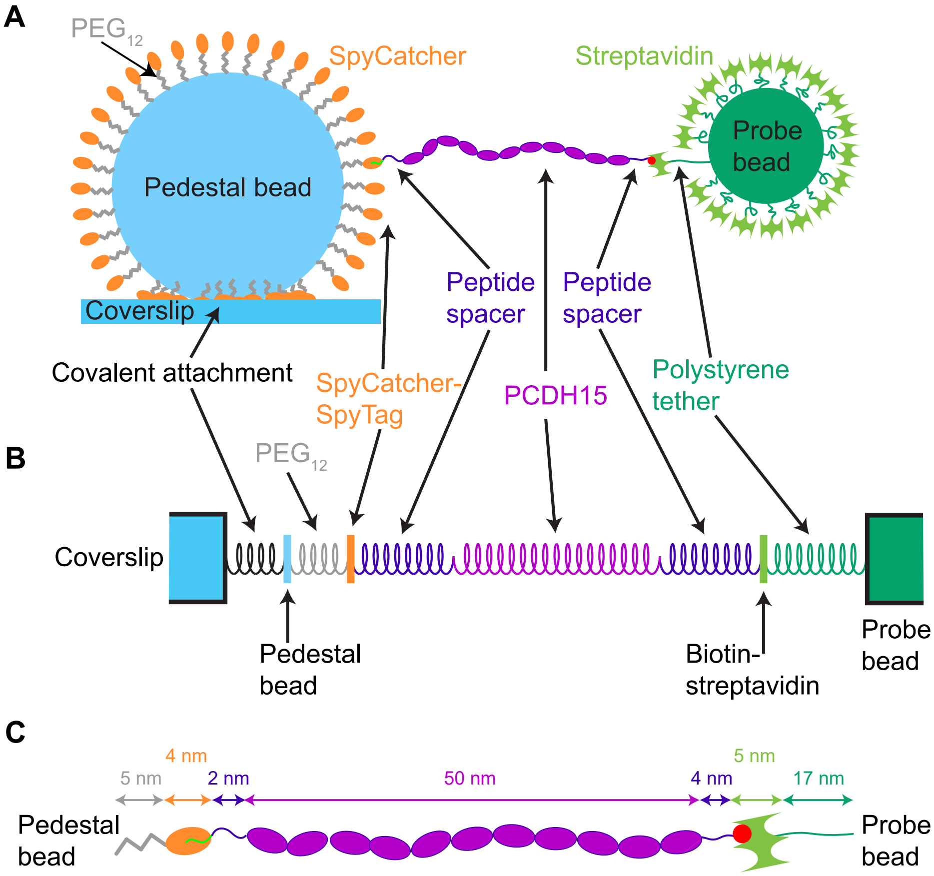

Figure S10. Compliant elements in the single-molecule assay. (*A*) To test the stiffness of PCDH15, we confined an individual monomer between a pedestal and a probe bead. Because each element of the single-molecule assay is compliant, however, the stiffness of the rest of the system—without the PCDH15—must be known in order to accurately determine the protein's stiffness. The components are not drawn to scale. (*B*) The assay's compliant elements include the covalent anchoring of the glass pedestal bead to the coverslip, the linkage between the pedestal bead and carboxy-terminus of the protein (polyethylene glycol [PEG], SpyCatcher, SpyTag, and peptide), and the connection between the protein's amino-terminus and the probe bead (peptide, biotin, and streptavidin). The latter linkage might also include a short polystyrene tether that extends from the probe bead's surface. (*C*) We designed the assay to contain anchor and linker elements that were as short and stiff as possible. Their approximate contour lengths are indicated. The size of the SpyCatcher, PCDH15, and streptavidin proteins were estimated from their crystal structures (PDB IDs 4MLI, 6CV7, and 1AVD). The lengths of the PEG and peptides are design lengths, and the length of the polystyrene tether was estimated from control experiments (*SI Appendix,* Fig. S11).

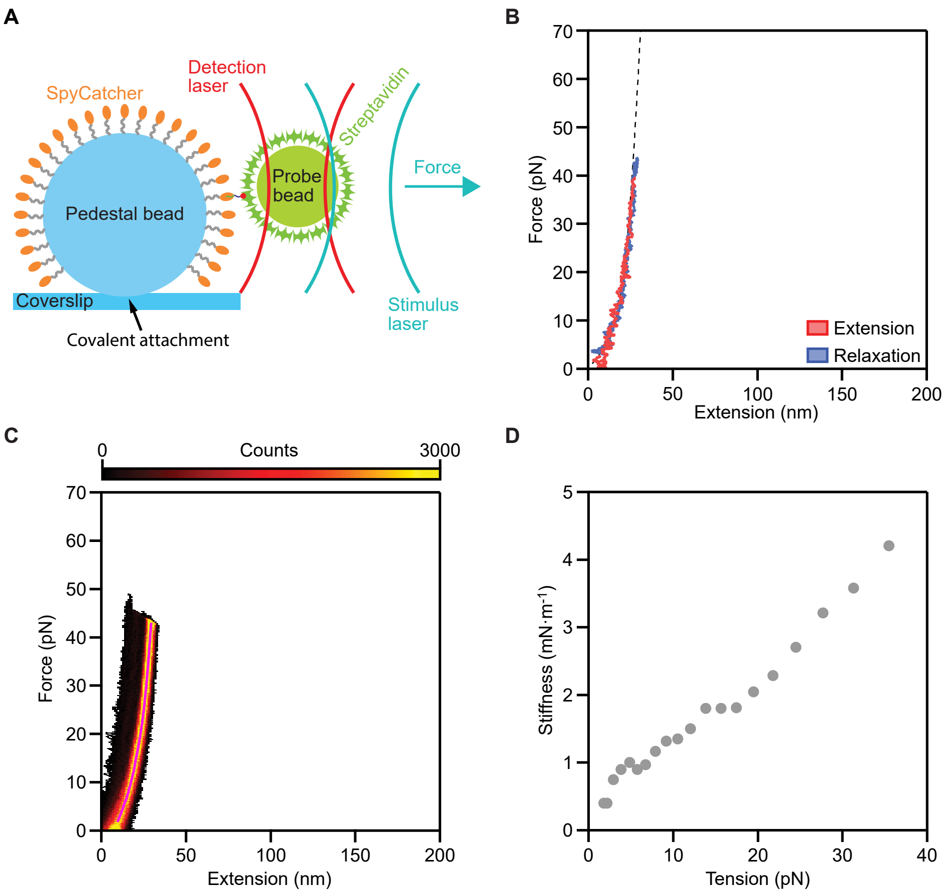

Figure S11. Mechanical properties of the anchors and linkers. (*A*) In order to measure the stiffness of the single-molecule assay system in the absence of PCDH15, we connected the molecular handles (SpyTag and biotinylation peptide) through an eight-amino-acid, flexible linker, anchored this short peptide between a pedestal and a probe bead, and determined its force-extension relation. (*B*) A representative extension-relaxation cycles features a small amount of extensibility that is well fit by a wormlike-chain model. Across nine experiments we found an average persistence length lp_{anchors} = 0.5 ± 0.1 nm, contour length lc_{anchors} = 37 ± 4 nm, and Hookean spring constant k_{anchors} = 7.2 ± 1.3 mNm^{-1} (means ± SEMs). The designed contour length of our tether including PEG, SpyCatcher, peptide, and streptavidin is 20 nm, shorter than the tether's experimentally determined contour length of 37 nm. We accordingly conclude that the extensible polystyrene hairs on the surface of the probe beads have an average length of 17 nm (*SI Appendix,* Fig. S10). (*C*) A state-space heatmap of 500 extension-relaxation cycles shows only the single conformational state expected for an unstructured peptide. These data confirm that neither of our proteinaceous anchors undergoes structural changes over the relevant force range. (*D*) To estimate the compliance of our system of anchors, we determined the average of the highly occupied region in the heat map (pink line in c) and computed its slope.

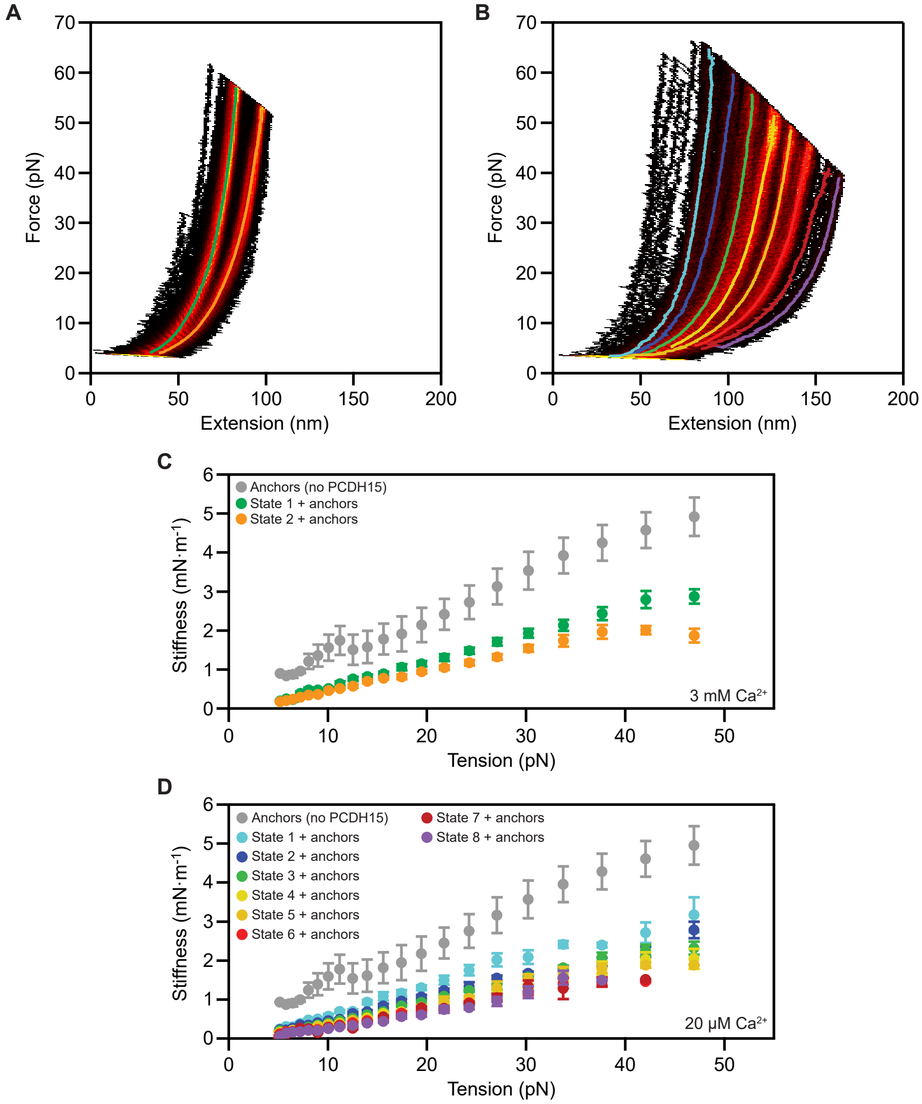

Figure S12. Total stiffness of the single-molecule assay system. (*A*) We determined the stiffness of PCDH15 in its different conformational states at a Ca^{2+} concentration of 3 mM by finding the Islope of each highly occupied region of the state-space heatmap. (*B*) The same operation was performed for PCDH15 in the presence of 20 µM Ca^{2+}. (*C*) The resulting total stiffnesses represent the compliances of the anchors and of PCDH15 at a Ca^{2+} concentration of 3 mM. (*D*) The result for 20 μM [Ca^{2+}] includes six additional unfolded states of progressively diminishing stiffness. As expected, for all states the total stiffness is lower than the stiffness of the anchors alone. By treating PCDH15 and its anchors as springs in series, we can compute from these data the stiffness of PCDH15 alone. The data in *C* and *D* are means ± SEMs for five molecules and six molecules at a Ca^{2+} concentration of respectively 3 mM and 20 μM.

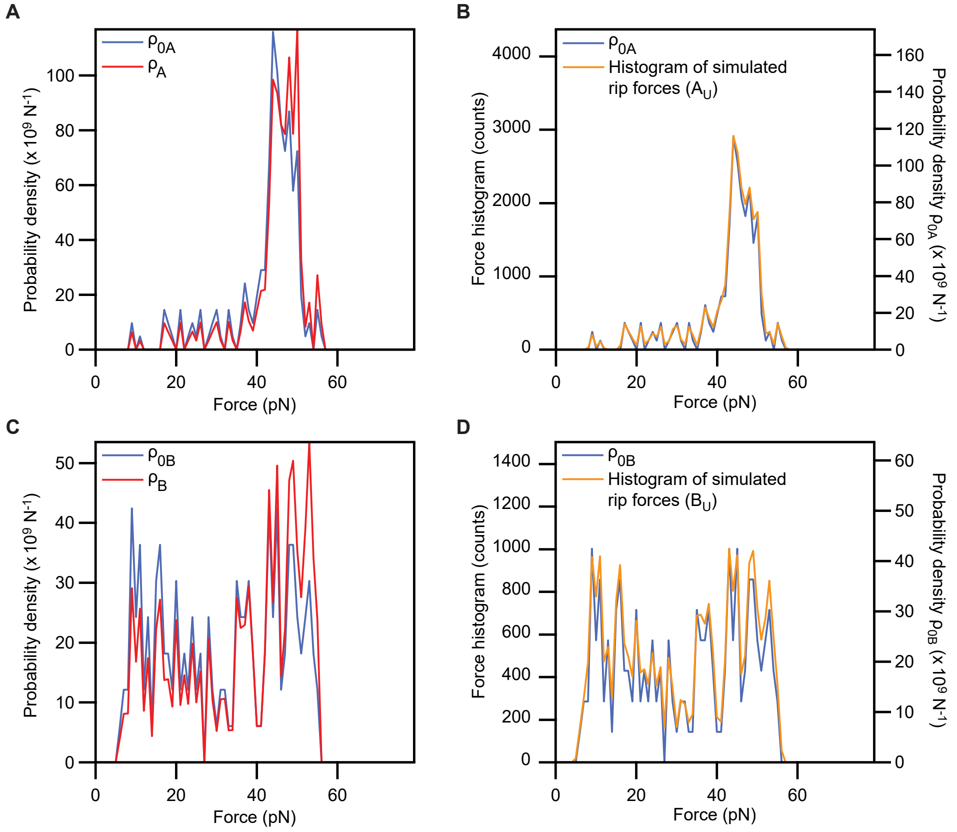

Figure S13. Simulation of the force distributions of the unfolding events A_u and B_u. (*A*) During an extension, a rip of class A occurs with probability $\rho_A(F)dF$. We calculated the probability density $\rho_A(F)$ from the experimentally observed force histogram of rips, $\rho_{0A}(F)$. (*B*) To confirm that our simulations successfully reproduced the experimentally observed force histograms, we simulated 200,000 extension trials, in each of which rips occurred with a probability $\rho_A(F)dF$. (*C*) A similar procedure was applied to events of class B. (*D*) A histogram displays the distribution expected from the simulation. For both classes of unfolding event, the histograms of simulated rip forces match the experimentally observed force histograms.

SI Tables

Table S1. Confidence of tethering a single PCDH15 molecule rather than several[17].

Ca^{2+} concentration	Sample number	Confidence of single-molecule tethers
0	1	> 90%
0	2	> 85%
0	3	> 95%
0	4	> 70%
0	5	> 85%
20 µM	6	> 85%
20 µM	7	> 85%
20 µM	8	> 95%
20 µM	9	> 90%
20 µM	10	> 95%
3 mM	11	> 95%
3 mM	12	> 85%
3 mM	13	> 90%
3 mM	14	> 95%

Table S2. Confinement of PCDH15 molecules through biotin-streptavidin and SpyCatcher-SpyTag interactions. We tested whether PCDH15 was specifically confined between pedestals and probe beads through its amino- and carboxy-terminal tags. Tether formation was abolished if components of either the SpyCatcher-SpyTag or of the biotin-streptavidin pair were missing.

	SpyCatcher-positive Biotinylation-positive		SpyCatcher-negative Biotinylation-positive		SpyCatcher-positive Biotinylation-negative	
	Field of view 1	Field of view 2	Field of view 1	Field of view 2	Field of view 1	Field of view 2
Number of pedestals	146	163	89	137	188	168
Number of probe beads	513	493	0	0	0	0
Mean probe beads per pedestal	3.5	3.0	0	0	0	0

Table S3. Sources of uncertainty in the photonic-force microscope and single-molecule experiment.

	Probe position detector: precision	
a	Over one extension-relaxation cycle (SD, 1 Hz – 1 MHz)	0.3 nm
b	Root-mean-square noise over 5 min	2 nm
	Probe position detector: accuracy	
c	Calibration error (SD computed from 12 independent probe beads)	5 %
	Position of the stimulus trap relative to the position-sensing trap	
d	Accuracy of location of origin (peak-to-peak)	± 4 nm
e	Total accuracy (RMS, from (c) and (d) for a displacement of 200 nm)	10 nm
f	Drift	
	Spring constant of the stimulus trap: precision	
g	Root-mean-square noise over 20 s	0.27 μN·m^{-1}
h	Drift	0 N·m^{-1}·s^{-1}
i	Spring constant of the stimulus trap: accuracy.	5%
	Force: precision (over 5 min for 200 nm displacement of the probe bead from the stimulus trap and at maximalm stimulus-laser power)	
j	Total precision computed from (b), (f), and (g)	0.7 pN
	Force: accuracy (for 200 nm displacement of the probe bead from the stimulus trap and maximal stimulus laser power)	
k	Total accuracy computed from (e) and (i)	3.8 pN

SI Notes

Note S1. Interpretation of State 1 as folded PCDH15

We verified that conformational State 1, that with the smallest contour length (Figure 2d,e), corresponds to fully folded PCDH15. First, we did not observe any reproducibly accessible states with contour lengths shorter than that of State 1. Although we sporadically observed individual force-extension relations to the left of State 1 in heatmaps, those curves were not reproducible and likely reflected nonspecific interactions between the pedestal or probe bead surfaces and the protein. Second, fits of our polymer model to the data for each State 1 yielded contour lengths of 46 ± 7 nm and 47 ± 7 nm for Ca^{2+} concentrations of respectively 3 mM and 20 µM (means ± SEMs for respectively five and eight molecules). These values accord well with a contour length of 50 nm expected for a chain of 11 cadherin domains, each 4.5 nm in length[23].

Note S2. Influence of possible molten-globule states on domain-unfolding rates.

At tensions below 20 pN and with Ca^{2+} concentrations of 20 µM or zero, the rate of unfolding of cadherin domains diverges from an exponential relationship and systematically reaches higher values than expected (Figure 4). What causes this effect? It is possible that cadherin domains refold through a long-lived molten-globule state, as occurs for other proteins with immunoglobin-like folds[24]. During the waiting time between trials, an unfolded domain might refold completely, fold into a molten-globule state, or not refold at all. If folding were to occur, the domain might unfold during the next extension from the completely folded state or from the molten-globule state. We cannot differentiate between these two possibilities, for they would result in indistinguishable contour-length changes. Molten globules are known to unfold readily at low forces[24,25]. Because such rapid unfolding events would increase our measured unfolding rates, they might explain the unexpected behavior observed at low tensions.

Note S3. An estimate for the enthalpic stiffness of full-length, dimeric tip links.

A full-length tip link consists of a dimer of PCDH15, which forms the lower one-third of the filament, and a dimer of CDH23 that constitutes the upper two-thirds of its length. For monomeric PCDH15 we found an enthalpic stiffness of 10 mN m^{-1}. A PCDH15 dimer consisting of two monomers in parallel should then exhibit a stiffness of roughly 20 mN m^{-1}. If CDH23 has a similar enthalpic stiffness per length, then the full-length dimeric tip link would have a stiffness one-third of that of dimeric PCDH15, about 6 mN m^{-1}.

SI References

1. Gibson, D. G. Enzymatic assembly of overlapping DNA fragments. in *Methods in Enzymology* **498**, 349–361 (Elsevier, 2011).
2. Aricescu, A. R., Lu, W. & Jones, E. Y. A time- and cost-efficient system for high-level protein production in mammalian cells. *Acta Crystallogr. D Biol. Crystallogr.* **62**, 1243–1250 (2006).
3. Zakeri, B. *et al.* Peptide tag forming a rapid covalent bond to a protein, through engineering a bacterial adhesin. *Proc. Natl. Acad. Sci. U. S. A.* **109**, E690-697 (2012).
4. Pincet, F. & Husson, J. The solution to the streptavidin-biotin paradox: the influence of history on the strength of single molecular bonds. *Biophys. J.* **89**, 4374–4381 (2005).
5. Tobin, M., Michel, V., Michalski, N. & Martin, P. Tonotopy of the mammalian cochlea is associated with stiffness and tension gradients of the hair cell's tip-link complex.: *bioRxiv* (2018). doi:10.1101/497222
6. Zhu, M., Lerum, M. Z. & Chen, W. How to prepare reproducible, homogeneous, and hydrolytically stable aminosilane-derived layers on silica. *Langmuir* **28**, 416–423 (2012).
7. Jahn, M. *et al.* The charged linker of the molecular chaperone Hsp90 modulates domain contacts and biological function. *Proc. Natl. Acad. Sci.* **111**, 17881–17886 (2014).
8. Swoboda, M. *et al.* Enzymatic oxygen scavenging for photostability without pH drop in single-molecule experiments. *ACS Nano* **6**, 6364–6369 (2012).
9. Bartsch, T. F., Kochanczyk, M. D., Lissek, E. N., Lange, J. R. & Florin, E.-L. Nanoscopic imaging of thick heterogeneous soft-matter structures in aqueous solution. *Nat. Commun.* **7**, (2016).
10. Pralle, A., Prummer, M., Florin, E.-L., Stelzer, E. H. K. & Hörber, J. K. H. Three-dimensional high-resolution particle tracking for optical tweezers by forward scattered light. *Microsc. Res. Tech.* **44**, 378–386 (1999).
11. Bartsch, T. F. *et al.* Detecting sequential nond formation using three-dimensional thermal fluctuation analysis. *ChemPhysChem* **10**, 1541–1547 (2009).

12. Kochanczyk, M. D., Bartsch, T. F., Taute, K. M. & Florin, E.-L. Power spectral density integration analysis and its application to large bandwidth, high precision position measurements. in (eds. Dholakia, K. & Spalding, G. C.) 84580H (2012). doi:10.1117/12.929349
13. Neuman, K. C., Chadd, E. H., Liou, G. F., Bergman, K. & Block, S. M. Characterization of Photodamage to Escherichia coli in Optical Traps. *Biophys. J.* **77**, 2856–2863 (1999).
14. Tischer, C., Pralle, A. & Florin, E.-L. Determination and correction of position detection nonlinearity in single particle tracking and three-dimensional scanning probe microscopy. *Microsc. Microanal.* **10**, 425–434 (2004).
15. Monkos, K. Viscosity of bovine serum albumin aqueous solutions as a function of temperature and concentration. *Int. J. Biol. Macromol.* **18**, 61–68 (1996).
16. Berg-Sørensen, K. & Flyvbjerg, H. Power spectrum analysis for optical tweezers. *Rev. Sci. Instrum.* **75**, 594–612 (2004).
17. Block, S. M., Goldstein, L. S. B. & Schnapp, B. J. Bead movement by single kinesin molecules studied with optical tweezers. *Nature* **348**, 348–352 (1990).
18. Rubinstein, M. & Colby, R. H. *Polymer physics*. (Oxford University Press, 2003).
19. Marko, J. F. & Siggia, E. D. Stretching DNA. *Macromolecules* **28**, 8759–8770 (1995).
20. Petrosyan, R. Improved approximations for some polymer extension models. *Rheol. Acta* **56**, 21–26 (2017).
21. Zhang, Y. & Dudko, O. K. A transformation for the mechanical fingerprints of complex biomolecular interactions. *Proc. Natl. Acad. Sci. U. S. A.* **110**, 16432–16437 (2013).
22. Chen, H. *et al.* Dynamics of equilibrium folding and unfolding transitions of titin immunoglobulin domain under constant forces. *J. Am. Chem. Soc.* **137**, 3540–3546 (2015).
23. Shapiro, L. *et al.* Structural basis of cell-cell adhesion by cadherins. *Nature* **374**, 327–337 (1995).
24. Rivas-Pardo, J. A. *et al.* Work done by titin protein folding assists muscle contraction. *Cell Rep.* **14**, 1339–1347 (2016).

25. Elms, P. J., Chodera, J. D., Bustamante, C. & Marqusee, S. The molten globule state is unusually deformable under mechanical force. *Proc. Natl. Acad. Sci.* **109**, 3796–3801 (2012).

3.5 Conclusions

One of the primary results from this study is that the stiffness of PCDH15 is in fact consistent with measurements of gating spring stiffness. The enthalpic stiffness of PCDH15, which represents the upper bound of molecular stiffness, was ~10 mN/m. When this value is extrapolated, the stiffness of the full tip link is approximately 6 mN/m. This value is much closer to the 1.3-3.7 mN/m range of gating spring stiffness.

Polymers in solution are not simple rigid springs, but rather long chains that are subject to thermal forces that induce variation in their structure. To more accurately capture this reality, the single molecule data were fitted to a set of models for a freely jointed chain in series with worm-like chain components. The folded cadherin domains were modeled by the freely jointed chain elements; the linker regions and unfolded cadherin domains were modeled by the worm-like chain elements. Fitting the parameters of these models to the data yielded parameters that accurately recapitulate the length of a cadherin domain, at 4.3 nm. Calcium had no effect on the stiffness of the PCDH15, as the fitted stiffness parameters between 3 mM calcium and 20 μM calcium were effectively the same.

For experiments at physiological concentrations of calcium, unfolding events that resulted in sudden 35 nm extensions were detected. These events are consistent with the unfolding of an entire cadherin domain. When calcium was removed, these domain-unfolding events became more frequent; agreeing with SMD data that calcium mechanically stabilizes a cadherin domain under force (Powers et al., 2017). Additionally, these experiments allowed for the extraction of unfolding rates for individual cadherin domains under physiological tensions, which was approximately 0.01 s^{-1}. Even at low frequencies, which cycle at a rate of 40 s^{-1}, the unfolding rate of a cadherin domain under physiological relevant forces, <20 pN, is too slow to occur in an individual cycle. However, for hair bundles with higher tip link tensions, such as high frequency outer hair cells, the tension may be great enough for some cadherin domains to exist in an unfolded state. Such unfolding may explain the variation observed in the lengths of tip links.

In addition to the observed 35 nm extension events that we have associated with the unfolding of whole cadherin domains, 4 and 15 nm extension events were routinely detected. The structural origins of these events are currently unknown. It is possible these correspond to ‘popping’ of one or more of the inter-cadherin domain linker regions. This is a feasible explanation for the 4 nm event, particularly considering the number of calcium deficient linkers in PCDH15. As for the 15 nm event, one possible explanation is the partial unfolding of a cadherin domain, however more studies are needed to explore this hypothesis.

The results in this paper indicate that the *in silico* experiments over estimated the forces needed to unfold cadherin domains. The SMD measurements typically predicted cadherin domains to unfold under tensions of hundreds to thousands of pN, while in this study, cadherin unfolding was observed under force regimes of only a few tens of pN. This overestimation of force may also be responsible for the higher stiffness measurements that were calculated for tip link cadherins. While the SMD simulations may overestimate the forces involved, they remain useful tools in generating structural hypotheses for these unfolding events.

3.6 Future Directions

An additional element not captured in this study is the contribution of the PICA domain. Recent SMD simulations using the crystal structure of the PICA domain suggests that it is mechanically weak, and prone to unfolding (De-la-Torre et al., 2018). Partial unfolding events of the PICA domain occur with peak forces approximately half of those observed in simulations of tip link cadherin domains. While the simulations may overestimate the forces involved, it may still be valid that the PICA domain would rupture before any cadherin domain. The result of PICA domain unfolding would be a reduced probability of unfolded cadherin domains *in situ,* but still allow for a variation in tip link length. At the time we designed the monomeric PCDH15 used in this chapter, no structure of the PICA domain was available and therefore it was simply deleted. However, now that crystal structure of the PICA domain is now available it would be possible to introduce structure guided point mutants that disrupt the PICA domain dimerization interface for single molecule PFM studies.

– Chapter 4–

Molecular characterization of the calcium and integrin binding proteins CIB2 and CIB3

4.1 Introduction

While previous studies have identified CIB2 as the cause of DFNB48, our understanding of the molecular role CIB2 plays in mechanoelectrical transduction is limited (Booth et al., 2018; Riazuddin et al., 2012). As discussed previously, CIB2 has been shown to interact with TMC1 (Giese et al., 2017). However, the functional consequences of this TMC1:CIB2 interaction have not been established. Giese et al. (2017) present data that suggest that TMC1 localization is unaffected by CIB2 mutagenesis or deletion. This indicates that CIB2 affects TMC1 function through a mechanism other than transport or localization. Since CIB2 is an EF-hand containing protein, it is possible that CIB2 acts as a calcium-sensing component in the MET machinery (Giese et al., 2017). However, evidence for CIB2 having this role is lacking, and Giese et al. (2017) neither demonstrated nor proposed specific models for CIB2-based modulation of MET in response to calcium. In this chapter, I will present the results of our work investigating CIB2 and its close homologue CIB3. Our findings redefine the CIB2/CIB3 interacting region of TMC1, elucidate a structural mechanism for CIB2/CIB3 dimerization that is potentially important in regulating interaction with TMC1, reveal the structural determinants of TMC1 binding, and suggest functional implications of the CIB:TMC1 interaction.

4.2 Redefining the CIB2 interacting region of TMC1

The initial mapping of the CIB2 interacting region of TMC1 emerged from a preliminary yeast two-hybrid screen (Giese et al., 2017). While the results of this screen indicated the presence of an interaction, there were unaddressed issues with these assays. The TMC1 fragment used in the assay – residue 1-193 – contains most of the first transmembrane helix of TMC1, which includes residues 179-206. The authors did not discuss the effects of including this transmembrane helix, and they did not employ a modified yeast two-hybrid protocol specific for transmembrane proteins (Lentze and Auerbach, 2008).

Giese et al. (2017) then used co-immunoprecipitation to screen TMC1 fragments that were further truncations of the previously identified fragment of residues 1-193. While they were able to successfully express and utilize a number of these fragments, it is possible these fragments are not physiologically relevant. Without structural knowledge of TMC1, such as domain structure, the random fragments they generated may be aberrantly folded. While CIB2 could co-precipitate the TMC1 1-193 fragment, other TMC1 truncations showed stronger co-precipitation, possibly indicating a stronger interaction. Removal of the first 61 residues dramatically improved the amount of TMC1 that co-precipitated with CIB2, however the authors offered no explanation as to what was driving this increased interaction. From their truncations, the authors mapped the CIB2 binding region of TMC1 to residues 80-130 (Giese et al., 2017).

One potential drawback of severely truncating a protein is the generation of fragments that are misfolded and not representative of the native protein. To mitigate this possibility, we performed a new mapping of the CIB2 interacting region on TMC1 with Co-IP experiments that introduced smaller deletions in the context of the full length TMC1. By using small deletions, we hoped to maintain a more native-like TMC1. When our deletion window scanned the region previously reported by Giese et al. (2017), there was an appreciable decrease in signal for residues at positions 100-121 (Figure 4.1A). However, when our deletion window scanned residues in the range of positions 305-344, the ability of CIB2 to Co-IP TMC1 was completely abolished (Figure 4.1B).

While these experiments were performed with the full length TMC1 and potentially represent a more physiologically relevant TMC1 molecule, without a structure to guide the deletions there still exists the possibility that the introduced deletions result in a spurious molecule. In order to confirm the findings from our TMC1 deletions, we performed Co-IP experiments on full length TMC1 that had multiple mutations to alanine. Mutations to alanine are milder than outright deletions as they do not disrupt the backbone register; the mutations to alanine still disrupt side-chain mediated interactions. In the first region identified by deletion scanning, 100-121, only mutation of residues Lys109, Lys110, and Ile111 resulted in a slight decrease in Co-IP signal between CIB2 and TMC1 (Figure 4.1C). In contrast, between residues 305 and 344, four separate mutation groups completely abolished the interaction between CIB2 and TMC1: Phe305, Asn306, and Phe307; Trp309, Lys310, and Phe311; Trp315, Asp316, Tyr317, and Leu318; Phe336, Lys337, and Glue338 (Figure 4.1C). While TMC1 residues 100-121 may contribute to the binding interface, the dramatic effects of alanine mutations in TMC1 residues 305-344 suggest it may contribute significantly more to the binding of CIB2.

Given the fact that CIB2 has a number of EF-hands coupled with the previous speculation that it plays the role of an intracellular calcium sensor for the MET machinery, we sought to determine the effects of calcium on the interaction between CIB2 and TMC1. Surprisingly, we found no difference in the ability of CIB2 to Co-IP full length TMC1 in the presence of either 1 mM Ca^{2+} or 1 mM EGTA (Figure 4.1D). This indicates that CIB2 binding to TMC1 is Ca^{2+} independent. Additionally, this could indicate that binding of TMC1 to CIB2 contributes to the stability of CIB2 in such a way as to compensate for the lack of calcium bound to CIB2's EF hands. There is some evidence that binding of integrin α7B to CIB2 has such a stabilizing effect, as inferred from the increased affinity for Ca^{2+} in the presence of an integrin α7B_M peptide (Vallone et al., 2018).

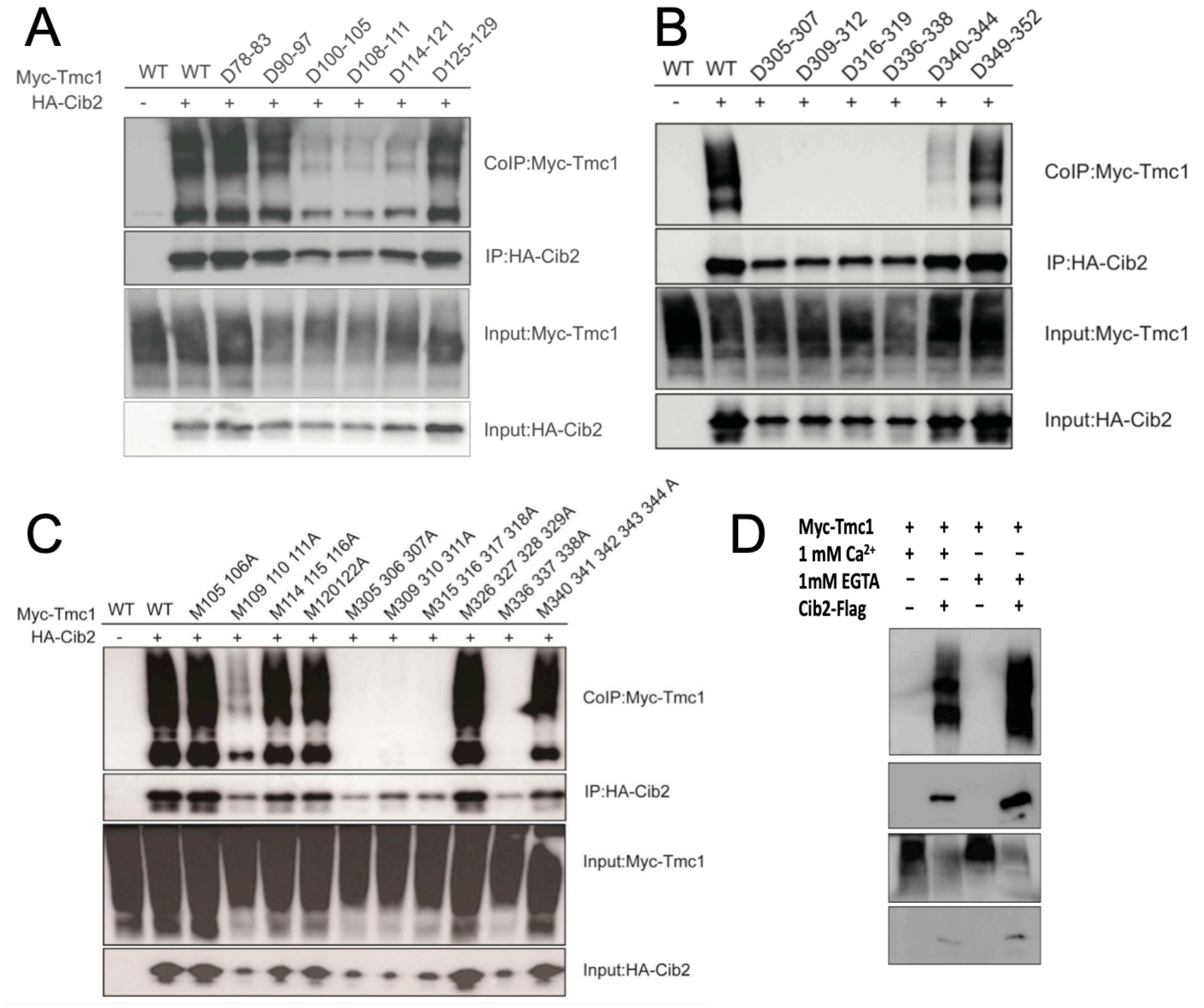

Figure 4.1: CIB2 binds to TMC1 residues 305-344 in a calcium independent manner
(A) Small deletions between TMC1 residues 100-121 can decrease CIB2's ability to co-immunoprecipitate TMC1. TMC1 residues 80-130 were previously identified as being able to interact with CIB2 by Geise et al. (2017) (B) Small deletions between TMC1 residues 305-344 can completely abolish CIB2's ability to co-immunoprecipitate TMC1. (C) Alanine-scanning mutagenesis reveal TMC1 residues 105-122 has limited effect on CIB2's ability to co-immunoprecipitate TMC1; Mutation of TMC1 residues 305-338 have a much greater effect. (D) CIB2 and TMC1 interaction is not dependent on Ca^{2+}, as evident by successful Co-IP in the presence of 1 mM EGTA.

Among the four CIB paralogues, CIB2 and CIB3 exhibit a higher degree of similarity (Figure 4.2A). The amino acid sequences of CIB2 and CIB3 from *Mus musculus* have 62% pairwise sequence identity. By comparison, the five other combinations of CIB paralogues have an average of 40.6% pairwise sequence identity. The pairwise similarity between CIB2 and CIB3 is 80%, while all other combinations of CIB proteins are on average 59.8% similar. This could indicate functional overlap between CIB2 and CIB3, which has been proposed previously to explain the lack of vestibular defects in CIB2 deficient mice (Giese et al., 2017). In order to explore this possibility, we performed Co-IP experiments with three CIB paralogs, demonstrating that both CIB2 and CIB3 are able to bind to full length TMC1, while CIB1 is not (Figure 4.2B). Given the high sequence similarity between CIB2 and CIB3 and their shared ability to bind TMC1, we consider CIB2 and CIB3 to be functional redundant.

Given the dramatic effect of alanine mutations for TMC1 residues in the 305-344 region, we decided to investigate these residues further, and set out to perform biophysical studies of the CIB3/TMC1 interaction. We cloned wild type CIB3 into a pET-14b expression vector, yielding a protein with an N-terminal 6xHis-tag that was cleavable by thrombin. We expressed this protein in BL21(DE3) RIPL cells. The protein was initially purified by affinity chromatography with nickel-charged IMAC sepharose. The affinity tag was cleaved off using thrombin and the protein was further purified by size exclusion chromatography. This protein was used in both biophysical experiments and in crystallization studies.

In addition, I designed and purchased a set of four peptides that 'walk' the TMC1 region with a twenty-five-residue window which were incremented by steps of five residues (Figure 4.3). Our original approach to study the interaction between CIB3 and these peptides was to use surface plasmon resonance (SPR), however we abandoned this approach due to technical issues.

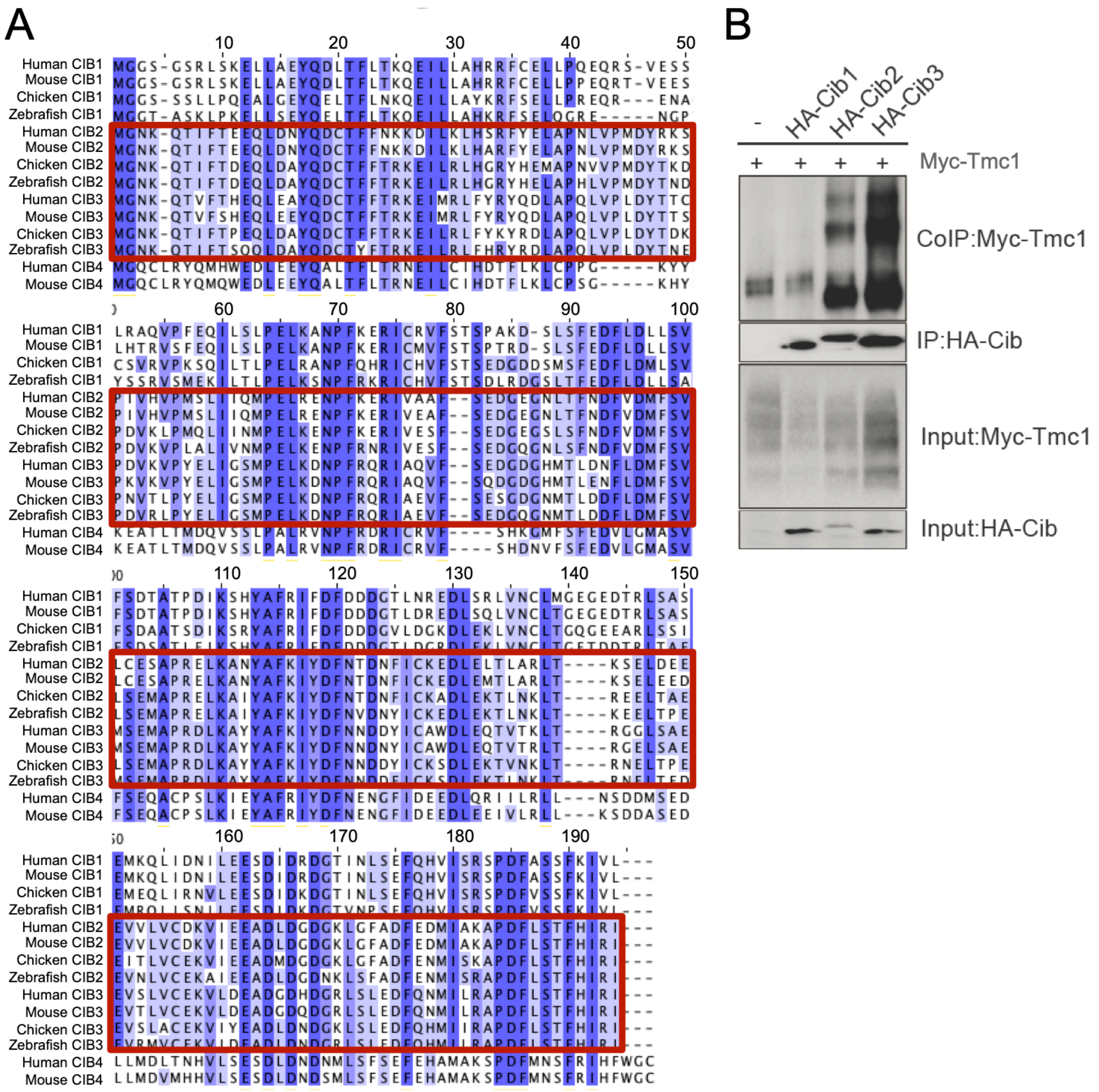

Figure 4.2: CIB2 and CIB3 are highly similar and both bind to TMC1
(A) Multiple sequence alignment of CIB1, CIB2, CIB3, and CIB4 amino acid sequences from human, mouse, chicken, and zebrafish. No CIB4 sequences were found for chicken or zebrafish. Sequences of CIB2 and CIB3 are outlined in red, making it easier to so the increased similarity. Residues are colored by percent identity. (B) Co-immunoprecipitation experiments demonstrating CIB2 and CIB3 both interact with TMC1.

The first issue was difficulty in coupling the protein to the SPR chip's surface. The most common approach to coupling a protein to the surface of an SPR chip uses amine coupling to covalently link the primary amines of a protein to the carboxyl groups of carboxymethyl dextran (CMD) molecules that have been conjugated to the chip surface (Johnsson et al., 1991). Our attempts to use amine coupling were hampered by electrostatics. The pI of CIB3 is 4.7 while the pK_a of commercially available SPR sensor chips with CMD surfaces is ~4.5. Thus there is a narrow range of pH that would promote electrostatic absorption of CIB3 to the chips surface, and as a result we were not able to couple a sufficient amount of CIB3 to the SPR senor chip via amine coupling. We attempted to overcome this by using an AviTag to generate a biotinylated CIB3 that could be coupled to the SPR sensor chip's surface via amine-coupled streptavidan. While this approach was successful, we then ran into an issue with nonspecific binding between the peptides and the SPR chip's surface. This nonspecific binding made proper interpretation of the SPR signal impossible and prompted us to design a new assay to study the interaction between CIB3 and the TMC1 peptides.

In order to study the interactions without SPR, I developed a binding assay using size exclusion chromatography that took advantage of a few properties of CIB3 and the TMC1 peptides. CIB3 behaves as a dimer in solution, but it interacts with its binding partners in a monomeric state (Dal Cortivo et al., 2019). When analyzed by size exclusion chromatography (SEC), CIB3 elutes with two peaks corresponding to a dimer and a monomer (Figure 4.3, Black trace). Additionally, CIB3 has a relatively weak extinction coefficient for 280 nm wavelength light, and the potential CIB3:peptide complexes have higher extinction coefficients (Figure 4.3). Thus, if a peptide binds to CIB3 it will shift the equilibrium to the monomeric state, and increase the absorbance of the monomer peak such that it will have a higher maximal value (Figure 4.3).

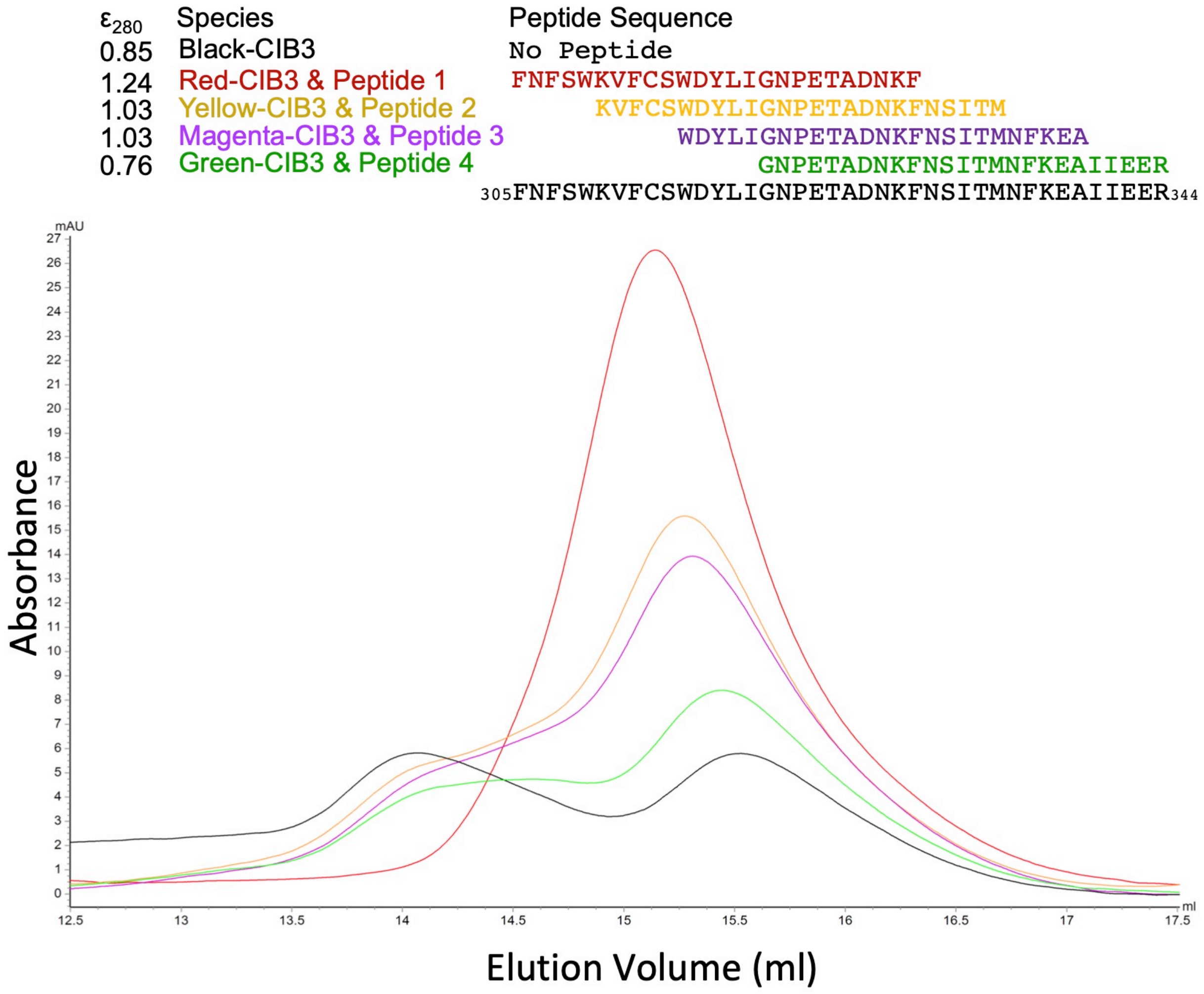

Figure 4.3: CIB3 binds peptides that correspond to TMC1 residues 305-344
Top, Color-coded legend of the peptides screened, including their sequences and extinction coefficients for 280 nm wavelength light. Bottom, size exclusion chromatograms of CIB3 or CIB3:peptide mixture over a GE Superdex 200 increase 10/300 gl column. The same amount of CIB3 was used in each run, thus difference in peak amplitude are due to changes in extinction coefficients, and shifts from dimeric to monomeric forms.

Of the four peptides I designed and tested, the first peptide completely abolished the dimer peak and the monomer peak dramatically increased in absorbance compared to the control, indicating a significant interaction between CIB3 and peptide 1. Peptides 2 and 3 did not remove the presence of the dimer peak, but the monomer peak had higher absorbance compared to the control. Thus peptides 2 and 3 potentially interacted with CIB3, but not as strongly as peptide 1. Peptide 4 also failed to remove the presence of the dimer peak, but the monomer peak increased in amplitude slightly. Peptide 4 is the only peptide that decreases the extinction coefficient of CIB3 and thus the slight increase in amplitude may indicating that peptide 4 interacts weakly with CIB3, however the data is not as definitive for peptide 1, 2, or 3. Overall these results suggested that TMC1 residues 305-319 are necessary for CIB3 binding.

4.3 Crystal Structures of the CIB3 Dimer

We expressed and purified full-length human CIB3 for crystallographic structure determination as described above. We determined crystal structures for human CIB3 in two distinct crystal forms to 1.88 Å and 1.83 Å (Figure 4.4A and 4.4B). The first structure, for crystal form 1, was determined by molecular replacement using the crystal structure of CIB1 (PDB: 1XO5) as a search model. The second structure, for crystal form 2, was of a double mutant CIB3 EK151QH, designed to aid in crystallization, and was determined using the crystal form 1 structure as a search model. Crystallographic statistics for all crystal structures discussed in this chapter are presented in Table 4.1.

Both crystal forms revealed human CIB3 engaged in a domain-swapped dimer, with the twelve most C-terminal residues swapped between both protomers and bound in a hydrophobic trench. Overall, the topology of the CIB3 protomer is similar to CIB1, with nine α-helices in total, eight of which participate in four helix-turn-helix motifs that form either functional EF-hands

(EF-hand 3 comprising helices 6-7 and EF-hand 4 comprising helices 8-9) or pseudo-EF-hands (EF-hand 1 comprising helices 2-3 and EF-hand 2 comprising helices 4-5). Each of the true EF-hands contains all of the canonical Ca^{2+}-binding ligands. The first pseudo-EF-hand does not contain any of the twelve canonical ion-binding residues of a typical EF-hand and instead contains an extended loop. The second pseudo-EF-hand contains a serine in place of a canonical Ca^{2+}-binding Asp/Glu ligand at position 71.

The CIB3 protomers have highly similar structures within each crystal form, with RMSDs between 168 corresponding $C\alpha$ atoms of 0.573 Å for both protomers of crystal form 1 and 0.843 Å for both protomers in crystal form 2. Even between the two crystal forms, the structures of the individual CIB3 molecules are highly similar. The RMSDs between the individual CIB3 molecules of both crystal forms are 0.692 Å, 0.866 Å, 0.837 Å, 0.931 Å. For all alignments and RMSD calculations, residues 5-174 were used, to exclude the highly variable C-terminus.

Larger differences between the two crystal forms, however, were observed for the relative arrangement of CIB3 protomers, consistent with the aforementioned structural variability of C-terminal residues. In the first crystal, the protomers are related by a non-crystallographic two-fold rotational symmetry axis, with the centers of mass between promoters spaced 36.6 Å apart. In the second crystal, the protomers are related by a 166° rotation around an axis, with the center of masses only 29.6 Å apart. When one chain of the first crystal form dimer is superposed onto one chain of the second crystal form dimer, the Euler angle that describes the relative postions between the two unaligned protomers is 80.42°, with a 25 Å shift in the centers of mass (Figure 4.4C).

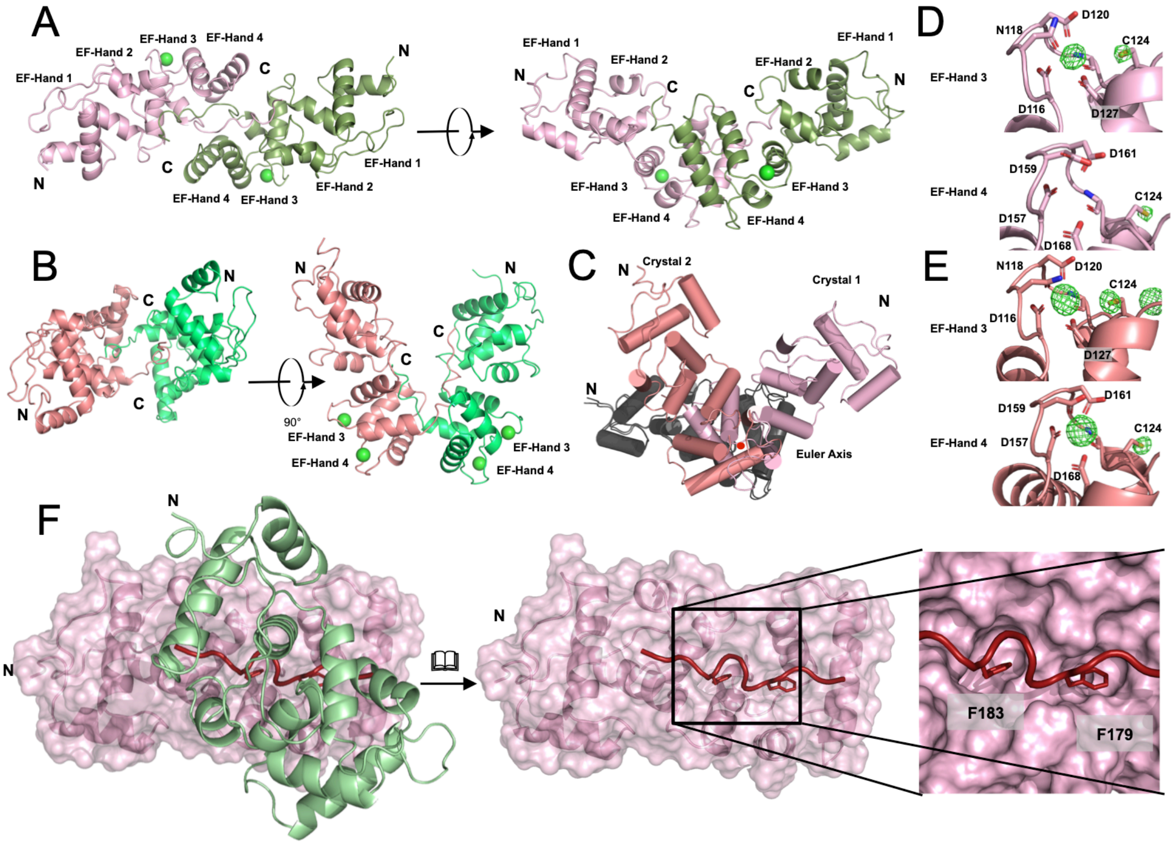

Figure 4.4: Overall Structure and Details of Human CIB3 Homodimer In Two Distinct crystal forms

(A and B) Dimers of human CIB3 from two crystal forms are shown in two orthogonal views. Different protomers are represented by shades of pink and green. Calcium ions are represented as green spheres. CIB3 Dimerizes through an exchange of C-termini in in both crystal forms 1(A) and 2 (B). (C) Orientation of the dimer protomers varies between crystal forms. After alignment of one chain from each crystal form, the unaligned protomers are rotated from one another by ~80° around the rotation axis indicated by a black dot. (D and E) Bijveot difference density, in green mesh, reveals calcium occupancy in EF-hand 3 for crystal form 1 (D) and EF-hands 3 and 4 for crystal form 2 (E). Ligand side chains are labeled and represented with sticks. The coordinating backbone carbonyl of residues Tyr126 and Arg163 are shown in EF hand 3 and 4, respectively. Anomalous density for the sulfur atom of cysteine 124 is labeled in each image. (F) The dimer interaction is anchored by a pair of phenylalanine residues, Phe179 and Phe183, in the swapped C-terminus from one protomer (red).

	hsCIB3	hsCIB3 EK151QH	hsCIB3:TMC1-peptide
Wavelength (Å)	1.46	1.46	1.77
Resolution range (Å)	60.32 – 1.879 (1.946 – 1.879)	73.08 - 1.837 (1.902 - 1.837)	87.17 - 1.838 (1.904 - 1.838
Space group	$P\ 3_2\ 2\ 1$	$P\ 3_1\ 2\ 1$	$P\ 3_2\ 2\ 1$
Unit cell	61.752 61.752 180.969 90 90 120	84.386 84.386 125.821 90 90 120	100.65 100.65 49.723 90 90 120
Total reflections			
Unique reflections	33540 (3270)	44456 (3797)	23158 (1806)
Multiplicity			
Completeness (%)	99.92 (99.33)	96.93 (84.12)	90.83 (72.18)
Mean I/sigma(I)	34.59 (2.28)	42.15 (7.12)	20.93 (2.47)
Wilson B-factor	37.57	28.59	27.65
R-merge	0.0427 (0.833)	0.05032 (0.2035)	0.08882 (0.5321)
R-meas	0.04391	0.05171	0.09123
CC1/2	0.999 (0.901)	0.998 (0.983)	0.999 (0.864)
CC*	1 (0.974)	0.999 (0.996)	1 (0.963)
Reflections used for R-free	3733	3793	3844
R-work	0.1769 (0.3164)	0.1671 (0.2029)	0.1657 (0.2589)
R-free	0.2044 (0.3222)	0.1954 (0.2462)	0.1867 (0.2753)
Number of non-hydrogen atoms	3132	3317	2045
macromolecules	2994	2988	1881
ligands	21	14	2
water	117	315	162
Protein residues	364	363	228
RMS(bonds)	0.011	0.008	0.006
RMS(angles)	1.21	1.07	0.97
Ramachandran favored (%)	99	99	100
Ramachandran allowed (%)	1	1	0
Ramachandran outliers (%)	0	0	0
Clashscore	2.73	2.92	0.55
Average B-factor	47.2	37.3	34.8
macromolecules	46.9	36.5	34.2
ligands	73.1	62.3	32.1
solvent	48.6	43.8	41

Table 4.1: Crystallography statistics for wild-type CIB3, crystallographic mutant CIB3, and CIB3:TMC1 peptide

In addition to differences in the overall relative geometry of the CIB3 dimers, the structures of the two crystal forms differ in the calcium occupancy of the EF hands. In the first crystal form, only the third EF hand of both molecules had electron density consistent with an occupying ion. In the second crystal form, both the third and fourth EF hands had sufficient electron density to be consistent with a bound Ca^{2+} ion. To confirm the identity and presence of these bound ions, we utilized the anomalous diffraction from our data (measured at 8.5 keV x-ray energy) to generate Bijvoet difference maps to visualize Ca^{2+} (Figure 4.4D and 4.4E). As expected, neither of the pseudo-EF hands showed evidence for Ca^{2+} binding, but the Bijvoet difference maps had clear anomalous density for the third EF hand in both crystal forms (Figure 4.4D and 4.4E, upper panels). Crystal form 2 also had anomalous density for the fourth EF hand, while crystal form 1 did not (Figure 4.4D and 4.4E, lower panels). This difference in occupancy likely results from the difference in calcium concentrations between the two crystallization conditions: crystal form 1 was grown in a solution that contained only 3 mM calcium that came from the protein buffer, while crystal form 2 was grown in a solution that contained 200 mM calcium.

The CIB3 dimer is formed through the domain-swapped binding of a C-terminal segment between the two protomers. This interface encompasses a surface area of 2017.3 $Å^2$ for crystal form 1, and 1764.1 $Å^2$ for crystal form 2. In both crystal forms, the swapped C-termini are anchored by a pair of aromatic residues – Phe179 and Phe183 – which project from the C-termini of one protomer and bury into a large hydrophobic trench on surface of the other (Figure 4.4F). These phenylalanine residues are completely or almost-completely buried by interface formation (>90% change in accessible surface area) and constitute ~15% of the interface's total surface area. The hydrophobic trench on the surface of CIB3 is lined by residues Phe70, Ile74, Phe78 on helix four, Met98 on helix five, Tyr110, Ala111, Ile114, Tyr115 on helix six, Leu128, Thr131, Val132, Leu135 on helix seven, Val152 on helix eight and Phe169, Met172 on helix nine.

4.4 CIB3:TMC1-Peptide Complex Crystal Structure

To understand the interaction between CIB2/3 and TMC1, we co-expressed human CIB3 with a 55 amino acid fragment of mouse TMC1 corresponding to residues 298-352 (Figure 4.5A). SEC revealed this fragment to form a complex with CIB3, as CIB3 behaved as a monomer when bound to the TMC1 fragment. We then determined the crystal structure of this complex to 1.83 Å resolution by molecular replacement using our crystal form 1 structure of CIB3 (Figure 4.5B) as a search model (crystallography statistics presented in Table 4.1).

The refined map for the CIB3:TMC1-peptide structure revealed electron density for forty-five residues (303-347) of the TMC1 peptide. The TMC1 peptide is folded into two α-helices, with the N-terminal helix being eight residues in length and the C-terminal helix being twenty-six residues in length. An eight-residue linker that spans residues 314-321 connects these helices. The TMC1 peptide interacts with CIB3 primarily through elements of the shorter N-terminal α-helix and the linker. These elements occupy the same hydrophobic trench that is utilized in the CIB3 domain-swapped dimer. The interface between the TMC1-peptide and CIB3 buries 1583.8 Å^2 of surface area between the two molecules. Interestingly, the CIB3:TMC1-peptide interaction is also anchored by two aromatic residues, Phe312 and Tyr317, which is strikingly similar to use of CIB3 residues Phe179 and Phe183 in the CIB3 C-terminus-swapped dimer. These two aromatic residues constitute ~21% of the interfacial surface area (Figure 4.5C). TMC1 residues Val311 and Trp315 also provide significant contributions to the buried surface area. The long C-terminal helix of the TMC1 peptide, corresponding to residues 322-347, makes contacts with CIB3 α-helices 7 and 8 and the linker between them. This interaction region is

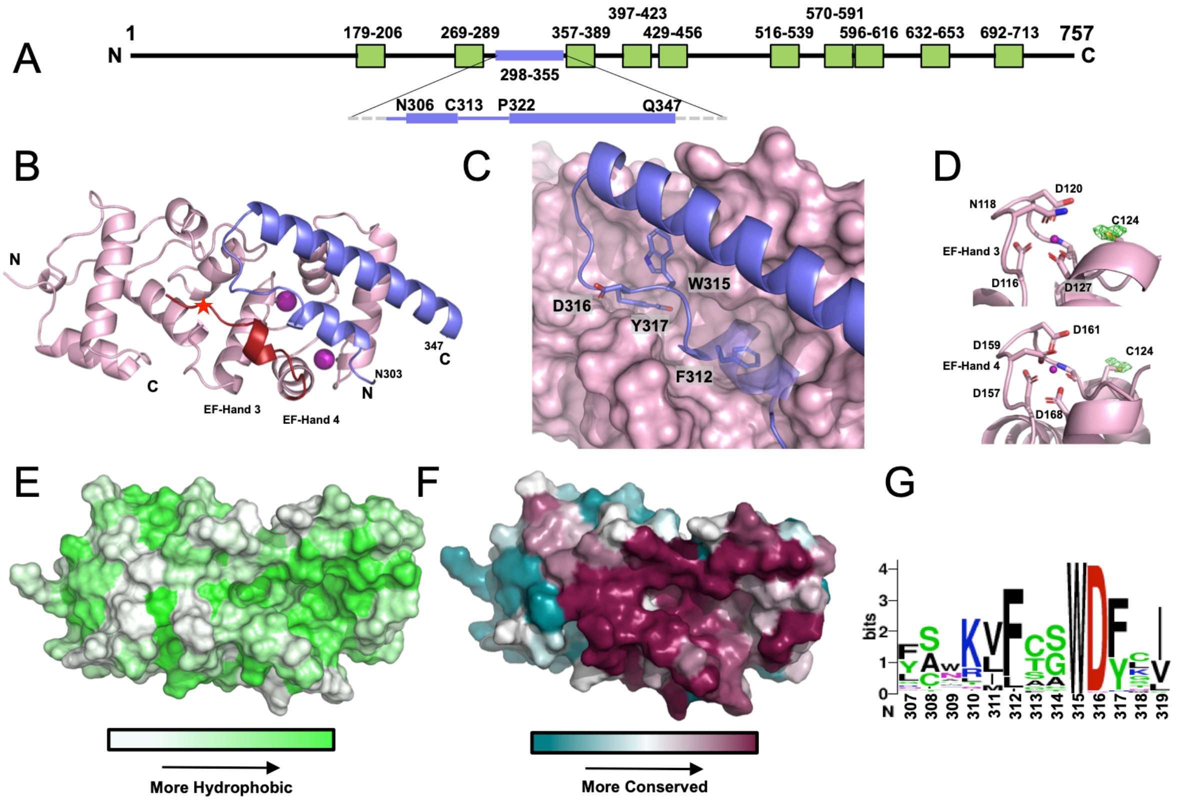

Figure 4.5: Structure and details of human CIB3:TMC1-peptide complex
(A) Schematic representation of TMC1 and the region (blue) used for structural studies. Transmembrane helices as predicted by Pan et al. 2018 are shown as green rectangles. (B) Crystal structure of the CIB3:TMC1 complex with CIB3 shown in pink and TMC1 peptide in slate. The C-terminal region of CIB3 that swaps in the homodimer is colored red. Magnesium atoms are represented as purple spheres. Location of Arg186 marked with a red star. (C) Close up view of TMC1 (ribbon) in complex with CIB3 (surface) with the side chains of key residues shown in stick representation and labeled. The N-terminal alpha helix has been made transparent to aid in visualization of Phe312. (D) Bijvoet difference map density, in green mesh, shows a lack of calcium occupancy in EF-hands 3 and 4. Ligand side chains are labeled and represented in sticks. Magnesium ions are represented as small purple spheres. Anomalous density for the sulfur atom of Cys124 is shown in each image. (E) Surface representation of CIB3 colored according to Eisenberg hydrophobicity scale. (F) View of the TMC1-peptide binding site with conservation scores from ConSurf mapped onto the structure. Color key is provided, with low conservation being teal and high conservation in burgundy (Landau et al., 2005). (G) Sequence logo for the TMC1 binding region, generated from sequence alignments across the TMC gene family. Numbering corresponds to full-length mouse sequence. (Crooks et al., 2004).

stabilized by hydrophobic interactions between TMC1 residues Leu332 and Phe336 with CIB3 residues Val132, Leu135, and Val148. In addition, two salt bridges are formed between TMC1 Asp326 and CIB3 Arg137 and TMC1 Arg344 and CIB3 Glu143. CIB3 binding of TMC1 displaces the CIB3 C-terminus that underlies dimer formation, explaining the monomeric state of the CIB3:TMC1-peptide complex. As the binding site for TMC1 on CIB3 overlaps the dimer-binding site for the C-terminus, many of the interfacial residues are the same. Of the fifteen hydrophobic-trench residues participating in C-terminus binding listed above, twelve take part in the TMC1 interface. The three residues that differ – Phe78, Tyr110, and Ala111 – are occluded from interacting with TMC1 by the C-terminus of CIB3. In the CIB3:TMC1-peptide structure, the CIB3 C-terminus sits to one side of the trench, contributing to the binding interface. Additionally, four residues, 179-182, fold into a small α-helix connected to the end of the α9-helix by a three-residue linker. The last five residues of the carboxyl terminus are extended and positioned at the edge of the binding trench, with the terminal carboxylic acid group forming a salt bridge with Arg29.

The binding pocket for TMC1 on CIB3 is highly conserved. We used the program ConSurf to calculate conservation scores, which we then mapped to the molecular surface of CIB3 (Figure 4.5F) (Landau et al., 2005). The most conserved residues of CIB3 are those in hydrophobic trench involved in the domain-swap dimerization/TMC1-binding site. Residues distal to this region show far less conservation. The TMC1 residues involved in CIB3 binding are also highly conserved as revealed by a sequence logo for TMC1 residues 307-319, which corresponds to the first α-helix and linker region (Figure 4.5G) (Crooks et al., 2004). The logo reveals residues Phe312 and Tyr317 to be highly conserved, with Trp315 and Asp316 showing near total conservation. While Trp315 makes hydrophobic contacts with CIB3, the side chain of

Asp316 is directed away from CIB3, and its function is not apparent from the CIB3:TMC1-peptide structure.

The CIB3:TMC1-peptide structure also allows us to explain the effects observed in the Co-IP experiments with alanine scanning mutants. The loss of binding due to mutation of residues Trp309, Lys310 and Val311 can be explained by the loss of Val311, which is buried into the hydrophobic trench of CIB3, and the loss of an interaction between the indole nitrogen of Trp309 and the backbone carbonyl of CIB3:Met172. The most straightforward residues to discuss are Trp315, Asp316, Tyr317, and Leu318 as mutations to alanine would decrease the amount of hydrophobic surface area provided by two key residues Trp315 and Tyr317. Mutating Phe336, Lys337, and Glu338 to alanine disrupts CIB2 binding mostly though the loss of hydrophobic surface area provided by Phe336. One set of residues – Phe305, Asn306, and Phe307– while containing two, large phenylalanine residues, doesn't contribute a large amount of interacting surface area. However, they are at the very start of the short α-helix that predominately buries into the hydrophobic trench of CIB3, and may be important for the proper formation and orientation of the TMC1 peptide.

The crystallization condition for the CIB3:TMC1-peptide structure contained 200 mM $MgCl_2$, and as a result it appears that EF Hands 3 and 4 of CIB3 are occupied by Mg^{2+} rather than Ca^{2+}. This determination is supported by the geometry of the ion coordination in the EF hands, which are coordinating their respective ions with octahedral geometry. Bijvoet difference maps (measured at 7 keV x-ray energy) showed no anomalous density in the metal-ion binding position – as expected for Mg^{2+} – while an anomalous density peak for the sulfur atom of cysteine 124 is clearly visible (Figure 4.5D). Together, these observations present strong evidence for Mg^{2+} occupying the EF hands of CIB3 in the CIB3:TMC1-peptide structure.

Despite the coordination of Mg^{2+}, no significant changes in Cα positions are observed for the residues in either EF hand. The RMSD between the twelve residues of EF hand 3 in the Mg^{2+}-bound and the Ca^{2+}-bound forms was only 0.460 Å; for EF-hand 4, the RMSD was 0.568 Å between Mg^{2+}-bound and the Ca^{2+}-bound forms. Since the complex was co-purified in the presence of calcium, this suggests that magnesium binding is not required for CIB3:TMC1-peptide interaction. Thus, we believe the presence of magnesium in our structure is simply the result of the high magnesium concentration of the crystallization condition and not the result of some underlying mechanism.

4.5 CIB2 Mutant Arg186Trp Affects MET Currents

In order to examine the effects CIB2 mutations on MET, we focused on the deafness causing Arg186Trp mutation, first identified by Patel et al. (2015). Arg186 is the penultimate residue of CIB2 and CIB3, and mutation to tryptophan would not readily occlude TMC1 binding (Figure 4.5B). $CIB2^{Arg186Trp/Arg186Trp}$ outer hair cells still exhibit MET currents in whole cell patch clamp recordings, however the maximal currents from a saturating stimulus is decreased in comparison to heterozygous cells. $CIB2^{+/Arg186Trp}$ OHCs are able to generate maximal currents of approximately 620 pA, while $CIB2^{Arg186Trp/Arg186Trp}$ OHCs were only able to generate about 150 pA, an approximate four-fold decrease in current (Figure 4.6A). This reduction in current for $CIB2^{Arg186Trp/Arg186Trp}$ OHCs is not associated with a shift in the current-displacement relationship, just a decrease in maximally evoked currents (Figure 4.6B). This suggests that CIB2 Arg186Trp does not affect the open state probability of the MET channel, or the set point of the MET adaptation machinery.

The reduction in maximally evoked currents from whole hair bundles could be due to a number of causes, such as a decrease in the number of MET channels, a decrease in single channel conductance, or a combination of both. In order to determine the origin of the reduction in current due to the CIB2 Arg186Trp mutation, we measured the unitary currents of OHCs by carefully treating hair bundles with BAPTA until only discrete binary current events were

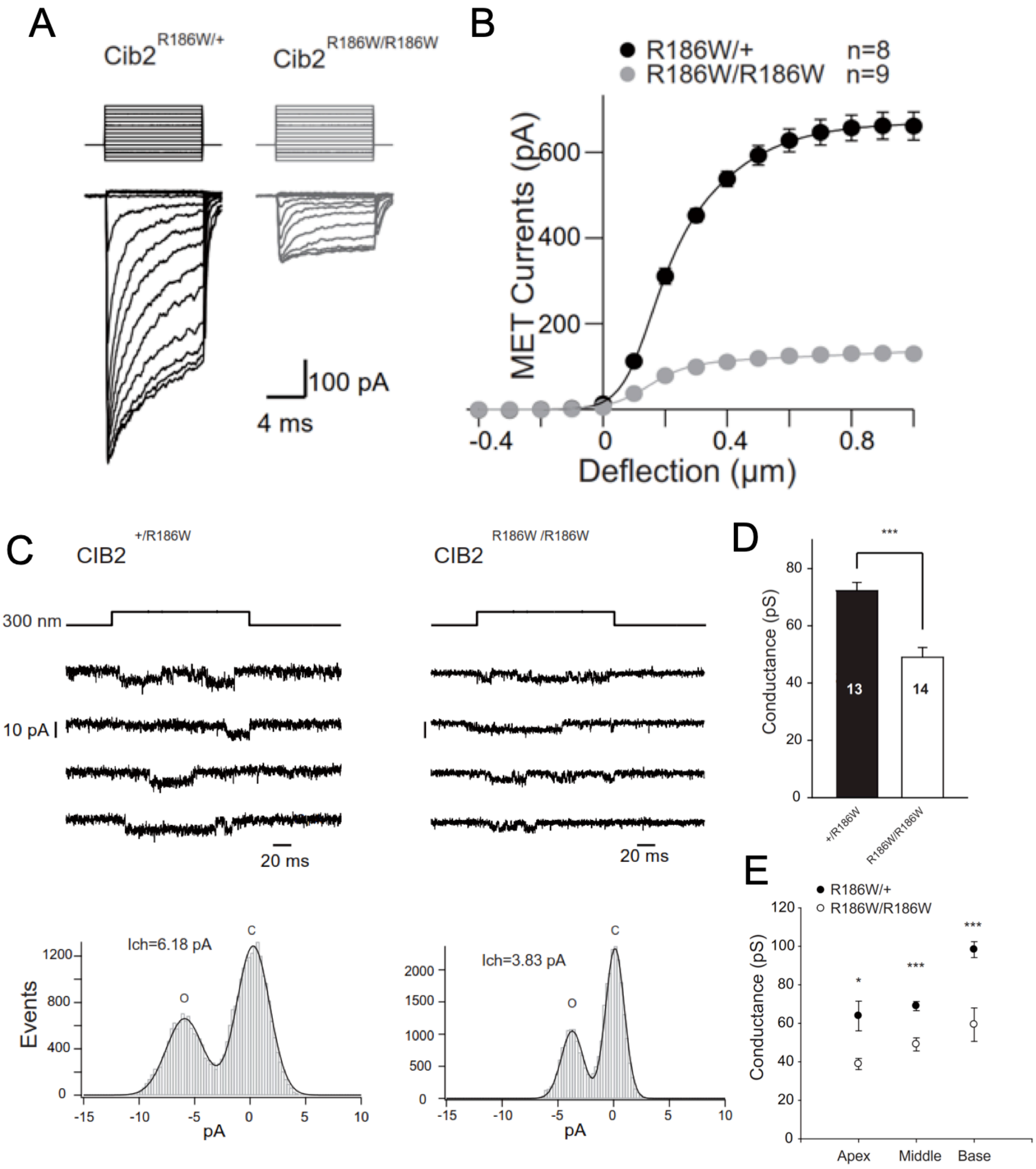

Figure 4.6: CIB2 deafness mutant Arg186Trp reduces the conductance of MET unitary currents (Legend on next page)

Figure 4.6: CIB2 Deafness mutant Arg186Trp reduces the conductance of MET unitary currents

(A) CIB2 Arg186Trp decreases whole cell MET currents. Whole cell patch clamp recordings of mouse outer hair cells. Left, current recordings from OHC of a CIB2$^{+/Arg186Trp}$ mouse can achieve >600 pA of current. Right, current recordings from OHC of a CIB2$^{Arg186Trp/Arg186Trp}$ mouse produces a maximal current of ~150 pA. (B) Current-displacement relationships measured in mouse OHC of CIB2$^{+/Arg186Trp}$ (black) and CIB2$^{Arg186Trp/Arg186Trp}$ (grey) animals. CIB2$^{Arg186Trp/Arg186Trp}$ have reduced maximal currents, but no apparent shift in the set-point of the current-displacement relationship, nor a change in open state probability of the channel. (C) CIB2 Arg186Trp decreases MET unitary channel currents. Upper left, sample unitary recordings in an outer hair cell from a CIB2$^{+/Arg186Trp}$ mouse in response to a 300 nm hair bundle deflection with a fluid jet. Lower left, histogram of current measurements from CIB2$^{+/Arg186Trp}$ unitary recordings. Upper right, sample unitary recordings in an outer hair cell from a CIB2$^{Arg186Trp/Arg186Trp}$ mouse in response to a 300 nm hair bundle deflection with a fluid jet. Lower left, histograms individual current recordings from CIB2$^{Arg186Trp/Arg186Trp}$ unitary recordings. (D) Single channel conductance measured across (E) CIB2 Arg186Trp reduces the variance in MET channel conductance observed over the tonotopic map.

detectable. For CIB2$^{+/Arg186Trp}$ OHCs, the mean MET unitary currents were 6.18 pA, while CIB2$^{Arg186Trp/Arg186Trp}$ OHCs had mean unitary currents of 3.83 pA (Figure 4.6C). These currents correspond to a single channel conductance of 71 pS for CIB2$^{+/Arg186Trp}$ OHCs and 44 pS for CIB2$^{Arg186Trp/Arg186Trp}$ OHCs (Figure 4.6D). Assuming the change in single channel conductance was the only change with regard to whole cell currants in CIB2$^{Arg186Trp/Arg186Trp}$ OHCs, the expected whole cell currents would be ~380 pA – much higher than the ~150 pA observed. Thus we can conclude that in addition to a reduced single channel conductance, CIB2$^{Arg186Trp/Arg186Trp}$ OHCs also have a decreased number of functional MET channels.

Lastly, CIB2$^{Arg186Trp/Arg186Trp}$ hair cells still display a variance of single channel conductance along the tonotopic map (Figure 4.6E). In CIB2$^{+/Arg186Trp}$ the single channel conductance varies from 65 pS at the apex and 98 pS at the cochlear base. For CIB2$^{Arg186Trp/Arg186Trp}$ hair cells the single channel conductance varies from ~38 pS to 59 pS over the same region. While the variation along the tonotopic map is lessened in CIB2$^{Arg186Trp/Arg186Trp}$ cells, it is roughly 60% the CIB2$^{+/Arg186Trp}$ conductance at the three points measured.

4.6 Conclusions

The data presented in this chapter has allowed us to accurately define the CIB2 interacting region on TMC1 involving residues 305-344. We were able to validate this interaction through the use of alanine scanning mutagenesis and by demonstrating the interaction between purified CIB3 and peptidic fragments of TMC1. While we cannot rule out a contribution to CIB2 binding from TMC1 residues 100-120, only alanine mutagenesis of residues 109-110 resulted in a slight decrease in binding to CIB2. A structure of CIB2 bound to full length TMC1 would reveal the structural mechanism for this observation.

The crystal structures of the CIB3 dimer establish a dimerization mechanism not previously observed in the related NCS family of proteins, which were discussed in Chapter 1. The domain swapping mechanism indicates that the carboxyl terminus of monomeric CIB3 must exist in equilibrium between bound and unbound conformations. While structures of NCS proteins with and without their cognate binding partner suggest that their C-termini must have some intrinsic flexibility, there is no evidence for their adopting conformations with their C-termini unbound and protruding into solvent. In the context of CIB2 and CIB3, it would suggest the enthalpy of self-binding is not enough to overcome the loss of entropy from no longer having the C-termini freely moving in solvent. However, when the C-termini are engaged in the domain-swapped dimer they still maintain a fair degree of flexibility, as evident by the different conformations observed in the two CIB3 dimer crystal forms. This flexibility suggests the possibility of a decreased entropic cost in dimerization compared to self-binding.

The interaction between CIB3 and TMC1 is highly similar to other interactions between NCS proteins and their binding partners. The interaction is similar to that observed between calcineurin B and residues 349–372 of calcineurin A, in that these calcineurin A residues adopt helical secondary structure and bind to calcineurin B with its N- and C- termini oriented in the same direction as the TMC1 peptide in CIB3 (Jin and Harrison, 2002). In contrast, the N-terminal helices of Kv4.3 and the N-terminus GRK1 bind in the reverse orientation to KChIP1 and NCS-1, respectively (Pandalaneni et al., 2015; Wang et al., 2007).

The whole cell MET currents from CIB2$^{Arg186Trp/Arg186Trp}$ OHCs establish CIB2 as having a direct role in MET and suggests that CIB2 influences MET via its interaction with TMC1. Indeed, one possible conclusion is that the 60% reduction of single channel conductance in CIB2$^{Arg186Trp/Arg186Trp}$ OHCs in comparison to CIB2$^{+/Arg186Trp}$ OHCs suggests that CIB2 modulates conductance by binding in close proximity to the MET channel pore, which TMC1 has been previously been implicated as being the pore-forming subunit of the MET channel (Pan et al., 2018). If this is the cause, the region that CIB2 binds to on TMC1 must also be in close proximity to the MET pore. This region was not screened in with cysteine mutants, and thus we have no information about how cysteine mutation and subsequent MTSET modification of TMC1 residues 305-344 affect MET channel properties (Pan et al., 2018). Interestingly, TMC1 has does have a natural cysteine at residue position 313. When bound to CIB2, this cysteine would be shielded from MTSET modification; MTSET modification in the absence of CIB2 could preclude CIB2 binding to TMC1 and thus affect MET properties.

Additionally, the idea that TMC1 is the MET pore is not definitive. For example, while the deafness mutants Met412Lys and Asp569Asn have effects on whole cell currents and ion selectivity they do not affect single channel conductance (Beurg et al., 2019; Beurg et al., 2015). As mentioned in Chapter 1, an alternative hypothesis is that TMC1 is a modulator of MET currents, an idea that has been suggested by Liu et al. 2019, albeit with no clear causative mechanism. Regardless of the exact mechanism, in this scenario CIB2 modulates TMC1, which in turn modulates MET channels. Liu et al. 2019 found TMC1 was associated with a leak current in hair cells, and while it would not be definitive it would be interesting to see if CIB2$^{Arg186Trp/Arg186Trp}$ hair cells have a decreased leak current.

The structure of the CIB3:TMC1-peptide complex also allows for speculation of how certain mutants establish their effects. In particular there are two mutations to tryptophan – Arg66Trp, Arg186Trp – that have some effect on MET but still permit the interaction of CIB2 with TMC1 (Giese et al., 2017). These residues are on the edge of the hydrophobic trench on CIB3. These residues are also in close proximity to the location where the highly conserved TMC1 residue Trp315 binds to CIB3. This Trp315 becomes sequestered upon interaction with CIB2/3. It may be possible that mutating CIB2/3 surface residues that are near the TMC1 Trp315 are able to mimic the CIB-free state of TMC1. Introducing novel to-tryptophan mutants in CIB2 in this region and seeing if they effect MET would be a straightforward way to test this hypothesis in absence of a TMC1 structure.

Investigating the conservation of TMC1 residues 305-344, we found that this sequence is conserved even in organisms that are separated by a large amount of evolutionary time. TMC and CIB proteins are found in the genomes of some cnideria, e.g. stony coral, a branch of organisms that humans last shared a common ancestor with bilateral organism over 500 million years ago (Erwin and Davidson, 2002). Additionally, the residues involved in the mammalian TMC1:CIB2 interaction are conserved even in their genetically distant cniderian orthologs. It is possible that the function of the TMC1:CIB2 interaction is a mechanism that predates the divergence of bilaterians, and this function was eventually co-opted for use in hair cells for MET.

4.7 Future Directions

The work presented in this chapter lays the foundation for new questions to be asked and enable a number of future experiments. The structure of the CIB3:TMC1-peptide complex will allow for the generation of structure guided mutants that can specifically disrupt their interaction. Examining the functional impact of disrupting the CIB3:TMC1 interactions with mutants from both proteins should allow for a more precise understanding of the functional roles of this interaction. Additionally, these potential experiments are not limited to hair cells. *Caenorhabditis elegans* have both CIB2 and TMC1 homologues and there are already established behavioral and cellular phenotypes for TMC-1 disruption in *C. elegans.* This may allow for the study of the CIB2:TMC-1 interaction in relatively simpler system. One caveat is that the controls establishing that the *C. elegans* CIB2 and TMC-1 homologs interact would need to be performed.

We were also able to demonstrate that peptides corresponding to TMC1 residues 305-344 are able to interact with CIB3. This peptide is an additional tool that can be used to interrogate the interaction between TMC1:CIB2 *in situ.* By injecting this peptide, it would allow for the disruption of the TMC1:CIB2 interaction without the need for mutants that could potentially affect the development of hair bundles.

– Chapter 5–

TMIE and TMC1 pilot studies

5.1 Introduction

While the higher order view of how hair cells are able to sense mechanical stimulus is mostly fleshed out, there remain a number of details about the components of the system that are not well understood. This lack of fine-grained knowledge stems, in part, from a lack of structural and biochemical characterization of the individual MET components. For example, the small membrane protein TMIE has been demonstrated to be critical for MET, with even single point mutants causing a complete loss of MET currents. However, no definitive function has been established for TMIE. Pacentine et al. (2019) have proposed TMIE helps traffic TMC1/2 to the hair bundle, but they also present some data that contradicts this hypothesis. Specifically, when they expressed TMIE truncations that disrupt MET, TMC1 was still present in the hair bundle. Our understanding of TMIE's function would be advanced by the ability to study purified samples of TMIE, which may eventually allow for its structural characterization. In the first part of this chapter, I will present preliminary data from experiments that seek to establish protocols for the expression, purification, and characterization of TMIE. This project is still ongoing, however results from these preliminary studies should enable future work to generate samples of TMIE for cryo-EM studies.

This chapter will also present a proof-of-concept experiment that looks into alternative approaches for generating a native-like sample of TMC1. TMC1 is one of the more well studied molecules involved in MET. Nevertheless TMC1 still remains enigmatic, with a number of seemingly contradictory results. While some have claimed that TMC1 is the pore of the MET channel, others in the field are not in strict agreement. Thus, more investigations of TMC1 are needed. When TMC1 (and similarly TMC2) are heterologously expressed, they fail to localize to the cell membrane, and remain in the endoplasmic reticulum (ER) (Labay et al., 2010). It is unknown what is the determining factor or factors responsible for this ER retention, and the implications for using purified ER-resident TMCs for biochemical and structural studies are unclear. There has been some effort in the field to find certain conditions that would permit the expression and surface targeting of TMC1, with one group reporting success in getting TMC1 to the cell surface of CHO cells and *Xenopus laevis* oocytes by co-expressing TMC1 with KCNQ1 (Harkcom et al., 2019). In these studies, Harkcom et al. (2019) demonstrated that TMC1 was able to traffic to the cell membrane with KCNQ1 co-expression, but found no evidence of mechanosensitive currents. However, these results may not be reproducible (Ulrich Muller, personal correspondence). Other groups have disregarded the failure of TMC1 to traffic to the cell surface and purified a protein sample directly from the ER (Jia et al., 2019; Pan et al., 2018). Pan et al. (2018) purified human TMC1 from the ER of HEK293 cells and examined samples with negative stain and cryo–electron microscopy. While the two micrographs they presented showed a fairly homogeneous population of particles, the class averages from 2D classification, which in cryo-EM studies provide a heuristic measure of sample quality, were less than stellar indicating a potential issue with the quality of the protein sample (Pan et al., 2018; Sigworth, 2016). Jia et al. (2019) employed a similar approach of expressing and purifying *Chelonia mydas* TMC1 and *Melopsittacus undulatus* TMC2 from Sf9 cells. They then reconstituted their purified protein into liposomes for electrophysiological assays. They were successful in measuring currents across these liposomes, however the single channel conductance they measured was much lower than the single channel conductance for the MET channel. It remains unknown whether the discrepancy in single channel conductance stems from their purification of non-surface targeting TMC proteins or from the variation that exists between species. Thus, establishing a protocol for generating a native-like TMC1 sample remains a significant goal for the field. To that end, the latter part of this chapter will present work that I undertook to explore the use *Caenorhabiditis elegans* as a tool for TMC1 expression.

5.2 TMIE

TMIE is a rather small protein – murine TMIE has 153 residues – that does not contain any putative glycosylation sites. The small size and lack of glycosylations make bacterial expression of TMIE a potentially viable route for generating a TMIE sample. Successful expression in a bacterial expression system would allow for inexpensive, fast, and easily scaled TMIE expression. Initial screening of different affinity-tagged *Mus musculus* TMIE constructs was performed by COMPPÅ, in which they had success in small-scale preparations with a construct of TMIE that had the ten most N-terminal residues replaced with a tandem FLAG/10xHis affinity tag (Figure 5.1). These ten residues have not been associated with any function of TMIE, and their deletion had previously been shown to have no effect on MET (Pacentine and Nicolson, 2019). This construct leaves intact both of the transmembrane helices and the entire carboxyl terminus, which may have some function in MET (Pacentine and Nicolson, 2019; Zhao et al., 2014).

For large scale expression, I screened four different bacterial expression strains of *Eschericia coli*: BL21(DE3), LEMO21(DE3), C41(DE3), and C43(DE3). LEMO21(DE3) cells are derived from BL21(DE3) and have been transformed with the pLemo plasmid which contains the gene for the lysY variant of T7 lysozyme under the control of the tunable P_{rhaBAD} promoter that is regulated by the concentration by L-rhamnose in the culture media. Elevated concentrations of L-rhamnose in the culture media turns on expression of lysY, which in turn inhibits T7 RNA polymerase. C41(DE3) was also derived from BL21(DE3), but as opposed to LEMO21(DE3) which arose from the transformtion of BL21(DE3) with a helper plasmid, the

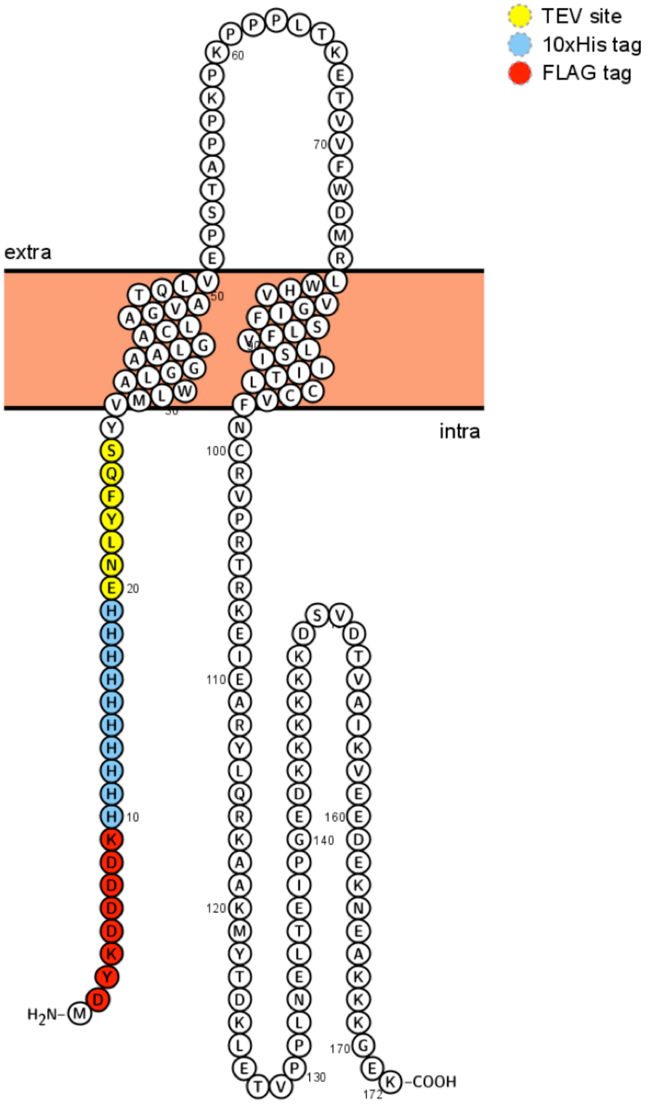

Figure 5.1: Schematic representation of TMIE construct
The bacterial produced TMIE construct contains an N-terminal FLAG tag, 10xHis tag, and a TEV site. FLAG tag was utilized for western blots, as the 10xHis tag was not visualized with anti-his western blot. While present, TEV site was not functional, most likely due to its proximity to the transmembrane helix.

C41(DE3) strain arose from the selection of mutants that permitted the expression of bovine oxoglutarate-malate transport protein (Miroux and Walker, 1996). C41(DE3) are able to express certain 'toxic' proteins as the result of a mutation that reverts the $P_{lac\text{UV5}}$ promoter back to wild type P_{lac} (Kwon et al., 2015). C43(DE3) were derived from C41(DE3) through an additional round of selection for the ability to express F-type ATPase subunit b; this is a result of a mutation in the lac repressor, *lacIV192F,* which inhibits the interaction of the repressor with inducer molecules (Kwon et al., 2015; Miroux and Walker, 1996). Thus LEMO21(DE3), C41(DE3), and C43(DE3) can all potentially increase yields of toxic proteins by slowing expression rates compared to BL21(DE3), whose highly efficient expression of these proteins kills the cell or inhibits growth which ultimately leads to decreased yields.

In order to quickly screen which of these *E. coli* strains were able to successfully express TMIE, aliquots of commercially purchased competent cells were transformed with 0.5 ng of the TMIE plasmid. After the recovery phase of the transformation, 50 µL from the same transformation were plated onto either ampicillin selective LB-agar plates, or ampicillin selective LB-agar plates with 100 µM IPTG. LEMO21(DE3) cells were plated similarly but on plates that additionally contained 2 mM L-rhamnose. Inoculated plates were incubated at 37 °C overnight to permit colony growth. The next day, plates were imaged and presented in Figure 5.2A. All strains produced colonies on the IPTG free plates, serving as both a positive control that the transformations were successful and as an indication that potential leaky expression is not toxic. BL21(DE3) and LEMO21(DE3) failed to produce colonies on the IPTG doped plates. This indicates that both BL21(DE3) and LEMO21(DE3) are unable to express TMIE without some detriment to their growth or survival, at least on an agar plate. The IPTG plates for C41(DE3)

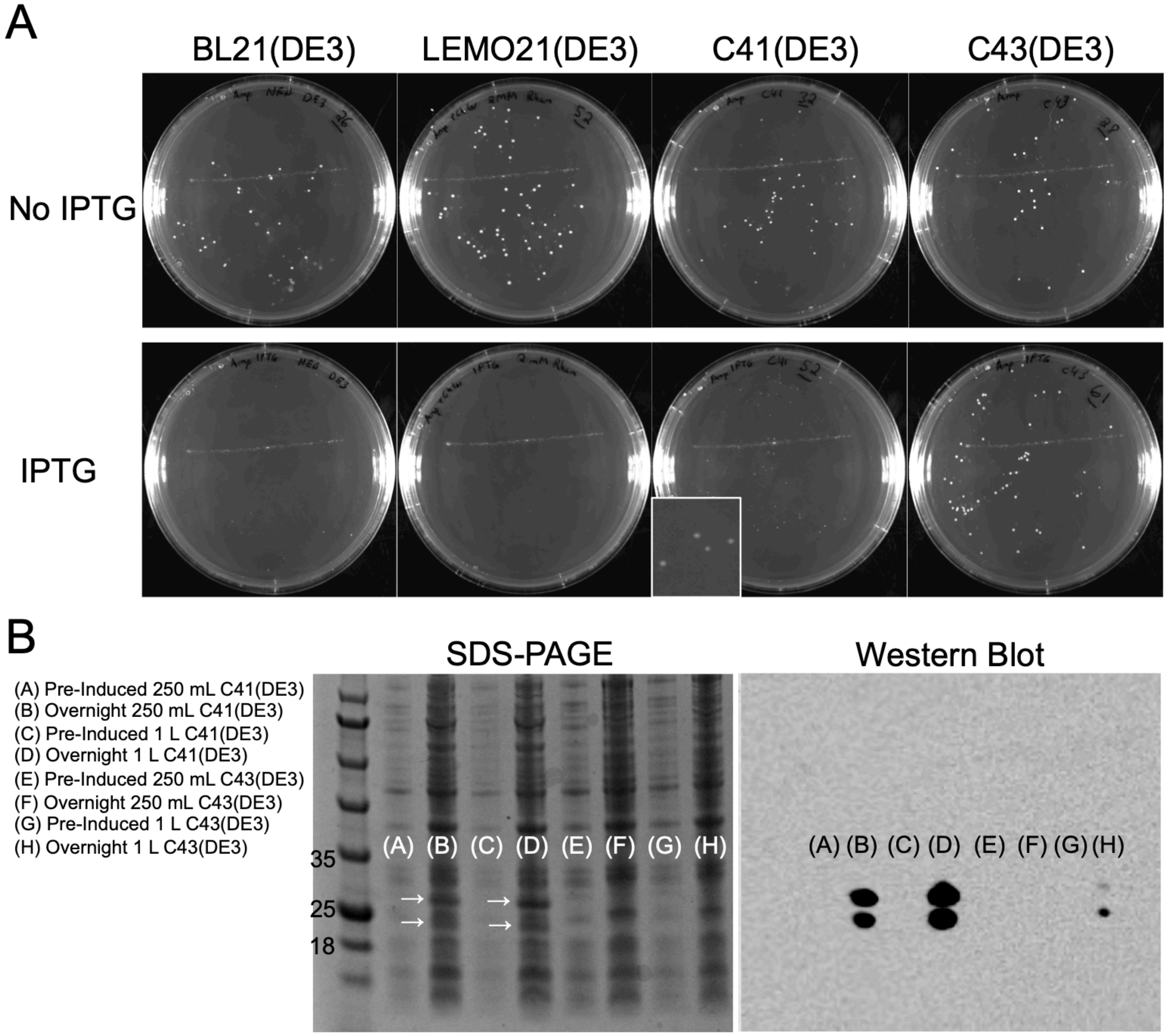

Figure 5.2: C41(DE3) permits the expression of TMIE
(A) Screening for TMIE expression in BL21(DE3), LEMO21(DE3), C41(DE3), and C43(DE3) using LB-agar plates or LB-agar plates with IPTG. BL21(DE3) and LEMO21(DE3) had no colonies on IPTG plates. C41(DE3) and C43(DE3) had colonies on IPTG plates. C41(DE3) image has an insert showing colonies after 6x magnification. (B) Expression tests of C41(DE3) and C43(DE3) in both 250mL and 1 L scales. Left, SDS-PAGE of culture samples taken before induction, and after addition of 100 µM IPTG and overnight growth at 18 °C. White arrows point to bands not present in pre-induced lanes or in TMIE negative lanes. Left most lane is protein latter with relevant molecular weights labeled in kDa. Right, western blot of the same samples as left. Positive signals were present only in IPTG induced C41(DE3) samples.

and C43(DE3) both had colonies, indicating that they may support expression of TMIE. However, while the colonies from C43(DE3) had a similar morphology to the non-inducing plate, the C41(DE3) colonies were diminutive in appearance.

While this assay presented a relatively quick way to screen for potential expression, the assay does not directly confirm that TMIE was being expressed. In order to confirm TMIE expression, C41(DE3) and C43(DE3) colonies were picked from the IPTG doped plates and cultured in LB broth in both a 250 mL and 1 L volumes. Cultures were grown at 37 °C to an OD of 0.4 and induced with 100 µM IPTG. Cultures were then grown overnight at 18 °C. The following day, samples were taken and TMIE expression was confirmed using a western blot (Figure 5.2B). C41(DE3) was positive for TMIE expression in both 250 mL and 1 L culture scales. The signal on the western blot corresponded to bands in SDS-PAGE that were present only in the post induction samples. Interestingly, the western blot for this *E.coli* expressed TMIE had two bands, consistent with western blots that were published in Zhao et al (2014).

I next focused on establishing a protocol to solubilize TMIE from the cell membranes. 1-L cultures of TMIE expressing C41(DE3) were pelleted and resuspended in approximately 35 mL of Tris-buffered saline (TBS). Cells were lysed by sonication using a probe style sonicator. Samples were kept cold with wet ice and sonicated for a total of 3 minutes in cycles of 15-second pulses followed by 45 seconds of rest. Sonicated samples were spun for 10 minutes at 8000 rpm to remove crude cellular debris. The supernatant from the low-speed centrifugation step was then spun for 50 minutes at 45000 rpm in order to pellet the membranes. Approximately 0.5 g of this membrane pellet was resuspend in 2 mL of TBS and homogenized with a glass Dounce-homogenizer. 100 µL of this homogenate was mixed with 400 µL of TBS that had 10 mg of one of twelve different detergents dissolved in it. Detergents that were screened include DDM, Cymal-5, LMNG, OG, NG, LDAO, TDAO, Fos-Choline 12 (FC12), FC12:CHAPS mixture, CHAPS, digitonin, GDN. Detergent samples were allowed to incubate overnight at 4 °C with gentle agitation. The following day, samples were centrifuged at 50000 rpm for 50 minutes to pellet insolubilized material. Samples of the supernatant were then analyzed by western blot (Figure 5.3). TMIE is adequately solubilized by most of the detergents screened. TMIE solubilized slightly better in zwitterionic detergents, with FC12 appearing to solubilize slightly more TMIE than the other detergents.

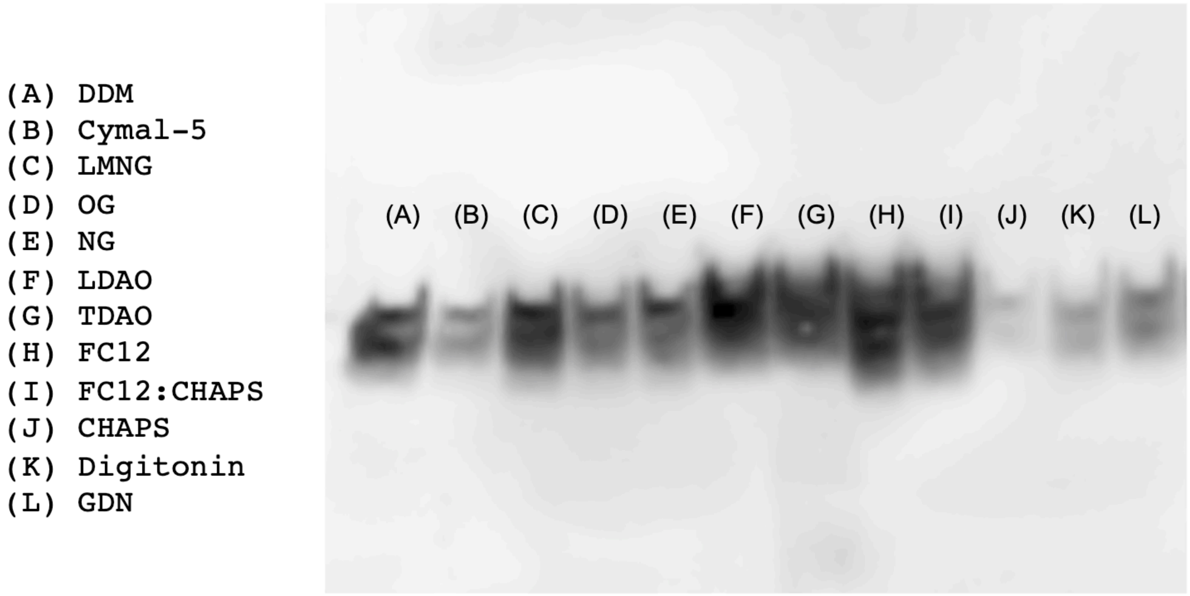

Figure 5.3: TMIE detergent solubilization screen
Western blot of TMIE solubilized with various detergents. Zwitterionic detergents LDAO, TDAO, Fos-choline 12 (FC12), FC12:CHAPS had slightly stronger signal.

In order to purify FC12 solubilized TMIE, I used nickel-charged IMAC sepharose in a gravity driven column, that had been pre-equilibrated with TBS and 0.2% FC12. Initial attempts at purification used a single washing step of 10 column volumes of TBS with 0.2% FC12, and 20 mM Imidazole added. TMIE was eluted with five separate applications of single column volumes of TBS, 0.2% FC12, and 200 mM imidazole (Figure 5.4A). To improve the purity, I modified the wash step, using 30 column volumes of a buffer composed of 750 mM NaCl, 250 mM KCl, 20 mM Imidazole, 10 mM Tris pH 8.0 5 mM $MgCl_2$, 5 mM ATP, and 0.2% FC12. This more aggressive washing was successful in increasing the purity of the TMIE sample. The final yields of TMIE after affinity purification were fairly high, with yields of 5-10 mg of TMIE per liter of C41(DE3) culture.

While FC12 was determined to be the best solubilization agent of TMIE, that does not imply it is the best detergent for solution behavior. In order to assess the solution behavior of TMIE in different detergents I used size-exclusion chromatography (SEC). SEC has been used successfully to characterize protein stability with different detergent, although it is typical to utilize GFP fluorescence to increase the sensitivity of the method (Kawate and Gouaux, 2006). However, since my TMIE yields were sufficiently high, this allowed for the use of standard absorbance of 280 nm wavelength light. In order trap TMIE in different detergents, I performed detergent exchange while TMIE was bound to nickel-charged IMAC sepharose during affinity purification by swapping in different detergents (at 2x their CMC) in the wash buffer. In addition to FC12, I screened DDM, CHAPS, and a mixture of FC12 and CHAPS. The combination of FC12 and CHAPS has been previously shown to improve solution behavior of membrane proteins, indicating that the two detergents can interact synergistically (Genji et al., 2010). The FC12:CHAPS mixture used had concentrations of 2mM and 0.5 mM, respectively. DDM, FC12, and CHAPS all had chromatograms with prominent void peaks which indicates some amount of aggregation. Their peaks were also not symmetric. The main peak for DDM-TMIE was broad and close to the void peak. The main peak for FC12-TMIE was sharper than the DDM peak, but did have mild shoulders, indicating heterogeneity. The main peak for CHAPS-TMIE had a

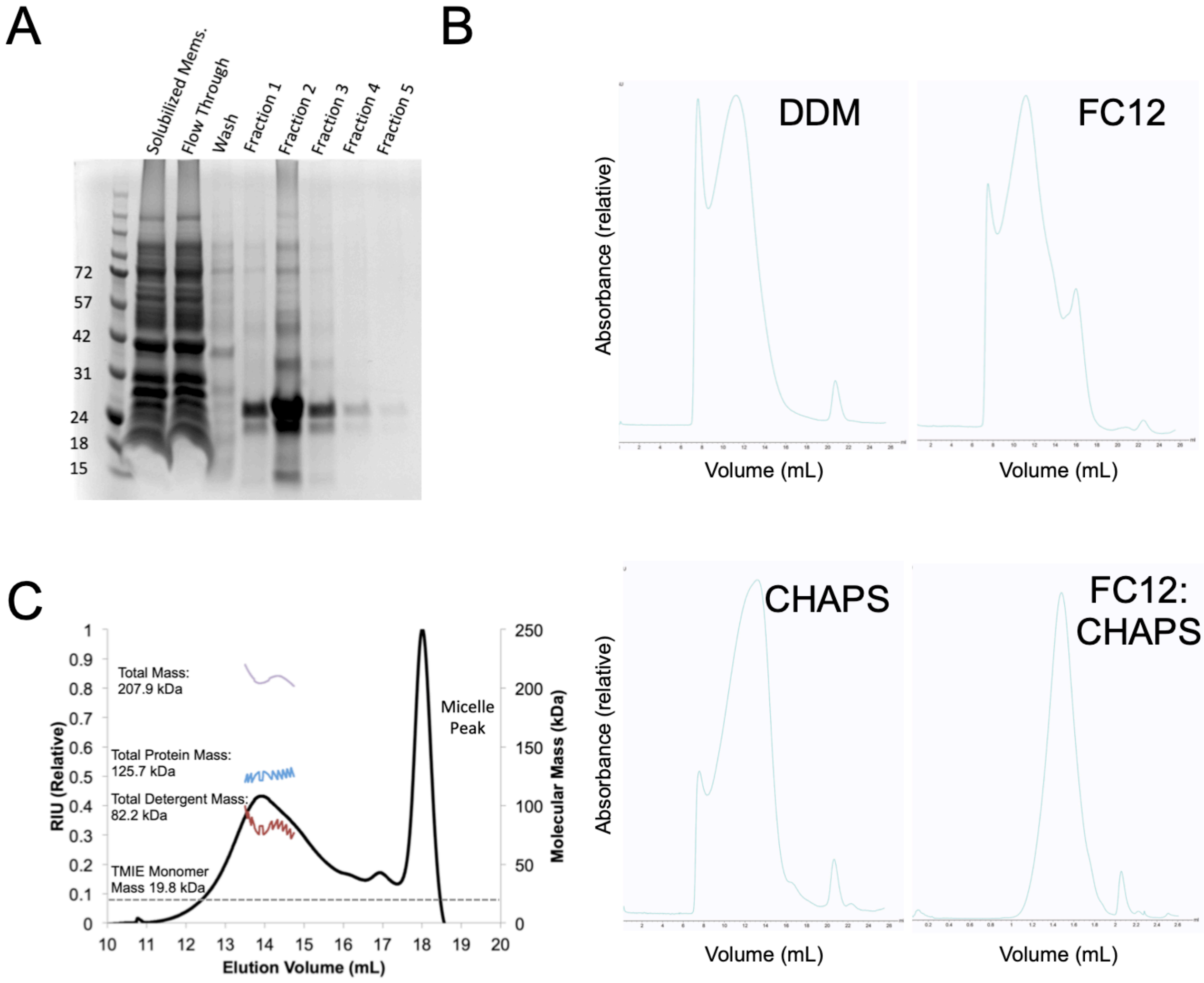

Figure 5.4: TMIE purification, solution behavior detergent screen, and MALS analysis (A) SDS-PAGE of initial purification of C41(DE3) expressed TMIE via nickel charged IMAC sepharose. TMIE was solubilized with 2% DDM. (B) Size exclusion profiles of TMIE exchanged into different detergent. TMIE had the best SEC profile in a detergent mixture of 2 mM FC12 and 0.5 mM CHAPS. DDM, FC12, and CHAPS samples were run over GE Superose 6 10/300 column. FC12:CHAPS was run over GE Superose 6 increase 3.2/300 column. (C) Size-exclusion chromatography with inline multi-angle light scattering measurements estimate the molecular mass of TMIE:FC12:CHAPS complex to be 207.9 kDa. Of this, 125.7 kDa is protein and 82.2 kDa is detergent.

shoulder on one side, but was smooth and sharp on the other. The chromatogram for the FC12 and CHAPS produced a nice elution profile with no signal in the void volume.

In order to measure the mass of the isolated TMIE species, I used size-exclusion chromatography with inline multi-angle light scattering measurements (SEC-MALS). With SEC-MALS it is possible to determine the mass of a membrane protein-micelle complex as well as the component masses of the detergent and protein constituents (Gimpl et al., 2016). In order to do this calculation, the refractive indexes (dn/dc) and extinction coefficients (ε_{280}) for both the protein and the detergent need to be known. These values for the protein species are fairly easy to procure, with the dn/dc of most proteins being 0.185 mL/g, and the ε_{280} being calculable from the protein sequence (Zhao et al., 2011). For detergents, these values are less readily available, particularly for mixtures of detergents. In order to obtain the ε_{280} for the FC12:CHAPS mixture, I measured the A_{280} of FC12:CHAPS solutions at 10% and calculated the extinction coefficient using the Beer-Lambert equation. In order to measure the dn/dc of FC12:CHAPS, mixture I measured the signal produced by 100 μL injections of 10%, 7.5%, 5%, and 2.5% solutions ran through the refractometer of our SEC-MALS. The dn/dc of the detergent is calculated from the relationship between the mass of injected detergent against the integral of the corresponding signal peak measured by the refractometer. I used this technique measure the mass of FC12:CHAPS micelles, as well as DDM micelles as a control. I was able to measure micelle masses of 26 kDa for the FC12:CHAPS mixture and 68 kDa for DDM. For DDM, this micelle mass is consistent with the reported range, 50-70 kDa. While there is no previously reported value for the micelle size of the FC12:CHAPS mixture, it is more similar to the micelle sizes of FC12 at 19 kDa than CHAPS, that forms 6 kDa micelles (Anatrace). I then used our SEC-MALS

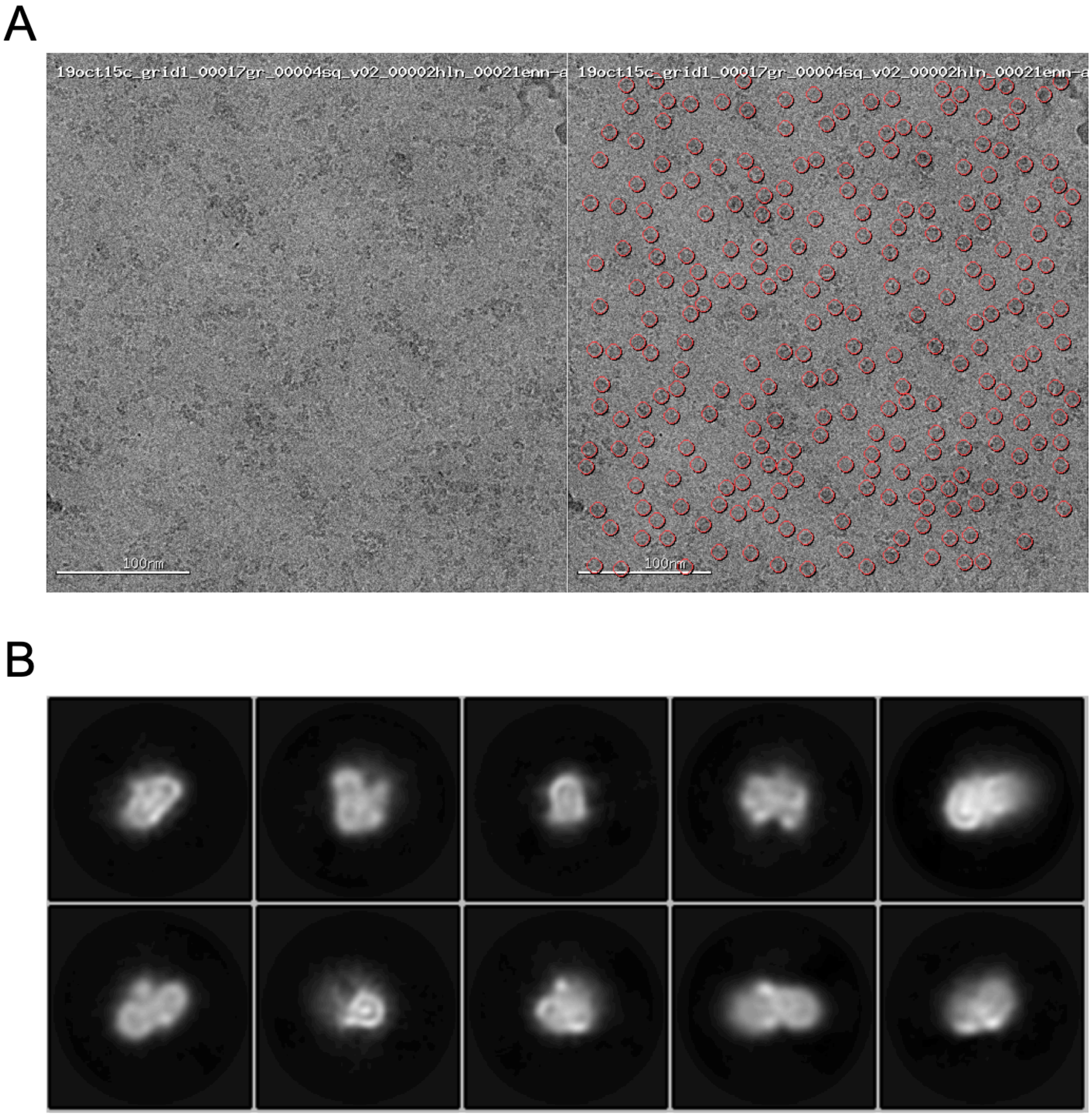

Figure 5.5: Cryo-EM micrographs of TMIE and class averages from 2D classification
(A) Representative electron micrograph of a sample of TMIE collected on a Titan Krios with K3 detector. Left, raw micrograph. Right, the same micrograph with picked particles circled in red. (B) Representative class averages did not reveal evidence of definable structural features. 2D classification and class averages were calculated with CryoSPARC.

equipment to perform the copolymer analysis with a sample FC12:CHAPS solubilized TMIE (Figure 5.4C). The total molecular mass of the protein:detergent complex was 207.9 kDa. Of this 82.2 kDa of mass corresponds to the FC12:CHAPS micelle, while the remaining 125.7 kDa corresponds with TMIE. The molecular weight of a single molecule of TMIE is 19.8 kDa, which is approximately one sixth the mass of TMIE measured by SEC-MALS, indicating that detergent solubilized TMIE may be a hexamer.

Despite the progress I have made thus far, I unfortunately was unable to get a sample that allowed for structural determination by single particle analysis cryo-EM. With the immense help of fellow lab member Micah Rapp, we have imaged a number of TMIE samples on a variety of electron microscopes. While we were able to generate flash frozen TMIE grids that had nice monodisperse particles, 2D classification of particles picked from the micrographs failed to produce class averages indicating an order structure was present (Figure 5.5). This includes samples of TMIE that were transferred from detergent micelles into various amphipols or nanodiscs. Thus, additional work will be required to generate a sample of TMIE that is of sufficient quality for structural studies.

5.3 TMC1

In order to overcome issues associated with the generation of TMC1 samples, we set out to explore the use of endogenous *C. elegans* expression in the production of TMC protein samples. As discussed in Chapter 1, *C. elegans* have their own ortholog of TMC1, TMC-1. While *C. elegans* TMC-1 has a slightly higher sequence identity with mammalian TMC3 – 30% pairwise sequence identity – it has a 28% pairwise sequence identity with mammalian TMC1. Additionally, mammalian TMC1 and TMC2 can compensate for the loss of TMC-1 in *C. elegans,* suggesting they have similar functionality. Structural and biochemical characterization of *C.*

elegans TMC-1 would thus be able to provide greater insight into the TMC protein family as an ortholog than have been obtained from suspected homologs such as TMEM16 (Ballesteros et al., 2018; Pan et al., 2018). *C. elegans* TMC-1 is expressed in a number of neuronal and muscular cells, increasing the potential yield (Figure 5.6A) (Yue et al., 2018). Our approach in this endeavor was to utilize a commercial service that performs CRISPR/Cas9 editing of *C. elegans* to append an affinity tag on the endogenously produced TMC-1. This approach was modeled after the one used in structural studies of the Plasmodium translocon of exported proteins (PTEX), a protein that has known issues with heterologous expression (Ho et al., 2018). In this study, CRISPR/Cas9 was used to edit the *Plasmodium falciparum* genome to append an affinity-tag to PTEX, facilitating the purification of the endogenously expressed protein.

The affinity tag that we chose comes from a recently proposed purification system based on the interaction between the bacterial toxin colicin E7 (CE7) and its anti-toxin immunity protein 7 (Im7) (Vassylyeva et al., 2017). In the wild, Colicin E7 is encoded on a plasmid carried by a host *E. coli* cell, which in turn produces and secretes CE7 to kill nearby sensitive *E.coli* that do not carry the plasmid. After entry into a susceptible *E. coli* cell, the DNase domain of Colicin E7 attacks the cells chromosome and kills the cell (Wallis et al., 1995a; Wallis et al., 1995b). Theoretically, apart from considerations of entry, a single molecule of CE7 is sufficient to kill a cell (Wallis et al., 1995b). To prevent the host cell, which produces and secretes CE7, from killing itself by producing the toxin and to protect the host cell immune from CE7 produced by another *E. coli* cell, the host cell also produces a 10 kDa immunity protein, IM7. Since a single molecule of CE7 can be cytotoxic, the IM7 antitoxin has evolved to have an extremely tight interaction with the DNase domain of CE7, with a dissociation constant on the order of 10^{-14}-10^{-17} M (Wallis et al., 1995a; Wallis et al., 1995b). In order to functionalize this high-affinity

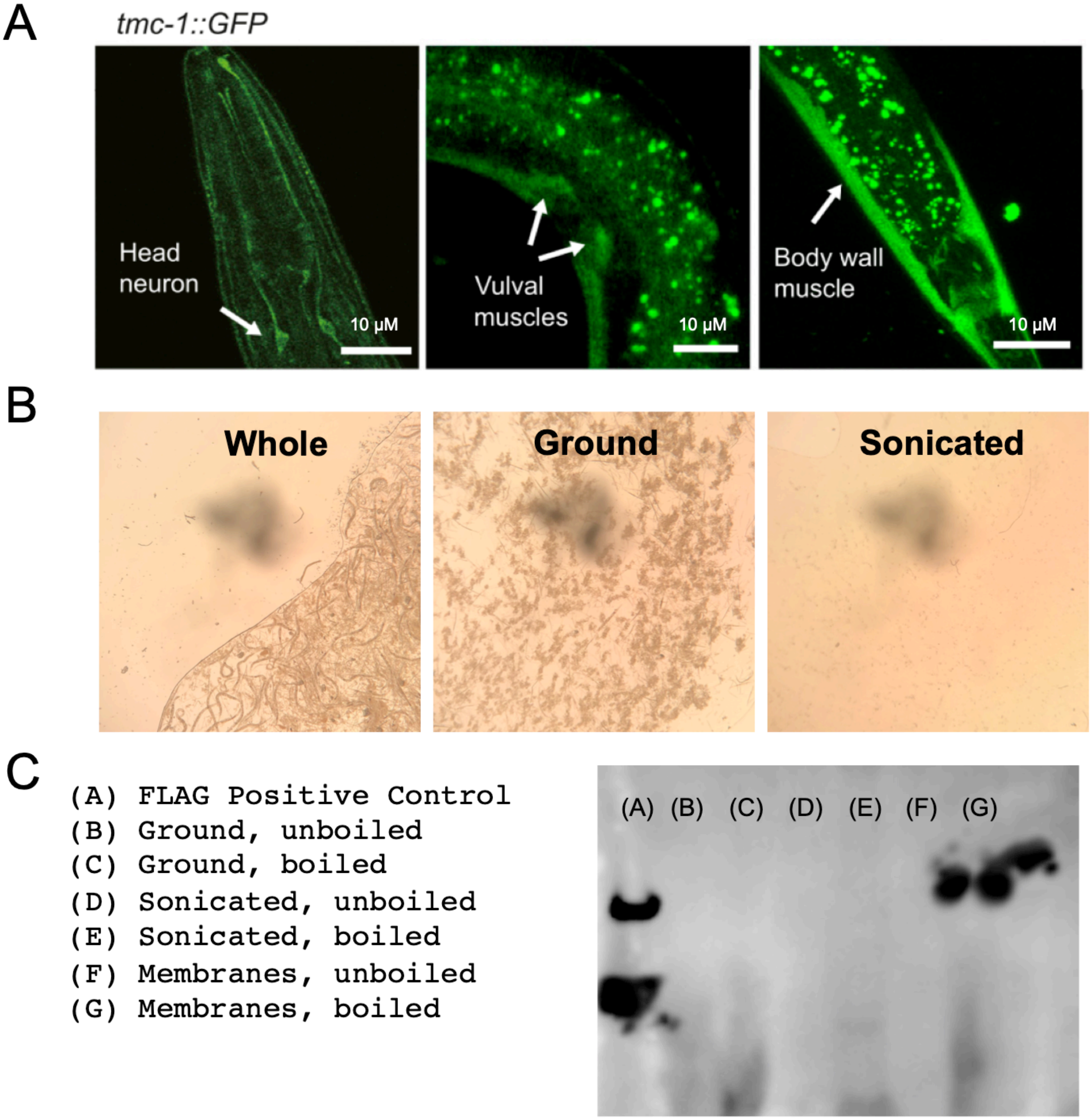

Figure 5.6: Western Blot confirms presence of FLAG tagged TMC-1 in CRISPR edited *Caenorhabditis elegans*

(A) GFP-tagged TMC-1 reveals TMC-1 is widely expressed in *C. elegans* neuronal and muscle cells. (Adapted from Yue et al. 2018). (B) Light micrographs showing the state of worm tissue during various stages of homogenization. Left is an image of whole animals, middle is after grinding with Wheaton Dura-grind™, right is after sonication. (C) Western blot showing positive detection of tagged TMC-1, only after separation of membrane components.

interaction, Vassylyeva et al. (2017) generated a modified version of CE7, which they termed CL7. They introduced twelve mutations in the DNase domain of CE7 that prevent the protein from both binding to DNA and catalyzing the hydrolytic cleavage of DNA. This non-toxic CL7 can be safely expressed, and conjugated to a resin for purification of IM7 tagged proteins. For our CRISPR-edited *C. elegans,* we appended the sequence of IM7 to the C-terminus of TMC-1, separated by a 6-residue serine-glycine linker. In addition to the IM7 domain, we also included a FLAG tag for detection of the protein by western blot.

Large amounts of CRISPR-edited *C. elegans* biomass were produced using a liquid culture format. Liquid growth media (nematode growth media, NGM) was composed of 50 mM NaCl, 2.5 g/L peptone, 25 mM KPO_4 at pH 6.0, 1mM $MgSO_4$, 1mM $CaCl_2$, 1 mg/L cholesterol with ampicillin and amphotericin B to control the growth of undesirable bacteria and mold. One liter *C. elegans* liquid cultures were inoculated with worms grown in a 150mm-diameter NMG-agar plate that had recently exhausted its food source. Plates used for inoculation were washed several times with ten milliliters of liquid culture media to suspend the *C. elegans;* suspended worms were then transferred by pipetted into the liquid culture. Additionally, each liter of culture was supplied with two pellets of previously grown NA22 *E. coli* grown in one liter of terrific broth. To prevent contamination from other bacteria, NA22 *E. coli* was transformed with a plasmid to confer ampicillin resistance. *C. elegans* liquid cultures were allowed to grow for approximately one week, or until the turbidity of the media began to decrease. *C. elegans* were harvested by centrifugation at 4000 RPM and subsequent filtration using a fine mesh screen. Final approximate yield of *C. elegans* biomass from a 1-liter culture was in the range of 5-15 grams.

C. elegans are protected by a tough cuticle that is capable of withstanding harsh chemical environments and pressures of 7400 psi (Bhaskaran et al., 2011). In order to extract protein, whole *C. elegans* pellets were first diluted with TBS to a final volume of ~35 mL and then disrupted using a Wheaton Dura-Grind™ dounce-type stainless steel tissue grinder. Ground *C. elegans* were further homogenized using sonication with a probe-type sonicator. After homogenization, no large animal debris was discernable upon inspection with a light microscope (Figure 5.6B). Similar to what was done for TMIE samples, sonicated *C. elegans* homogenate was spun for 10 minutes at 8000 rpm to remove crude debris. The supernatant from the low-speed centrifugation step was then spun for 50 minutes at 45000 rpm in order to pellet membranes. Throughout this process, samples were taken for analysis by western blot (Figure 5.6C). Interestingly, while our CRISPR edited TMC-1 was detected, it only became detectable after the isolation of membranes from *C. elegans* homogenate.

While I was able to show that our CRISPR-edited *C. elegans* TMC-1 was being expressed with the tag, I ran into issues with purification using the CL7:IM7 purification system. In our implementation of the CL7:IM7 purification system, we generated a version of CL7 that had an N-Terminal 8xHis-tag. We expressed this His-tagged CL7 in very high quantities, which enabled us to saturate a small nickel-charged IMAC sepharose column. After binding of our IM7 tagged protein to the CL7-saturated-nickel column we intended to elute using high concentrations of imidazole, thus purifying a TMC-1 with attached CL7. Unfortunately, only the CL7 was detected in elution. With a capacity of approximately 20 mg of protein per mL of nickel-charged IMAC sepharose resin, this is unsurprising. Thus, lower amounts of target protein can easily become lost in the high amount of CL7 bait.

5.4 Discussion and Future Directions

By utilizing a bacterial expression system, I developed protocols to produce high yields of TMIE in a relatively short amount of time. The yields could prove to be invaluable in future experimentation to optimize TMIE sample generation. While the samples of TMIE produced were of insufficient quality for single particle cryo-EM studies, the results thus far are encouraging. These samples have provided evidence of TMIE forming a higher-order oligomer, with a total molecular mass consistent with a hexamer. This hexameric nature may explain the dominant negative effects of certain TMIE constructs (Pacentine and Nicolson, 2019; Zhao et al., 2014). One of the limitations for sample optimization has been the long turnaround time for feedback of TMIE sample quality with cryo-EM data. With scope time being a relatively limited resource, it was often several weeks between the generation of a TMIE sample and the procurement of sufficient cryo-EM data to assess its quality. For future samples of TMIE, it may be prudent to optimize samples of TMIE by characterization of some other biophysical parameters, such as circular dichroism analysis. Additional optimization could come from characterization of TMIE with thermal shift assays. High throughput thermal shift assays using a thermofluor such as SPYRO Orange or the thiol reactive CPM would allow assessment of TMIE stability in a number of different buffer conditions as well as in different membrane-mimetics.

Through the use of CRISPR mediated genome editing, we generated a *C. elegans* line with a tagged TMC-1. While the particular affinity-tag used in our CRISPR-edited *C. elegans* was not immediately capable of generating a TMC-1 sample, the overall principle offers an attractive solution to generating a native-like TMC sample. Future work developing this methodology can be improved by using an affinity tag that has been validated and used successfully in other studies. For example, the purification of PTEX used a 3xFLAG tag (Ho et al., 2018). Alternatively, modifying of the IM7 tag to include an intein would allow for thiol induced self-cleavage and thus specific elution from the column (Chong et al., 1997). In addition to changes to the affinity tag, there is also the possibility to swap the *C. elegans* TMC-1 for mammalian TMC1 or TMC2. It has already been established that the mammalian homologues can be expressed in *C. elegans*, and their ability to alleviate the ΔTMC-1 phenotype indicates the mammalian TMC1 would be in a functionally relevant state.

Recently, our collaborator Ulirich Müller has conveyed that his group has had some success with TMC1 expression and surface trafficking in *Xenopus laevis* oocytes (personal correspondence). Previously, Harkom et al. (2019) used *Xenopus* oocytes to express TMC1 for some of their electrophysiology studies. However, they did not report experiments that investigated whether TMC1 expressed the absence of KCNQ1 made it to the cell surface of oocytes, which appears to be the case. However, generation of a sufficient amount of TMC1 protein from *Xenopus* oocytes may require cRNA microinjection of hundreds of individual oocytes. Despite this, *Xenopus* oocytes could prove to be an invaluable tool for expressing TMC1 for electrophysiology and structural studies.

– Chapter 6–

Conclusions and Outlook

6.1 Conclusions and Outlook

Through a biophysical dissection of the PCDH15 extracellular domain coupled with electron microscopy studies we were able to identify the two *cis*-dimeric interfaces that facilitate the overall double-helical architecture this component of the tip link. Our results suggest that helical unwinding of PCDH15, and presumably CDH23, can provide one mechanism for tip link extension on the order of 12 nm. The high-resolution crystal structure of the PCDH15 EC1-EC3 dimer allowed us to visualize how this fragment undergoes self-interaction through cadherin noncanonical features. This structure allowed us to design mutants that were capable of disrupting dimerization, as well as mutants that modified interactions at the PCDH15 EC1-EC3 dimer interface. By expressing these mutant forms of PCDH15 in hair cells, we were able to demonstrate that disruption of this critical interface leads to decreased mechanoelectrical transduction signals *in situ*. Thus PCDH15 dimerization is a critical mechanism for MET.

We used photonic force microscopy to directly measure the physical properties of a monomeric PCDH15 extracellular domain fragment that was generated using the knowledge from our structural studies of PCDH15. By measuring the force-extension relationships from single molecules of this monomeric PCDH15 fragment with a custom built photonic force microscope, we were able to demonstrate experimentally that its stiffness is consistent with the stiffness of the gating spring, contrasting with numerous prior results from steered molecular dynamics simulations indicating the contrary. These data allowed us to suggest that the tip link proteins are indeed the MET gating spring. Additionally, the data from these single molecule experiments also allowed us to characterize the unfolding rates of the PCDH15 cadherin domains, when coupled with other data that suggest that some tip links that are held at a higher resting tensions such as those in high frequency outer hair cells, may have persistently unfolded domains. We suggest that this is an additional mechanism for tip link extension. However, it remains to be seen how the unfolding rates of cadherin domains in PCDH15 are affected by dimerization, which would be expected to provide increased structural stability.

Using small serial deletions of full length TMC1 we were able to define a novel region of TMC1 that is necessary for interaction with the EF-hand Ca^{2+} binding protein CIB2, known to be critical for MET. Through alanine-scanning mutagenesis, we found that mutation of this previously uncharacterized region results in a more dramatic and consistent loss of CIB2 interaction than the TMC1 region previously reported by Giese et al (2017). While the TMC1 region defined by Giese et al (2017) may contribute to CIB2 binding, the TMC1 region we defined is far more sensitive to mutations and is highly conserved. We used size-exclusion chromatography to preform peptide-binding assays to confirm this interaction with purified CIB3 and synthesized peptides. From these data, we can infer that this 50-residue TMC1 fragment is sufficient for CIB2 binding. It also suggests that this fragment on TMC1 has some flexibility and is not tightly packed into a uniquely defined structure. We determined high-resolution crystal structures that revealed unexpectedly that CIB3 homodimerize through a domain-swap mechanism, which contrasts with the dimerization mechanism reported for related NCS proteins. We determined a crystal structure of the biochemically identified TMC1 peptide bound to CIB3, allowing us to visualize the molecular underpinnings of this interaction. Unitary channel recordings demonstrate that CIB2 mutation modulates the single channel conductance of the MET channel. Thus, CIB2 is a regulator of MET and binding of CIB2 to TMC1 is necessary for proper MET function. Analysis of conservation shows that the residues involved in the CIB3:TMC1 interaction are highly conserved, suggesting that the mechanism by which CIB2 regulates TMC1 is also conserved.

Lastly, this thesis has presented preliminary data aimed at establishing protocols for the generation of samples of TMIE. Through a series of experiments, I devised methods for expressing and purifying milligram quantities of TMIE. I used SEC-MALS experiments to measure the molecular mass of detergent solubilized TMIE. Using copolymer analysis from these SEC-MALS data, I found evidence that TMIE forms a hexamer. While structural studies of TMIE have up to this point been unsuccessful, the protocols I have established provide a strong foundation for continued work. Additionally, I have outlined proof-of-concept work for generating samples of native-like of a TMC family protein using endogenous expression of TMC-1 in *C. elegans* of CRISPR-tagged protein. While this work is still in preliminary stages, it outlines an interesting approach that could be adapted for the generation mammalian TMC protein samples.

While the work presented in this thesis have contributed to our understanding of the molecular principles at play in MET, there remain many unanswered questions. What is the identity of the MET channel? What are the structural determinants of MET channel gating? How does the CDH23 ectodomain dimerize, what is its structure, and how does it contribute to its gating spring function? What are the mechanical and elastic properties of CDH23 and of the entire tip link? What are the structures of TMC1, TMIE, and the putative complex formed between them? What are the molecular mechanisms that CIB2 and CIB3 use to modulate TMC1? And at the upper-insertion point of the tip link, what are the specific roles of the various myosin isozymes?

The next decade holds great promise for extending our understanding of hair cell mechanoelectrical transduction. With the maturation of single particle cryo-EM analysis as a tool for near-atomic resolution structure determination, structural information for the membrane components of MET are far more accessible than they were previously. Additionally, single particle cryo-EM is an attractive approach for studying other components of the hair bundle, in particular the large extracellular regions of VLGR1, USH2A, and PTPRQ. VLGR1 and USH2A are associated with the ankle linkages of hair bundles and there remains a severe lack of biochemical and structural characterization of these proteins. The extracellular domains of these proteins are massive with molecular weights of 640 kDa and 548 kDa, respectively. Additionally, they have fairly simple domain structures. VLGR1 has 35 Calx-beta domains and 6 EAR domains between Calx-beta domains 22 and 23. USH2A has 10 laminin EGF-like domains, 36 fibronectin type-3 domains, and 2 laminin G-like domains between the fifth and sixth fibronectin domains. Due to their large size, these proteins would be prime candidates for single particle analysis with Cryo-EM. While smaller in size at 209 kDa, the extracellular domain of PTPRQ that is associated with the shaft connectors of the hair bundle also lacks biochemical characterization. The extracellular domain of PTPRQ, similar to USH2A, is predicted to have 17 fibronectin type-3 domains. While it should be possible to study PTPRQ with cryo-EM, it is also feasible to make serial domain deletions to detect the potential binding regions and crystalize those fragments.

In addition to structural studies, the emergence of CRISPR/Cas9 genome editing tools provides a powerful way to hasten the development of edited animal models. In particular, myosin IIIa, myosin VIa, myosin VII, and myosin XVa can all be modified by a similar tyrosine to glycine mutations used in the Myosin Ic experiments. This mutation would make the particular edited myosin isozyme susceptible to inhibition by NMB-ADP; wild type myosins would remain unaffected by the bulkier nucleotide. Thus far, studies have attempted to assign function to these myosin isozymes by studying the effect of knockouts or functionally null mutants. Myosin IIIa has been implicated as a regulator of stereocilia height (Salles et al., 2009). Myosin VI, which moves in retrograde, has been suggested to be necessary for the removal of proteins that have an ephemeral role in the development of MET machinery (Marcotti et al., 2016). Myosin VII, which localizes to the upper tip link density, has been implicated as being necessary for putting tension on the tip link as hair cells with mutant Myosin VII require much greater displacements to evoke currents (Kros et al., 2002). Myosin XVa has been shown to have a role in adaptation and in calcium modulation of the channel open state probability (Stepanyan and Frolenkov, 2009). However, all of the functional experiments of these myosin isozymes assigned function based on observation of homozygous mutants. Thus, there is the potential that the effect of these mutations on MET properties arise as the result of developmental issues rather than a disruption of an active role in MET. Use of isoform-specific chemical inhibition by NMB-ADP would allow for a more accurate understanding of a particular myosin isozyme's role in MET while minimizing potential contributions from defects in hair bundle development. Overall, understanding of the nuances of mechanoelectrical transduction will undoubtedly be enabled by the continued advancement of the structural and biochemical descriptions of its molecular machinery.

REFERENCES

Adato, A., Lefevre, G., Delprat, B., Michel, V., Michalski, N., Chardenoux, S., Weil, D., El-Amraoui, A., and Petit, C. (2005a). Usherin, the defective protein in Usher syndrome type IIA, is likely to be a component of interstereocilia ankle links in the inner ear sensory cells. Human molecular genetics *14*, 3921-3932.

Adato, A., Michel, V., Kikkawa, Y., Reiners, J., Alagramam, K.N., Weil, D., Yonekawa, H., Wolfrum, U., El-Amraoui, A., and Petit, C. (2005b). Interactions in the network of Usher syndrome type 1 proteins. Human molecular genetics *14*, 347-356.

Ahmed, Z.M., Goodyear, R., Riazuddin, S., Lagziel, A., Legan, P.K., Behra, M., Burgess, S.M., Lilley, K.S., Wilcox, E.R., Riazuddin, S.*, et al.* (2006). The tip-link antigen, a protein associated with the transduction complex of sensory hair cells, is protocadherin-15. The Journal of neuroscience : the official journal of the Society for Neuroscience *26*, 7022-7034.

Ahmed, Z.M., Morell, R.J., Riazuddin, S., Gropman, A., Shaukat, S., Ahmad, M.M., Mohiddin, S.A., Fananapazir, L., Caruso, R.C., Husnain, T.*, et al.* (2003a). Mutations of MYO6 are associated with recessive deafness, DFNB37. American journal of human genetics *72*, 1315-1322.

Ahmed, Z.M., Riazuddin, S., Ahmad, J., Bernstein, S.L., Guo, Y., Sabar, M.F., Sieving, P., Riazuddin, S., Griffith, A.J., Friedman, T.B.*, et al.* (2003b). PCDH15 is expressed in the neurosensory epithelium of the eye and ear and mutant alleles are responsible for both USH1F and DFNB23. Human molecular genetics *12*, 3215-3223.

Ahmed, Z.M., Riazuddin, S., Bernstein, S.L., Ahmed, Z., Khan, S., Griffith, A.J., Morell, R.J., Friedman, T.B., Riazuddin, S., and Wilcox, E.R. (2001). Mutations of the protocadherin gene PCDH15 cause Usher syndrome type 1F. American journal of human genetics *69*, 25-34.

Ahmed, Z.M., Smith, T.N., Riazuddin, S., Makishima, T., Ghosh, M., Bokhari, S., Menon, P.S., Deshmukh, D., Griffith, A.J., Riazuddin, S.*, et al.* (2002). Nonsyndromic recessive deafness DFNB18 and Usher syndrome type IC are allelic mutations of USHIC. Human genetics *110*, 527-531.

Al-Amoudi, A., Norlen, L.P., and Dubochet, J. (2004). Cryo-electron microscopy of vitreous sections of native biological cells and tissues. Journal of structural biology *148*, 131-135.

Alagramam, K.N., Murcia, C.L., Kwon, H.Y., Pawlowski, K.S., Wright, C.G., and Woychik, R.P. (2001). The mouse Ames waltzer hearing-loss mutant is caused by mutation of Pcdh15, a novel protocadherin gene. Nature genetics *27*, 99-102.

Ames, J.B. (2018). Dimerization of Neuronal Calcium Sensor Proteins. Frontiers in molecular neuroscience *11*, 397.

Ames, J.B., and Lim, S. (2012). Molecular structure and target recognition of neuronal calcium sensor proteins. Biochimica et biophysica acta *1820*, 1205-1213.

Araya-Secchi, R., Neel, B.L., and Sotomayor, M. (2016). An elastic element in the protocadherin-15 tip link of the inner ear. Nature communications *7*, 13458.

Asai, Y., Pan, B., Nist-Lund, C., Galvin, A., Lukashkin, A.N., Lukashkina, V.A., Chen, T., Zhou, W., Zhu, H., Russell, I.J.*, et al.* (2018). Transgenic Tmc2 expression preserves inner ear hair cells and vestibular function in mice lacking Tmc1. Scientific reports *8*, 12124.

Ashmore, J.F. (1987). A fast motile response in guinea-pig outer hair cells: the cellular basis of the cochlear amplifier. The Journal of physiology *388*, 323-347.

Assad, J.A., Hacohen, N., and Corey, D.P. (1989). Voltage dependence of adaptation and active bundle movement in bullfrog saccular hair cells. Proceedings of the National Academy of Sciences of the United States of America *86*, 2918-2922.

Assad, J.A., Shepherd, G.M., and Corey, D.P. (1991). Tip-link integrity and mechanical transduction in vertebrate hair cells. Neuron *7*, 985-994.

Auer, M., Koster, A.J., Ziese, U., Bajaj, C., Volkmann, N., Wang da, N., and Hudspeth, A.J. (2008). Three-dimensional architecture of hair-bundle linkages revealed by electron-microscopic tomography. Journal of the Association for Research in Otolaryngology : JARO *9*, 215-224.

Ballesteros, A., Fenollar-Ferrer, C., and Swartz, K.J. (2018). Structural relationship between the putative hair cell mechanotransduction channel TMC1 and TMEM16 proteins. eLife *7*.

Bartsch, T.F., Hengel, F.E., Oswald, A., Dionne, G., Chipendo, I.V., Mangat, S.S., El Shatanofy, M., Shapiro, L., Muller, U., and Hudspeth, A.J. (2019). Elasticity of individual protocadherin 15 molecules implicates tip links as the gating springs for hearing. Proceedings of the National Academy of Sciences of the United States of America *116*, 11048-11056.

Basu, A., Lagier, S., Vologodskaia, M., Fabella, B.A., and Hudspeth, A.J. (2016). Direct mechanical stimulation of tip links in hair cells through DNA tethers. eLife *5*.

Belyantseva, I.A., Boger, E.T., and Friedman, T.B. (2003). Myosin XVa localizes to the tips of inner ear sensory cell stereocilia and is essential for staircase formation of the hair bundle. Proceedings of the National Academy of Sciences of the United States of America *100*, 13958-13963.

Belyantseva, I.A., Boger, E.T., Naz, S., Frolenkov, G.I., Sellers, J.R., Ahmed, Z.M., Griffith, A.J., and Friedman, T.B. (2005). Myosin-XVa is required for tip localization of whirlin and differential elongation of hair-cell stereocilia. Nature cell biology *7*, 148-156.

Beurg, M., Barlow, A., Furness, D.N., and Fettiplace, R. (2019). A Tmc1 mutation reduces calcium permeability and expression of mechanoelectrical transduction channels in cochlear hair cells. Proceedings of the National Academy of Sciences of the United States of America *116*, 20743-20749.

Beurg, M., Cui, R., Goldring, A.C., Ebrahim, S., Fettiplace, R., and Kachar, B. (2018). Variable number of TMC1-dependent mechanotransducer channels underlie tonotopic conductance gradients in the cochlea. Nature communications *9*, 2185.

Beurg, M., Fettiplace, R., Nam, J.H., and Ricci, A.J. (2009). Localization of inner hair cell mechanotransducer channels using high-speed calcium imaging. Nature neuroscience *12*, 553-558.

Beurg, M., Goldring, A.C., and Fettiplace, R. (2015a). The effects of Tmc1 Beethoven mutation on mechanotransducer channel function in cochlear hair cells. The Journal of general physiology *146*, 233-243.

Beurg, M., Nam, J.H., Chen, Q., and Fettiplace, R. (2010). Calcium balance and mechanotransduction in rat cochlear hair cells. Journal of neurophysiology *104*, 18-34.

Beurg, M., Nam, J.H., Crawford, A., and Fettiplace, R. (2008). The actions of calcium on hair bundle mechanics in mammalian cochlear hair cells. Biophysical journal *94*, 2639-2653.

Beurg, M., Xiong, W., Zhao, B., Muller, U., and Fettiplace, R. (2015b). Subunit determination of the conductance of hair-cell mechanotransducer channels. Proceedings of the National Academy of Sciences of the United States of America *112*, 1589-1594.

Bhaskaran, S., Butler, J.A., Becerra, S., Fassio, V., Girotti, M., and Rea, S.L. (2011). Breaking Caenorhabditis elegans the easy way using the Balch homogenizer: an old tool for a new application. Analytical biochemistry *413*, 123-132.

Blazejczyk, M., Sobczak, A., Debowska, K., Wisniewska, M.B., Kirilenko, A., Pikula, S., Jaworski, J., Kuznicki, J., and Wojda, U. (2009). Biochemical characterization and expression analysis of a novel EF-hand Ca2+ binding protein calmyrin2 (Cib2) in brain indicates its function in NMDA receptor mediated Ca2+ signaling. Archives of biochemistry and biophysics *487*, 66-78.

Bleckmann, H., and Zelick, R. (2009). Lateral line system of fish. Integrative zoology *4*, 13-25.

Boggon, T.J., Murray, J., Chappuis-Flament, S., Wong, E., Gumbiner, B.M., and Shapiro, L. (2002). C-cadherin ectodomain structure and implications for cell adhesion mechanisms. Science *296*, 1308-1313.

Bolz, H., von Brederlow, B., Ramirez, A., Bryda, E.C., Kutsche, K., Nothwang, H.G., Seeliger, M., del, C.S.C.M., Vila, M.C., Molina, O.P.*, et al.* (2001). Mutation of CDH23, encoding a new member of the cadherin gene family, causes Usher syndrome type 1D. Nature genetics *27*, 108-112.

Booth, K.T., Kahrizi, K., Babanejad, M., Daghagh, H., Bademci, G., Arzhangi, S., Zareabdollahi, D., Duman, D., El-Amraoui, A., Tekin, M.*, et al.* (2018). Variants in CIB2 cause DFNB48 and not USH1J. Clinical genetics *93*, 812-821.

Bork, J.M., Peters, L.M., Riazuddin, S., Bernstein, S.L., Ahmed, Z.M., Ness, S.L., Polomeno, R., Ramesh, A., Schloss, M., Srisailpathy, C.R*., et al.* (2001). Usher syndrome 1D and nonsyndromic autosomal recessive deafness DFNB12 are caused by allelic mutations of the novel cadherin-like gene CDH23. American journal of human genetics *68*, 26-37.

Bosher, S.K., and Warren, R.L. (1971). A study of the electrochemistry and osmotic relationships of the cochlear fluids in the neonatal rat at the time of the development of the endocochlear potential. The Journal of physiology *212*, 739-761.

Bosher, S.K., and Warren, R.L. (1978). Very low calcium content of cochlear endolymph, an extracellular fluid. Nature *273*, 377-378.

Bozovic, D., and Hudspeth, A.J. (2003). Hair-bundle movements elicited by transepithelial electrical stimulation of hair cells in the sacculus of the bullfrog. Proceedings of the National Academy of Sciences of the United States of America *100*, 958-963.

Brasch, J., Goodman, K.M., Noble, A.J., Rapp, M., Mannepalli, S., Bahna, F., Dandey, V.P., Bepler, T., Berger, B., Maniatis, T*., et al.* (2019). Visualization of clustered protocadherin neuronal self-recognition complexes. Nature *569*, 280-283.

Brasch, J., Harrison, O.J., Ahlsen, G., Carnally, S.M., Henderson, R.M., Honig, B., and Shapiro, L. (2011). Structure and binding mechanism of vascular endothelial cadherin: a divergent classical cadherin. Journal of molecular biology *408*, 57-73.

Brasch, J., Harrison, O.J., Honig, B., and Shapiro, L. (2012). Thinking outside the cell: how cadherins drive adhesion. Trends in cell biology *22*, 299-310.

Burgoyne, R.D. (2004). The neuronal calcium-sensor proteins. Biochimica et biophysica acta *1742*, 59-68.

Butler, R.A., and Honrubia, V. (1963). Responses of Cochlear Potentials to Changes in Hydrostatic Pressure. The Journal of the Acoustical Society of America *35*, 1188-1192.

Caberlotto, E., Michel, V., Foucher, I., Bahloul, A., Goodyear, R.J., Pepermans, E., Michalski, N., Perfettini, I., Alegria-Prevot, O., Chardenoux, S*., et al.* (2011). Usher type 1G protein sans is a critical component of the tip-link complex, a structure controlling actin polymerization in stereocilia. Proceedings of the National Academy of Sciences of the United States of America *108*, 5825-5830.

Caprara, G.A., Mecca, A.A., Wang, Y., Ricci, A.J., and Peng, A.W. (2019). Hair Bundle Stimulation Mode Modifies Manifestations of Mechanotransduction Adaptation. The Journal of neuroscience : the official journal of the Society for Neuroscience *39*, 9098-9106.

Chatzigeorgiou, M., Bang, S., Hwang, S.W., and Schafer, W.R. (2013). tmc-1 encodes a sodium-sensitive channel required for salt chemosensation in C. elegans. Nature *494*, 95-99.

Chong, S., Mersha, F.B., Comb, D.G., Scott, M.E., Landry, D., Vence, L.M., Perler, F.B., Benner, J., Kucera, R.B., Hirvonen, C.A*., et al.* (1997). Single-column purification of free recombinant proteins using a self-cleavable affinity tag derived from a protein splicing element. Gene *192*, 271-281.

Ciatto, C., Bahna, F., Zampieri, N., VanSteenhouse, H.C., Katsamba, P.S., Ahlsen, G., Harrison, O.J., Brasch, J., Jin, X., Posy, S.*, et al.* (2010). T-cadherin structures reveal a novel adhesive binding mechanism. Nature structural & molecular biology *17*, 339-347.

Cooper, S.R., Jontes, J.D., and Sotomayor, M. (2016). Structural determinants of adhesion by Protocadherin-19 and implications for its role in epilepsy. eLife *5*.

Corey, D.P., and Hudspeth, A.J. (1979). Ionic basis of the receptor potential in a vertebrate hair cell. Nature *281*, 675-677.

Corey, D.P., and Hudspeth, A.J. (1983a). Analysis of the microphonic potential of the bullfrog's sacculus. The Journal of neuroscience : the official journal of the Society for Neuroscience *3*, 942-961.

Corey, D.P., and Hudspeth, A.J. (1983b). Kinetics of the receptor current in bullfrog saccular hair cells. The Journal of neuroscience : the official journal of the Society for Neuroscience *3*, 962-976.

Corns, L.F., Johnson, S.L., Kros, C.J., and Marcotti, W. (2014). Calcium entry into stereocilia drives adaptation of the mechanoelectrical transducer current of mammalian cochlear hair cells. Proceedings of the National Academy of Sciences of the United States of America *111*, 14918-14923.

Corns, L.F., Johnson, S.L., Kros, C.J., and Marcotti, W. (2016). Tmc1 Point Mutation Affects Ca2+ Sensitivity and Block by Dihydrostreptomycin of the Mechanoelectrical Transducer Current of Mouse Outer Hair Cells. The Journal of neuroscience : the official journal of the Society for Neuroscience *36*, 336-349.

Crawford, A.C., Evans, M.G., and Fettiplace, R. (1989). Activation and adaptation of transducer currents in turtle hair cells. The Journal of physiology *419*, 405-434.

Crawford, A.C., Evans, M.G., and Fettiplace, R. (1991). The actions of calcium on the mechano-electrical transducer current of turtle hair cells. The Journal of physiology *434*, 369-398.

Crawford, A.C., and Fettiplace, R. (1985). The mechanical properties of ciliary bundles of turtle cochlear hair cells. The Journal of physiology *364*, 359-379.

Crooks, G.E., Hon, G., Chandonia, J.M., and Brenner, S.E. (2004). WebLogo: a sequence logo generator. Genome research *14*, 1188-1190.

Dal Cortivo, G., Marino, V., Iacobucci, C., Vallone, R., Arlt, C., Rehkamp, A., Sinz, A., and Dell'Orco, D. (2019). Oligomeric state, hydrodynamic properties and target recognition of human Calcium and Integrin Binding protein 2 (CIB2). Scientific reports *9*, 15058.

De-la-Torre, P., Choudhary, D., Araya-Secchi, R., Narui, Y., and Sotomayor, M. (2018). A Mechanically Weak Extracellular Membrane-Adjacent Domain Induces Dimerization of Protocadherin-15. Biophysical journal *115*, 2368-2385.

Denk, W., Holt, J.R., Shepherd, G.M., and Corey, D.P. (1995). Calcium imaging of single stereocilia in hair cells: localization of transduction channels at both ends of tip links. Neuron *15*, 1311-1321.

Denk, W., Keolian, R.M., and Webb, W.W. (1992). Mechanical response of frog saccular hair bundles to the aminoglycoside block of mechanoelectrical transduction. Journal of neurophysiology *68*, 927-932.

Di Palma, F., Holme, R.H., Bryda, E.C., Belyantseva, I.A., Pellegrino, R., Kachar, B., Steel, K.P., and Noben-Trauth, K. (2001). Mutations in Cdh23, encoding a new type of cadherin, cause stereocilia disorganization in waltzer, the mouse model for Usher syndrome type 1D. Nature genetics *27*, 103-107.

Dionne, G., Qiu, X., Rapp, M., Liang, X., Zhao, B., Peng, G., Katsamba, P.S., Ahlsen, G., Rubinstein, R., Potter, C.S.*, et al.* (2018). Mechanotransduction by PCDH15 Relies on a Novel cis-Dimeric Architecture. Neuron *99*, 480-492 e485.

Eatock, R.A., Corey, D.P., and Hudspeth, A.J. (1987). Adaptation of mechanoelectrical transduction in hair cells of the bullfrog's sacculus. The Journal of neuroscience : the official journal of the Society for Neuroscience *7*, 2821-2836.

Ebermann, I., Scholl, H.P., Charbel Issa, P., Becirovic, E., Lamprecht, J., Jurklies, B., Millan, J.M., Aller, E., Mitter, D., and Bolz, H. (2007). A novel gene for Usher syndrome type 2: mutations in the long isoform of whirlin are associated with retinitis pigmentosa and sensorineural hearing loss. Human genetics *121*, 203-211.

Effertz, T., Becker, L., Peng, A.W., and Ricci, A.J. (2017). Phosphoinositol-4,5-Bisphosphate Regulates Auditory Hair-Cell Mechanotransduction-Channel Pore Properties and Fast Adaptation. The Journal of neuroscience : the official journal of the Society for Neuroscience *37*, 11632-11646.

Elledge, H.M., Kazmierczak, P., Clark, P., Joseph, J.S., Kolatkar, A., Kuhn, P., and Muller, U. (2010). Structure of the N terminus of cadherin 23 reveals a new adhesion mechanism for a subset of cadherin superfamily members. Proceedings of the National Academy of Sciences of the United States of America *107*, 10708-10712.

Engstrom, H., and Engstrom, B. (1978). Structure of the hairs on cochlear sensory cells. Hearing research *1*, 49-66.

Erwin, D.H., and Davidson, E.H. (2002). The last common bilaterian ancestor. Development *129*, 3021-3032.

Fang, Q., Indzhykulian, A.A., Mustapha, M., Riordan, G.P., Dolan, D.F., Friedman, T.B., Belyantseva, I.A., Frolenkov, G.I., Camper, S.A., and Bird, J.E. (2015). The 133-kDa N-terminal domain enables myosin 15 to maintain mechanotransducing stereocilia and is essential for hearing. eLife *4*.

Farris, H.E., LeBlanc, C.L., Goswami, J., and Ricci, A.J. (2004). Probing the pore of the auditory hair cell mechanotransducer channel in turtle. The Journal of physiology *558*, 769-792.

Faucher, K., Parmentier, E., Becco, C., Vandewalle, N., and Vandewalle, P. (2010). Fish lateral system is required for accurate control of shoaling behaviour. Animal Behaviour *79*, 679-687.

Fettiplace, R. (2017). Hair Cell Transduction, Tuning, and Synaptic Transmission in the Mammalian Cochlea. Comprehensive Physiology *7*, 1197-1227.

Fettiplace, R., and Kim, K.X. (2014). The physiology of mechanoelectrical transduction channels in hearing. Physiological reviews *94*, 951-986.

Flock, A., and Strelioff, D. (1984). Graded and nonlinear mechanical properties of sensory hairs in the mammalian hearing organ. Nature *310*, 597-599.

Fontilla, M.F., and Peterson, E.H. (2000). Kinocilia heights on utricular hair cells. Hearing research *145*, 8-16.

Furness, D.N., and Hackney, C.M. (1985). Cross-links between stereocilia in the guinea pig cochlea. Hearing research *18*, 177-188.

Furness, D.N., Katori, Y., Nirmal Kumar, B., and Hackney, C.M. (2008). The dimensions and structural attachments of tip links in mammalian cochlear hair cells and the effects of exposure to different levels of extracellular calcium. Neuroscience *154*, 10-21.

Ge, J., Elferich, J., Goehring, A., Zhao, H., Schuck, P., and Gouaux, E. (2018). Structure of mouse protocadherin 15 of the stereocilia tip link in complex with LHFPL5. eLife *7*.

Genji, T., Nozawa, A., and Tozawa, Y. (2010). Efficient production and purification of functional bacteriorhodopsin with a wheat-germ cell-free system and a combination of Fos-choline and CHAPS detergents. Biochemical and biophysical research communications *400*, 638-642.

Gentry, H.R., Singer, A.U., Betts, L., Yang, C., Ferrara, J.D., Sondek, J., and Parise, L.V. (2005). Structural and biochemical characterization of CIB1 delineates a new family of EF-hand-containing proteins. The Journal of biological chemistry *280*, 8407-8415.

Giese, A.P.J., Tang, Y.Q., Sinha, G.P., Bowl, M.R., Goldring, A.C., Parker, A., Freeman, M.J., Brown, S.D.M., Riazuddin, S., Fettiplace, R., *et al.* (2017). CIB2 interacts with TMC1 and TMC2 and is essential for mechanotransduction in auditory hair cells. Nature communications *8*, 43.

Gillespie, P.G., Gillespie, S.K., Mercer, J.A., Shah, K., and Shokat, K.M. (1999). Engineering of the myosin-ibeta nucleotide-binding pocket to create selective sensitivity to N(6)-modified ADP analogs. The Journal of biological chemistry *274*, 31373-31381.

Gillespie, P.G., Wagner, M.C., and Hudspeth, A.J. (1993). Identification of a 120 kd hair-bundle myosin located near stereociliary tips. Neuron *11*, 581-594.

Gimpl, K., Klement, J., and Keller, S. (2016). Characterising protein/detergent complexes by triple-detection size-exclusion chromatography. Biological procedures online *18*, 4.

Gleason, M.R., Nagiel, A., Jamet, S., Vologodskaia, M., Lopez-Schier, H., and Hudspeth, A.J. (2009). The transmembrane inner ear (Tmie) protein is essential for normal hearing and balance in the zebrafish. Proceedings of the National Academy of Sciences of the United States of America *106*, 21347-21352.

Goldring, A.C., Beurg, M., and Fettiplace, R. (2019). The contribution of TMC1 to adaptation of mechanoelectrical transduction channels in cochlear outer hair cells. The Journal of physiology.

Goodman, K.M., Rubinstein, R., Dan, H., Bahna, F., Mannepalli, S., Ahlsen, G., Aye Thu, C., Sampogna, R.V., Maniatis, T., Honig, B.*, et al.* (2017). Protocadherin cis-dimer architecture and recognition unit diversity. Proceedings of the National Academy of Sciences of the United States of America *114*, E9829-E9837.

Goodman, K.M., Rubinstein, R., Thu, C.A., Bahna, F., Mannepalli, S., Ahlsen, G., Rittenhouse, C., Maniatis, T., Honig, B., and Shapiro, L. (2016a). Structural Basis of Diverse Homophilic Recognition by Clustered alpha- and beta-Protocadherins. Neuron *90*, 709-723.

Goodman, K.M., Rubinstein, R., Thu, C.A., Mannepalli, S., Bahna, F., Ahlsen, G., Rittenhouse, C., Maniatis, T., Honig, B., and Shapiro, L. (2016b). gamma-Protocadherin structural diversity and functional implications. eLife *5*.

Goodyear, R.J., Forge, A., Legan, P.K., and Richardson, G.P. (2010). Asymmetric distribution of cadherin 23 and protocadherin 15 in the kinocilial links of avian sensory hair cells. The Journal of comparative neurology *518*, 4288-4297.

Goodyear, R.J., Jones, S.M., Sharifi, L., Forge, A., and Richardson, G.P. (2012). Hair bundle defects and loss of function in the vestibular end organs of mice lacking the receptor-like inositol lipid phosphatase PTPRQ. The Journal of neuroscience : the official journal of the Society for Neuroscience *32*, 2762-2772.

Goodyear, R.J., Legan, P.K., Wright, M.B., Marcotti, W., Oganesian, A., Coats, S.A., Booth, C.J., Kros, C.J., Seifert, R.A., Bowen-Pope, D.F*., et al.* (2003). A receptor-like inositol lipid phosphatase is required for the maturation of developing cochlear hair bundles. The Journal of neuroscience : the official journal of the Society for Neuroscience *23*, 9208-9219.

Grati, M., and Kachar, B. (2011). Myosin VIIa and sans localization at stereocilia upper tip-link density implicates these Usher syndrome proteins in mechanotransduction. Proceedings of the National Academy of Sciences of the United States of America *108*, 11476-11481.

Guo, Y., Wang, Y., Zhang, W., Meltzer, S., Zanini, D., Yu, Y., Li, J., Cheng, T., Guo, Z., Wang, Q*., et al.* (2016). Transmembrane channel-like (tmc) gene regulates Drosophila larval locomotion. Proceedings of the National Academy of Sciences of the United States of America *113*, 7243-7248.

Hacohen, N., Assad, J.A., Smith, W.J., and Corey, D.P. (1989). Regulation of tension on hair-cell transduction channels: displacement and calcium dependence. The Journal of neuroscience : the official journal of the Society for Neuroscience *9*, 3988-3997.

Hahn, Y., Kim, D.S., Pastan, I.H., and Lee, B. (2009). Anoctamin and transmembrane channel-like proteins are evolutionarily related. International journal of molecular medicine *24*, 51-55.

Harkcom, W.T., Papanikolaou, M., Kanda, V., Crump, S.M., and Abbott, G.W. (2019). KCNQ1 rescues TMC1 plasma membrane expression but not mechanosensitive channel activity. Journal of cellular physiology *234*, 13361-13369.

Harrison, O.J., Bahna, F., Katsamba, P.S., Jin, X., Brasch, J., Vendome, J., Ahlsen, G., Carroll, K.J., Price, S.R., Honig, B., *et al.* (2010). Two-step adhesive binding by classical cadherins. Nature structural & molecular biology *17*, 348-357.

Harrison, O.J., Brasch, J., Katsamba, P.S., Ahlsen, G., Noble, A.J., Dan, H., Sampogna, R.V., Potter, C.S., Carragher, B., Honig, B., *et al.* (2020). Family-wide Structural and Biophysical Analysis of Binding Interactions among Non-clustered delta-Protocadherins. Cell reports *30*, 2655-2671 e2657.

Harrison, O.J., Brasch, J., Lasso, G., Katsamba, P.S., Ahlsen, G., Honig, B., and Shapiro, L. (2016). Structural basis of adhesive binding by desmocollins and desmogleins. Proceedings of the National Academy of Sciences of the United States of America *113*, 7160-7165.

Harrison, O.J., Jin, X., Hong, S., Bahna, F., Ahlsen, G., Brasch, J., Wu, Y., Vendome, J., Felsovalyi, K., Hampton, C.M., *et al.* (2011). The extracellular architecture of adherens junctions revealed by crystal structures of type I cadherins. Structure *19*, 244-256.

He, L., Gulyanon, S., Mihovilovic Skanata, M., Karagyozov, D., Heckscher, E.S., Krieg, M., Tsechpenakis, G., Gershow, M., and Tracey, W.D., Jr. (2019). Direction Selectivity in Drosophila Proprioceptors Requires the Mechanosensory Channel Tmc. Current biology : CB *29*, 945-956 e943.

Hirono, M., Denis, C.S., Richardson, G.P., and Gillespie, P.G. (2004). Hair cells require phosphatidylinositol 4,5-bisphosphate for mechanical transduction and adaptation. Neuron *44*, 309-320.

Ho, C.M., Beck, J.R., Lai, M., Cui, Y., Goldberg, D.E., Egea, P.F., and Zhou, Z.H. (2018). Malaria parasite translocon structure and mechanism of effector export. Nature *561*, 70-75.

Holt, J.R., Gillespie, S.K., Provance, D.W., Shah, K., Shokat, K.M., Corey, D.P., Mercer, J.A., and Gillespie, P.G. (2002). A chemical-genetic strategy implicates myosin-1c in adaptation by hair cells. Cell *108*, 371-381.

Howard, J., and Ashmore, J.F. (1986). Stiffness of sensory hair bundles in the sacculus of the frog. Hearing research *23*, 93-104.

Howard, J., and Hudspeth, A.J. (1988). Compliance of the hair bundle associated with gating of mechanoelectrical transduction channels in the bullfrog's saccular hair cell. Neuron *1*, 189-199.

Hudspeth, A. (1997). Mechanical amplification of stimuli by hair cells. Current opinion in neurobiology *7*, 480-486.

Hudspeth, A.J. (1982). Extracellular current flow and the site of transduction by vertebrate hair cells. The Journal of neuroscience : the official journal of the Society for Neuroscience *2*, 1-10.

Hudspeth, A.J. (1985). The cellular basis of hearing: the biophysics of hair cells. Science *230*, 745-752.

Hudspeth, A.J. (2014). Integrating the active process of hair cells with cochlear function. Nature reviews Neuroscience *15*, 600-614.

Hudspeth, A.J., and Jacobs, R. (1979). Stereocilia mediate transduction in vertebrate hair cells (auditory system/cilium/vestibular system). Proceedings of the National Academy of Sciences of the United States of America *76*, 1506-1509.

Indzhykulian, A.A., Stepanyan, R., Nelina, A., Spinelli, K.J., Ahmed, Z.M., Belyantseva, I.A., Friedman, T.B., Barr-Gillespie, P.G., and Frolenkov, G.I. (2013). Molecular remodeling of tip links underlies mechanosensory regeneration in auditory hair cells. PLoS biology *11*, e1001583.

Jaiganesh, A., De-la-Torre, P., Patel, A.A., Termine, D.J., Velez-Cortes, F., Chen, C., and Sotomayor, M. (2018). Zooming in on Cadherin-23: Structural Diversity and Potential Mechanisms of Inherited Deafness. Structure *26*, 1210-1225 e1214.

Jaramillo, F., and Hudspeth, A.J. (1993). Displacement-clamp measurement of the forces exerted by gating springs in the hair bundle. Proceedings of the National Academy of Sciences of the United States of America *90*, 1330-1334.

Jewett, D.L., Romano, M.N., and Williston, J.S. (1970). Human auditory evoked potentials: possible brain stem components detected on the scalp. Science *167*, 1517-1518.

Jia, Y., Zhao, Y., Kusakizako, T., Wang, Y., Pan, C., Zhang, Y., Nureki, O., Hattori, M., and Yan, Z. (2019). TMC1 and TMC2 Proteins Are Pore-Forming Subunits of Mechanosensitive Ion Channels. Neuron.

Jin, L., and Harrison, S.C. (2002). Crystal structure of human calcineurin complexed with cyclosporin A and human cyclophilin. Proceedings of the National Academy of Sciences of the United States of America *99*, 13522-13526.

Jin, X., Walker, M.A., Felsovalyi, K., Vendome, J., Bahna, F., Mannepalli, S., Cosmanescu, F., Ahlsen, G., Honig, B., and Shapiro, L. (2012). Crystal structures of Drosophila N-cadherin ectodomain regions reveal a widely used class of Ca(2)+-free interdomain linkers. Proceedings of the National Academy of Sciences of the United States of America *109*, E127-134.

Johnson, S.L., Beurg, M., Marcotti, W., and Fettiplace, R. (2011). Prestin-driven cochlear amplification is not limited by the outer hair cell membrane time constant. Neuron *70*, 1143-1154.

Johnsson, B., Lofas, S., and Lindquist, G. (1991). Immobilization of proteins to a carboxymethyldextran-modified gold surface for biospecific interaction analysis in surface plasmon resonance sensors. Analytical biochemistry *198*, 268-277.

Kachar, B., Parakkal, M., Kurc, M., Zhao, Y., and Gillespie, P.G. (2000). High-resolution structure of hair-cell tip links. Proceedings of the National Academy of Sciences of the United States of America *97*, 13336-13341.

Kalay, E., Li, Y., Uzumcu, A., Uyguner, O., Collin, R.W., Caylan, R., Ulubil-Emiroglu, M., Kersten, F.F., Hafiz, G., van Wijk, E*., et al.* (2006). Mutations in the lipoma HMGIC fusion partner-like 5 (LHFPL5) gene cause autosomal recessive nonsyndromic hearing loss. Human mutation *27*, 633-639.

Kawashima, Y., Geleoc, G.S., Kurima, K., Labay, V., Lelli, A., Asai, Y., Makishima, T., Wu, D.K., Della Santina, C.C., Holt, J.R*., et al.* (2011). Mechanotransduction in mouse inner ear hair cells requires transmembrane channel-like genes. The Journal of clinical investigation *121*, 4796-4809.

Kawate, T., and Gouaux, E. (2006). Fluorescence-detection size-exclusion chromatography for precrystallization screening of integral membrane proteins. Structure *14*, 673-681.

Kazmierczak, P., Sakaguchi, H., Tokita, J., Wilson-Kubalek, E.M., Milligan, R.A., Muller, U., and Kachar, B. (2007). Cadherin 23 and protocadherin 15 interact to form tip-link filaments in sensory hair cells. Nature *449*, 87-91.

Kennedy, H.J., Crawford, A.C., and Fettiplace, R. (2005). Force generation by mammalian hair bundles supports a role in cochlear amplification. Nature *433*, 880-883.

Kennedy, H.J., Evans, M.G., Crawford, A.C., and Fettiplace, R. (2003). Fast adaptation of mechanoelectrical transducer channels in mammalian cochlear hair cells. Nature neuroscience *6*, 832-836.

Kenyon, E.J., Kirkwood, N.K., Kitcher, S.R., O'Reilly, M., Derudas, M., Cantillon, D.M., Goodyear, R.J., Secker, A., Baxendale, S., Bull, J.C*., et al.* (2017). Identification of ion-channel modulators that protect against aminoglycoside-induced hair cell death. JCI insight *2*.

Keresztes, G., Mutai, H., and Heller, S. (2003). TMC and EVER genes belong to a larger novel family, the TMC gene family encoding transmembrane proteins. BMC genomics *4*, 24.

Kim, K.X., Beurg, M., Hackney, C.M., Furness, D.N., Mahendrasingam, S., and Fettiplace, R. (2013). The role of transmembrane channel-like proteins in the operation of hair cell mechanotransducer channels. The Journal of general physiology *142*, 493-505.

Koppl, C., Wilms, V., Russell, I.J., and Nothwang, H.G. (2018). Evolution of Endolymph Secretion and Endolymphatic Potential Generation in the Vertebrate Inner Ear. Brain, behavior and evolution *92*, 1-31.

Kros, C.J., Marcotti, W., van Netten, S.M., Self, T.J., Libby, R.T., Brown, S.D., Richardson, G.P., and Steel, K.P. (2002). Reduced climbing and increased slipping adaptation in cochlear hair cells of mice with Myo7a mutations. Nature neuroscience *5*, 41-47.

Kudo, S., Caaveiro, J.M., and Tsumoto, K. (2016). Adhesive Dimerization of Human P-Cadherin Catalyzed by a Chaperone-like Mechanism. Structure *24*, 1523-1536.

Kurima, K., Ebrahim, S., Pan, B., Sedlacek, M., Sengupta, P., Millis, B.A., Cui, R., Nakanishi, H., Fujikawa, T., Kawashima, Y.*, et al.* (2015). TMC1 and TMC2 Localize at the Site of Mechanotransduction in Mammalian Inner Ear Hair Cell Stereocilia. Cell reports *12*, 1606-1617.

Kurima, K., Peters, L.M., Yang, Y., Riazuddin, S., Ahmed, Z.M., Naz, S., Arnaud, D., Drury, S., Mo, J., Makishima, T.*, et al.* (2002). Dominant and recessive deafness caused by mutations of a novel gene, TMC1, required for cochlear hair-cell function. Nature genetics *30*, 277-284.

Kurima, K., Yang, Y., Sorber, K., and Griffith, A.J. (2003). Characterization of the transmembrane channel-like (TMC) gene family: functional clues from hearing loss and epidermodysplasia verruciformis☆. Genomics *82*, 300-308.

Kwon, S.K., Kim, S.K., Lee, D.H., and Kim, J.F. (2015). Comparative genomics and experimental evolution of Escherichia coli BL21(DE3) strains reveal the landscape of toxicity escape from membrane protein overproduction. Scientific reports *5*, 16076.

Labay, V., Weichert, R.M., Makishima, T., and Griffith, A.J. (2010). Topology of transmembrane channel-like gene 1 protein. Biochemistry *49*, 8592-8598.

Lagziel, A., Ahmed, Z.M., Schultz, J.M., Morell, R.J., Belyantseva, I.A., and Friedman, T.B. (2005). Spatiotemporal pattern and isoforms of cadherin 23 in wild type and waltzer mice during inner ear hair cell development. Developmental biology *280*, 295-306.

Landau, M., Mayrose, I., Rosenberg, Y., Glaser, F., Martz, E., Pupko, T., and Ben-Tal, N. (2005). ConSurf 2005: the projection of evolutionary conservation scores of residues on protein structures. Nucleic acids research *33*, W299-302.

Lelli, A., Kazmierczak, P., Kawashima, Y., Muller, U., and Holt, J.R. (2010). Development and regeneration of sensory transduction in auditory hair cells requires functional interaction between cadherin-23 and protocadherin-15. The Journal of neuroscience : the official journal of the Society for Neuroscience *30*, 11259-11269.

Lentze, N., and Auerbach, D. (2008). Membrane-based yeast two-hybrid system to detect protein interactions. Current protocols in protein science *Chapter 19*, Unit 19 17.

Liu, S., Wang, S., Zou, L., Li, J., Song, C., Chen, J., Hu, Q., Liu, L., Huang, P., and Xiong, W. (2019). TMC1 is an essential component of a leak channel that modulates tonotopy and excitability of auditory hair cells in mice. eLife *8*.

Liu, X.Z., Walsh, J., Mburu, P., Kendrick-Jones, J., Cope, M.J., Steel, K.P., and Brown, S.D. (1997a). Mutations in the myosin VIIA gene cause non-syndromic recessive deafness. Nature genetics *16*, 188-190.

Liu, X.Z., Walsh, J., Tamagawa, Y., Kitamura, K., Nishizawa, M., Steel, K.P., and Brown, S.D. (1997b). Autosomal dominant non-syndromic deafness caused by a mutation in the myosin VIIA gene. Nature genetics *17*, 268-269.

Longo-Guess, C.M., Gagnon, L.H., Cook, S.A., Wu, J., Zheng, Q.Y., and Johnson, K.R. (2005). A missense mutation in the previously undescribed gene Tmhs underlies deafness in hurry-scurry (hscy) mice. Proceedings of the National Academy of Sciences of the United States of America *102*, 7894-7899.

Lu, H., Isralewitz, B., Krammer, A., Vogel, V., and Schulten, K. (1998). Unfolding of titin immunoglobulin domains by steered molecular dynamics simulation. Biophysical journal *75*, 662-671.

Lumpkin, E.A., and Hudspeth, A.J. (1995). Detection of Ca2+ entry through mechanosensitive channels localizes the site of mechanoelectrical transduction in hair cells. Proceedings of the National Academy of Sciences of the United States of America *92*, 10297-10301.

Lumpkin, E.A., and Hudspeth, A.J. (1998). Regulation of free Ca2+ concentration in hair-cell stereocilia. The Journal of neuroscience : the official journal of the Society for Neuroscience *18*, 6300-6318.

Lumpkin, E.A., Marquis, R.E., and Hudspeth, A.J. (1997). The selectivity of the hair cell's mechanoelectrical-transduction channel promotes Ca2+ flux at low Ca2+ concentrations. Proceedings of the National Academy of Sciences of the United States of America *94*, 10997-11002.

Maerker, T., van Wijk, E., Overlack, N., Kersten, F.F., McGee, J., Goldmann, T., Sehn, E., Roepman, R., Walsh, E.J., Kremer, H., *et al.* (2008). A novel Usher protein network at the periciliary reloading point between molecular transport machineries in vertebrate photoreceptor cells. Human molecular genetics *17*, 71-86.

Marcotti, W., Corns, L.F., Goodyear, R.J., Rzadzinska, A.K., Avraham, K.B., Steel, K.P., Richardson, G.P., and Kros, C.J. (2016). The acquisition of mechano-electrical transducer current adaptation in auditory hair cells requires myosin VI. The Journal of physiology *594*, 3667-3681.

Markin, V.S., and Hudspeth, A.J. (1995). Gating-spring models of mechanoelectrical transduction by hair cells of the internal ear. Annual review of biophysics and biomolecular structure *24*, 59-83.

Marquis, R.E., and Hudspeth, A.J. (1997). Effects of extracellular Ca2+ concentration on hair-bundle stiffness and gating-spring integrity in hair cells. Proceedings of the National Academy of Sciences of the United States of America *94*, 11923-11928.

Martin, P., Mehta, A.D., and Hudspeth, A.J. (2000). Negative hair-bundle stiffness betrays a mechanism for mechanical amplification by the hair cell. Proceedings of the National Academy of Sciences of the United States of America *97*, 12026-12031.

Mburu, P., Mustapha, M., Varela, A., Weil, D., El-Amraoui, A., Holme, R.H., Rump, A., Hardisty, R.E., Blanchard, S., Coimbra, R.S.*, et al.* (2003). Defects in whirlin, a PDZ domain molecule involved in stereocilia elongation, cause deafness in the whirler mouse and families with DFNB31. Nature genetics *34*, 421-428.

McGlone, F.P., Russell, I.J., and Sand, O. (1979). Measurement of calcium ion concentrations in the lateral line cupulae of Xenopus laevis. The Journal of experimental biology *83*, 123-130.

McGrath, J., Roy, P., and Perrin, B.J. (2017). Stereocilia morphogenesis and maintenance through regulation of actin stability. Seminars in cell & developmental biology *65*, 88-95.

Melchionda, S., Ahituv, N., Bisceglia, L., Sobe, T., Glaser, F., Rabionet, R., Arbones, M.L., Notarangelo, A., Di Iorio, E., Carella, M.*, et al.* (2001). MYO6, the human homologue of the gene responsible for deafness in Snell's waltzer mice, is mutated in autosomal dominant nonsyndromic hearing loss. American journal of human genetics *69*, 635-640.

Michel, V., Booth, K.T., Patni, P., Cortese, M., Azaiez, H., Bahloul, A., Kahrizi, K., Labbe, M., Emptoz, A., Lelli, A.*, et al.* (2017). CIB2, defective in isolated deafness, is key for auditory hair cell mechanotransduction and survival. EMBO molecular medicine *9*, 1711-1731.

Miroux, B., and Walker, J.E. (1996). Over-production of proteins in Escherichia coli: mutant hosts that allow synthesis of some membrane proteins and globular proteins at high levels. Journal of molecular biology *260*, 289-298.

Mitchem, K.L., Hibbard, E., Beyer, L.A., Bosom, K., Dootz, G.A., Dolan, D.F., Johnson, K.R., Raphael, Y., and Kohrman, D.C. (2002). Mutation of the novel gene Tmie results in sensory cell defects in the inner ear of spinner, a mouse model of human hearing loss DFNB6. Human molecular genetics *11*, 1887-1898.

Modak, D., and Sotomayor, M. (2019). Identification of an adhesive interface for the non-clustered delta1 protocadherin-1 involved in respiratory diseases. Communications biology *2*, 354.

Nagar, B., Overduin, M., Ikura, M., and Rini, J.M. (1996). Structural basis of calcium-induced E-cadherin rigidification and dimerization. Nature *380*, 360-364.

Nam, J.H., Peng, A.W., and Ricci, A.J. (2015). Underestimated sensitivity of mammalian cochlear hair cells due to splay between stereociliary columns. Biophysical journal *108*, 2633-2647.

Nayak, G.D., Ratnayaka, H.S., Goodyear, R.J., and Richardson, G.P. (2007). Development of the hair bundle and mechanotransduction. The International journal of developmental biology *51*, 597-608.

Naz, S., Giguere, C.M., Kohrman, D.C., Mitchem, K.L., Riazuddin, S., Morell, R.J., Ramesh, A., Srisailpathy, S., Deshmukh, D., Riazuddin, S*., et al.* (2002). Mutations in a novel gene, TMIE, are associated with hearing loss linked to the DFNB6 locus. American journal of human genetics *71*, 632-636.

Neuman, K.C., Chadd, E.H., Liou, G.F., Bergman, K., and Block, S.M. (1999). Characterization of photodamage to Escherichia coli in optical traps. Biophysical journal *77*, 2856-2863.

Neuman, K.C., and Nagy, A. (2008). Single-molecule force spectroscopy: optical tweezers, magnetic tweezers and atomic force microscopy. Nature methods *5*, 491-505.

Nishikawa, S., and Sasaki, F. (1996). Internalization of styryl dye FM1-43 in the hair cells of lateral line organs in Xenopus larvae. The journal of histochemistry and cytochemistry : official journal of the Histochemistry Society *44*, 733-741.

O'Maoileidigh, D., and Ricci, A.J. (2019). A Bundle of Mechanisms: Inner-Ear Hair-Cell Mechanotransduction. Trends in neurosciences *42*, 221-236.

Oberhauser, A.F., Hansma, P.K., Carrion-Vazquez, M., and Fernandez, J.M. (2001). Stepwise unfolding of titin under force-clamp atomic force microscopy. Proceedings of the National Academy of Sciences of the United States of America *98*, 468-472.

Ohmori, H. (1985). Mechano-electrical transduction currents in isolated vestibular hair cells of the chick. The Journal of physiology *359*, 189-217.

Pacentine, I.V., and Nicolson, T. (2019). Subunits of the mechano-electrical transduction channel, Tmc1/2b, require Tmie to localize in zebrafish sensory hair cells. PLoS genetics *15*, e1007635.

Pan, B., Akyuz, N., Liu, X.P., Asai, Y., Nist-Lund, C., Kurima, K., Derfler, B.H., Gyorgy, B., Limapichat, W., Walujkar, S*., et al.* (2018). TMC1 Forms the Pore of Mechanosensory Transduction Channels in Vertebrate Inner Ear Hair Cells. Neuron *99*, 736-753 e736.

Pan, B., Geleoc, G.S., Asai, Y., Horwitz, G.C., Kurima, K., Ishikawa, K., Kawashima, Y., Griffith, A.J., and Holt, J.R. (2013). TMC1 and TMC2 are components of the mechanotransduction channel in hair cells of the mammalian inner ear. Neuron *79*, 504-515.

Pan, B., Waguespack, J., Schnee, M.E., LeBlanc, C., and Ricci, A.J. (2012). Permeation properties of the hair cell mechanotransducer channel provide insight into its molecular structure. Journal of neurophysiology *107*, 2408-2420.

Pandalaneni, S., Karuppiah, V., Saleem, M., Haynes, L.P., Burgoyne, R.D., Mayans, O., Derrick, J.P., and Lian, L.Y. (2015). Neuronal Calcium Sensor-1 Binds the D2 Dopamine Receptor and G-protein-coupled Receptor Kinase 1 (GRK1) Peptides Using Different Modes of Interactions. The Journal of biological chemistry *290*, 18744-18756.

Patel, K., Giese, A.P., Grossheim, J.M., Hegde, R.S., Delio, M., Samanich, J., Riazuddin, S., Frolenkov, G.I., Cai, J., Ahmed, Z.M.*, et al.* (2015). A Novel C-Terminal CIB2 (Calcium and Integrin Binding Protein 2) Mutation Associated with Non-Syndromic Hearing Loss in a Hispanic Family. PloS one *10*, e0133082.

Patel, S.D., Ciatto, C., Chen, C.P., Bahna, F., Rajebhosale, M., Arkus, N., Schieren, I., Jessell, T.M., Honig, B., Price, S.R.*, et al.* (2006). Type II cadherin ectodomain structures: implications for classical cadherin specificity. Cell *124*, 1255-1268.

Peng, A.W., Effertz, T., and Ricci, A.J. (2013). Adaptation of mammalian auditory hair cell mechanotransduction is independent of calcium entry. Neuron *80*, 960-972.

Peng, A.W., Gnanasambandam, R., Sachs, F., and Ricci, A.J. (2016). Adaptation Independent Modulation of Auditory Hair Cell Mechanotransduction Channel Open Probability Implicates a Role for the Lipid Bilayer. The Journal of neuroscience : the official journal of the Society for Neuroscience *36*, 2945-2956.

Pepermans, E., Michel, V., Goodyear, R., Bonnet, C., Abdi, S., Dupont, T., Gherbi, S., Holder, M., Makrelouf, M., Hardelin, J.P.*, et al.* (2014). The CD2 isoform of protocadherin-15 is an essential component of the tip-link complex in mature auditory hair cells. EMBO molecular medicine *6*, 984-992.

Pepermans, E., and Petit, C. (2015). The tip-link molecular complex of the auditory mechano-electrical transduction machinery. Hearing research *330*, 10-17.

Pertz, O., Bozic, D., Koch, A.W., Fauser, C., Brancaccio, A., and Engel, J. (1999). A new crystal structure, Ca2+ dependence and mutational analysis reveal molecular details of E-cadherin homoassociation. The EMBO journal *18*, 1738-1747.

Phillips, K.R., Tong, S., Goodyear, R., Richardson, G.P., and Cyr, J.L. (2006). Stereociliary myosin-1c receptors are sensitive to calcium chelation and absent from cadherin 23 mutant mice. The Journal of neuroscience : the official journal of the Society for Neuroscience *26*, 10777-10788.

Pickles, J.O., Comis, S.D., and Osborne, M.P. (1984). Cross-links between stereocilia in the guinea pig organ of Corti, and their possible relation to sensory transduction. Hearing research *15*, 103-112.

Powers, R.E., Gaudet, R., and Sotomayor, M. (2017). A Partial Calcium-Free Linker Confers Flexibility to Inner-Ear Protocadherin-15. Structure *25*, 482-495.

Pralle, A., Prummer, M., Florin, E.L., Stelzer, E.H., and Horber, J.K. (1999). Three-dimensional high-resolution particle tracking for optical tweezers by forward scattered light. Microscopy research and technique *44*, 378-386.

Riazuddin, S., Belyantseva, I.A., Giese, A.P., Lee, K., Indzhykulian, A.A., Nandamuri, S.P., Yousaf, R., Sinha, G.P., Lee, S., Terrell, D*., et al.* (2012). Alterations of the CIB2 calcium- and integrin-binding protein cause Usher syndrome type 1J and nonsyndromic deafness DFNB48. Nature genetics *44*, 1265-1271.

Ricci, A.J., Crawford, A.C., and Fettiplace, R. (2000). Active hair bundle motion linked to fast transducer adaptation in auditory hair cells. The Journal of neuroscience : the official journal of the Society for Neuroscience *20*, 7131-7142.

Ricci, A.J., Crawford, A.C., and Fettiplace, R. (2003). Tonotopic variation in the conductance of the hair cell mechanotransducer channel. Neuron *40*, 983-990.

Ricci, A.J., and Fettiplace, R. (1997). The effects of calcium buffering and cyclic AMP on mechano-electrical transduction in turtle auditory hair cells. The Journal of physiology *501 (Pt 1)*, 111-124.

Ricci, A.J., and Fettiplace, R. (1998). Calcium permeation of the turtle hair cell mechanotransducer channel and its relation to the composition of endolymph. The Journal of physiology *506 (Pt 1)*, 159-173.

Ricci, A.J., Kennedy, H.J., Crawford, A.C., and Fettiplace, R. (2005). The transduction channel filter in auditory hair cells. The Journal of neuroscience : the official journal of the Society for Neuroscience *25*, 7831-7839.

Ricci, A.J., Wu, Y.C., and Fettiplace, R. (1998). The endogenous calcium buffer and the time course of transducer adaptation in auditory hair cells. The Journal of neuroscience : the official journal of the Society for Neuroscience *18*, 8261-8277.

Richardson, G.P., and Petit, C. (2019). Hair-Bundle Links: Genetics as the Gateway to Function. Cold Spring Harbor perspectives in medicine *9*.

Rohrbach, A., and Stelzer, E.H. (2002). Three-dimensional position detection of optically trapped dielectric particles. Journal of Applied Physics *91*, 5474-5488.

Rubinstein, R., Goodman, K.M., Maniatis, T., Shapiro, L., and Honig, B. (2017). Structural origins of clustered protocadherin-mediated neuronal barcoding. Seminars in cell & developmental biology *69*, 140-150.

Russell, I.J., and Sellick, P.M. (1976). Measurement of potassium and chloride ion concentrations in the cupulae of the lateral lines of Xenopus laevis. The Journal of physiology *257*, 245-255.

Salles, F.T., Merritt, R.C., Jr., Manor, U., Dougherty, G.W., Sousa, A.D., Moore, J.E., Yengo, C.M., Dose, A.C., and Kachar, B. (2009). Myosin IIIa boosts elongation of stereocilia by transporting espin 1 to the plus ends of actin filaments. Nature cell biology *11*, 443-450.

Salt, A.N., Inamura, N., Thalmann, R., and Vora, A. (1989). Calcium gradients in inner ear endolymph. American journal of otolaryngology *10*, 371-375.

Schneider, M.E., Dose, A.C., Salles, F.T., Chang, W., Erickson, F.L., Burnside, B., and Kachar, B. (2006). A new compartment at stereocilia tips defined by spatial and temporal patterns of myosin IIIa expression. The Journal of neuroscience : the official journal of the Society for Neuroscience *26*, 10243-10252.

Schwander, M., Xiong, W., Tokita, J., Lelli, A., Elledge, H.M., Kazmierczak, P., Sczaniecka, A., Kolatkar, A., Wiltshire, T., Kuhn, P.*, et al.* (2009). A mouse model for nonsyndromic deafness (DFNB12) links hearing loss to defects in tip links of mechanosensory hair cells. Proceedings of the National Academy of Sciences of the United States of America *106*, 5252-5257.

Seco, C.Z., Giese, A.P., Shafique, S., Schraders, M., Oonk, A.M., Grossheim, M., Oostrik, J., Strom, T., Hegde, R., van Wijk, E.*, et al.* (2016). Novel and recurrent CIB2 variants, associated with nonsyndromic deafness, do not affect calcium buffering and localization in hair cells. European journal of human genetics : EJHG *24*, 542-549.

Sellick, P.M., Patuzzi, R., and Johnstone, B.M. (1982). Measurement of basilar membrane motion in the guinea pig using the Mossbauer technique. J Acoust Soc Am *72*, 131-141.

Senften, M., Schwander, M., Kazmierczak, P., Lillo, C., Shin, J.B., Hasson, T., Geleoc, G.S., Gillespie, P.G., Williams, D., Holt, J.R.*, et al.* (2006). Physical and functional interaction between protocadherin 15 and myosin VIIa in mechanosensory hair cells. The Journal of neuroscience : the official journal of the Society for Neuroscience *26*, 2060-2071.

Shabbir, M.I., Ahmed, Z.M., Khan, S.Y., Riazuddin, S., Waryah, A.M., Khan, S.N., Camps, R.D., Ghosh, M., Kabra, M., Belyantseva, I.A.*, et al.* (2006). Mutations of human TMHS cause recessively inherited non-syndromic hearing loss. Journal of medical genetics *43*, 634-640.

Shapiro, L., Fannon, A.M., Kwong, P.D., Thompson, A., Lehmann, M.S., Grubel, G., Legrand, J.F., Als-Nielsen, J., Colman, D.R., and Hendrickson, W.A. (1995). Structural basis of cell-cell adhesion by cadherins. Nature *374*, 327-337.

Shen, Y.C., Jeyabalan, A.K., Wu, K.L., Hunker, K.L., Kohrman, D.C., Thompson, D.L., Liu, D., and Barald, K.F. (2008). The transmembrane inner ear (tmie) gene contributes to vestibular and lateral line development and function in the zebrafish (Danio rerio). Developmental dynamics : an official publication of the American Association of Anatomists *237*, 941-952.

Shotwell, S.L., Jacobs, R., and Hudspeth, A.J. (1981). Directional sensitivity of individual vertebrate hair cells to controlled deflection of their hair bundles. Annals of the New York Academy of Sciences *374*, 1-10.

Siemens, J., Lillo, C., Dumont, R.A., Reynolds, A., Williams, D.S., Gillespie, P.G., and Muller, U. (2004). Cadherin 23 is a component of the tip link in hair-cell stereocilia. Nature *428*, 950-955.

Sigworth, F.J. (2016). Principles of cryo-EM single-particle image processing. Microscopy *65*, 57-67.

Sotomayor, M., Weihofen, W.A., Gaudet, R., and Corey, D.P. (2010). Structural determinants of cadherin-23 function in hearing and deafness. Neuron *66*, 85-100.

Sotomayor, M., Weihofen, W.A., Gaudet, R., and Corey, D.P. (2012). Structure of a force-conveying cadherin bond essential for inner-ear mechanotransduction. Nature *492*, 128-132.

Spoor, F., and Zonneveld, F. (1998). Comparative review of the human bony labyrinth. American journal of physical anthropology *Suppl 27*, 211-251.

Stauffer, E.A., Scarborough, J.D., Hirono, M., Miller, E.D., Shah, K., Mercer, J.A., Holt, J.R., and Gillespie, P.G. (2005). Fast adaptation in vestibular hair cells requires myosin-1c activity. Neuron *47*, 541-553.

Stepanyan, R., and Frolenkov, G.I. (2009). Fast adaptation and Ca2+ sensitivity of the mechanotransducer require myosin-XVa in inner but not outer cochlear hair cells. The Journal of neuroscience : the official journal of the Society for Neuroscience *29*, 4023-4034.

Tamura, K., Shan, W.S., Hendrickson, W.A., Colman, D.R., and Shapiro, L. (1998). Structure-function analysis of cell adhesion by neural (N-) cadherin. Neuron *20*, 1153-1163.

Tanaka, K., and Smith, C.A. (1978). Structure of the chicken's inner ear: SEM and TEM study. The American journal of anatomy *153*, 251-271.

Tobin, M., Chaiyasitdhi, A., Michel, V., Michalski, N., and Martin, P. (2019). Stiffness and tension gradients of the hair cell's tip-link complex in the mammalian cochlea. eLife *8*.

Tsuprun, V., Goodyear, R.J., and Richardson, G.P. (2004). The structure of tip links and kinocilial links in avian sensory hair bundles. Biophysical journal *87*, 4106-4112.

Twomey, E.C., Yelshanskaya, M.V., Grassucci, R.A., Frank, J., and Sobolevsky, A.I. (2016). Elucidation of AMPA receptor-stargazin complexes by cryo-electron microscopy. Science *353*, 83-86.

Vallone, R., Dal Cortivo, G., D'Onofrio, M., and Dell'Orco, D. (2018). Preferential Binding of Mg(2+) Over Ca(2+) to CIB2 Triggers an Allosteric Switch Impaired in Usher Syndrome Type 1J. Frontiers in molecular neuroscience *11*, 274.

Vassylyeva, M.N., Klyuyev, S., Vassylyev, A.D., Wesson, H., Zhang, Z., Renfrow, M.B., Wang, H., Higgins, N.P., Chow, L.T., and Vassylyev, D.G. (2017). Efficient, ultra-high-affinity chromatography in a one-step purification of complex proteins. Proceedings of the National Academy of Sciences of the United States of America *114*, E5138-E5147.

Verpy, E., Leibovici, M., Michalski, N., Goodyear, R.J., Houdon, C., Weil, D., Richardson, G.P., and Petit, C. (2011). Stereocilin connects outer hair cell stereocilia to one another and to the tectorial membrane. The Journal of comparative neurology *519*, 194-210.

Verpy, E., Leibovici, M., Zwaenepoel, I., Liu, X.Z., Gal, A., Salem, N., Mansour, A., Blanchard, S., Kobayashi, I., Keats, B.J*., et al.* (2000). A defect in harmonin, a PDZ domain-containing protein expressed in the inner ear sensory hair cells, underlies Usher syndrome type 1C. Nature genetics *26*, 51-55.

Vollrath, M.A., and Eatock, R.A. (2003). Time course and extent of mechanotransducer adaptation in mouse utricular hair cells: comparison with frog saccular hair cells. Journal of neurophysiology *90*, 2676-2689.

von Bekesy, G. (1970). Travelling waves as frequency analysers in the cochlea. Nature *225*, 1207-1209.

Vreugde, S., Erven, A., Kros, C.J., Marcotti, W., Fuchs, H., Kurima, K., Wilcox, E.R., Friedman, T.B., Griffith, A.J., Balling, R*., et al.* (2002). Beethoven, a mouse model for dominant, progressive hearing loss DFNA36. Nature genetics *30*, 257-258.

Walker, R.G., and Hudspeth, A.J. (1996). Calmodulin controls adaptation of mechanoelectrical transduction by hair cells of the bullfrog's sacculus. Proceedings of the National Academy of Sciences of the United States of America *93*, 2203-2207.

Wallis, R., Leung, K.Y., Pommer, A.J., Videler, H., Moore, G.R., James, R., and Kleanthous, C. (1995a). Protein-protein interactions in colicin E9 DNase-immunity protein complexes. 2. Cognate and noncognate interactions that span the millimolar to femtomolar affinity range. Biochemistry *34*, 13751-13759.

Wallis, R., Moore, G.R., James, R., and Kleanthous, C. (1995b). Protein-protein interactions in colicin E9 DNase-immunity protein complexes. 1. Diffusion-controlled association and femtomolar binding for the cognate complex. Biochemistry *34*, 13743-13750.

Walsh, T., Walsh, V., Vreugde, S., Hertzano, R., Shahin, H., Haika, S., Lee, M.K., Kanaan, M., King, M.C., and Avraham, K.B. (2002). From flies' eyes to our ears: mutations in a human class III myosin cause progressive nonsyndromic hearing loss DFNB30. Proceedings of the National Academy of Sciences of the United States of America *99*, 7518-7523.

Wang, A., Liang, Y., Fridell, R.A., Probst, F.J., Wilcox, E.R., Touchman, J.W., Morton, C.C., Morell, R.J., Noben-Trauth, K., Camper, S.A*., et al.* (1998). Association of unconventional myosin MYO15 mutations with human nonsyndromic deafness DFNB3. Science *280*, 1447-1451.

Wang, H., Yan, Y., Liu, Q., Huang, Y., Shen, Y., Chen, L., Chen, Y., Yang, Q., Hao, Q., Wang, K*., et al.* (2007). Structural basis for modulation of Kv4 K+ channels by auxiliary KChIP subunits. Nature neuroscience *10*, 32-39.

Wang, M.D., Yin, H., Landick, R., Gelles, J., and Block, S.M. (1997). Stretching DNA with optical tweezers. Biophysical journal *72*, 1335-1346.

Wang, X., Li, G., Liu, J., Liu, J., and Xu, X.Z. (2016). TMC-1 Mediates Alkaline Sensation in C. elegans through Nociceptive Neurons. Neuron *91*, 146-154.

Weil, D., Blanchard, S., Kaplan, J., Guilford, P., Gibson, F., Walsh, J., Mburu, P., Varela, A., Levilliers, J., Weston, M.D., *et al.* (1995). Defective myosin VIIA gene responsible for Usher syndrome type 1B. Nature *374*, 60-61.

Weil, D., El-Amraoui, A., Masmoudi, S., Mustapha, M., Kikkawa, Y., Laine, S., Delmaghani, S., Adato, A., Nadifi, S., Zina, Z.B., *et al.* (2003). Usher syndrome type I G (USH1G) is caused by mutations in the gene encoding SANS, a protein that associates with the USH1C protein, harmonin. Human molecular genetics *12*, 463-471.

Weil, D., Kussel, P., Blanchard, S., Levy, G., Levi-Acobas, F., Drira, M., Ayadi, H., and Petit, C. (1997). The autosomal recessive isolated deafness, DFNB2, and the Usher 1B syndrome are allelic defects of the myosin-VIIA gene. Nature genetics *16*, 191-193.

Wu, Y.C., Ricci, A.J., and Fettiplace, R. (1999). Two components of transducer adaptation in auditory hair cells. Journal of neurophysiology *82*, 2171-2181.

Xiong, W., Grillet, N., Elledge, H.M., Wagner, T.F., Zhao, B., Johnson, K.R., Kazmierczak, P., and Muller, U. (2012). TMHS is an integral component of the mechanotransduction machinery of cochlear hair cells. Cell *151*, 1283-1295.

Xiong, W., Wagner, T., Yan, L., Grillet, N., and Muller, U. (2014). Using injectoporation to deliver genes to mechanosensory hair cells. Nature protocols *9*, 2438-2449.

Yagi, H., Tokano, H., Maeda, M., Takabayashi, T., Nagano, T., Kiyama, H., Fujieda, S., Kitamura, K., and Sato, M. (2007). Vlgr1 is required for proper stereocilia maturation of cochlear hair cells. Genes to cells : devoted to molecular & cellular mechanisms *12*, 235-250.

Yamoah, E.N., Lumpkin, E.A., Dumont, R.A., Smith, P.J., Hudspeth, A.J., and Gillespie, P.G. (1998). Plasma membrane Ca2+-ATPase extrudes Ca2+ from hair cell stereocilia. The Journal of neuroscience : the official journal of the Society for Neuroscience *18*, 610-624.

Yue, X., Zhao, J., Li, X., Fan, Y., Duan, D., Zhang, X., Zou, W., Sheng, Y., Zhang, T., Yang, Q., *et al.* (2018). TMC Proteins Modulate Egg Laying and Membrane Excitability through a Background Leak Conductance in C. elegans. Neuron *97*, 571-585 e575.

Zenner, H.P. (1986). Motile responses in outer hair cells. Hearing research *22*, 83-90.

Zhao, B., and Muller, U. (2015). The elusive mechanotransduction machinery of hair cells. Current opinion in neurobiology *34*, 172-179.

Zhao, B., Wu, Z., Grillet, N., Yan, L., Xiong, W., Harkins-Perry, S., and Muller, U. (2014). TMIE is an essential component of the mechanotransduction machinery of cochlear hair cells. Neuron *84*, 954-967.

Zhao, H., Brown, P.H., and Schuck, P. (2011). On the distribution of protein refractive index increments. Biophysical journal *100*, 2309-2317.

Zhao, Y., Yamoah, E.N., and Gillespie, P.G. (1996). Regeneration of broken tip links and restoration of mechanical transduction in hair cells. Proceedings of the National Academy of Sciences of the United States of America *93*, 15469-15474.